

**JERS-1 SAR and Landsat-5 TM image data fusion: an
application approach for lithological mapping**

by

Abdullah Khzam M. Al-Mahri

A thesis submitted to the University of London for the Degree of Doctor of Philosophy in
Electronic and Electrical Engineering

Department of Electronic and Electrical Engineering
University College London

July 1999

ProQuest Number: 10609798

All rights reserved

INFORMATION TO ALL USERS

The quality of this reproduction is dependent upon the quality of the copy submitted.

In the unlikely event that the author did not send a complete manuscript and there are missing pages, these will be noted. Also, if material had to be removed, a note will indicate the deletion.



ProQuest 10609798

Published by ProQuest LLC (2017). Copyright of the Dissertation is held by the Author.

All rights reserved.

This work is protected against unauthorized copying under Title 17, United States Code
Microform Edition © ProQuest LLC.

ProQuest LLC.
789 East Eisenhower Parkway
P.O. Box 1346
Ann Arbor, MI 48106 – 1346

Abstract

Satellite image data fusion is an image processing set of procedures utilise either for image optimisation for visual photointerpretation, or for automated thematic classification with low error rate and high accuracy. Lithological mapping using remote sensing image data relies on the spectral and textural information of the rock units of the area to be mapped. These pieces of information can be derived from Landsat optical TM and JERS-1 SAR images respectively. Prior to extracting such information (spectral and textural) and fusing them together, geometric image co-registration between TM and the SAR, atmospheric correction of the TM, and SAR despeckling are required. In this thesis, an appropriate atmospheric model is developed and implemented utilising the dark pixel subtraction method for atmospheric correction. For SAR despeckling, an efficient new method is also developed to test whether the SAR filter used remove the textural information or not. For image optimisation for visual photointerpretation, a new method of spectral coding of the six bands of the optical TM data is developed. The new spectral coding method is used to produce efficient colour composite with high separability between the spectral classes similar to that if the whole six optical TM bands are used together. This spectral coded colour composite is used as a spectral component, which is then fused with the textural component represented by the despeckled JERS-1 SAR using the fusion tools, including the colour transform and the PCT. The Grey Level Co-occurrence Matrix (GLCM) technique is used to build the textural data set using the speckle filtered JERS-1 SAR data making seven textural GLCM measures.

For automated thematic mapping and by the use of both the six TM spectral data and the seven textural GLCM measures, a new method of classification has been developed using the Maximum Likelihood Classifier (MLC). The method is named the sequential maximum likelihood classification and works efficiently by comparison the classified textural pixels, the classified spectral pixels, and the classified textural-spectral pixels. and gives the means of utilising the textural and spectral information for automated lithological mapping.

*I dedicate this work to my mother, my wife, my son Saud,
and my daughter Haifa.*

Declaration

I hereby declare this Ph.D. thesis is my own work and has not been submitted before as a thesis to any University department or Educational institute. Every part of this thesis is my own work except where otherwise indicated.

Abdullah K. Al-Mahri

Acknowledgements

My grateful thanks go to my supervisor Professor Hugh Griffiths firstly for introducing me to the field of radar remote sensing and secondly for his continuous advice and constructive discussions during the period of the preparation of this thesis. I am most grateful also to my wife Laila for her patience and understanding and for her sharing with me the hard days of being a postgraduate student.

Thanks also go to King Abdulaziz City for Science and Technology (KACST) for giving me the opportunity and sponsoring me to carry out this work. Thanks also go to MITI/NASDA, ERSDAC for allowing me to use their SAR data of JERS-1.

Thanks also go to Richard Bullock and Dr. Lluís Vinagre, my colleagues of the Antennas and Radar group for responding when help or advice was needed.

List of contents

Abstract	2
Acknowledgements	5
List of contents	6
List of figures	9
List of tables	16
Chapter 1-Introduction	19
1.1 Materials used in the study	21
1.2 Objectives of the thesis	22
1.3 The test site	22
1.3.1 Physiography of the test site	23
1.3.2 Lithology of the test site	23
Chapter 2- Platforms and sensors	30
2.1 Landsat-5	30
2.2 JERS-1	32
2.2.1 JERS-1 SAR image construction	35
2.3 Interaction of electromagnetic waves with matter	40
Chapter 3- Synthetic Aperture Radar	52
3.1 Historical background	52
3.2 Geometry of imaging radar	54
3.3 Pulse compression	56
3.4 Azimuth compression and the synthetic aperture technique	58
3.5 The SAR radar equation	70
3.6 Ambiguities in SAR	71
3.7 Geometric distortions in SAR	73
3.8 SAR data processing	79
Chapter 4- Pre-processing of optical TM and JERS-1 SAR data	82
4.1 The JERS-1 SAR 16-bit to 8-bit compression	83
4.2 Mosaicking and image to image registration	84
4.3 Atmospheric correction of the optical TM data	91

4.4 SAR speckle reduction	98
4.5 SAR speckle filters	102
4.6 Results and comparison of speckle filters	106
4.7 Conclusions and remarks	113
Chapter 5- JERS-1 spatial information extraction	115
5.1 Parameters controlling SAR for texture and lineation detection	117
5.2 Previous studies in texture, and texture analysis in geology	120
5.3 Strategy used in this study for texture enhancement	126
5.4 Conclusions and remarks	138
Chapter 6- Image data fusion - Optimisation for visual analysis	139
6.1 Introduction	139
6.2 Models of data fusion	142
6.3 Background and previous work in image data fusion	145
6.4 The colour composite band selection/reduction - A new solution	154
6.5 Using the spectral unit as a method of TM spectral coding	157
6.5.1 Properties of the spectral coding algorithm	158
6.5.2 Procedure of producing the spectral coded image	160
6.5.3 Results of using the spectral coded image of TM data and creating colour composite	161
6.6 Comparison between the spectral coded colour composite and the traditional methods of colour composite selection	168
6.7 Image fusion using colour transform	179
6.8 TM and SAR colour transform fusion	185
6.9 Data fusion using the principal component transform	202
6.10 Conclusions and remarks	207
Chapter 7- Image data fusion for automated mapping	210
7.1 The maximum likelihood classifier	211
7.2 The post classification filtering	212
7.3 Previous work in classification	213
7.4 The sequential approach of classification used for both the spectral and textural input data.	219

7.5 Classification results	223
7.6 Accuracy estimation	235
7.7 Conclusions and remarks	243
Chapter 8- Conclusions	245
8.1 Ideas for further work	247
Appendix	249
References	264

List of figures

- Figure 1.1 The area of study as shown by NOAA 12 AVHRR band 2.
- Figure 1.2 Geologic map of the test site.
- Figure 1.3 A photograph shows the Jurfayn complex (in dark green) and the Atiyah monzogranite (light brown).
- Figure 1.4 Nutaysh formation.
- Figure 1.5 Nutaysh overlies Musayr.
- Figure 1.6 Bad' formation.
- Figure 1.7 The Sabkhah as photographed during the test site field work.
- Figure 2.1 JERS-1 SAR observation geometry.
- Figure 2.2 Spectral reflectance of rock sample taken from Al' Bad formation.
- Figure 2.3 Spectral reflectance of sample collected from Nutaish Formation.
- Figure 2.4 Measured spectral reflectance of a sample taken from Atiyah monzogranite.
- Figure 2.5 Spectral reflectance measurement of sample taken from Jurfayn complex.
- Figure 2.6 The spectral reflectance of Sabkhah deposits.
- Figure 2.7 The spectral reflectance of the gravel sheet deposits.
- Figure 2.8 Locations of rock unit classes of the study area marked on TM band 5.
- Figure 3.1 (a) Basic geometry of imaging radar. (b) viewing the geometry from azimuth, the ground swath is clearly demonstrated as a function of the beamwidth.
- Figure 3.2 (a) Reconstruction of linear frequency modulated JERS-1 SAR signal. The bandwidth (Δf) 15 MHz is represented by the y-axis and centred at the frequency (f_0) of 1275 MHz. The frequency is decreasing along the x-axis (the dispersion) in 35

microsecond. (b) The waveform of the JERS-1 SAR FM signal.

- Figure 3.3 SAR co-ordinate system.
- Figure 3.4 Echo phase changes as a function of x .
- Figure 3.5 Doppler frequency as a function of x .
- Figure 3.6 SAR imaging geometry.
- Figure 3.7 Synthetic aperture technique using long synthetic array.
- Figure 3.8 Range curvature and range walk.
- Figure 3.9 The depth of focus.
- Figure 3.10 Synthesising the aperture using Doppler technique. The upper figure is representing the Doppler shift.
- Figure 3.11 Doppler equi-distances and equi-Doppler of Synthetic Aperture Imaging Systems.
- Figure 3.12 The oblate ellipsoid model of the Earth.
- Figure 3.13 (a) Satellite yaw displacement, and (b) pitch displacement.
- Figure 3.14 Target location error as a result of the target location.
- Figure 3.15 comparison between ground range and slant range image.
- Figure 3.16 Geometric distortion in SAR images.
- Figure 3.17 SAR image processing data flow diagram.
- Figure 3.18 SAR processing using FFT correlator.
- Figure 4.1 shows a schematic presentation of the JERS-1 SAR and Landsat-5 TM optical data of the study area.
- Figure 4.2 JERS-1 SAR range illumination angles variations.
- Figure 4.3 a: The JERS-1 registered, mosaicked and contrast averaged 4 SAR scenes of the study area.
- b: The reference Landsat 5 optical TM band 5 image. Band 5 has been selected because of its high contrast where control points can be selected easily.
- Figure 4.4 Theoretical scattering of the model λ^{-3} which precisely matches scattering of the area of study. Note that the scattering

in band 1 is 44.5% and decrease exponentially to approach zero in the infra-red wavelengths. The axis y = the percentage probability.

- Figure 4.5 Speckle formation of a distributed targets A and B separated by distance d . The SAR returns amplitude fluctuate with width equal to $\lambda h / dv$.
- Figure 4.6 Original JERS-1 SAR 3-look image after applying Balance Contrast Stretching Technique.
- Figure 4.7 Frost 3 by 3 filtered image, note how speckle is removed.
- Figure 4.8 Frost 5 by 5 filtered image, speckle is removed completely but with very little textural information loss.
- Figure 4.9 The speckle image extracted through the Frost 3 by 3 filtering process, note that there are no recognised textural or shape patterns indicating no textural information loss.
- Figure 5.1 SAR illumination angle and lineation orientation relationships.
- Figure 5.2 Binary filters implemented on the FFT transformed images, the size of the filter has to be equal to the size of the image. Black = zero, white = 1. (a) lowpass-filter, (b) highpass-filter, (c) bandpass-filter, (d) cut pass filter, (e) directional filter eliminates all 45 degree lineation features, and (f and g) are wedge-ring intersection filters of different angles.
- Figure 5.3 GLCM of an image of grey level g_n ranges from 0-3. If the image is 8 bit, the GLCM will be 256 by 256 in dimension. The $\#(i,j)$ entry refers to the number of times grey level in the image of intensity I and j in the GLCM separated by a distance d and angle θ have been neighbours. Note that the GLCM is symmetrical along its diagonal (i.e. $\#(i,j) = \#(j,i)$).
- Figure 5.4 GLCM texture measure of Inverse Difference Moment.
- Figure 5.5 GLCM texture measure of contrast.
- Figure 5.6 GLCM texture measure of dissimilarity.

Figure 5.7	GLCM texture measure of mean.
Figure 5.8	GLCM texture measure of Entropy.
Figure 5.9	GLCM texture measure of angular second moment ASM.
Figure 5.10	GLCM texture measure of correlation.
Figure 6.1	All possible information which can be collected by remote sensing platforms.
Figure 6.2	Configuration of fusion models (A) the multispectral model, (B) the multispectral / multisensor fusion model.
Figure 6.3	A theoretical image set consists of four bands, band-1 shows clear feature (class-a), band-2 shows feature b, band-3 shows feature c, and band-4 shows feature d.
Figure 6.4	Figure 6.4 A grey scaled TM spectral coded image after applying 5x5mode filter and scaled to 8-bit.
Figure 6.5	Pseudo-colour coded image of the spectral coding of the 6 TM image data.
Figure 6.6	Class ellipsoids of the test site using the TM spectral coded image plotted on the abscissa and the TM albedo and topographic information image plotted in the ordinate.
Figure 6.7	Representing a pixel vector of colour composite using the spectral code value, the albedo-topographic information, and the range value. Pixel number 3 in table 6.1 is taken for the representation.
Figure 6.8	a colour composite using spectral code of the 6 TM bands, the albedo-topographic image, and the range image displayed in red, green, and blue respectively. Automatic stretching has been applied on the green and blue bands only.
Figure 6.9	Colour composite of TM bands 3,2, and 1 displayed in red, green, and blue respectively. Data is firstly BCET stretched.
Figure 6.10	Colour composite using bands 4, 3, and 2 displayed in red, green, and blue respectively. Data are stretched using BCET.
Figure 6.11	Colour composite using bands 5, 3, and 1 displayed in red,

- green, and blue respectively. Data are stretched using BCET.
- Figure 6.12 Colour composite using bands 7, 4, and 1 displayed in red, green, and blue respectively. Data are stretched using BCET.
- Figure 6.13 Colour composite using bands 7, 5, and 1 displayed in red, green, and blue respectively. Data are stretched using BCET.
- Figure 6.14 The RGB colour model (modified from [60])
- Figure 6.15 The IHS model (modified from [118]).
- Figure 6.16 $IHS \Rightarrow RGB$ TM spectral coded colour composite transformed image. The image created using the intensity component (I) as the albedo-topographic information image, the hue component (H) as the spectral coded image after being histogram equalised, and finally the saturation component (S) as the range image.
- Figure 6.17 Fused colour composite of the test site. The spectral coded image assigned to red, 5 by 5 Frost filtered and stretched SAR assigned to green, and range image assigned to blue.
- Figure 6.18 Reverse $IHS \Rightarrow RGB$ fused colour composite image using the TM spectral coded image as hue, the SAR image as intensity, and the range image as saturation components.
- Figure 6.19 $RGB \Rightarrow IHS \Rightarrow RGB$ fused colour composite image using the 6 TM spectral coded image as red, albedo-topographic information image as green, and range image as blue. The intensity output image result is replaced by SAR image, and a reverse procedure is applied to reconstruct a RGB model. The replaced SAR is 5 by 5 Frost filter and automatic stretched.
- Figure 6.20 $RGB \Rightarrow IHS \Rightarrow RGB$ fused colour composite image using TM bands 7, 5, and 1 as red, green, and blue respectively. The intensity output image result is replaced by SAR image, and a reverse procedure is applied to reconstruct a RGB model. The

replaced SAR is 5 by 5 Frost filter and automatic stretched.

- Figure 6.21 Brovey transformed colour composite image using the six TM spectral coded image, albedo and topographic information image, the range image, and finally the JERS-1 SAR after being 5 by 5 Frost filtered. All images are automatically stretched (except the spectral coded image).
- Figure 6.22 Brovey transformed colour composite image using the TM spectral bands 7, 5, 1, and the JERS-1 SAR after being 5 by 5 Frost filtered and automatically stretched. The TM bands are BCET stretched.
- Figure 6.23 Reversed principal components transformed applied on the six TM spectral coded colour composite image after replacing the first principal component by the JERS-1 SAR after being 5 by 5 Frost filtered and automatically stretched.
- Figure 6.24 Reversed principal components transformed colour composite image using the TM spectral bands 7, 5, 1, and replacing the first principal component by the JERS-1 SAR after being 5 by 5 Frost filtered and automatically stretched.
- Figure 6.25 An interpretation lithologic map of the test site
- Figure 7.1 Flow diagram shows the MLC sequential classification scheme used to lithologically classify the test site.
- Figure 7.2 The classified image pixels of stage zero sequential classification using textural information only. Classification is poor but many pixels are classified correctly.
- Figure 7.3 The classified image pixels of stage zero sequential classification using spectral information only. Classification is reliable but many pixels are classified incorrectly based on geologic point of view.
- Figure 7.4 The classified image pixels of stage zero sequential classification using the textural-spectral information. Classification is good but many pixels are biased and may be

classified incorrectly. This classified image is the basic image for sequential classification tests.

Figure 7.5 The classified image pixels of stage one sequential classification. Biased pixels are detected and set to black, non biased pixels set to their appropriate classes and no further test will be carried out on these pixels.

Figure 7.6 The detected biased pixels of stage one sequential classification. Biased pixels are detected and set to black, non biased pixels set to white, note that the black pixels represent patterns such as rock boundaries (spectrally contaminated classes), valley deposits, and geometric and systematic errors, etc. .

Figure 7.7 Sequential classified pixels of stage 2 showing the texturally classified pixels which agree to have the same class of the spectrally classified pixels. This image also show the correctly classified pixels texturally.

Figure 7.8 Final classified pixels of stage 3 sequential classification. Pixels which are negatively biased are set to black (unclassified).

Figure 7.9 Final classified pixels of stage 3 sequential classification. Pixels which are negatively biased are set to their source of texturally-spectrally classified image.

Figure 7.10 An integrated lithologic map of the test site used as a reference data (ground truth) for accuracy estimation of the classified images previously produced in section 7.5.

List of tables

Table 2.1	The optical spectral bands of the TM imaging system.
Table 2.2	JERS-1 main characteristics.
Table 2.3	JERS-1 SAR system characteristics.
Table 2.4	Levels of corrections of JERS-1 SAR images.
Table 4.1	Calculations of atmospheric scattering of the test site.
Table 5.1	Textural signature separability table of the test site training classes after using The co-occurrence texture measure of the SAR image data. The Transformed Divergence separability test algorithm is used to calculate training class separability.
Table 6.1	A numerical example of applying the spectral coding method.
Table 6.2	The Transformed divergence separability test of class pairs of the training areas using the TM spectral coded colour composite image data (Albedo-topographic image and the range image are automatically stretched).
Table 6.3	Transformed divergence separability test using all TM bands (1-5,7) between the training areas of the test site. BCET is applied firstly on the image data
Table 6.4	The first, second, and worst bands combination of the six TM bands after applying BCET.
Table 6.5	Separability measure of the lithologic classes using bands combination 3,2,1 of the TM image data. Data are BCET stretched.
Table 6.6	Separability measures between class pairs of the test site using the bands combination 4,3, and 2 of TM data. BCET is firstly applied.
Table 6.7	Separability measures between class pairs of the test site using the bands combination 5,3, and 1 of TM data. BCET is firstly applied.
Table 6.8	Separability measures between class pairs of the test site using

the bands combination 7, 4, and 1 of TM data. BCET is firstly applied.

Table 6.9 Separability measures between class pairs of the test site using the bands combination 7, 5, and 1 of TM data. BCET is firstly applied.

Table 6.10 Transformed divergence separability test of the lithologic training areas of the test site using $IHS \Rightarrow RGB$ where I = the 6 TM spectral coded image after being histogram equalised, I = albedo-topographic information image, and finally S = the range image. Data are automatic stretched after restoring to RGB model.

Table 6.11 Transformed divergence separability test of the training lithologic classes in the fused colour composite shown in figure 6.17.

Table 6.12 Transformed divergence separability test results applied on the fused $IHS \Rightarrow RGB$ colour composite image using the TM spectral coded image as hue, the SAR image as intensity, and the range image as saturation components.

Table 6.13 Transformed divergence separability test of the lithologic classes using the image constructed in figure 6.19.

Table 6.14 Transformed divergence separability test of the lithologic classes using the image constructed in figure 6.20.

Table 6.15 Transformed divergence separability test of Brovey transformed fused images of the six TM spectrally coded image, the albedo-topographic information image, the range image, and the JERS-1 SAR image after Frost filtered. All images were automatically stretched except the spectral coded image.

Table 6.16 Transformed divergence separability test of Brovey transformed images using bands 7, 5, 1, and JERS-1 SAR.

Table 6.17 Transformed divergence separability test of the reversed principal component transform using the input image data: the

six TM spectral coded image; the albedo and topographic information image; and the range image. The first principal component output is replace by 5 by 5 Frost and automatic stretched image.

Table 6.18	Transformed divergence separability test of the reversed principal component transform using the input image data of TM bands 7, 5, and 1. The first principal component output is replace by 5 by 5 Frost filtered and automatic stretched image.
Table 7.1	Transformed divergence separability test using both of all TM bands (1-5,7) and the seven GLCM textural measures between the training areas of the test site. The TM data is BCET stretched and the GLCM measures are automatically stretched.
Table 7.2	Statistics of stage zero classification results using the seven GLCM textural measures alone, the six TM optical data alone, and the combined textural-spectral data.
Table 7.3	Statistics of each stage during the sequential classification of lithologic units of the test site.
Table 7.4	Classification accuracy confusion matrix of every lithologic unit of the test site using textural classification.
Table 7.5	Classification accuracy confusion matrix of every lithologic unit of the test site using the spectral classification.
Table 7.6	Classification accuracy confusion matrix of every lithologic unit of the test site using textural-spectral classification.
Table 7.7	Classification accuracy confusion matrix of every lithologic unit of the test site using the sequential classified image where biased pixels are filled by the textural-spectral classified image.

1.0 Introduction

Images acquired from Landsat-1, launched in 1972, have largely replaced the traditional techniques of mapping by aerial photography where the scanning system aboard the satellite showed for the first time information from an extended region of the infrared wavelength in which aerial photography films cannot be employed [1]. Consequently, the application of such an imaging system has had a strong impact in many disciplines, including forest inventory, urban planning, coastal mapping, and geological mapping. As a result of this success, remote sensing has become more oriented towards the use of orbital Earth monitoring satellites, including the Landsat series, SPOT series, ERS SAR, and multifrequency/multipolarisation radar imaging satellites including the Shuttle imaging radar missions and more recently RADARSAT, which was launched in the middle of 1995.

In the case of geological mapping, orbital remote sensing satellites play a key role for precise and detailed regional mapping, which includes scales of 1:100,000, 1:50,000 and even 1:20,000 sheet maps using high spatial resolution satellites employing data fusion techniques, where data from different sources are combined and visually or automatically assessed using the spectral behaviour of the imaged lithologic units. Parallel to the spectral behaviour, or spectral signature, the lithologic unit texture is found to be a characteristic of paramount importance for geological mapping, where every rock type found has its own potential resistivity and way of behaviour against external processes such as weathering, erosion and tectonic fracturing. Such information (spectral and textural signature) is the subject of this thesis, which shows how the spectral and textural information can be extracted, manipulated, and combined to produce two sets of image data, one set for direct manual or visual photo-interpretation and the second for automatic pattern recognition to directly create a lithologic map.

Two raw image data sets have been used in this work. One data set was acquired by the Thematic Mapper of Landsat-5, and this data is dedicated to the extraction of spectral information. The second data set is the radar imagery acquired by the JERS-1 SAR, and

this data is dedicated to the extraction of textural information. A test site has been chosen to demonstrate the techniques of enhancing and delineating the test site lithologic rock units.

Prior to fusing the image data, information on the characteristics of the imaging sensors have been found to be vital in this thesis, because this information provides the means of properly interpreting the output results. The image data fusion aimed at lithological mapping can be found in the body of the thesis as a group of procedures which include: preparation of data for fusion or pre-processing, enhancing the spectral and textural (spatial) information, and finally using data fusion tools to produce the output. The development of this group of procedures are the objective of this thesis, discussing in depth the spectral band selection/reduction problem and proposing a new method for solving this problem.

All of these procedures are found in their appropriate chapters, and at each stage, a review is given of previous work in the particular subject, so the thesis is deliberately structured in a form that treats each issue of the data fusion independently. The first chapter discusses the background material used in the work, and the selected test site and its lithology. In the second chapter, the acquisition system platforms are briefly described as well as the interaction of electromagnetic radiation with Earth's material with respect to the rock samples collected from the test site during the field visit to the area. The locations of these samples and other field observed rock units are also shown, which are then used as training areas during the pattern recognition image data classification in the automated mapping procedure. In the third chapter, a detailed description is given of the synthetic aperture radar imaging technique. Chapter four discusses the preparation of the two image data sets (the optical TM and the JERS-1 SAR) for fusion. The preparation of the two data sets includes making the two data compatible with each other, mosaicking of the SAR scenes and geometric co-registration of the two data sets, and atmospheric correction of the optical TM data. The methods used for reducing speckle in SAR images, and finally the results of preparation of these two data set are discussed. Chapter five is dedicated to a discussion of the textural information extraction implemented on

the JERS-1 SAR, and its importance for geological mapping. In chapter six, where the data are now prepared for image fusion, a full definition of data fusion is established. The colour composite band selection/reduction problem is discussed and a new method of colour composite production is established and implemented to extract the spectral information from the optical TM data. The spectral and spatial or textural data are then combined and fused using fuser tools such as colours transform and principal component transforms. The output data of these techniques are used for visual photo-interpretation to lithologically delineate the test site. In chapter seven the automated classification is implemented on the two manipulated spectral and textural information of the image data. Chapter eight presents the conclusions, as well as some suggestions for future work.

The literature review presented in this thesis forms an important part because firstly it shows the previous work of the particular subject, but secondly and most importantly it served as the source of ideas and inspiration during the preparation of this thesis work.

1.1 Materials used in the study

Two satellites image data sets are used in the work in their digital format: Landsat TM data and JERS-1 SAR data. The data from both satellites were acquired in the same year in 1992. This is to insure there are no temporal changes in the test site between the two data, the seasonal changes are usually not high because the area of study is arid and the lack of vegetation throughout the year. A geologic map compiled by Clark in 1987 [2] in parallel with two large 40 by 40 inches hard copy colour composite images (one is natural colour and one is infrared) are used as ground truth based data. Field checks and sample collection have also been carried out for ground truth verifications and training areas selection registering their geographic coordinates using hand held GPS. A spectrometer has also been used to measure the spectral reflectance of the collected samples and compared with the TM data which helped to select the training areas properly.

The software/hardware used in this thesis work is a combination of pre-processing of the data (image co-registration) using MERIDIAN® VAX/VMS platform, and processing techniques which are prepared essentially through PC based C-Programming and EASI/PACE® image processing software. MATLAB® UNIX based system is also used for many of the graphical outputs.

1.2 Objectives of the thesis

The main thesis objective is to implement, test, modify, and improve the image processing techniques used for image data fusion for lithological mapping and apply these techniques on a selected test site. In particular, this includes: the geometric co-registration between the two data sets; test of speckle filter reduction applied on the SAR data; atmospheric correction of the optical TM data; implementing texture analysis on SAR data used for lithology; colour composite selection, and developing a new method of colour composition with high separability between the spectral classes; a test of colour transforms and principal component transforms used for introducing the spatial information with spectral information; and finally a test of automated mapping (classification) and introducing a new method of classification using both of textural and spectral information. Other secondary objectives include: production of a lithologic map of the test site because the previous work carried out by Clark in 1987 [2] of the same area is not accurate, and finally; a major literature review on image processing techniques used for image data fusion.

1.3 The test site

The test site occupies nearly a quarter of the Al Bad' quadrangle in the north-western part of Saudi Arabia (Lat. 28° 13.6' - 28° 28.6' N and Long. 34° 47' - 35° 04' E). It has an area of around 852 km² and lies in the north western Midyan Terrain exactly adjacent to the eastern part of the Gulf of Aqaba. Figure 1.1 shows the area of study and the location of the test site.

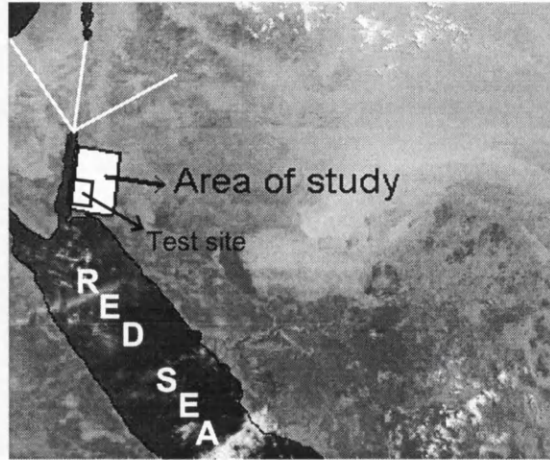


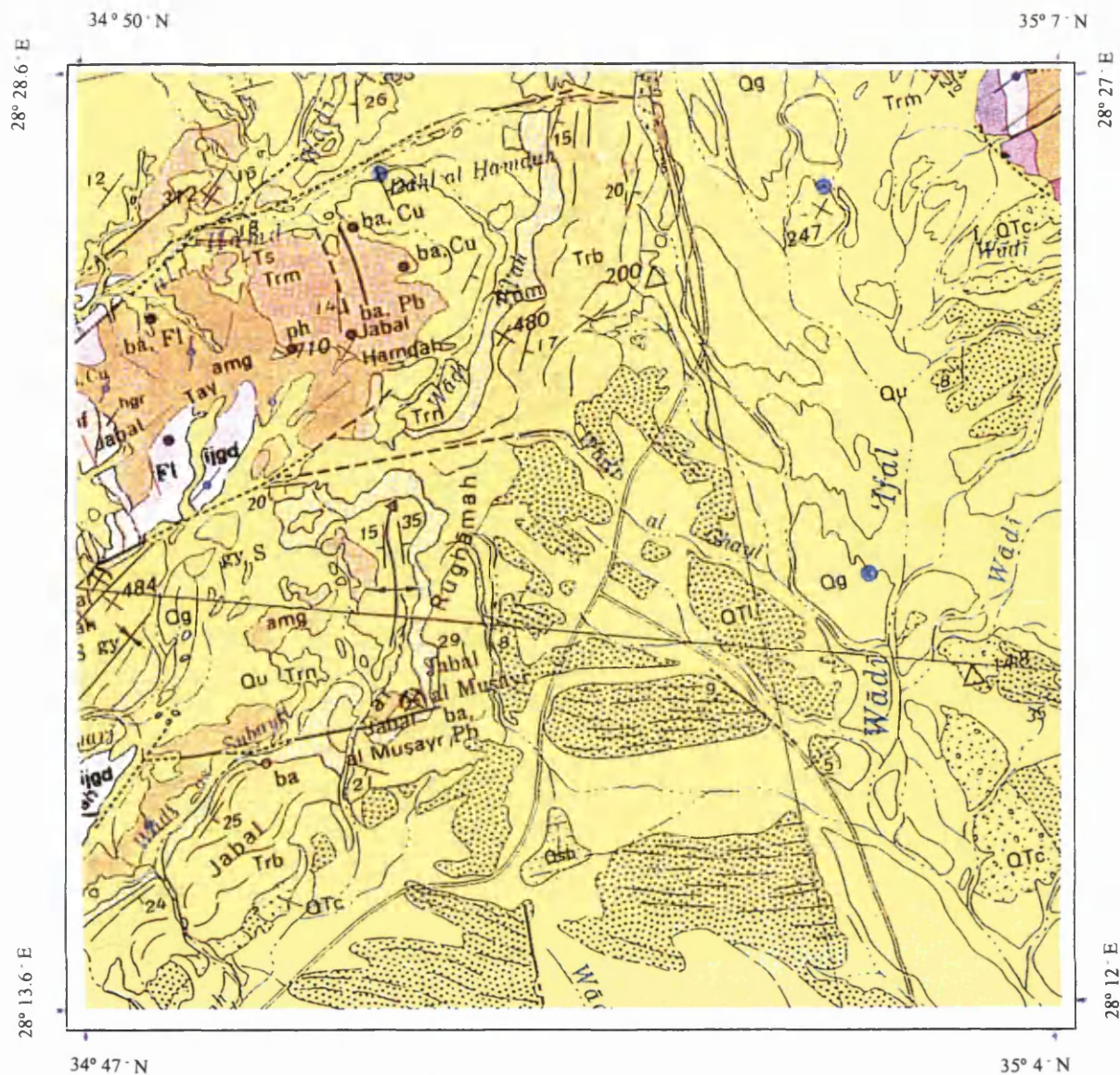
Figure 1.1. The area of study as shown by NOAA 12 AVHRR band 2.

1.3.1 Physiography of the test site

The test site is physiographically divided into two units [2]. The first is the lowland which is the Afal plain, which occupies the lower and eastern part of the area and is distinguished by its very low relief. The second unit is the upland zone in the west. It is called the Maqnah Massif, and is composed of sedimentary rocks underlain by Proterozoic rocks of the Arabian Shield. Some of these Proterozoic rocks are exposed in many areas in this zone. This zone is distinguished by its varying heights, ranging from 200 to 700 metres above sea level.

1.3.2 Lithology of the test site

As interpreted by Clark [2], the oldest rocks in the test site are a metamorphic rock unit represented by the Hegaf formation. Younger igneous rocks in the test site are represented by Jurfayn, Atiyah, and Haql rock units. All these metamorphic and igneous rocks belong to the Arabian Shield, which covers most of the west, north-west, and south-west of Saudi Arabia. Figure 1.2 shows a detailed geologic map of the test site as previously compiled by Clark in 1987 [2].



Rock units

Qu	Undifferentiated Sand and Gravel
Qsb	Sabkha
Qg	Gravel sheets
QTc	Conglomerate
QTI	Lisan Formation
Trb	Bad' Formation
Trm	Nutaysh Formation
Trm	Musayr Formation
Ts	Sharik Formation
hgr	Haql suite
amg	Atyah Monzogranite
ijgd	Jurfayn complex
hf	Hegaf Formation

Symbols

- x = Height
- = Inclined bedding
- = Syncline fold
- = Structural trend
- = Fault
- = Dikes
- = Highway
- = mineral occurrence
- = Prospect

ba, Cu, Pb, Ph, S, gy = Economic elements

Scale 1:250 000

Figure 1.2 Geologic map of the test site. (Source [2]).

The metamorphic Heqaf formation which is partly exposed in the test site, and located in the far west of the geologic map in figure 1.2, consists of a variety of highly folded volcanic rocks consisting of meta-andesite and meta-basalt, few meta-rhyolite, amphibolite, and mafic schist. They are subordinated by epiclastic rocks which are metamorphosed to greenschist facies [2]. The Heqaf formation thickness is unknown, but could be several thousands of metres.

The igneous rocks in the test site are basically intrusive; the oldest of which is the Jurfayn complex. It is distinguished as irregular in shape, medium to low relief and traversed by numerous mafic and felsic composite dikes. Its mineralogy is granodiorite. It is located in the western part of the test site in Magna Massif and can also be found in the north-east of the test site. Younger and larger granitic bodies are mostly located in the western part but are also exposed in the north-east of the test site and belong to a unit called Atiyah monzogranite. The Atiyah monzogranite is massive with medium to coarse grained texture. Figure 1.3 is a photograph taken during the field work and shows the contact between Jurfayn complex (dark green) and Atiyah monzogranite (light brown).



Figure 1.3 A photograph shows the Jurfayn complex (in dark green) and the Atiyah monzogranite (light brown).

Sedimentary rocks in the test site are all Cenozoic in age. They outcrop in both the Maqna Massif and the Afal plain. The oldest sedimentary rock unit in the test site is the Sharik formation, dated to the Oligocene. The Sharik formation, located in the north-western part of the test site, is composed of red-tinted conglomerate, sandstone and subordinate siltstone. It is poorly consolidated and unconformably overlies the Proterozoic basement in many places.

Miocene rocks in the test site are represented by what is called the Raghama group. The group is subdivided into the Musayr formation at the bottom, the Nutaysh formation in the middle, and the Bad' formation at the top. The Musayr formation overlies the Sharik formation locally but also overlies the basement rocks and forms a major unconformity in the north-western part of the test site. The Musayr formation lithology varies from reef limestone, limestone interbedded with sandstone, to conglomerate and sandstone. The thickness of the formation is about 100 to 130 metres. The Nutaysh formation overlies conformably the Musayr formation. It is characterised by distinct lateral facies changing from coarse detrital to fine grained shallow marine sedimentary rocks. Its lower part consists of an alternating sequence of yellow marl, sandstone, and red limestone which changes laterally to conglomerate and sandstone. Its upper part is fine grained, variegated, and composed of marl and subordinate gypsum, sandstone, and siltstone. The thickness of this formation is recorded to be 400 metres, and it dips from east to west [2]. Figures 1.4 and 1.5 are photographs taken during the field work and show the Nutaysh, and Nutaysh overlies Musayr formation (Nutaysh is a creamy tan in colour and overlies the light-red bedded layers of Musayr).

The Bad' formation, which is the uppermost formation of the Raghama group in the test site, conformably overlies the Nutaysh formation and consists mainly of sequences of anhydrite and gypsum evaporites interbedded with dolomite, marl, and sandstone. It is middle to late Miocene and is reported to be 300 metres in thickness [2]. Figure 1.6 is a photograph showing the Bad' formation.

The deposits that fill the Afal plain are named the Lisan formation. This has some economic importance as a source of water, oil, and gas reservoirs. It is about 3000 metres thick, consisting of poorly consolidated yellow to red sandstone, conglomerate, and gypsum. This formation unconformably overlies the Bad'a formation in the west [2].



Figure 1.4 Nutaysh formation.



Figure 1.5 Nutaysh overlies Musayr



Figure 1.6 Bad' formation.

The Quaternary deposits are everywhere in the study area, and cover many rock units. They fill most of the Wadis channels and low lands. They are classified to be either continental such as aeolian windblown silt and sand, Wadi terraces, gravel, or marine deposits of sand and gravel sheets. They are grouped as: conglomerates, gravel sheets, sabkhah, and eolian and undifferentiated Wadi alluvium [2].

The conglomerate consists of poorly consolidated fragments of pebbles, cobbles, and small boulders, and is Pliocene (Tertiary-Quaternary) in age. It caps and obscures the Lisan formation in many places. It is located almost everywhere in the test site, but dominates most of the southern part of the Afal plain. The gravel sheets which dominate the eastern part are also found in the north of the test site. These sheets consist of materials derived from the older rock units. The Sabkhah can be found in the lower middle part of the Afal plain. It consists of saline silt, clay, and muddy sand. Figure 1.7 is

a photograph showing the Sabkhah. The aeolian sand, silt, and alluvium units dominate the middle and southern part of the Afal plain respectively.



Figure 1.7 The Sabkhah as photographed during the test site field work. The GPS receiver shows the scale.

2.0 Platforms and sensors

As mentioned in section 1.1, two image data sets were used in this study. The first data set is the optical imagery data acquired by the Landsat-5 Thematic Mapper, and the second is the SAR imagery data acquired by the Japanese satellite JERS-1 SAR system. This chapter describes both satellites and the properties of their sensors.

The basics of the interaction between electromagnetic radiation, atmosphere, and the rock units of the study area are also discussed in this chapter. Results from spectral reflectance measurements of the rock units collected using a portable spectrometer from the study area during the field visit are presented. The spectrometer measures the spectral reflectance of the collected rock samples using 861 optical channels. These spectral reflectances are then used and compared with the reflectance of the TM image data for photo-interpretation in the primary stage of rock unit delineation, and for selecting the training areas representing the lithologic spectral classes.

2.1 Landsat-5

The Landsat program started with the 1972 launch of Landsat-1, which carried the scanning optical system, MSS. The program continued with the launch of Landsat-2 and 3, carrying optical systems similar to MSS. The Landsat series further continued with the launch of Landsat-4 and 5 in 1982 and 1984 respectively, which are both characterised by an advanced scanning optical system called the Thematic Mapper. In that time and in terms of spectral information, the TM imaging system was superior to other optical orbiting imaging systems and is widely used by Earth remote sensing scientists and geologists in particular [3].

The Thematic Mapper systems aboard Landsat-4 and 5 are identical, and acquire images using the same principle of the previous MSS optical system. The differences lie in the higher spatial resolution, of pixel size of 30 by 30 metres, and the spectral resolution

represented by seven spectral bands extending from the visible to short, mid, and thermal infrared. Table 2.1 shows the TM imaging system spectral band characteristics and their main applications.

Band	Wavelength	Main application
Band-1	0.45-0.52 μm (Blue)	Used for water penetration, forest type, and soil vegetation mapping
Band-2	0.52-0.60 μm (Green)	Used to measure green reflectance peak of vegetation and discrimination
Band-3	0.63-0.69 μm (Red)	Used for Chlorophyll absorption aiding in plant species differentiation
Band-4	0.76-0.90 μm (NRIR)	Water-Land boundary and soil moisture mapping
Band-5	1.55-1.75 μm (MIR)	Snow/cloud differentiation, soil moisture, and vegetation mapping
Band-6	10.4-12.5 μm (Thermal)	Thermal band, used for thermal mapping (Not used in this study)
Band-7	2.08-2.35 μm (MIR)	Mineral and rock types mapping

Table 2.1 The optical spectral bands of the TM imaging system [4].

The imaging technique of the TM system relies on a scanning mirror, which rotates normal to the satellite orbit with total field of view (FOV) of 14.95 degrees, giving a swath width equal to 185 km. The mirror reflects the light collected from the Earth's surface to the system optics, which in turn projects the reflected light to the band detectors which measure the intensity of the projected reflected light. The measured radiance is converted to digital form through the onboard A/D converter, recorded in the satellite's data storage system and then telemetered to the ground receiving stations.

Except in the thermal band (band 6), the instantaneous field of view (IFOV) of the TM bands is 0.043 mrad. where every band employs 16 detectors. The thermal band employs only 4 detectors and has an IFOV of 0.17 mrad. This results in 30 metre spatial resolution in the bands 1-5, and 7. Band 6 has a lower resolution equal to 120 metres.

The Landsat satellites are all sun-synchronous and near polar orbital. For example, Landsat-5 has an inclination angle of 98.2 degrees with nominal altitude of 705 km and crosses the equator from north to south of each orbit at 9:45 a.m. local time, passing the same area every 16 days [4].

2.2 JERS-1

JERS-1, or Fuyo-1, is the first Japanese Earth Resources Satellite. It was launched in February 1992 by the National Space Development Agency of Japan (NASDA). The satellite mission was designed to perform many tasks, including the establishment of the Japanese Earth Resources integrated observation system and the observation of the Earth using Synthetic Aperture Radar (SAR), simultaneously with optical visible and near infrared imaging systems [5].

As common for Earth observing satellites, the JERS-1 system is divided into two parts: one is the satellite itself which collect the data and transmits it or records it through its two Mission Data Transmitters (MDT) or the Mission Data Recorder (MDR), when there are no ground receiving stations linked with the satellite. The second part is the ground segment of the system, which is the tracking and control system. This controls the satellite orbit and attitude, in addition to the data acquisition and processing system which links to the ground receiving stations that receive the data, process it, and distribute it to the users [5].

The JERS-1 satellite carries two observation sensors: the SAR sensor and the optical OPS sensor. The SAR is designed specifically for Earth resources exploration, topographic mapping and geological surveying. The optical OPS system is designed for water quality and vegetation surveying, environment preservation, and stereoscopic viewing through bands 3 and 4. Table 2.2 shows the JERS-1 main specifications.

Spacecraft Altitude	568 km over the equator
Period (T)	96 minutes
Inclination angle	97.67 degree
Orbit	Sun-synchronous
Recurrent period	44 days and 659 revolutions
Mean local time at descending node	10:30-11:00 AM
Distance between adjacent orbit Earth track	60.7 km
Mission equipments	SAR,OPS,2HDTs,1HDR.
Spacecraft weight	1340 kg
Communication links	2GHz for telemetry & 8GHz image data
Operational duration	2 years

Table 2.2 JERS-1 main characteristics [5].

The geometrical aspect of the JERS-1 SAR observation system is shown in figure 2.1, the SAR system transmits microwave pulsed signals downwards perpendicular to the spacecraft flight direction. The received radar echoes are then telemetred to the ground by the mission data transmitter MDT, after being detected and digitised onboard the spacecraft. The SAR system onboard JERS-1 transmits 1505-1600 linear frequency modulated chirped pulses per second from its antenna and receives the reflected echoes

through the same antenna. The intensities and phases of these reflected echoes are measured. By adding the reflected wave intensities through the movement of the satellite, high resolution is achieved by JERS-1 after phase equalisation (range and azimuth compression). Theoretically, the resolution is half of the real aperture length which means the smaller the antenna, the higher the resolution, but as a result of a limitation of real aperture length, the antenna gains decrease and the S/N deteriorates as the antenna aperture length decreases. Because of this the JERS-1 SAR real aperture length is designed to be 11.9 metres [5]. The major JERS-1 SAR system characteristics are shown in table 2.3.

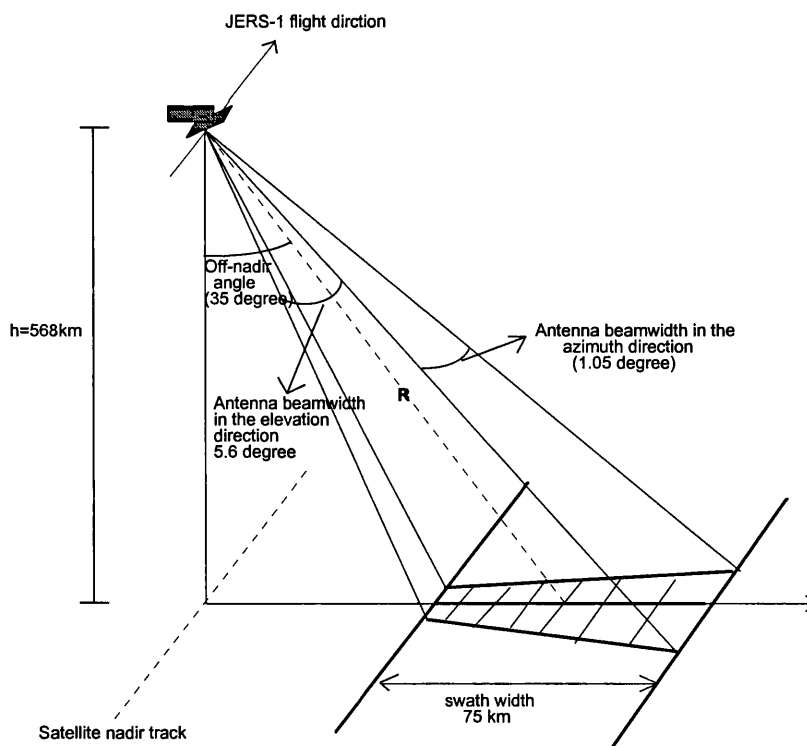


Figure 2.1 JERS-1 SAR observation geometry [5].

Title	Performance	Remarks
Observation frequency	1275 MHz (L band 0.235m)	(At swath centre 3 multilook)
Bandwidth	15MHz	
Polarisation	H-H	
Off-Nadir angle	35 degrees	
Range resolution	18 metre	
Azimuth resolution	18 metre	
Swath width	75 Km	
Transmission Power	1100~1500 Watts	
Pulse width (τ)	35 μs	
PRF	1505.8Hz, 1530.1Hz 1555.2Hz, 1581.0Hz 1606.0Hz	
Antenna gain	33.5 dB	At the beam centre
Beam angle in range	5.6 degree	Observed 5.4 degree
Beam angle in azimuth	1.05 degree	Observed 0.98 degree
Side-lobe level (both in range and azimuth	-11.5dB	
Antenna length/width	11.92/2.2 metre	

Table 2.3 JERS-1 SAR system characteristics (Source:[5])

2.2.1 JERS-1 SAR image construction

The first step used to construct the JERS-1 SAR imagery is performing range compression, in which each echo is correlated with a replica of the transmitted pulse (the matched filter). This is achieved in the frequency domain by a Fast Fourier Transform (*FFT*) approach.

The JERS-1 SAR system onboard transmits down-chirped signals with a carrier frequency (f_o) with pulse repetition frequency (PRF) and pulse width (τ).

The JERS-1 SAR transmitted signal is:

$$f(x) = \cos 2\pi(f_o + \frac{C_R}{2} \times t)t \quad (2.1)$$

where:

$$-\tau/2 \leq t \leq \tau/2$$

C_R = the chirp rate

Ignoring the antenna pattern and the path attenuation, the amplitude of the received signal is normalised to 1. The received reflected and scattered signal is calculated using the equation:

$$S_R = e^{2j\pi[\frac{C_R}{2}(t-t_r)^2 - f_o \times t_r + d(t) \times (t-t_r)]} \quad (2.2)$$

where :

$$-\frac{\tau}{2} + t_r < t \leq \frac{\tau}{2} + t_r$$

$t - t_r$ = the two-way propagation delay.

$d(t)$ = the Doppler component resulting from the satellite motion.

Equation (2.2) is used for range compression, and the matched filter used for the compression is defined by:

$$g(x) = e^{j[-2\pi(k/2 \times t^2)]} \quad (2.3)$$

where:

$$-\tau/2 \leq t \leq \tau/2$$

When the SAR image is created, the geometric correction process is then applied to clean up artifacts resulting from the system instability, platform instability (attitude and altitude variations), signal propagation effects, the imaged targets, and processor induced errors. These artifacts are corrected based on the levels of correction shown in table 2.4

Level 0.0	Unprocessed raw signal data product
Level 1.0	Partially processed raw signal data
Level 1.1	Basic image product
Level 2.0	Bulk image product
Level 2.1	Standard georeferenced UTM image product (The data used in this work)
Level 3.0	Precise corrected images (not corrected from topographic effects)
Level 4.0	High accuracy corrected images using DEM (Geocoded imagery corrected from foreshortening)

Table 2.4 Levels of corrections of JERS-1 SAR images (Source:[5]).

The JERS-1 SAR processor is designed to produce four types of images based on the level of correction. Such corrections are based on parameters including system parameter information, platform orbit and attitude information, and external data information including ground control points (GCP's) and digital elevation models (DEM's). For example, the slant range to ground range correction is performed in level 2.0; the standard geographic coordinate correction is performed in level 2.1; and the high accuracy rectified image is performed in level 4 only if DEM data is available.

The slant range images, which have strong geometric distortion (shortened pixels toward near range), are interpolated either using cubic convolution or nearest neighbourhood. This is through the use of pseudo affine transformation equations for

every block of the compressed range and azimuth image and producing corrected ground range images. These equations used by JERS-1 SAR are [5]:

$$\begin{aligned} u &= axy + bx + cy + d \\ v &= exy + fx + gy + h \end{aligned} \quad (2.4)$$

where:

(u, v) = input image coordinates.

(x, y) = output image coordinates.

a, b, c, d, e, f, g, h are coefficients determined for each block based on JERS-1 SAR geometry.

The resultant output images, after applying equation 2.4, are classified to be corrected to level 2.1 which is the level of correction of the data used in this thesis.

Some important JERS-1 SAR system characteristics are calculated during the preparation of this work. These are shown in the following section using some of the known SAR parameters.

$$\lambda = 0.235 \text{ metres}$$

$$\text{Swath width } (S) = 75,000 \text{ metres}$$

$$\text{Off nadir angle } \theta = 35^\circ$$

$$\text{Satellite height above the equator } (h) = 568,000 \text{ metres}$$

The antenna length on JERS-1 is given as 11.9 metres, which achieves maximum azimuth resolution R_a , $R_a = L/2 \approx 6$ metres

Also $R_r = NR_a$, where R_r is the resolution in the range direction on JERS-1 = 18 metres, and N is the number of looks of the processed images = 3. From that $R_a = 18/3 = 6$ metres.

Antenna height (width) = $W = \frac{\lambda h}{S \cos \theta} = \frac{0.235 \times 568,000}{75,000 \times \cos(35)} = 2.17$ metre. The system designers made it 2.20 metres.

$$\text{Maximum } PRF = \frac{c}{2S \sin \theta} = 3486.8 \text{ Hz}.$$

Therefore PRF should be < 3.48 kHz.

The satellite velocity can be measured over the equator, based on the equation:

$$g_s \left(\frac{R}{r} \right)^2 = \frac{v^2}{r}$$

where:-

g_s = Earth gravitational attraction = 9.81 metre/sec².

R = radius of the Earth = 6380,000 metres.

v = satellite velocity.

r = satellite height measured from the centre of the Earth.

From the equation, the velocity (v) is:

$$v = \sqrt{\frac{g_s R^2}{r}}$$

$$\therefore v = \sqrt{\frac{9.81 \times (6380,000)^2}{6380,000 + 568,000}} = 7.5809 \text{ km/sec}.$$

To calculate the satellite period (T)

$$T = \frac{2\pi r}{v} = 5758.6 \text{ seconds} = 95.977 \text{ minutes}.$$

$$\text{Minimum } PRF \text{ of the radar is } > \frac{2v}{L} = 1.26 \text{ kHz}.$$

$$\text{Azimuth footprint } F_a = \frac{h\lambda}{L \cos \theta} = 13.596 \text{ km (note that it is equal to the length of the synthetic array).}$$

Satellite integration time $T_i = \frac{F_a}{\nu} = 1.79$ second.

System bandwidth $(B) = \frac{c}{2 \times R_r \sin \theta} = 14.52\text{MHz}$. The system designers made it 15MHz.

The leading edge of the returned echo (t_1) arrived at time (accounted after transmission)

$t_1 = \frac{2h}{c \cos \delta}$ where δ is the angle between the near range and the satellite nadir. The

leading edge equation is used to avoid the received echoes from the satellite nadir.

$$\therefore t_1 = 7.1 \times 10^{-3} \text{ seconds}$$

Satellite range curvature $M_c = \frac{h\lambda^2 B}{16cR_a^2 \cos \theta} = 3.324$ unit range resolution

Depth of focus $(F) = \frac{2N^2 L^2}{\lambda} = \frac{2(3)^2 (12)^2}{0.235} = 11.03 \text{ km}$.

Processing complexity PT (if time domain is used) $= \frac{2\lambda h B}{(L)^2 \cos \theta} = 3.394 \times 10^{10}$ operation/sec.

Processing complexity (if frequency domain is used) $= B \times \log_{10}(PT) = 157 \times 10^6$ operation/sec.

2.3 Interaction of electromagnetic waves with matter

When electromagnetic solar radiation interacts with matter, either in its gas, liquid, or solid state, a variety of energy exchange mechanisms occur between the matter and the solar radiation, which depend upon the wavelength (i.e. photon energy) and the energy levels of the matter's structure. This occurs because the electrons of the matter which are in a stationary state are put into motion, leading to an exchange of energy between the wave and matter.

In the case of isolated atoms, the energy levels are related to the orbits and spins of the electrons, called the electronic levels. For molecules (e.g. gases), additional rotational and vibrational energy levels exist as a result of bond interaction. The rotational and vibrational energy levels correspond to the dynamics of the constituent atoms relative to each other. Rotational excitations occur only in gases where the molecules are free to rotate [6].

In the visible and infrared region of the spectrum, where the energy is in the range of 0.2 to 3.0 eV, vibrational and electronic transitions occurs. The gases show well defined absorption as spectral lines and these lines are broadened due to the temperature and the pressure.

The Earth's atmosphere interacts with electromagnetic waves, leading to a limitation on the spectral regions that can be used for remote sensing. This is because the atmosphere and/or the ionosphere absorb or highly attenuate these spectral regions and hence remote sensing sensors are usually designed to operate in specific regions of the electromagnetic spectrum away from the spectral absorption regions. The regions used for remote sensing are called "atmospheric windows".

For active remote sensing such as radar imaging systems, the ionosphere blocks any transmission to or from the Earth surface below about 10 MHz. In the rest of the radio frequency region up to 10 GHz, the atmosphere is effectively transparent, but there are a number of strong absorption bands in the microwave region basically associated with water vapour and oxygen [6]. At a frequency of 22 GHz the transmission of the microwave signal is reduced to less than 15% as a result of the water vapour in the atmosphere and transmission is completely blocked at 180 GHz . Oxygen has similar effects by blocking the frequencies 50-60 GHz and near 120 GHz [7].

In the submillimetre and far-infrared region of the electromagnetic solar spectrum, the atmosphere is almost opaque, as a result of absorption of the radiation by the atmospheric

constituents. In the visible and near infrared region of the spectrum, the atmosphere has many opaque windows, resulting from electronic and vibrational processes which occur due to the presence of water vapour and carbon dioxide molecules. In the ultraviolet region of the spectrum, the atmosphere is completely opaque due to the ozone absorption layer in the upper atmosphere [6].

Solid matter shows a wide variety of energy transfer interactions including molecular vibration, ionic vibration, crystal field effects, charge transfer, and electronic conduction.

Spectral absorption of rocks and minerals is an important subject in the field of geologic remote sensing because it is the key factor of manual photo-interpretation and mapping using the image data. The spectral absorption of rocks and minerals is caused by the transition between the energy levels of the atoms and molecules of the minerals which form rocks. The transition may result from processes which are mainly vibrational or electronic.

Vibrational transitions occurs as a result of small displacement of the atoms from their original positions. In the visible and near-infrared wavelengths, the vibrational processes occur in minerals containing hydroxyl ions (OH^-) or water molecules (H_2O) either bounded in the mineral structure or as fluid inclusions. Due to water molecules, absorption occurs in the infrared at wavelengths of $1.45\text{ }\mu\text{m}$ and $1.9\mu\text{m}$. If the water molecules are well defined and are ordered in the mineral structure, a sharp and narrow absorption feature can be depicted in the spectral signature of the rock. A broad absorption shape is caused by water molecules unordered in the mineral framework [6] and generally, both absorptions occur simultaneously.

Most of the silicate minerals group contain hydroxyl ions (OH^-) in their structures, vibrational absorption features occur in such minerals (e.g. Al-O-H) in the infrared bands centred at $1.6\mu\text{m}$ and $2.2\mu\text{m}$ [8]. The best example of such phenomena can be

demonstrated by clay minerals, which are very important indicators of alteration zones. TM bands 5 and 7 are usually used for mapping these minerals.

Carbonate minerals (CO_3^{2-} ions) also show the vibrational absorption features resulting from the Ca-O bond. This process can be depicted in many wavebands in the mid infrared spectrum including 1.9 μ m, 2.0 μ m, 2.16 μ m, and 2.35 μ m [8]. An example of the carbonate minerals are the Calcite and Dolomite, which are the main constituents of Limestone, which is abundant in the sedimentary rocks found in the selected test site.

The electronic processes are associated with the electronic energy levels where every electron in an atom only occupies a single quantised orbit with a specific energy level. Such processes occur as a result of crystal field, charge transfer or conduction band effects.

When the atoms are introduced into a crystal lattice, they split into many different energy levels because of the influence of the crystal field and hence show absorption features of specific wavelengths. The most common elements from which minerals are formed are silicon, oxygen, and aluminium, and these show little or no electronic transition in the visible and near-infrared wavelength. In the presence of the transition metal elements, especially iron which is common in most igneous and metamorphic rocks, they show a crystal field absorption effect in the visible and infrared. The mineral Hematite is the best example [9].

The charge transfer absorption effects result from the movement of the electrons between the neighbouring cations or between cations and ligands (e.g. Fe-O) as a result of the excitation of the incident wavelength. It is distinguished by its narrow band and is common in most iron bearing minerals, and needs high energy such as within the visible wavelength.

The conduction band transition absorption effect occurs when electrons in the crystal lattice become delocalised and wander freely throughout the lattice. This effect is very common in most metallic mineral crystals, giving them high electric conductivity. These minerals are opaque as a result of this effect, and always show absorption features in the visible wavelength. Generally speaking the electronic processes can easily be depicted in the visible wavelengths and are mainly broad spectral bands

The spectral reflectance of rocks and minerals were intensively studied by Hunt and Salisbury for silicate minerals in 1970, and carbonates in 1971. They also studied oxides and hydroxides in partnership with Lenhoff in 1971. They studied igneous rocks in 1973 and 1974. Their work introduced the basics of image interpretation for remote sensing to geologists.

To some extent, data collected by remote sensing satellites is considerably inferior to such laboratory measurements. This is as a result of many factors, including the influence of the atmosphere, soil, and vegetation; grain size and mixtures of minerals; desert varnish or coating which influences arid areas; humidity and temperature; organic content; and texture. In the case of radar imaging systems, other factors such as the viewing angle, dielectric properties, polarisation and texture, all contribute to modification of the spectral signatures.

In the following section the laboratory spectral measurements for the rock samples collected during the field visit of the study area are discussed. The rock samples were carefully selected to represent the lithologic rock units of the test site. The portable field reflectance spectrometer (PFRS) used in this work is very similar to that described by Kahle [8] and measures the reflectance of the samples in 861 channels ranging from 0.314 μm to 2.534 μm of the electromagnetic spectrum. The spectrometer is supported by a portable notebook computer which records the output data digitally and stores it on its hard disk. In this work, the output results of the rock samples reflectance were then transferred to a floppy disk, read using MATLAB software, and displayed graphically

with the x-axis representing the wavelength in micrometres and the y-axis representing rock sample reflectance. The location of every selected rock sample was recorded using the Global Positioning System (GPS) and the corresponding spectral reflectance of this location in the TM image data compared with the sample spectral reflectance read by the spectrometer. The location of every sample is used as a training area representing the rock unit, and hence used for the transformed divergence separability test between classes. Furthermore the selected classes are used for automated mapping (classification) procedure, other training areas have been selected based on their spectral similarities to the measured spectral reflectance of the rock samples. Figure 2.8 shows the location of rock samples collected and selected training areas.

1- Al Bad' rock sample reflectance.

The sample of Al Bad' is taken from undisturbed surface selected from the northern part of Al Bad' formation with geographic coordinates measured by the GPS of 28° 26.37' N and 35° 00.115' E. This coordinate is used as a spectral reference point and one of the training area of Al Bad' class in the TM image data. The spectral reflectance of Al' Bad as shown in figure 2.2 exactly mimics the Gypsum spectral reflectance. It has two distinct vibrational absorption features at 1.45µm and 1.9µm due to the presence of water. The absorption feature around 0.5µm is due to electronic process resulting from desert varnish (iron oxides) occurring on the rock sample surface.

During the literature review in this thesis, it has been found that an image plate¹ shown by Drury [9] visually misinterpreted the Al Bad' formation using TM data as Lava flow. If band 7 of the TM image data is used for the interpretation and compared with the other TM spectral bands to trace where the absorption features occur, the interpretation of Al' Bad rock unit will definitely be Gypsum, even without referring to figure 2.2 shown or collecting rock samples from the study area.

¹ A colour plate in Drury [9] (figure 3.41) showing the Gulf of Aqaba. Landsat 4 TM colour composite of bands 7, 5, 4 displayed in red, green, and blue respectively. The Al Bad' formation is shown as light blue and marked by the letter D and interpreted as silicic lava flows.

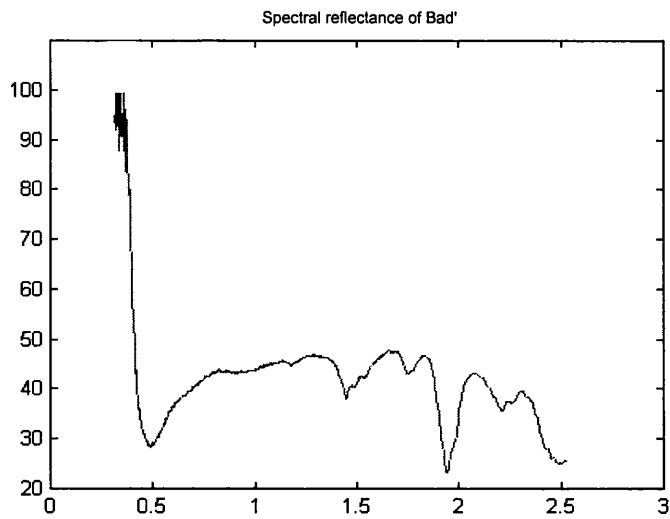


Figure 2.2 Spectral reflectance of rock sample taken from Al Bad' formation.

2- Spectral reflectance of Nutaysh Formation

The Nutaish rock sample was taken from an area located in the northern part of Nutaysh formation at $28^{\circ} 27.804' \text{ N}$ and $34^{\circ} 55.434' \text{ E}$. The area location is also marked as a TM spectra reference of the formation and one of the training areas for classification procedure. The collected sample consists of dark to medium brown siltstone, and the reflectance of the rock sample is shown in figure 2.3.

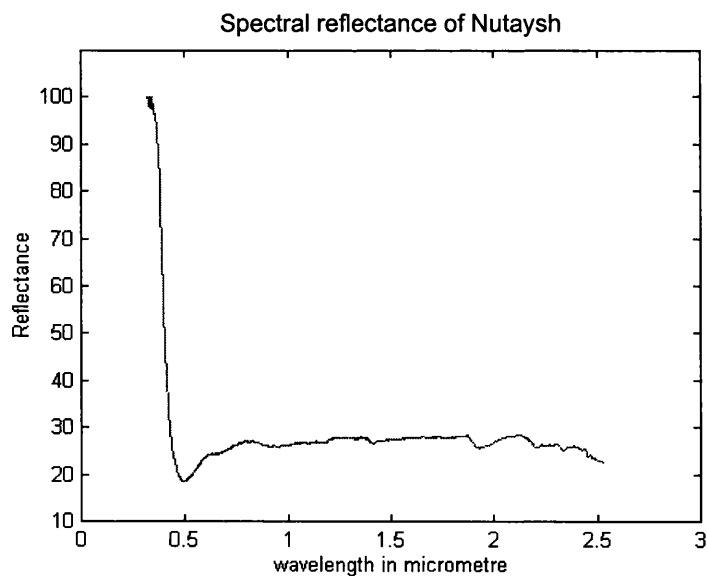


Figure 2.3 Spectral reflectance of sample collected from Nutaysh Formation.

The absorption features which can be distinguished in the Nutaysh's sample spectral reflectance show weak reflectance along the spectrum (low albedo) with distinct electronic absorption feature around the wavelength $0.5\mu\text{m}$ due to weathering (i.e. desert varnish). A small vibrational absorption feature occurs at $1.9\mu\text{m}$ due to water and Si-O bond.

3- Spectral reflectance of Atiyah monzogranite

A medium to coarse grained red granitic sample is taken from Atiyah Monzogranite to represent the rock unit. The sample is taken from location with geographic coordinates of $28^{\circ} 26.742' \text{ N}$ and $34^{\circ} 50.49' \text{ E}$ and this location is also marked as a spectral reference of the rock unit and selected as one of the training area in the TM data. In the measured spectral reflectance of the sample as shown in figure 2.4, a clear electronic absorption feature occurs due to desert varnish around the wavelength $0.5\mu\text{m}$. Another electronic absorption feature occurs at $0.9\mu\text{m}$ due to iron. Low albedo also characterises the rock sample.

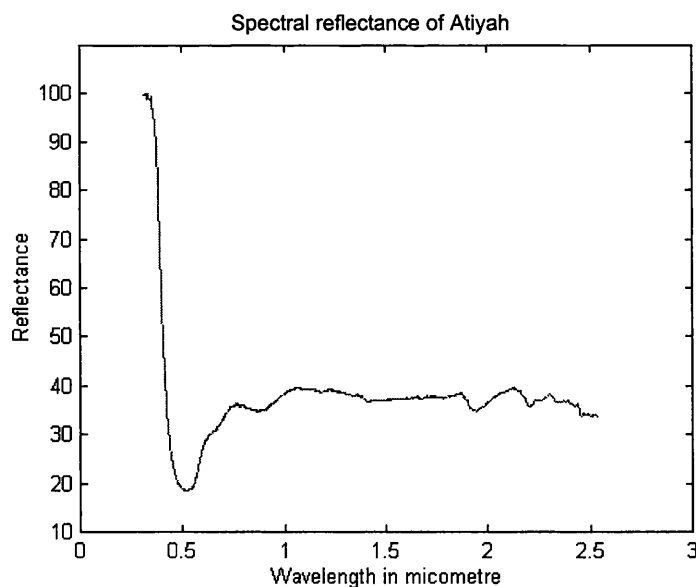


Figure 2.4 Measured spectral reflectance of a sample taken from Atiyah monzogranite.

A vibrational absorption features occurs in the rock sample at $1.9\mu\text{m}$ and is due to water molecules and Si-O bond which is usually occurs in the silicate minerals (i.e. water molecules associated with Mica minerals in the rock sample). Another small vibrational feature occurs at $2.2\mu\text{m}$ as a result of O-H bearing silicates.

4- Spectral reflectance of Jurfayn complex rock sample

The Jurfayn complex rock unit is represented by the spectral reflectance of its collected rock sample shown in figure 2.5. The sample is dark grey medium grained granodiorite selected from an area at geographic coordinate $28^{\circ} 25.921' \text{ N}$ and $34^{\circ} 48.136' \text{ E}$. As shown in the figure, there are no spectral absorption features to characterise the rock unit, and it shows only weak albedo (reflectance) along the wave spectrum. The location of the sample is also taken as a reference representing the spectral identity of the rock unit of the TM data and used as one of the training areas for the rock unit.

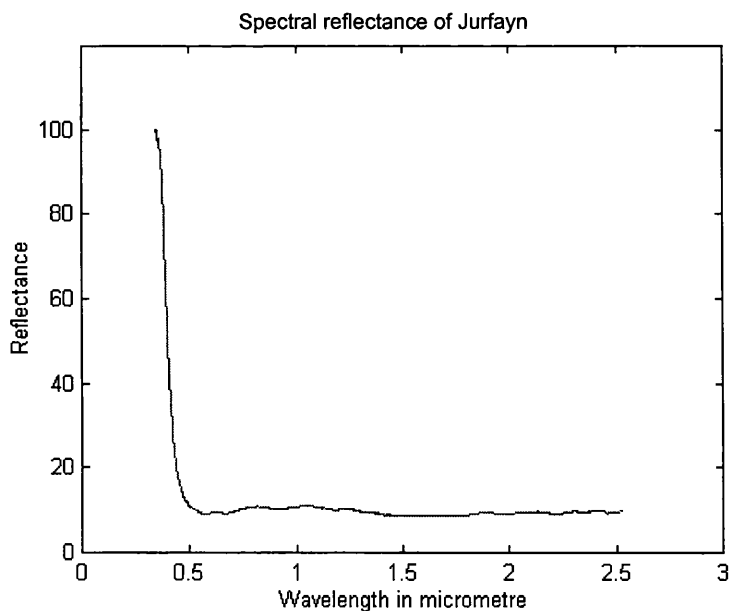


Figure 2.5 Spectral reflectance measurement of sample taken from Jurfayn complex.

5- The spectral reflectance of the Sabkhah deposits

The measured reflectance of a friable sample taken from the Sabkhah at geographic coordinates $28^{\circ} 16.343' \text{ N}$ and $34^{\circ} 55.045' \text{ E}$ is shown in figure 2.6. The sample is creamy white in colour and consists mainly of clay, silt, and evaporitic minerals (i.e. salt and gypsum). Three distinct vibrational absorption features can be depicted in the measured spectra of the sample due to the presence of water molecules at $1.45\mu\text{m}$, $1.9\mu\text{m}$ and O-H bearing minerals absorption feature at $2.2\mu\text{m}$. The geographic location of the sample is marked to be used as a training area in the TM image data. Higher albedo is characteristic of the rock sample.

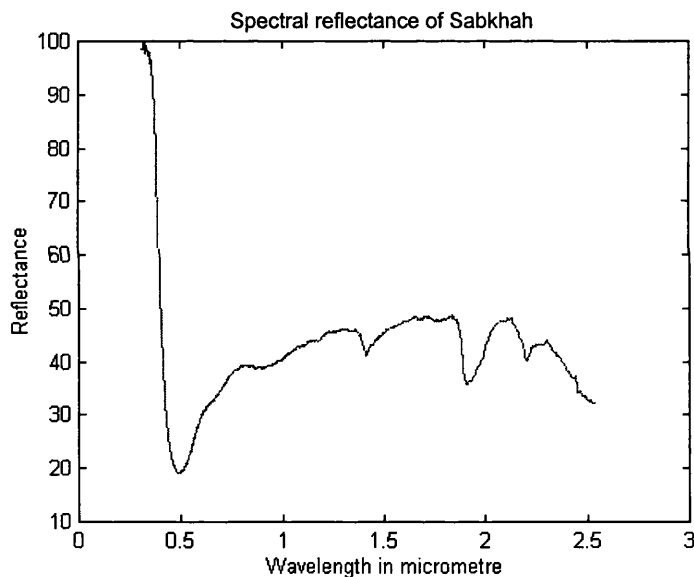


Figure 2.6 The spectral reflectance of Sabkhah.

6- The spectral reflectance of the gravel sheets deposits.

The gravel sheets deposits are represented by a friable sample to measure its spectral reflectance. The sample consists mainly of a mixture of sand, pebbles, and cobbles varying in shape, size, and origin. The sample is taken north of the middle of the test area at location $28^{\circ} 25.572' \text{ N}$ and $35^{\circ} 00.401' \text{ E}$. This location is also selected as a spectral

reference and one of the training areas of the gravel sheets deposits. Figure 2.7 shows its measured reflectance, which is characterised by low reflectance (low albedo) along the measured wavelength mainly due to the metamorphic and igneous source of this sample. No strong absorption feature can be depicted in the measured reflectance of the sample.

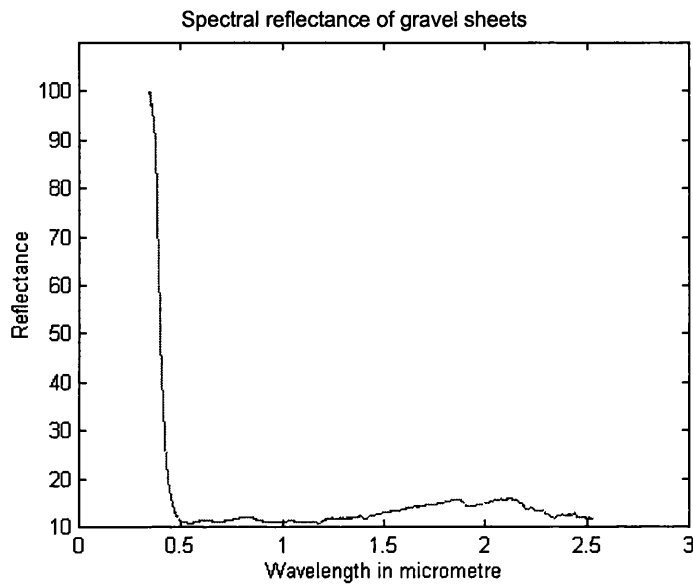


Figure 2.7 The spectral reflectance of the gravel sheets deposits.

Beside the rock unit locations marked as a spectral reference areas during the field work, other areas spectrally similar to the marked areas in the TM (and SAR after being registered with TM) image data are also marked as training areas, representing the individual rock classes. Pixels of these classes are always statistically analysed using the Transformed Divergence (TD) separability test after implementing data fusion and/or an image processing algorithm. The locations of these training areas and the GCPs are shown in figure 2.8. The Transformed Divergence separability measures of the training areas is used as judgement for fusion evaluations. The Transformed Divergence algorithm is described in appendix A-4.

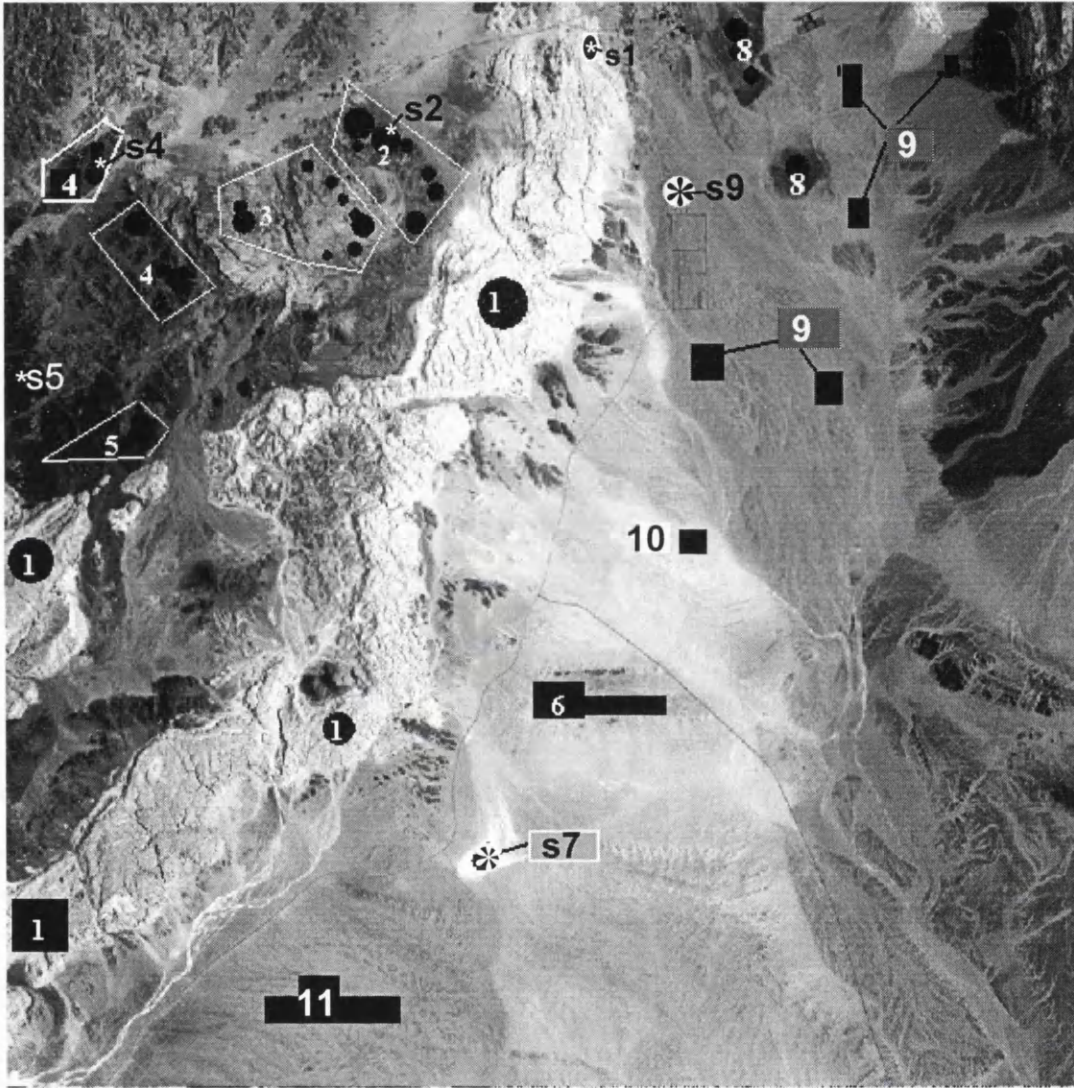


Figure 2.8 Locations of rock unit classes of the study area marked on TM band 5, these classes are (1= Bad'), (2= Nutaysh), (3= Musayr), (4= Atiyah), (5= Jurfayn), (6= Lisan), (7= Sabkhah), (8= conglomerate + gravel), (9= Gravel sheets), (10=Aeolian silt and sand), (11= Alluvium). The (*s) sign represent the location where the sample has been taken for laboratory spectral measurement and also the measured GCP coordinates.

Scale 1:204084

3.0 Synthetic Aperture Radar

In chapter 2, the Landsat 5 TM and the JERS-1 SAR have been described. The acquisition and image construction of the optical TM data is simple and straightforward, and has been discussed briefly in chapter 2. The generation of SAR images is somewhat complicated, and this chapter is devoted to a description of the techniques underlying the method of SAR image generation, including the geometrical aspects of the SAR.

3.1 Historical background

Radar has long been recognised as a tool for detection, tracking, and ranging of targets such as aircraft and ships. It uses radio waves to detect the presence of objects and identify their position. The word RADAR is an acronym of RAdio Detection And Ranging, firstly introduced by the US Navy in 1940. The first record of discovery of radar, after 15 years of the discovery and study of generation, reception, and scattering of electromagnetic radiation carried out by Hertz, was in 1903, when a German scientist demonstrated a radar system for ship collision avoidance [7]. In 1922, Marconi recognised the value and importance of radar for the detection and tracking of ships. The first airborne pulsed radar system operating at carrier frequency of 60MHz was developed by the NRL (Naval Research Laboratory) in the US in 1934. In parallel, radar systems for tracking and detection of aircraft were developed in Great Britain and Germany during the early 1930s. By 1935, each of these countries had successfully demonstrated the capability of tracking aircraft targets using short pulse ranging measurements. In 1937, Sir Robert Watson-Watt built the first operational radar network, which was used to track aircraft across Western Europe, and this network was used in World War II [7]. During the War, improvements in these systems were carried out by the US, Great Britain, and Germany, which include the development of high frequency hardware and systems, high peak power microwave transmitters, and the development of image display systems such as the CRT, B-Scan, and PPI. In 1950, films were used to record the CRT display of the pulse echoes.

Side Looking Airborne Radar (SLAR) was the second step in the development of radar technology and was firstly introduced and intended for use for military reconnaissance purposes [10]. In the mid-1960s the first high resolution SLAR (10-20 metre resolution) became available for scientific applications. The first mapping project using radar (SLAR) was in 1967 in the Darien province in Panama. Scientists have increased their studies of SLAR since this time for geoscience applications. These systems were then used extensively for rapid reconnaissance mapping with scales of 1:250,000 for non previously mapped areas, and especially for tropical vegetation covered areas such as Brazil, Venezuela, Panama, Guatemala, Nigeria, and parts of Indonesia, the Philippines, Colombia, Peru, and USA [10].

The first SAR system was developed by the Goodyear research group in Litchfield, Arizona, where the research group pursued Wiley's Doppler beam sharpening concept (called squint mode SAR). The SAR system was carried aboard a DC-3 aeroplane in 1953. The system operated at 930MHz with a real aperture beamwidth of 100° using Yagi antennas. The first strip map SAR images were produced through a collaboration between a research group in the University of Michigan and the US Army in 1958 [7].

Seasat was the first satellite-borne SAR system, developed by NASA and became operational in July 1978. The satellite had a 100 day lifetime, and supplied scientists with hundreds of radar images of the Earth's surface [11]. The Shuttle Imaging Radar (SIR) series was then introduced in NASA programs after the success of the Seasat SAR. The SIR-A mission was carried out in 1982, and the system was designed by JPL of NASA primarily for geological and land applications. The system was equipped with an optical recorder and fixed antenna elevation angle of 45° off-nadir. This was followed by the SIR-B mission in 1984, with a steerable antenna with off-nadir angles ranging from 15° to 60°. The system was fully digital, with selectable quantization of 3-6 bits per sample [7]. The SIR-C system was developed jointly with NASA by Germany and Italy, and the system was flown in 1993 and 1994 with L, C, and X bands recording nine channels (L and C bands HH, HV, VH, VV, and X-band VV) capability.

Recently, Canada, Japan, and Europe have also made their contributions in imaging SAR satellites, through Radarsat of Canada, the ERS series of the European Space Agency, and the JERS-1 satellite of Japan. Furthermore, future plans for monitoring the Earth by SAR, thermal, and optical sensors flown by satellites are underway, collaboratively between NASA, ESA, and NASDA of Japan. This is an international remote sensing program called the Earth Observing System (EOS) and plans for placing in orbit a series of remote sensing platforms carrying a wide variety of instruments spanning the electromagnetic spectrum [10].

The Synthetic Aperture Radar is characterised by its coherency, which retains both phase and magnitude of the backscattered echo signal. Its high resolution is achieved by synthesising in the signal processor an extremely long antenna aperture. This is performed digitally in the ground segment processing by compensating the quadratic phase characteristic associated with what is effectively near field imaging by the long synthetic array. From this, SAR is capable of achieving a resolution independent of the platform altitude, which gives the system enormous value in remote sensing and space observation. SAR is characterised by day and night, all-weather imaging capability, its spatial resolution is independent of sensor altitude and wavelength (but the signal gain should be taken into account), the SAR signal (i.e. frequency, pulse length, direction, and modulation) can be explicitly controlled, and the data characteristics collected by the SAR allow the geophysical properties of the imaged targets to be determined.

3.2 Geometry of imaging radar

A simplified and general geometry of an imaging radar is shown in figure 3.1. The radar system is carried on a platform moving at constant speed v_s and constant altitude h . The radar beam is directed perpendicular to the flight path and downwards towards the Earth's surface at a pointing angle or look angle γ (measured from the beam centre relative to vertical or nadir track). Neglecting the Earth's curvature, the radar signals strike the surface at incident angle η .

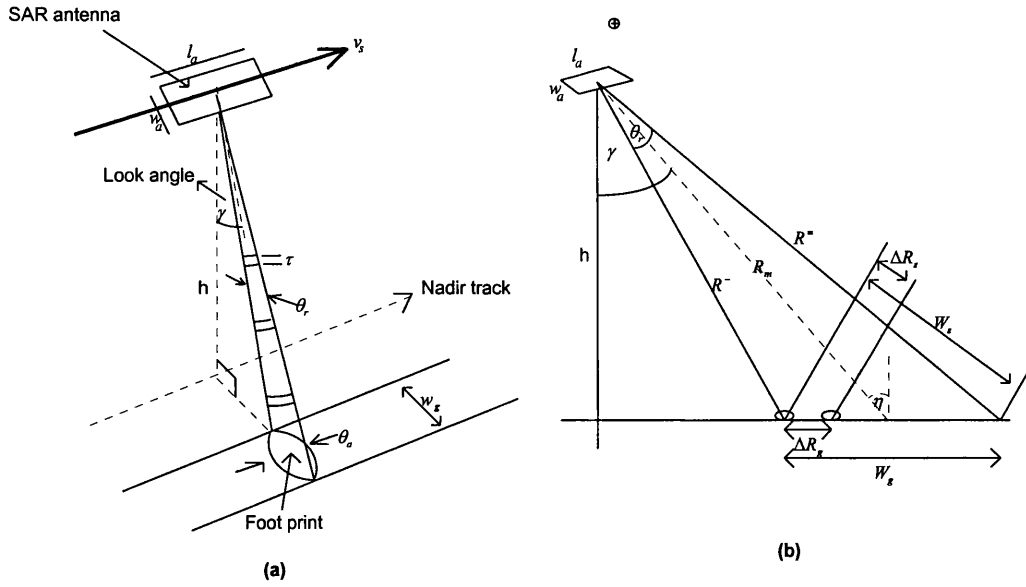


Figure 3.1 (a) Basic geometry of imaging radar. (b) viewing the geometry from azimuth, the ground swath is clearly demonstrated as a function of the beamwidth (Source:[7]) .

The radar system transmits pulses of electromagnetic energy of wavelength λ . The return echoes are then sampled for future time coherent signal processing. In figure 3.1, the ground swath width w_g (ground range) is established by the antenna width w_a , which determines the elevation beamwidth θ_r :

$$\theta_r = \frac{\lambda}{w_a} \quad \text{radians} \quad (3.1)$$

The antenna length l_a also determines the azimuth beamwidth θ_a by the relation:

$$\theta_a = \frac{\lambda}{l_a} \quad \text{radians} \quad (3.2)$$

If R_m is the slant range from the radar to the midswath, then:

$$w_g = \frac{\theta_r R_m}{\cos \eta} = \frac{\lambda R_m}{w_a \cos \eta} \quad (3.3)$$

Also the swath width w_g in equation (3.3) can be rewritten as:

$$w_g = \frac{h \theta_r}{\cos^2 \gamma} \quad (3.4)$$

The ground resolution of the radar is defined as the minimum distance between two points that can be distinguished as separate by the system. If τ is the radar pulse length, the minimum slant range separation of two resolvable points is:

$$\Delta R_s = c\tau / 2 \quad (3.5)$$

where :

c = speed of radar signal propagation

$$\tau = \frac{1}{B} \text{ and } B \text{ is the bandwidth of the radar signal} \quad (3.6)$$

$$\text{The resolution in the range direction } \Delta R_g = \frac{\Delta R_s}{\sin \gamma} = \frac{c\tau}{2 \sin \gamma} = \frac{c}{2B \sin \gamma} \quad (3.7)$$

$$\text{The resolution in the azimuth direction } \Delta R_a = \frac{h\theta_a}{\cos \gamma} = \frac{h\lambda}{l_a \cos \gamma} \quad (3.8)$$

Equation 3.8 is applicable in Real Aperture Radar (RAR), where the resolution in the azimuth direction depends on the length of the imaging system antenna (l_a) and the satellite height from the Earth's surface (h). In the case of synthetic aperture radar (SAR), a different technique is used to increase range and azimuth resolutions, which is by the use of range or what are called pulse compression and azimuth compression or correlation respectively.

3.3 Pulse Compression

Pulse compression refers to the implementation of a matched filter used in the radar system [12]. Two types of pulse compression are commonly used to increase the radar range resolution; one is frequency modulation (FM), the second is phase coding [13]. The frequency modulation FM is called chirping, and is widely used in SAR imaging systems.

The technique of linear FM or chirping is simply to keep the carrier signal f_0 linearly changing either increasing or decreasing throughout the pulse from f_0 to $f_0 \pm \Delta f$. If f_0 is increasing (i.e. $f_0 + \Delta f$), the modulation is called up chirp. If f_0 is decreasing it is called down chirp and this method is used in JERS-1 SAR. Figure 3.2 shows the linear FM modulation of down chirping of the JERS1 SAR.

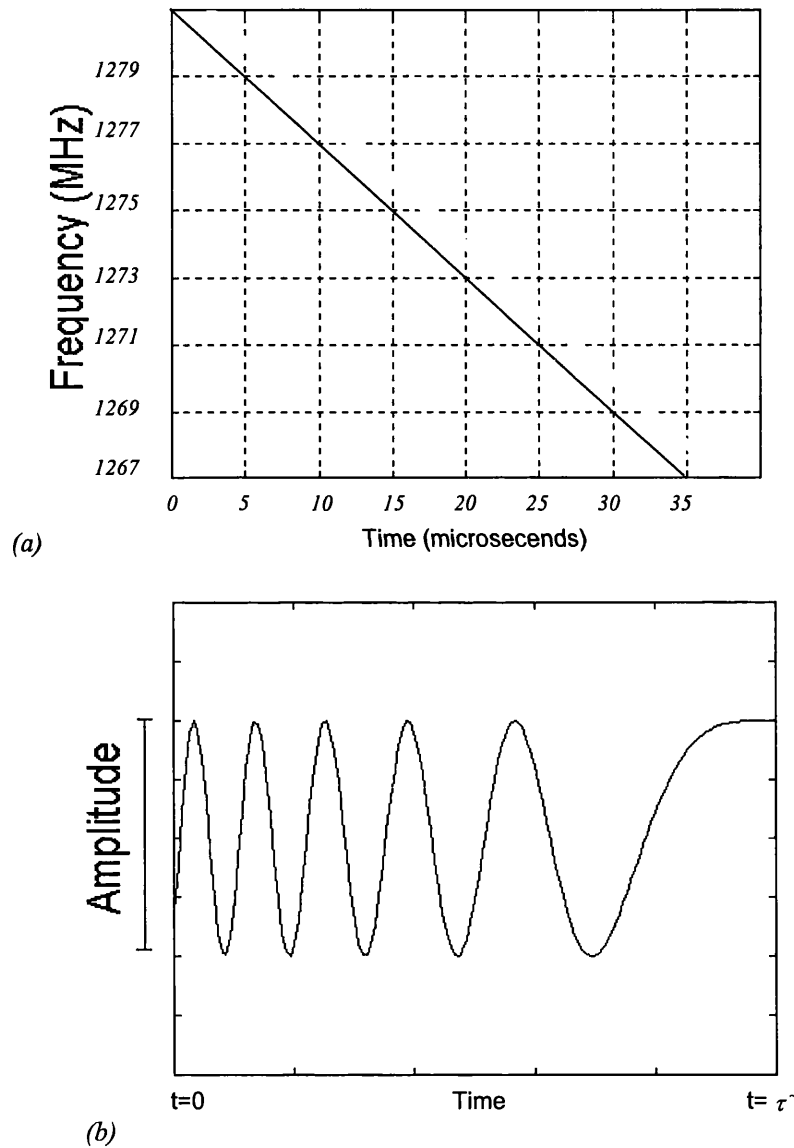


Figure 3.2 (a) Reconstruction of linear frequency modulated JERS-1 SAR signal. The bandwidth (Δf) 15 MHz is represented by the y-axis and centred at the frequency (f_0) of 1275 MHz. The frequency is decreasing along the x-axis (the dispersion) in 35 microsecond. (b) The waveform of the JERS-1 SAR FM signal.

Since $\tau = 1 / B$ before chirping, the bandwidth B after chirping is:

$$\begin{aligned} B &= |(f_0 + \Delta f) - f_0| \\ &= |\Delta f| \end{aligned} \quad (3.9)$$

From equation 3.9, it is clear that the bandwidth is independent of the pulse length τ . Thus large τ and large B can be constructed using the chirping technique, allowing high range resolution (i.e. small ΔR_r) to be achieved.

3.4 Azimuth compression and the synthetic aperture technique

High resolution in the azimuth direction cannot be achieved using the RAR technique, because of its dependence upon l_a and h . To achieve high azimuth resolution, the synthetic aperture technique is used, which makes the azimuth resolution independent of l_a and h . Altitude is still a major factor in determining the power required to record a detectable echo and so determines the size of the antenna.

The synthetic aperture technique relies on making the target stay in the radar beam for a significant amount of time, and observing the target from a sequence of locations throughout the platform movement. For simplicity, assumptions have been made such as ignoring the motion of the platform through transmission-reception of the echoes, Earth rotation, and assuming a straight path for the platform movement. From figure 3.3, the range from the satellite to the target is r , and the closest range is r_o [14].

$$\begin{aligned} r &= (r_o^2 + x^2)^{1/2} \\ &= r_o \left(1 + \frac{x^2}{r_o^2} \right)^{1/2} \\ &= r_o \left(1 + \frac{1}{2} \frac{x^2}{r_o^2} - \frac{1}{8} \frac{x^4}{r_o^4} + \dots - \dots \right) \end{aligned}$$

$$\cong r_o + \frac{x^2}{2r_o} \quad (3.10)$$

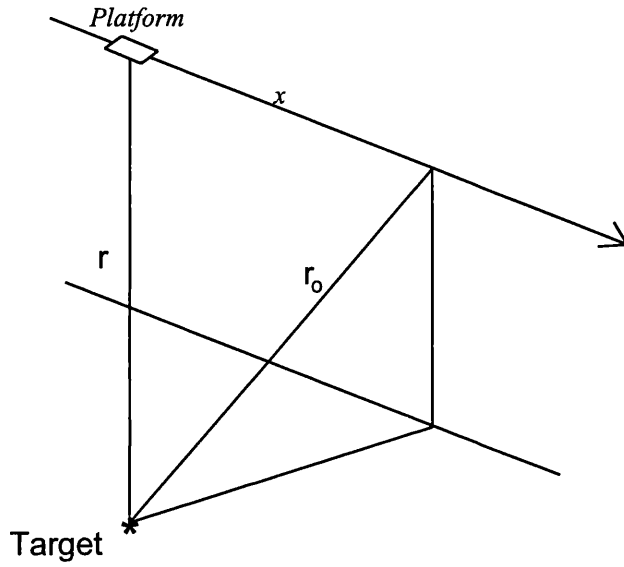


Figure 3.3 SAR co-ordinate system (source:[14]).

The two-way phase of the sequence of echoes is

$$\begin{aligned} \phi(x) &= -\frac{2r}{\lambda} \times 2\pi \\ &= -\left(\frac{2r}{\lambda} \times 2\pi + \frac{2x^2}{2r_o\lambda} \times 2\pi \right) \\ &= \phi_o - \frac{2\pi x^2}{r_o\lambda} \end{aligned} \quad (3.11)$$

Equation 3.11 represents a quadratic variation of phase, and can be shown in figure 3.4.

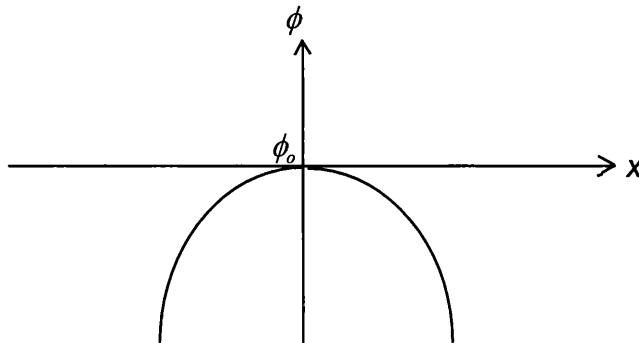


Figure 3.4 Echo phase changes as a function of x (source:[14]).

Also, the phase variation can be considered as a function of time t to give the Doppler frequency f_D , therefore equation 3.11 can be reconstructed as:

$$\phi(t) = \phi_o - \frac{2\pi v^2 t^2}{r_o \lambda} \quad (3.12)$$

and

$$\begin{aligned} f_D &= \frac{1}{2\pi} \frac{d\phi}{dt} \\ &= -\frac{2v^2 t}{r_o \lambda} = \frac{2vx}{r_o \lambda} \end{aligned} \quad (3.13)$$

So this quadratic variation of phase as show in figure 3.4 is a linear varying in Doppler. This is shown in figure 3.5.

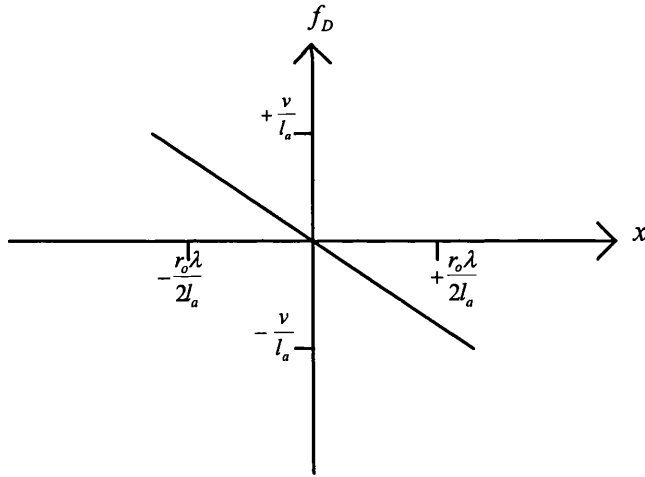


Figure 3.5 Doppler frequency as a function of x . The extremes of the footprint of the SAR antenna are $\pm r_o \lambda / 2l_a$ and the limits of the Doppler frequency are $\pm v / l_a$ (source:[14]).

From figure 3.5, it is clear that matching the phases of the echoes is a frequency domain matched filtering process, and can be seen as similar to matched filtering of a chirp signal

in the pulse compression process. For this reason, this process is referred as azimuth compression (or azimuth correlation) [14].

The range and azimuth resolution of focused aperture synthesis can be calculated in several ways. A simplified method is shown in figure 3.6 [14].

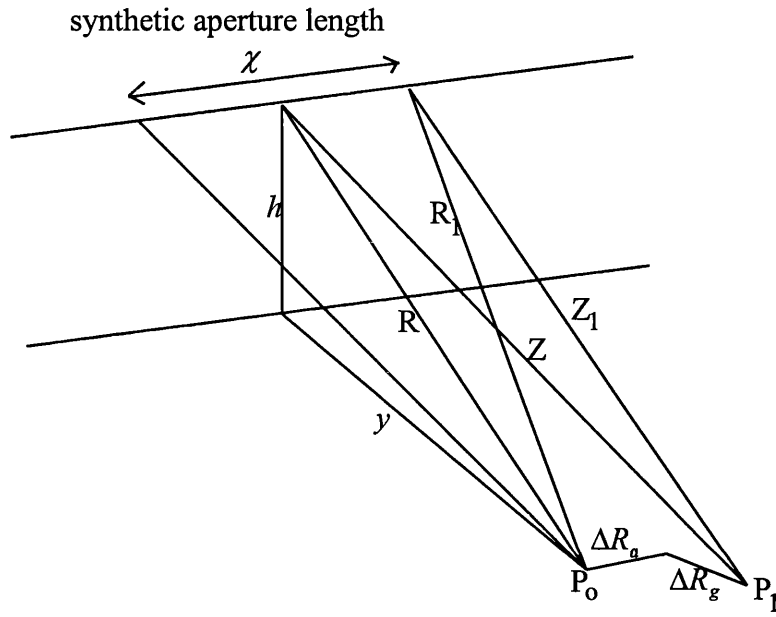


Figure 3.6 SAR imaging geometry (source: [14]).

The net path error is:

$$\begin{aligned}\delta &= (R - Z) - (R_1 - Z_1) \\ &= (Z_1 - Z) - (R_1 - R)\end{aligned}\quad (3.14)$$

$$R_1^2 = R^2 + \frac{\chi^2}{4}\quad (3.15)$$

$$\begin{aligned}R_1 &= R \left(1 + \frac{\chi^2}{4R^2} \right)^{1/2} = R \left(1 + \frac{\chi^2}{8R^2} + \dots \right) \\ &\cong R + \frac{\chi^2}{8R}\end{aligned}\quad (3.16)$$

$$Z^2 = (R + \Delta R_g)^2 + \Delta R_a^2\quad (3.17)$$

$$\begin{aligned}
Z &= (R + \Delta R_g) \left(1 + \frac{\Delta R_a^2}{(R + \Delta R_g)^2} \right)^{1/2} = (R + \Delta R_g) \left(1 + \frac{\Delta R_a^2}{2(R + \Delta R_g)^2} + \dots \right) \\
&\cong (R + \Delta R_g) + \frac{\Delta R_a^2}{2(R + \Delta R_g)}
\end{aligned} \tag{3.18}$$

and finally:

$$Z_1^2 = (R + \Delta R_g)^2 + \left(\frac{\chi}{2} - \Delta R_a \right)^2 \tag{3.19}$$

$$\begin{aligned}
Z_1 &= (R + \Delta R_g) \left(1 + \frac{\left(\frac{\chi}{2} - \Delta R_a \right)^2}{(R + \Delta R_g)^2} \right)^{1/2} \\
&= (R + \Delta R_g) \left(1 + \frac{\left(\frac{\chi}{2} - \Delta R_a \right)^2}{2(R + \Delta R_g)^2} + \dots \right) \\
&\cong (R + \Delta R_g) + \frac{\left(\frac{\chi}{2} - \Delta R_a \right)^2}{2(R + \Delta R_g)}
\end{aligned} \tag{3.20}$$

So, equation 3.14 can be rewritten as:

$$\begin{aligned}
&\frac{\left(\frac{\chi}{2} - \Delta R_a \right)^2}{2(R + \Delta R_g)} - \frac{\chi^2}{8R} \\
&= -\frac{\chi \Delta R_a}{2(R + \Delta R_g)} - \frac{\chi^2}{8R(R + \Delta R_g)} \\
&\cong -\frac{\chi \Delta R_a}{2R} - \frac{\Delta R_g \chi^2}{8R}
\end{aligned} \tag{3.21}$$

The terms of equation 3.21 can be set separately to $\lambda / 8$ which is $\pi / 2$ (or two-way phase error). Then:

$$\frac{\chi \Delta R_a}{2R} = \frac{\lambda}{8} \Rightarrow \Delta R_a = \pm \frac{\lambda R}{4\chi} \text{ (azimuth resolution)} \tag{3.22}$$

$$\frac{\Delta R_g \chi^2}{8R^2} = \frac{\lambda}{8} \Rightarrow \Delta R_g = \pm \frac{\lambda R^2}{\chi^2} \text{ (range resolution)} \quad (3.23)$$

The maximum aperture length χ depends on the SAR antenna beamwidth in the azimuth direction θ_a , which depends on the antenna length l_a as shown in equation 3.2, and from figure 3.7:

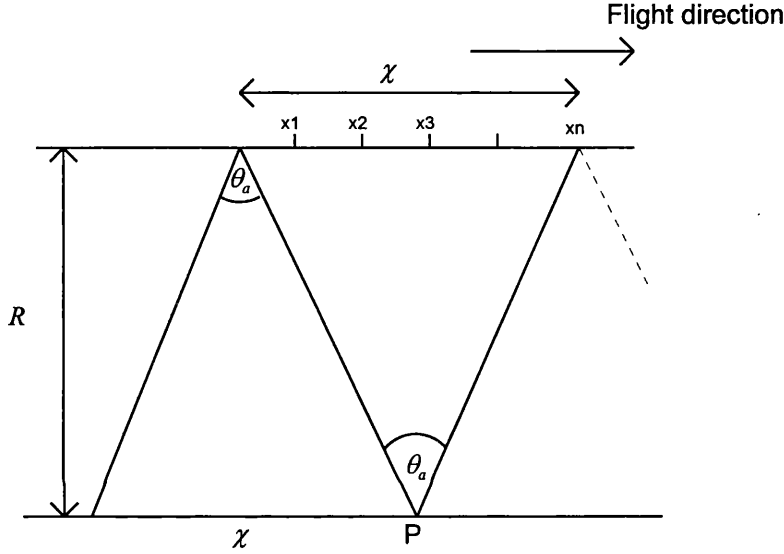


Figure 3.7 Synthetic aperture technique using long synthetic array.

$$\chi = R\theta_a = \frac{R\lambda}{l_a} \quad (3.24)$$

From equation 3.22, the azimuth resolution is:

$$\Delta R_a = \frac{\lambda R}{2\chi} = \frac{\lambda R}{2} \times \frac{l_a}{\lambda R} = \frac{l_a}{2} \quad (3.25)$$

and the range resolution in equation 3.23 becomes:

$$\Delta R_g = \frac{2l_a^2}{\lambda} \quad (3.26)$$

From equation (3.25), the achievable resolution is half of the antenna real aperture as a result of the larger synthetic aperture χ .

From figure 3.7, the resulting echoes (after adding their proper phase shifts) are then added together as long as the point P is still in the radar beam. If all received echoes are added without using their proper phase shifts, the echoes received are called unfocused to the point P and the azimuth resolution in this case is $\Delta R_a = \sqrt{2\lambda h}$ which is still better than the RAR technique [11].

An important factor to be taken into account during the processing for aperture synthesis is the range migration or what is known as range curvature and range walk. This is because the range between the satellite and the target P during the formation of the synthetic aperture technique does not change linearly. From figure 3.8, and assuming the antenna is exactly boresighted, then:

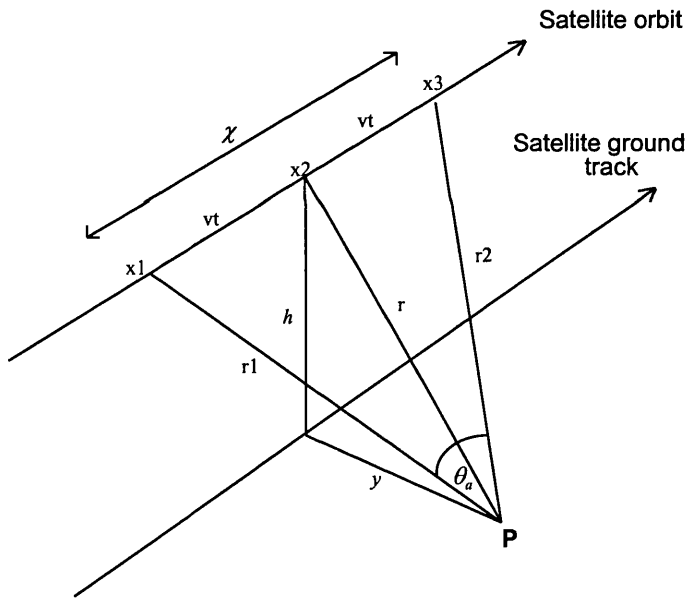


Figure 3.8 Range curvature and range walk.

$$r = \sqrt{(h)^2 + (y)^2} \quad (3.27)$$

Note that vt is the distance equal to $\frac{\chi}{2}$ and is equal to $r \frac{\theta_a}{2}$.

$$r_1 = r_2 = \sqrt{(r)^2 + (vt)^2}$$

$$\begin{aligned}
&= r \sqrt{1 + \frac{(vt)^2}{r^2}} \\
&= r \left[1 + \frac{1}{2} \frac{(vt)^2}{r^2} - \frac{1}{8} \frac{(vt)^4}{r^4} + \dots \right] \\
&= r + \frac{(vt)^2}{2r}
\end{aligned} \tag{3.28}$$

The range curvature $r_c = r_1 - r$.

$$\begin{aligned}
r_1 - r &= \frac{(vt)^2}{2r} = \frac{r^2 \theta_a^2}{8r} \\
&= \frac{r}{8} (\lambda / l_a)^2 \\
&= \frac{r \lambda^2}{32 R_a^2}
\end{aligned} \tag{3.29}$$

The maximum range curvature r_{mc} is:

$$\begin{aligned}
r_{mc} &= \frac{r \lambda^2}{32 R_a^2 w_g \sin \theta} \quad \text{in which } \theta \text{ is the look angle.} \\
&= \frac{h \lambda^2 B}{16 c R_a^2 \cos \theta}
\end{aligned} \tag{3.30}$$

The depth of focus F_D as shown in figure 3.9 is:

$$\begin{aligned}
F_D &= \frac{2 \lambda r^2}{\chi^2} \\
&= 2 l_a^2 / \lambda
\end{aligned} \tag{3.31}$$

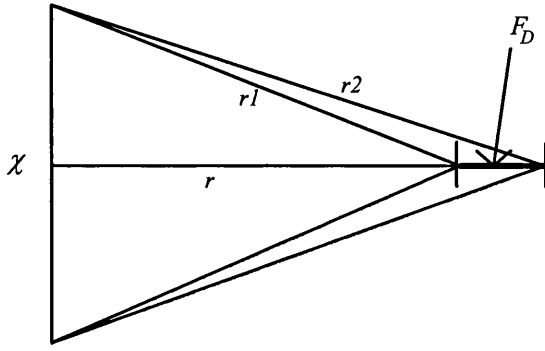


Figure 3.9 The depth of focus.

When N looks are used to process an image, the depth of focus becomes [11]:

$$F_D = 2N^2 l_a^2 / \lambda \quad (3.32)$$

The range walk r_w results when the target is not at boresight and tilted by an angle β which leads to $r_1 \neq r_2$, then:

$$\begin{aligned} r_1 &= \sqrt{(r)^2 + [(r)^2 (\beta \frac{\theta_a}{2})^2]} \\ &\approx r[1 + \frac{1}{2}(\beta + \frac{\theta_a}{2})^2] \\ &= r[1 + \frac{\theta_a^2}{8} + \frac{\beta\theta_a}{2}] \end{aligned} \quad (3.33)$$

$$\begin{aligned} r_2 &= r[1 + \frac{1}{2}(-\beta + \frac{\theta_a}{2})^2] \\ &\approx r[1 + \frac{\theta_a^2}{8} - \frac{\beta\theta_a}{2}] \end{aligned} \quad (3.34)$$

The range walk is then $r_w = r_1 - r_2$.

$$\begin{aligned} r_1 - r_2 &= r\beta\theta_a \\ &= r\lambda\beta / l_a \end{aligned} \quad (3.35)$$

Synthesising the SAR aperture through utilising the process in terms of the Doppler shift f_D can also lead to the same result as shown in equation 3.25, for example, when the satellite flies towards the target P , the target enters the radar beam and the Doppler shift f_D is positive. The shift then decreases until it becomes zero when the target P lies exactly in the centre of the radar beam, and then becomes negative as the satellite flies away from the point P [11]. This can be illustrated by figure 3.10.

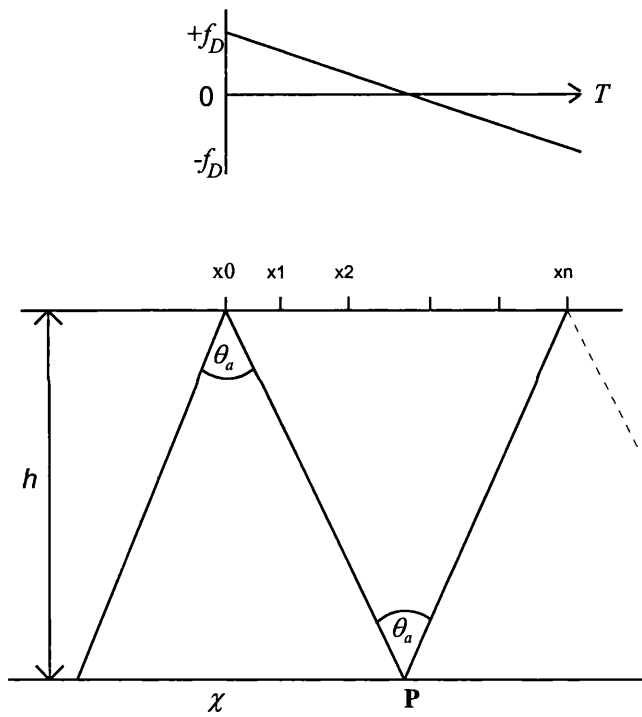


Figure 3.10 Synthesising the aperture using Doppler technique. The upper figure represents the Doppler shift..

$$\begin{aligned}
 f_D &= \frac{2v}{\lambda} \sin \frac{\theta_a}{2} \\
 &\cong \frac{v \theta_a}{\lambda} \\
 &= \frac{v}{l_a}
 \end{aligned} \tag{3.36}$$

When a neighbouring target P' is displaced from P by a distance x_i which is equal to R_a along the azimuth direction, the Doppler history will be a replica of P with time displacement t_d

$$t_d = \frac{R_a}{v}. \quad (3.37)$$

and the shortest time displacement that can be measured is:

$$\begin{aligned} t_d &= 1 / 2f_D \\ &= l_a / 2v \end{aligned} \quad (3.38)$$

From (3.37) and (3.38), the finest possible resolution in azimuth ΔR_a is:

$$\begin{aligned} R_a &= v \cdot t_d \\ &= \frac{vl_a}{2v} \\ &= \frac{l_a}{2} \end{aligned} \quad (3.39)$$

which is exactly the same as equation 3.25. A similar results for azimuth resolution can also be derived using change of aspect angle $\Delta\theta$.

An important property of synthesising the SAR aperture is what is called points of equi-distances and equi-Doppler in the radar scene. This property can be used as a coordinate system for the imaged area. Figure 3.11 shows equi-distance and equi-Doppler of synthetic aperture imaging system.

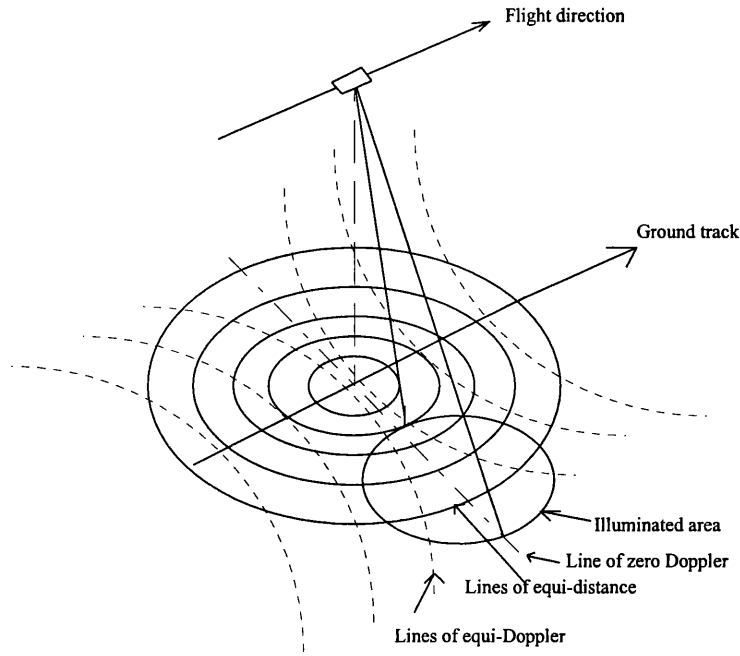


Figure 3.11 Doppler equi-distances and equi-Doppler of Synthetic Aperture Imaging Systems (source: [11]).

As shown in figure 3.11, all lines or points located at circles centred on the radar ground track location (nadir point) have echoes which will be received simultaneously. These points or lines are called points of equi-distance. All lines or points located on coaxial cones, with the flight line as the axis and the radar location as the apex (dashed curves in figure 3.11), have echoes with identical Doppler shift [11].

The Earth's rotation has an influence on the Doppler shift, and has to be included in the shift. A point target P on the Earth's surface has a linear velocity depending on its geographic latitude. The point target P has the velocity:

$$V_p = R_E \varpi_E \cos \gamma_p \quad (3.40)$$

where:

R_E = Earth's radius, equal to 6367 km.

ϖ_p = angular rotational velocity of the Earth = $2\pi / 24$ radian./hour.

γ_p = Point target P geographic latitude.

$$\begin{aligned}\therefore V_p &= \frac{2\pi}{24} \times 6367 \times \cos \gamma_p \quad \text{km/hour.} \\ &= 0.463 \cos \gamma_p \quad \text{km/sec.}\end{aligned}$$

The Doppler shift resulting from the velocity of the point target P by the Earth's rotation ($0.463 \cos \gamma_p$ km/sec) should be added in addition to the Doppler shift caused by the satellite movement for precise synthetic array. The velocity of the point target caused by the Earth's rotation is equal to zero if located at the poles and equal to $R_E \varpi_E$ if located on the equator.

3.5 The SAR radar equation

At the raw data level (i.e. before compression), the received peak power P_r from a target of radar cross section σ is:

$$P_r = \frac{P_t G^2 \lambda^2 \sigma}{(4\pi)^3 R^4} + N_n \quad (3.41)$$

where:

N_n = the average thermal noise power (assuming a white stationary Gaussian process).

G = antenna gain.

σ = target radar cross section.

P_t = peak transmitted power.

In equation (3.41), ambiguity noise and speckle (discussed in 4.4) are considered an inherent part of the received signal. At the image level, the received power from a point target P_i is:

$$P_i = n^2 P_r + n N_n \quad (3.42)$$

where:

n = the product of range and azimuth samples integrated during the compression

processing. $n = t f_r \left[\frac{\lambda R}{2 v R_a} PRF \right]$, noting that t is the pulse time duration and

f_r is the range sampling frequency.

In the case of a distributed target where the received power is assumed to be the mean power averaged over all the elementary scatterers of a statistically homogenous area, the radar equation for the raw data is:

$$P_r = \frac{P_t G^2 \lambda^2 R_r R_a \sigma_0 c \tau B_p}{(4\pi)^3 R^3 2 \sin \theta} + N_n \quad (3.43)$$

where:

σ_0 = the backscatter coefficient.

B_p = the 3dB azimuth antenna power beamwidth.

At the image level, the radar equation for a distributed target is the same as equation (3.43) with the replacement of the received power P_r of a point target with the received power of the distributed target. Thus the radar equation becomes:

$$P_r = n^2 \frac{P_t G^2 \lambda^2 R_r R_a \sigma_0 c \tau B_p}{(4\pi)^3 R^3 2 \sin \theta} + n N_n \quad (3.44)$$

3.6 Ambiguities in SAR

Because SAR uses repetitive pulses, its performance is limited by the presence of ambiguities. These ambiguities are related to the range and azimuth, other ambiguities are related to the system design and the SAR processing [11]. For example, in order to do the synthetic processing it is important to make an adequate sampling of the Doppler spectrum.

$$PRF > 2 f_D \quad \Rightarrow \quad PRF > 2 v / l_a \quad (3.45)$$

Equation 3.45 is the Nyquist criterion for the sampling of the synthetic aperture and indicates that a sample should be taken every time the satellite moves half of the antenna length.

Successive pulses should be far enough apart from each other so that they will not be received simultaneously, leading to range ambiguity.

$$\frac{c}{2PRF} > w_g \text{ where } w_g \text{ is the swath width} \quad (3.46)$$

$$w_g = \frac{h\theta_r}{\cos^2 \theta}$$

$$\therefore PRF < \frac{cw_a}{2\lambda h} \times \frac{\cos^2 \theta}{\sin \theta} \quad (3.47)$$

From 3.45 and 3.47, the limits of PRF to avoid ambiguities are:

$$\frac{2v}{l_a} < PRF < \frac{cw_a \cos^2 \theta}{2\lambda h \sin \theta} \quad (3.48)$$

Equation 3.48 leads to an important relation involving the antenna area:

$$w_a l_a > \frac{4\lambda h v \sin \theta}{c \cos^2 \theta} \quad (3.49)$$

The left side of the relation (3.49) represented by w_a and l_a determines the swath width and the resolution in the same time. In the right side of the relation, h and v determine the orbit characteristics, where λ and θ determine the frequency and the look angle respectively [11].

Because of the large distance between the satellite and the ground surface, several pulses and echoes are present in the propagation path at any instant of time. The *PRF* should be selected such that no pulse is transmitted while a pulse is being received and that echoes from only one transmitted pulse are received at any instant.

3.7 Geometric distortions in SAR

SAR is influenced greatly by geometric distortions as a result of sensor instability, platform instability, signal propagation effects, terrain height, and processor induced errors [7].

Sensor stability is a key factor controlling the internal geometric fidelity of the data. An example is the consistency of the interpulse or intersample period which is governed by the accuracy of timing signals sent to the pulse generator and the analogue to digital converter (ADC). Variations of these timing signals are dependent on the stable local oscillator (STALO).

Electronic delay affects the geometric fidelity of the data sets. The electronic delay (τ_e) of the signal through the radar transmitter and receiver must be subtracted from the total delay to derive the actual propagation time used in the slant range calculation:

$$R = c(\tau - \tau_e) / 2 \quad (3.50)$$

The signal propagation delay through the atmosphere may cause slant range error. Propagation timing error arises when it is assumed that the propagation velocity of the electromagnetic wave is equal to the speed of light. Under certain ionospheric conditions, an increase in the signal propagation time relative to the propagation time in vacuum can occur due to the Earth's atmosphere. Solar activities, which occur approximately every 11 years have a similar influence. The ranging error will result in a cross-track target location error.

$$\Delta r = \frac{c\Delta\tau}{2\sin\eta} \quad (3.51)$$

where :

$\Delta\tau$ =slant-range timing error.

η = the grazing angle.

Another type of error may result from the drift of the spacecraft clock. Any offset between the spacecraft clock and the clock used to derive the ephemeris file from the spacecraft tracking data will result in target location errors [7].

Exact target location can be determined by simultaneous solution of three equations: the range equation, the Doppler equation, and the Earth model equation.

$$\text{The range equation: } R = |R_s - R_t| \quad (3.52)$$

where R_s and R_t are the sensor and the target position vectors respectively.

$$\text{The Doppler equation: } f_{DC} = \frac{2}{\lambda R} (V_s - V_t) \times (R_s - R_t) \quad (3.53)$$

where:

f_{DC} =Doppler centroid frequency.

V_s and V_t are the sensor and the target velocity vectors.

The target velocity can be derived from the relation: $V_t = \omega_E \times R_t$ where ω_E = Earth rotational velocity vector and $R_t = R_E \cos\gamma_p$.

The Earth model equation; Usually an oblate ellipsoid model is used to model the Earth's shape. Figure 3.12 shows the oblate ellipsoid Earth model:

$$\frac{x_t^2 + y_t^2}{(R_E + h)^2} + \frac{z_t^2}{R_p^2} = 1 \quad (3.54).$$

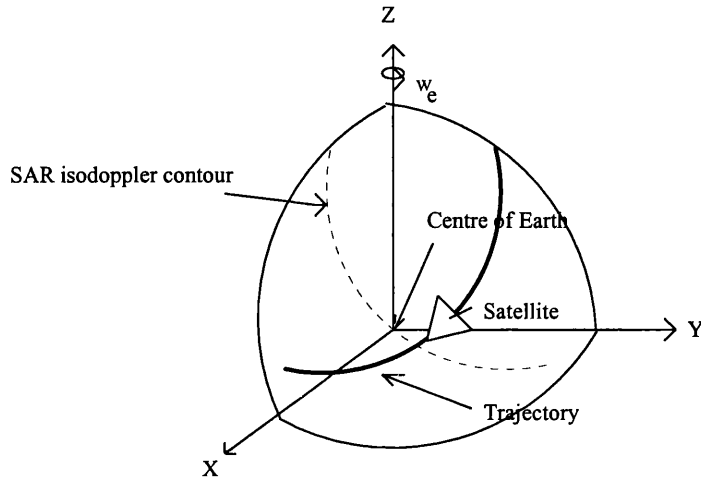


Figure 3.12 The oblate ellipsoid model of the Earth (source: [7]).

where R_E is the radius of the Earth at the equator = 6378.137km, h is the local target elevation relative to the assumed model, and R_p is the polar radius = 6356.752km.

The latitude of the point (P) is γ_p :

$$\gamma_p = \tan^{-1} \frac{z_t}{\sqrt{x_t^2 + y_t^2}} \quad (3.55)$$

Beside the location errors, satellite altitude and position errors are very common in SAR. They can be classified as yaw, pitch, and roll errors [11]. The satellite yaw error occurs as a result of the satellite displacement or rotation around its vertical axis (figure 3.13 a). Such error has a significant effect because it displaces the antenna footprint away from zero Doppler and the return radar echo will be displaced by a frequency:

$$\Delta f_y = \frac{2v}{\lambda} \sin \theta \sin \alpha \quad (3.56)$$

Satellite pitch error is similar to the yaw error but the displacement angle occurs relative to the satellite's nadir point (Figure 3.13 b). The received signal will have an additional Doppler shift Δf_p equal to:

$$\Delta f_p = \frac{2v}{\lambda} \sin \alpha \quad (3.57)$$

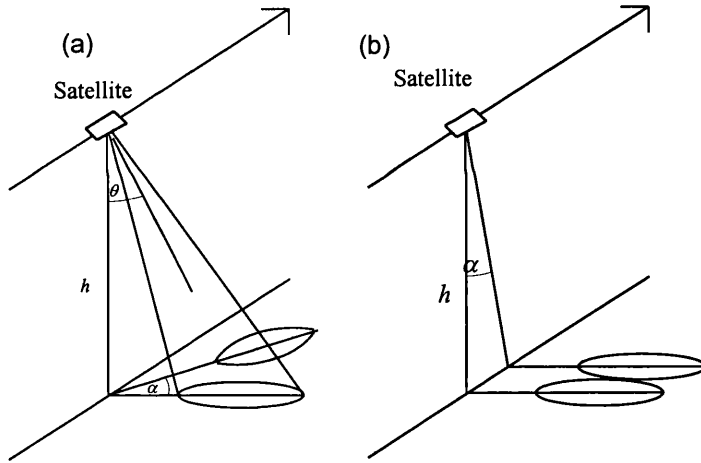


Figure 3.13. (a) Satellite yaw displacement, and (b) pitch displacement (Source:[11])

If the yaw and pitch angles of the satellite are known, the correction is straightforward, if not the clutter lock system may be used for the correction. The clutter lock system measures the shift and adds or subtracts it from the original shift [11].

The roll error results from the movement or rotation of the satellite around its horizontal axis. A small roll of the satellite does not affect the location of the imaged swath. If the roll is large, a range-dependant variable gain can be used to compensate the weighting factor added by the antenna pattern on the echo shape [11].

For the target elevation error correction, the radius of the assumed oblate ellipsoid earth model should be adjusted by the elevation of the target (h). An error may occur in the effective slant-range as a result of estimating the target height which leads to error in the target location [7]. This is shown in figure 3.14.

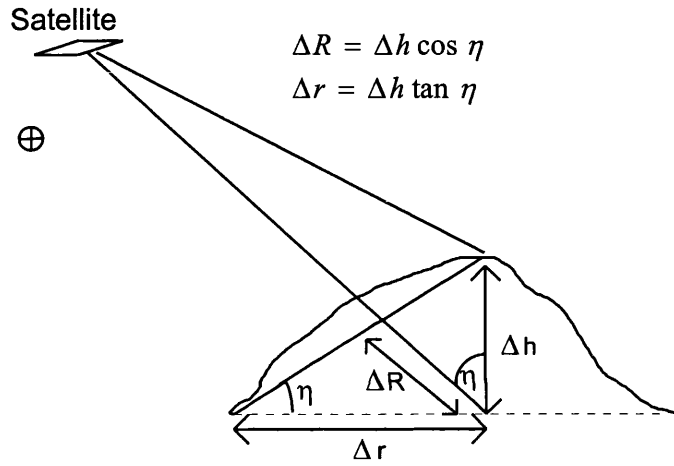


Figure 3.14. Target location error as a result of the target location (Source:[7]).

For example, assuming a grazing angle of 35° , and assuming the target height Δh is 5 metres, the target location error in the range direction is 7.14 metres. This is because SAR is a ranging device and produces a cross-track reflectivity map based on the sensor to target range distance. For smooth surfaces, there is an inherently non-linear relationship $1/\sin \eta$ between the sensor-to-target range and the cross-track target position in the image [7]. Figure 3.15 shows this relationship. Since the angle varies across the swath, the ground distance for each sample is not uniform, which results in the near-range appearing compressed with respect to the far-range. Only for smooth surfaces can the slant-range spacing and ground-range spacing be related by $\sin \eta$.

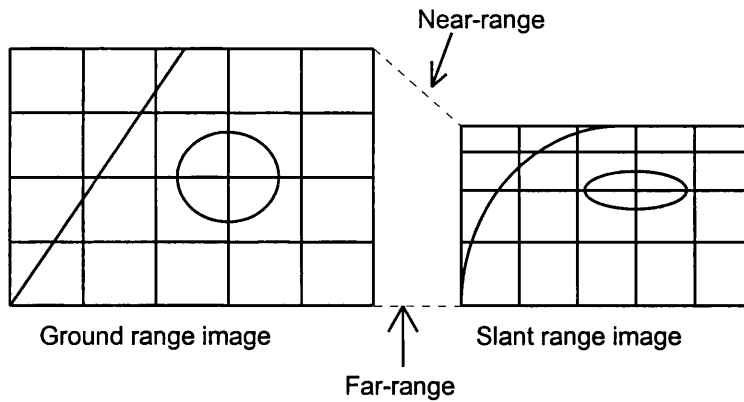


Figure 3.15 comparison between ground range and slant range image (Source:[7]).

Because natural terrain surfaces deviate from smooth surfaces, additional geometric distortions occur. These distortions are foreshortening, layover, and shadowing (figure 3.16).

Foreshortening distortion occurs when the hill or the mountain is viewed by the radar beam and ($\alpha < \eta$), the side of the hill or the mountain facing the radar beam will be shortened and the other side will be stretched. Layover distortion is similar to that of foreshortening but with $\alpha \geq \eta$ (i.e. steep terrain). Shadowing occurs when the ground area is not visible to the radar.

For such distortions, it is extremely difficult to correct SAR data without using a DEM and incident angle map for each pixel in the DEM. In the rectified image, shadows will be filled by an intensity value equal to that of the thermal noise power [7].

Another source of geometric distortions is specular point migration. This occurs as a result of rounded hilltops where the predominant scatterer location is dependent on the incident angle of the transmitted wave. When the incident angle is perpendicular to the hilltop strong backscatter occurs.

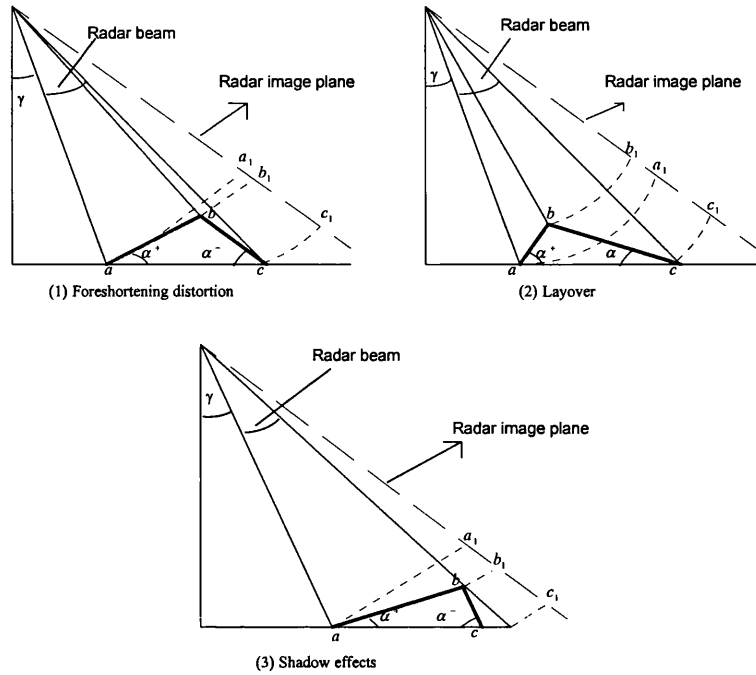


Figure 3.16. Geometric distortion in SAR images (Source: [7]).

3.8 SAR data processing

As mentioned earlier in this chapter, the formation of each pixel involves the combination of data from many thousands of echoes (synthetic array elements) and the platform is orbiting at high speed determining the swath width elements and the sensor resolution. These parameters lead to a high data handling rate [11].

The received data are processed in the ground receiving station by correlating in the SAR processor using a two dimensional reference function as a matched filter. Optical processors or digital processors can be used to perform the image construction derived from the signals. Optical processors were used in the early SAR imaging developments, where each echo is downconverted to baseband and biased in its amplitude to keep it positive then intensity modulated to be displayed on a CRT. The phase variation of the echoes is matched by a Fresnel zone plate and the echoes are then recorded as lines which

form an image on a film. The film is then illuminated by laser beam. Several lenses are used in the optical processing technique for range corrections (e.g. range walk and curvature). The Seasat SAR and SIR-A SAR data were processed in an optical fashion. Limitations of optical processors are related to dynamic range, the radiometric calibrations and the delay involved in the development and handling of film [11].

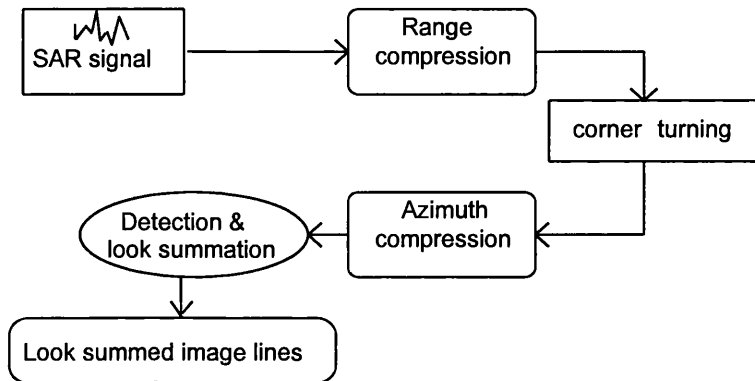


Figure 3.17 SAR image processing data flow diagram.

With the advent of fast digital electronics, a number of SAR processing algorithms have been developed to reduce the data handling by the use of digital processors. The main advantage of such processors is their high speed of processing and the ease of access to the pixel phase of the data [11]. A schematic diagram showing the fundamental SAR processing operations is shown in figure 3.17.

To illustrate the processing of SAR received signals to construct the image, a point target response is used within either the time domain or the frequency domain. The necessary parameters for the compression algorithms, including the pulse replica, Doppler centroid, FM rate and number of looks are determined before the processing for range compression. These are dynamically estimated with the use of other data such as platform attitude and orbit for azimuth compression. Algorithms for SAR processing are much more complicated than this short description, and can be found in many SAR text books. A good article describing SAR processing techniques is by Barber, 1985 [15]. The following describes two methods of processing, the time domain and the frequency domain processing.

In the time domain processing, the matching process uses convolution in the time domain and the range compression is performed through the use of SAW (surface acoustic wave). The range migration correction can be partially performed using interpolation by convolving adjacent samples with a suitable spreading function. An alternative technique for range migration correction is through the modification of the addressing strategy of the range samples from the corner turning memory array [11].

To reduce the computation needed to process SAR image, the frequency domain approach can be used where each received echo signal is Fast Fourier Transformed (FFT) and multiplied by the range reference function for the range compression process. The output is then inversely Fast Fourier Transformed (FFT)⁻¹. The output range compressed signal is then input to a corner turn memory in one row in the SAR processor. Successive echoes will follow the same procedure until the number of memory rows is equal to the length of the synthetic array. The data is then read one column at a time and an azimuth correlator is applied using FFT and multiplication by the reference function. (FFT)⁻¹ is then applied on the output and input to the multilook memory. Figure 3.18 shows the SAR processing scheme using the frequency domain procedure [11].

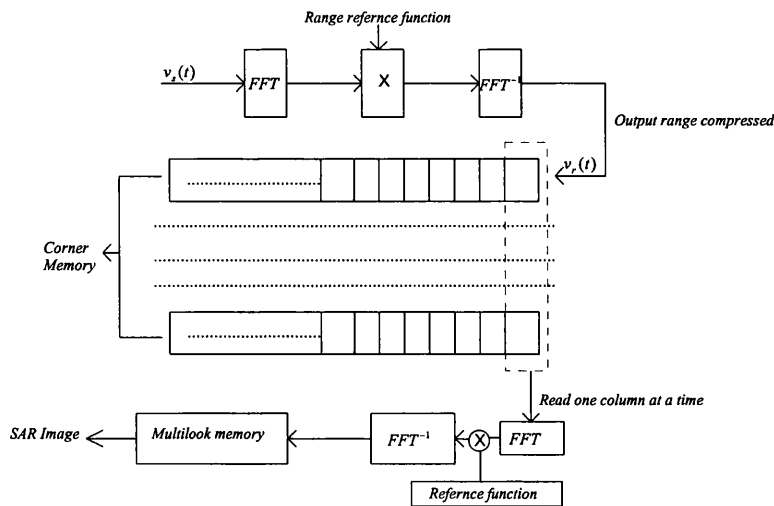


Figure 3.18. SAR processing using FFT correlator.

4.0 Pre-processing optical TM and JERS-1 SAR data

Image analysis is the fundamental aim of satellite digital data, performed using computer aided decision making algorithms for classification purposes or manual photo-interpretation. Such analysis cannot be achieved without making certain geometric and radiometric corrections. In general, image data is downloaded to the ground receiving stations directly from satellites, with many artifacts due to the sensor itself. These include: system noise, line dropouts and stripping, platform yaw, pitch and roll, orbit ellipticity, system field of view and viewing angle geometry. Natural artifacts arise from Earth rotation and atmospheric effects. These limitations in the recorded data are usually corrected in the receiving ground stations throughout a clean up set of procedures in the primary stage of correction, and produce what is called raw data. If desired, a higher level of correction can be achieved if the relevant parameters are available, these parameters include: the system; the atmosphere; and the imaged area.

In this work, the optical data is provided from the Saudi Centre of Remote Sensing (SCRS) of King Abdulaziz City of Science and Technology (KACST) in Saudi Arabia. The radar data is provided by the National Space Development of Japan (NASDA). SCRS provided a 6500bpi 2-CCT's radiometrically and geometrically (level-5) corrected Landsat-5 Thematic Mapper (TM) data acquired at 7.35 a.m. (GMT) on the 8th of June 1992 of the satellite descending node of orbit number 43988. The Sun elevation angle was 62.15° and the Sun azimuth was 95.22° during the image acquisition. The test site is covered by quad-2 and quad-4 of the image scene of the Landsat-5 of path number 174 and row number 40 of the Landsat-5 satellite's world reference system (WRS). The JERS-1 SAR data has been provided by NASDA in 4- 6500bpi CCT's which cover the study area through the JERS-1 paths of 252 and 253 and rows of 252 and 253 for both paths (4-full scenes). Data was acquired in descending node of the satellite and processed in October 1992. The exact acquisition date and time was not shown in the header files in the CCT's and could not be obtained. Radiometric and geometric pre-processing correction of the SAR raw data has been performed previously by NASDA/ERSDAC of Japan. The pre-processing level of the SAR data is 2.1.

Further pre-processing for both SAR and TM data has been performed in this thesis work to achieve compatibility between the two data sets. These pre-processing procedures are divided into two stages. The first stage includes: the SAR 16-bit to 8-bit compression, SAR to TM image registration, and SAR mosaicking, all of which have been performed in an early stage of this thesis work in the SCRS using the hardware and software facilities available. Meridian image processing software has been used to perform the first stage. After that, one selected test site of size 1024 pixels \times 1024 lines from the area of study was transferred from the SCRS SVAX mainframe and backed up to 3.5" floppy disks, occupying more than 7.34 Mbyte for both of the JERS-1 and TM data. The second stage of the pre-processing is the optical TM atmospheric correction and the JERS-1 SAR despeckling, all of which have been performed in the Electronic & Electrical Engineering Department at UCL using PV-Wave and MATLAB software on SUN workstations. Intensive C programming work, and EASI/PACE image processing software were also used for data fusion and image analysis at a later stage of the thesis.

4.1 The JERS-1 SAR 16-bit to 8-bit compression

JERS-1 SAR images recorded from NASDA in CCT's are 16-bit (2 bytes for each recorded pixel); this data is not compatible with the optical Landsat-5 TM data which is 8-bit (256 levels) in its dynamic range. For this reason, 16-bit to 8-bit conversion is needed for the SAR data to make it statistically compatible with the TM during the processing and/or analysis in a later stages of the work.

There are many methods which can be used for conversions. One method takes the square root of every pixel value in the 16 bit SAR image and stores the results in an 8 bit file after rounding off. The drawback of this method is the bad grey level distribution of the resultant output image (i.e. low image variance) [16], but it gives suppressed speckle noise [17]. Another method is using a simple linear operation for the conversion based on dividing every single pixel in the 16 bit SAR image by 256 and rounding the result to an integer. The most appropriate method is finding the maximum and the minimum of the input 16 bit SAR image and assigning them to 255 and 0 respectively. A simple division

factor can be used to set up the values that lie between the maximum and minimum values, rounding off the results to achieve integer numbers in the output image. The final method has been utilised in this work because it showed better appearance in the image display and better distribution in the output image histograms.

4.2 Mosaicking and image to image registration

The second stage of the SAR pre-processing is mosaicking. Mosaicking refers to assembling the four SAR images as shown in figure 4.1 to form a continuous pictorial representation for the whole area of study, so as to extract the test site. This process was performed before image to image registration simply because instead of registering every single JERS-1 SAR image to a portion of Landsat-5 TM image, it is easier to register the four mosaicked images of the SAR to the whole TM image that covers the area. Unfortunately the mosaicking process has failed, because the edges of images of path 252 are at the far range of the JERS-1 satellite, while the edges of the images of path 253 are at the near range of the satellite.

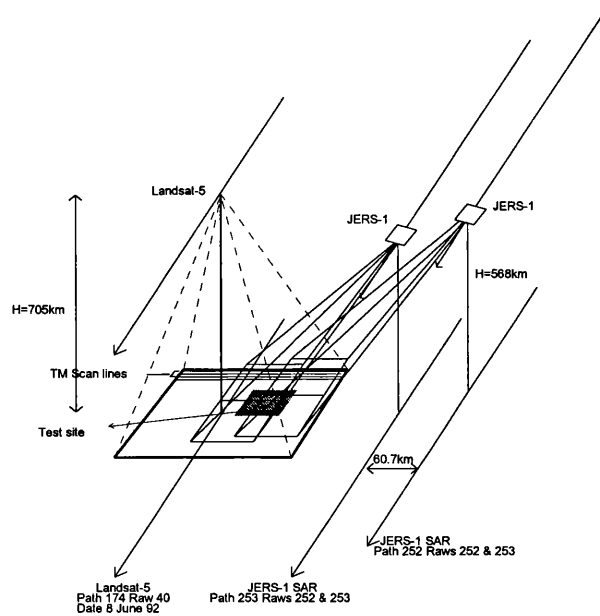


Figure 4.1 Schematic presentation of the JERS-1 SAR and Landsat-5 TM optical data of the study area.

This failure of the mosaicking process occurred due to the differences in the illumination angles of the scene borders along the range. This problem cannot be solved without using a digital elevation model (DEM) to rectify the distortion and remove the topographic effects. Unfortunately a DEM was not available for the test site, so for this reason a decision has been taken to register every single SAR image to its adjacent portion of the TM with the use of intensive control points. This was especially important in the mountainous areas and along the mosaicking borders where the illumination angle varies from near range and far range. Figure 4.2 shows how the illumination angles varies from near range to far range in the JERS-1 SAR case.

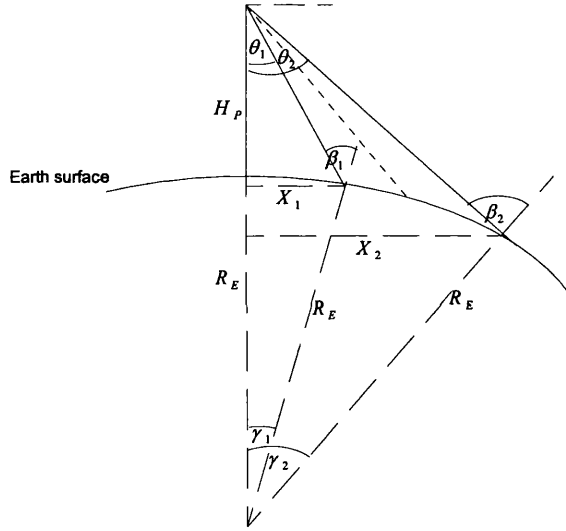


Figure 4.2. JERS-1 SAR range illumination angles variations .

From figure 4.2, the near range incident angle β_1 and far range incident angle β_2 are calculated as follows, noting that $H_p = 568\text{km}$, $\theta_1 = 32.2^\circ$, $\theta_2 = 37.8^\circ$, $R_E = 6380\text{km}$.

From figure 4.2:

$$\frac{R_E}{\sin \theta_1} = \frac{H_p + R_E}{\sin \beta_1} \Rightarrow \beta_1 = 35.47^\circ \quad (4.1)$$

$$\frac{R_E}{\sin \theta_2} = \frac{H_p + R_E}{\sin \beta_2} \Rightarrow \beta_2 = 41.87^\circ \quad (4.2)$$

The SAR images were registered with the reference image of Landsat TM, where the SAR spatial resolution is reduced to 28.5 metres, and hence the variation between the far range and near range angles was also reduced.

In the literature there are two types of geometric correction technique: geometric rectification and geometric registration. Geometric rectification is a process of producing an image in its planimetric form. This process involves the uses of accurate map co-ordinates and digital elevation models to correct image distortions in three dimensions. Geometric registration is the translation and rotation alignment process by which two image sets of like geometries whose objects in the two images are positioned coincident with each other [18,19].

Two steps have to be performed throughout the registration or rectification technique. One is spatial interpolation, and the second is intensity interpolation. Throughout the spatial interpolation, the pixel location (measured as row and column in the image) has its location co-ordinates in the reference image (e.g. TM) based on a relation which should be identified (e.g. equations 4.3 and 4.4). This process is called spatial interpolation and produces an empty mesh (new output image grid) of output that is identical in its co-ordinates to the reference image. This procedure involves defining control points in the reference image and finding the co-ordinates of these points in the image to be registered (e.g. SAR). Affine parameters of the relation (e.g. equations 4.3 and 4.4) have also to be calculated to translate the image either to x-y direction, image scale change, skew correction, and rotation [20]. These parameters are based on the “warping equations” which could be first order with three affine coefficients, second order with six affine coefficients, or third order equations with ten affine coefficients. The second order equations have been used in this work, as suggested by Cheng *et. al.* [21] after investigation of many types of rectification algorithms using images from many satellite platforms including SAR and optical data. Cheng showed that the second order of polynomial equation for co-registration gives less RMS error. The equations of the spatial interpolation are as follows:

$$\text{In } x \text{ space } F(x, y) = a_1 + a_2x + a_3y + a_4x^2 + a_5y^2 + a_6xy \quad (4.3)$$

$$\text{In } y \text{ space } G(x, y) = b_1 + b_2x + b_3y + b_4x^2 + b_5y^2 + b_6xy \quad (4.4)$$

where:

$F(x, y)$, $G(x, y)$ = the position of the control points co-ordinates in the non-registered image (SAR).

x, y = the new position co-ordinates of the control point in the output image and equal to the reference image (TM).

The affine coefficients ($a_1, b_1, a_2, b_2, a_3, \dots$) can be calculated using least square regression of the ground control points. The geometric distortion of the ground control points (the shift between $F(x, y)$, $G(x, y)$ and x, y) is measured by its RMS error. Geometric correction and registration techniques are explained in detail in most image processing books. Registration for multisensor image data has also been reviewed in detail by Leila *et. al.* [22] and Stanton *et. al.* [23].

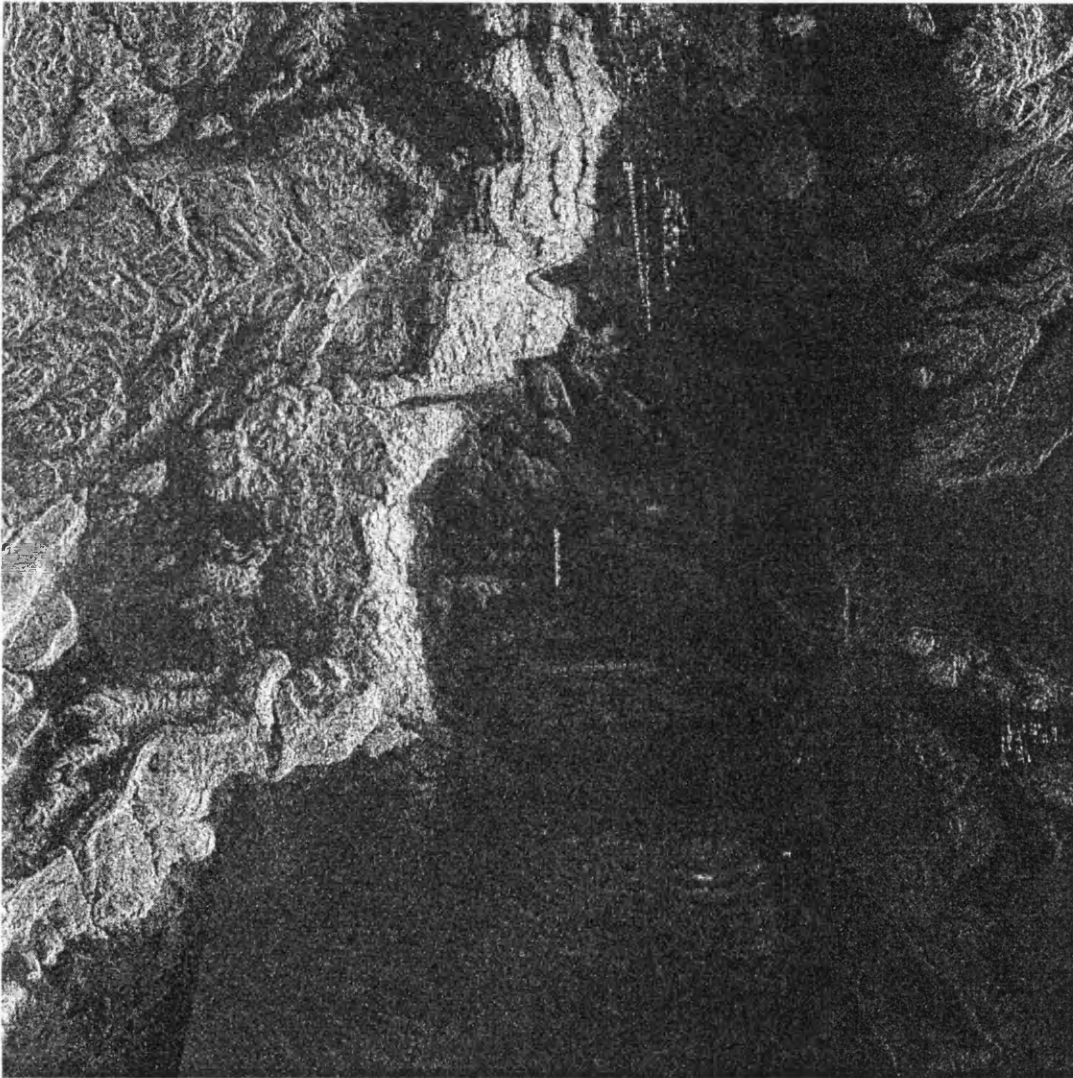
The affine coefficients measured in this work during the geometric co-registration process using the second order equation (equations 4.3 and 4.4) were extracted using MERIDIAN image processing software as follows:

$a_1=201.43$	$b_1=-50.21$
$a_2=2.688$	$b_2=0.186$
$a_3=-0.0126$	$b_3=2.28$
$a_4=-0.000236$	$b_4=-0.0000231$
$a_5=-0.0000229$	$b_5=-0.0000028$
$a_6=-0.0001$	$b_6=-0.0000078$

Once the output image grid is created by the above process, it has to be filled by the intensity interpolation as the second step of registration technique. The intensity interpolation is usually called resampling. It refers to reading the pixel intensity values in the unregistered input image and locating their proper position on the output image grid. There are many methods that can be used for intensity interpolation, including: nearest neighbour interpolation, bilinear interpolation, and cubic interpolation. Geologists prefer the nearest neighbour interpolation filling because it does not alter the original pixel brightness values. This method has been applied in this thesis work.

The registration process was successfully applied with total of 280 ground control points (GCPs) for the four whole scenes of JERS-1 SAR (70 GCP for each SAR scene). Spatial resolution has been reduced from the original 18 metres to 28.5 metres as a result of registration matching to the Landsat optical TM.

SAR images in paths 252 and 253 have a different range of brightness level values. The images of path 253 have less contrast compared with the images of path 252. This must be corrected before mosaicking can take place. To solve this problem, histograms of the side-lap area (around 17% side-lap) between the two paths have been compared and a Look-Up-Table (LUT) for each histogram has been produced. The two LUT's have been averaged to produce a common LUT. The common LUT is then applied to all images of paths 252 and 253. This is a popular solution for solving contrast differences in the mosaicked images. The results of the registered, mosaicked, and contrast averaged JERS-1 SAR scenes were satisfactory. The mosaicking procedure was successful except that small contrast differences could be noticed only in the lower left part between images 253/253 and 252/253 of the test site as shown in figure 4.3 a. The reference image of Landsat-5 optical TM data is also shown in figure 4.3 b.



*Figure 4.3 a: The JERS-1 registered, mosaicked and contrast averaged 4 SAR scenes of the study area.
"MITI/NASDA retain ownership of data".*

Scale 1:204084



Figure 4.3 b: The reference Landsat 5 optical TM band 5 image. Band 5 has been selected because of its high contrast where control points can be selected easily.

Scale 1:204084

4.3 Atmospheric correction of the optical TM data

The atmosphere influences the amount of reflected or emitted electromagnetic energy that is sensed by optical imaging systems, and modifies and scatters the signals being used and makes the acquired images blurred and poorly contrasted. Absorption of the signals by the atmosphere is usually not counted in the atmospheric correction procedures because remote sensing imaging systems are designed to operate away from the absorption windows of the atmosphere [24].

It has been found that the atmosphere has an effect on the measured reflected waveband from the target (i.e. pixel brightness value) where the Sun is the source of the electromagnetic energy. If the atmosphere is absent, the measured reflected waveband is only a function of the energy from the Sun reflected from the target and the reflectance properties of the target itself. Because the atmosphere is present, the reflectance is modified.

The Sun radiates electromagnetic wave energy termed the spectral irradiance ($E_{\Delta\lambda}$), which describes how much power density is available incrementally across the wavelength range. At the Earth's surface, if this surface is diffuse (i.e. scattered uniformly in all direction), the measured energy reflected from the surface is called the radiance (L). The target which reflects this energy has reflectance properties (R) which describe the proportion of the incident energy which is reflected. With the assumption of no atmospheric effects and the target being diffuse, the measured radiance scattered is:

$$L = E_{\Delta\lambda} \cos\theta \Delta\lambda R / \pi \quad (4.5)$$

where θ = the solar zenith angle measured from normal.

Because the atmosphere is present, the following parameters should be taken into account and calculated to obtain the atmospheric correction. These parameters are :

- a) Atmospheric transmittance along two pathways; one is from the Sun to the target or pixel (T_θ), and the other is from the target to the imaging system (T_ϕ). Both are measured from the normal.
- b) Sky irradiance, which is diffuse reflection caused by the atmospheric constituents and also from the surrounding targets or pixels (E_D).
- c) Path radiance, which is scattering due to the atmosphere direct to the imaging system, or the surrounding targets direct to the imaging system (L_p), or both.
- d) Various effects due to: temperature, relative humidity, atmospheric pressure, and visibility, all of which should be measured during the time of image acquisition, to extract what is so called the total normal optical thickness of the atmosphere (τ) knowing that $T_\theta = e^{-\tau \sec \theta}$ and $T_\phi = e^{-\tau \sec \phi}$.

From the above parameters, the final atmospheric correction equation becomes:

$$L = \frac{RT_\phi}{\pi} [E_{\Delta\lambda} T_\theta \cos \theta \Delta\lambda + E_D] + L_p \quad (4.6)$$

This equation should be used in combination with the equation of radiance-digital value conversion for the atmospheric correction process. The radiance-digital value conversion is used aboard the satellite in the digitising process to convert radiance to digital pixel values and to extract the reflectance of the target (R). The equation of radiance to digital value conversion is:

$$L = Ck + L_{\min} \quad (4.7)$$

where :

C = Digital brightness value of the pixel.

$$k = \frac{L_{\max} - L_{\min}}{C_{\max}}.$$

L_{\max} and L_{\min} are the maximum and minimum measurable radiances of the sensor, and are usually given by the manufacturer during the ground spectral response tests for each band. C_{\max} is the maximum digital value in the digitiser.

Application of the above procedure is sometimes difficult for atmospheric correction, because the atmospheric parameters cannot be always gathered at the time of image acquisition. For that reason, atmospheric correction has become an important subject in optical remote sensing, and many alternative techniques have been suggested. Crippen [25] described the atmospheric correction methods in the literature and classified them into four methods. These are (1) atmospheric measurements and modelling combined with knowledge of the sensor calibration, (2) radiance - to - reflectance conversion, (3) the regression method, and (4) the dark - pixel subtraction method. Another method used is the image histograms zero shift which is known as the simplest way of haze removal approximation, its drawback is inaccuracy and image data may be overcorrected and the band-to-band spectral relationship may be lost because of no specific atmospheric model is selected.

Throughout this work, it has been found that the dark - pixel method shows a very good approximation for atmospheric correction. The method is simple and straightforward and does not need the use of ground measurements during the time of image acquisition, which makes this method the most practical.

The dark - pixel subtraction method developed by Chavez [26] was used. Modifications of the method were made in this thesis including: selecting the appropriate atmospheric model and; using the exact spectral response of the TM imaging system. The TM spectral response was demonstrated by Markham and Barker [27] during the ground measurement and calibration process of the TM system.

The method developed by Chavez is based on the assumption that images being sensed should have black pixels as a result of shadows, and these shadows should have zero values in their pixel brightness values in the visible spectral band images. However, the atmospheric scattering adds a constant value (radiance) to these pixels, and this radiance should be appropriately measured and subtracted.

Scattering of the electromagnetic energy in the atmosphere is an additive component and is wavelength dependent. It is mainly due to molecules of O_2 , CO_2 , O_3 and H_2O , and is called Rayleigh scattering. This type of scattering is inversely proportional to the fourth power of the wavelength $S \approx \lambda^{-4}$, which means that the shorter wavelengths (i.e. visible light) scatter much more than the longer wavelengths (i.e. infrared light). It occurs in a very clear atmosphere and is the cause of the blue appearance of the sky. Particles in the atmosphere ranging from 0.01 to 0.1 wavelengths in size, such as smoke, haze, and fumes particles also cause scattering, and this type of scattering is called aerosol or Mie scattering. Mie scattering is inversely proportional to the wavelength $S \approx \lambda^{-1}$ but this scattering is not as strong as Rayleigh but is still wavelength dependent. When the particles are larger than the wavelength, scattering is no longer wavelength dependent and complete scattering occurs in all bands [24,26].

From the scattering types where the relation varies between the power of -4 and -1, Chavez [26] determined new scattering models using the power law. These models are shown as follows: very clear atmosphere = λ^{-4} ; clear atmosphere = λ^{-2} ; moderate atmosphere = λ^{-1} ; hazy atmosphere = $\lambda^{-0.7}$; and very hazy atmosphere = $\lambda^{-0.5}$. Chavez also suggested that the selection of the atmospheric model of an imaged area for atmospheric correction is based upon the magnitude of the brightness values of the shadows in one of the visible bands. This can be taken from the image histogram, such as band 1 of TM (as used in this thesis), and this value is named the starting haze value, and assumes that it reflects the atmospheric condition at the time of data acquisition.

For different types of atmospheric models, Chavez produced tables of calculations to be used for scattering corrections to the optical data for TM and MSS images. Values including gain and offset of every band from the TM system used by Chavez are calculated from the pre-launch test by Markham and Barker [27].

Following the approach by Chavez, and developing a new method for selecting the exact atmospheric model based on the dependency of scattering on wavelength, the magnitude of starting haze value of the data used in this study found in the TM of band 1 is 63 based on using the numerical histogram of the whole TM band 1 image. This contributes around 43% of all TM data of the test site. A model of λ^{-3} has been chosen because band 1 in a model of λ^{-3} contributes 44.51%, as shown graphically in figure 4.4. Table 4.1 shows the actual calculation of the TM data used in the study with a model of λ^{-3} . It is important to mention that there are some differences in table 4.1 from the results from the Chavez calculations. This is because a nearly precise model is calculated, and also the precise spectral response of TM bands of Landsat-5 measured by Markham and Barker [27] is used. Chavez [26] did not follow the precise bands spectral responses and did not suggested how to accurately select haze models, but limits them to 5 models.

B	λ_b	λ^3	$P_R(\%)$	M_b	G_b	O_b	N_b	C_b	P_b	R_b
1	0.485	8.765	44.51	1.000	15.78	2.58	1.00	63	60	63
2	0.568	5.457	27.71	0.622	8.1	2.44	0.51	27	38	22
3	0.660	3.478	17.66	0.396	10.63	1.58	0.67	26	24	18
4	0.840	1.687	8.57	0.192	10.9	1.91	0.69	16	12	10
5	1.675	0.213	1.08	0.024	77.24	3.02	4.49	10	1	8
7	2.223	0.091	0.46	0.010	147.12	2.41	9.32	5	1	12

Table 4.1 Calculations of atmospheric scattering of the test site.

The following describes table 4.1 and the method of calculation, following exactly the same procedure as suggested by Chavez [26]:-

B = band number of Landsat-5-TM.

λ_B = centre of spectral response of Landsat-5 TM band B .

λ^{-3} = selected atmospheric model.

P_B % = theoretical magnitude of scattering of band B in percent = $\frac{\lambda_B^{-3}}{\sum \lambda_B^{-3}} \times 100$.

M_B = multiplication factor = $\frac{(\lambda_B)^{-3}}{(\lambda_1)^{-3}}$.

G_B = TM sensor gain of band B .

O_B = TM sensor offset of band B .

N_B = normalisation factor = $\frac{G_B}{G_1}$.

C_B = calculated haze value from the image histogram.

P_B = predicted magnitude of scattering after applying equation 4.9.

C_B = real magnitude of scattering after applying equation 4.10.

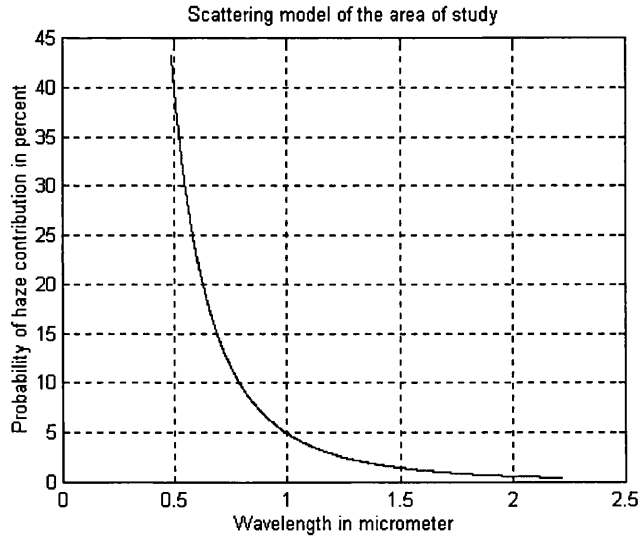


Figure 4.4. Theoretical scattering of the model λ^{-3} which precisely matches scattering of the area of study. Note that the scattering in band 1 is 44.5% and decreases exponentially to approach zero in the infra-red wavelengths. The axis y is percentage probability.

Many factors contribute to the digital brightness value recorded by the optical imaging system, including system gain and offset, sun elevation angle during image acquisition, and slope conditions of image. The output digital brightness equation of the image is [26]:

$$BV_{i,j,B} = G_B \times R_{i,j,B} + O_B \quad (4.8)$$

where:

$BV_{i,j,B}$ = output brightness value of a target (pixel) of band B at i,j position.

$R_{i,j,B}$ = input target (pixel) radiance of band B at i,j position.

Predicted haze values for other bands after taking the haze of band 1 as a starting haze value are calculated based on the equation:

$$P_B = (C_1 - O_B) \times M_B \quad (4.9)$$

where:

P_B = predicted haze value of band B .

C_1 = starting haze value of band 1.

Finally, the correct haze value to be subtracted from every band can be calculated by the following equation:

$$R_B = (N_B \times P_B) + O_B \quad (4.10)$$

where:

R_B = final correct haze value of band B .

When the final haze values are calculated from equation 4.10 for every band, all of these values must be subtracted from their corresponding bands of the image scene to account

for the scattering. All of these values of final scattering calculation (shown in table 4.1) were subtracted from the imagery bands of the test site.

Geologic applications require atmospheric correction especially, because haze generally affects the image processing techniques. These include colour displaying, linear combination such as data rationing, subtraction, multitemporal fusion techniques, spectral signature extension, and spectral relationships between bands [26, 28].

4.4 SAR speckle reduction

In the JERS-1 SAR image used in this study, further pre-processing correction is needed to eliminate the speckle in the image. This kind of noise greatly reduces the image quality and makes photo or machine interpretability less effective.

Ford [29] studied SAR images intended for geological mapping and found that there are three factors controlling the interpretability: the spatial resolution; the image speckle; and the range of contrast. The spatial resolution and the range of contrast of the JERS-1 SAR data used in this study is adequate, but speckle is extensively present in the data. This speckle should be removed because it obscures the real reflectivity differences of the geological features.

Speckle is a random effect present in all active coherent imaging systems such as radar, and is fundamentally a result of the fluctuation in the target echoes. Noise is also present in radar images and due to receiver system such as thermal noise; small surface scatterers which are less than the pixel resolution; the antenna viewing position; man made constructions; the atmosphere; and the specular reflection of ground surfaces where the reflected signals return perpendicularly to the antenna as strong echoes. Speckle and noise make contributions to the degradation of the radar images [10] and characterise radar images with a granular appearance which highly reduce SAR image interpretability.

Ulaby *et. al.* [30] and Elachi [11] described how speckle occurs as a result of adding many echo returns from the scatterers. The returns are added vectorially from the elementary vectors of each return of the single scatterer to form a single vector which has amplitude V and phase ϕ of the total echo. The phase ϕ_i of each elementary single vector is related to the distance between the SAR antenna and the scattering points. When the satellite moves, all phases ϕ_i will change, leading to a change in the composite amplitude V . As a result of many observations of the same target recorded during the satellite movement, fluctuations in the amplitude V of the target scatterers leads to speckle or fading. To overcome this problem, the amplitudes V 's may be spatially averaged.

Mathematically, the received amplitude V from two scatterers A and B separated by a distance d observed by a constantly moving platform over period t and velocity v can change dramatically, causing the speckle or fading. If the viewing angle θ is small, the received amplitude is:

$$|V| = 2 \left| V_0 \cos \left(\frac{2\pi d v t}{\lambda} \sin \theta \right) \right| \quad (4.11)$$

Graphically, equation (4.11) shows how speckle can be created as a result of amplitude fluctuation. This is shown in figure 4.5. From the figure:

$$r_1 = r_o + \frac{1}{2} d \sin \theta \quad (4.12)$$

$$r_2 = r_o - \frac{1}{2} d \sin \theta \quad (4.13)$$

As derived by Ulaby *et. al.* [30], the first null away from the origin occurs when:

$$\frac{2\pi d}{\lambda} \sin \theta_1 = \frac{\pi}{2}$$

$$\sin \theta_1 = \frac{\lambda}{4d} \Rightarrow \theta_1 \approx \frac{\lambda}{4d}$$

$$\text{and similarly } \theta_2 \approx \frac{3\lambda}{4d}.$$

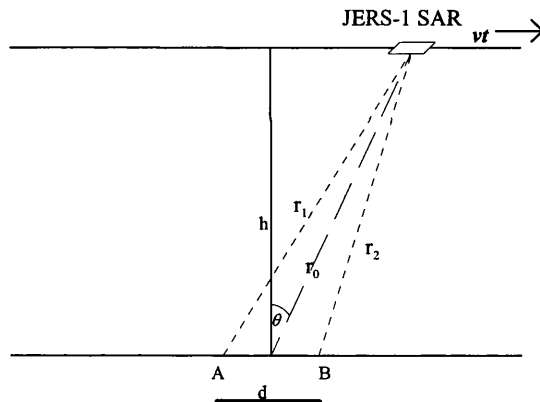
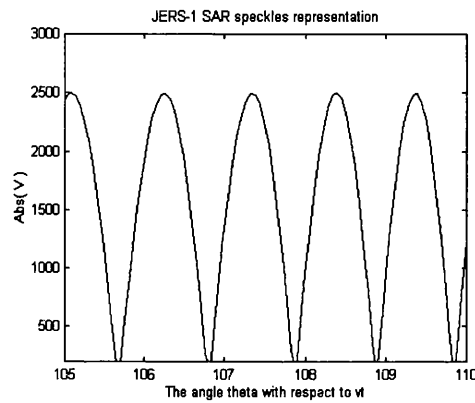


Figure 4.5 Speckle formation of a distributed targets A and B separated by distance d . The SAR returns amplitude fluctuate with width equal to $\lambda h / dv$.

The width of the lobe, which is the spacing between the two nulls $(\theta_2 - \theta_1)$, is equal to

$\frac{\lambda}{2d}$. The spacing between the two nulls along the flight path Δx is:

$$\Delta x = r_o \Delta \theta = \frac{r_o \lambda}{2d}. \quad (4.14)$$

From equation (4.14), the spacing is proportional to the wavelength used for the imaging system and the distance r_o , and also inversely proportional to the spacing between the scatterers d .

There are two stages of treatment for speckle reduction. One is called pre-image speckle reduction, or incoherent averaging of multiple looks or frames during the SAR image construction. The second is called the post-image speckle reduction, and involves the techniques of using spatial filtering to smooth images which have been formed through multi-look processing [30,31].

Multi-look processing can be accomplished by partitioning the samples of the coherent imaging period or signal history into M frames to form images, where the number of samples for each frame is $1/M$ of the original single-look image. The azimuth resolution is then reduced by a factor of M . For example, if M is 4, the result is a 4-look image and the SNR is increased by a factor $M^{1/2}$ [10]. In other words, it is the process of squaring the pixels of the azimuth direction or averaging the pixels in the range line, as the resolution in the range direction is much coarser than the azimuth direction in the original single-look image. So the resulting pixels cover a square area on the ground, but with less spatial resolution. If they are averaged, images with less speckle can be achieved. Such a method is especially effective when the image or area of interest is homogenous [31].

Early attempts to eliminate or at least suppress speckle used is the spatial filtering as a second stage or post-image speckle reduction. Such filters were originally non-speckle specific [32] and have been used for noise reduction in general, being very well known in the image processing literature. These include mean, median, and low pass filters. Their disadvantage is in altering high frequency image features such as texture and edges, which occurs because they are not designed for radar images. Such filters used by Blom *et. al.* [33] and Mueller *et. al.* [34]. The median filter works well if two iterations are used, but it makes the image blocky in appearance. The mean filter can also be used, but it blur the images and smooth the edges, which is not advisable for Earth science applications.

Recently, advanced types of spatial filters designed specifically for removing SAR speckle and (to some extent) retain edges, boundaries, and preserve textures became available as a result of increased work on radar images. Among the most well known filters are the: Lee filter [17,35-36]; Frost filter [37]; and Kuan filter [38]. Lately Lopez *et. al.* [39] revised and modified these filters to speed up the processing time and preserve the echoes of strong scatterers, by assuming that the SAR image can be categorised into: flat homogenous areas, for which low pass filter is used (e.g. the mean grey level of the filter window); the second category is heterogeneous areas in which the speckle should be filtered by the original filter algorithm; and the third category is areas of isolated point targets (e.g. strong backscatterers), and in this case the filter should preserve the observed (original) grey values.

4.5 SAR Speckle filters

The SAR spatial filters were proposed specifically to achieve high quality images based on removing speckle and retaining subtle texture and boundary features. They commonly utilise convolving odd square boxes and use the local statistics (e.g. local mean and variance). The Rayleigh fading statistic (called contrast) is used in the filter algorithms by assuming it is $1/N$ where N is the number of looks in the SAR image. If the SAR number of looks is not known, it can be calculated as σ / μ where σ and μ are the standard deviation and mean of the SAR image respectively [16]. This value can be calculated precisely if a small flat homogenous window in the image is used. The following is a brief description of these filters.

A) Lee filter

The Lee filter was the first convolving spatial filter designed for speckle; it is a square odd moving window. Lee [17, 35-36] proposed this filter designed for additive,

multiplicative, and both additive and multiplicative noise¹ in images. In the case of SAR imagery the noise is a multiplicative component as for all types of coherent monochromatic illumination systems [17, 40]. The rougher the areas in an image are the noisier they are and the implementation of the Lee filter algorithm is different based on the type of noise. As mentioned earlier, the Rayleigh fading statistic (contrast) is needed for Lee filter processing. As assumption is that the noise is uniformly distributed and its mean is equal to unity (i.e.1) for multiplicative noise and zero for additive noise.

In the case of multiplicative noise, where the degraded returned signal results from a non-linear combination of noise and signal, the processed central pixel in the Lee filtered window CP_{out} is based on the equation [41]:

$$CP_{out} = \mu_w + K \times (CP_{in} - \mu \times \mu_w) \quad (4.15)$$

where:

μ_w = mean grey level in the filter window.

μ = mean value of the multiplicative noise = 1 on the assumption that the noise is uniformly distributed.

CP_{in} = central pixel value in the filter window to be processed.

K = gain factor, equal to:

$$K = 1 - \frac{\sigma^2 / \mu^2}{\sigma_w^2 / \mu_w^2}$$

σ_w^2 = variance of the filtered window.

σ^2 = multiplicative noise variance = $1/N$.

Lee [42] has improved this filter to remove speckle along edges and boundaries and determine the edge orientation through slight modification of the above algorithm. He

¹ Lee [17] proved that SAR speckle is multiplicative, based on the fact that the local standard deviation is directly proportional to the local mean.

uses the idea of subdividing the filter window into small window subsets of 3 by 3 pixel size so as use their local variance thresholds for processing.

B) Frost filter

Frost *et. al.* [37] designed a spatial filter aimed at SAR speckle elimination. The derived filter algorithm is based upon the scene reflectivity estimated by convolving the observed image with the impulse response of the SAR system. The impulse response of the SAR system is obtain by minimising the mean square error (MSE) between the observed image and the scene reflectivity model, which is assumed to be an autoregressive process [31].

The Frost filter window is an odd but not necessarily square kernel. A damping constant (K) is required for the filter, which controls the damping rate of the impulse response function. The implementation of the filter consists of determining a circularly symmetric filter with a set of weighting values M for each pixel based on the equation [41]:

$$M_i = e^{-A \times T} \quad (4.16)$$

where:

$$A = K \times (\sigma_w^2 / \mu_w^2)$$

T = absolute value of the pixel distance from the central pixel to its neighbours in the filter window.

K = damping factor (e.g. 1).

σ_w^2 = variance of the grey-level in the filter window.

μ_w = mean grey level of the filter window.

The output of a processed central pixel in the moving filter window is CP_{out} :

$$CP_{out} = \frac{\sum_{i=1}^n P_i M_i}{\sum_{i=1}^n M_i} \quad (4.17)$$

where:

P_1, \dots, P_n = the grey level of each pixel in the filter window.

M_1, \dots, M_n = weightings as defined in equation (4.16).

The important characteristics of the filter are: preserving linear features and edge structures; brightening the foreslopes of terrain; and averaging pixels in the homogeneous regions as it works as a low pass filter in these regions. It also performs well on low contrast edges [37].

The damping factor should be carefully selected; if large values are used, edges will be preserved better but at the expense of the speckle smoothing effect. If small values are used, the smoothing effect will be increased but lineation and textural features will be altered or decreased.

C) Kuan Filter

Kuan *et. al.* [38] proposed his filter by transforming the multiplicative noise model into a signal dependent additive noise model. He assumes that the multiplicative noise model is only a rough approximation for fully developed speckle. The minimum mean square error (MMSE) criterion was then applied to the additive noise model. The filter is very similar to the Lee filter but its algorithm uses a different weighting function. The Kuan filter algorithm is:

$$CP_{out} = CP_{in} \times W + \mu_w \times (1 - W) \quad (4.18)$$

where:

$$W = \frac{\sqrt{N} - 1}{\sqrt{N} + 1} \times \frac{\mu_w}{\sigma_w^2}$$

N = number of looks.

μ_w = mean grey level in the filter window.

σ_w^2 = variance of the filter window.

CP_{in} = input central pixel in the moving filter window.

CP_{out} = output central pixel in the moving filter window.

D) Lopes modifications on the speckle filters

Lopes *et. al.* [39] introduced the concept that the SAR scene can be categorised into three classes. The first class is homogenous areas of the scene which are characterised by the coefficient of variation of the filter window: if CV_w is smaller or equal to $1 / \sqrt{N}$ then only a low pass filter (LPF) is applied to such areas (i.e. $CP_{out} = \mu_w$). The second scene class is heterogeneous areas, and in this case either the Lee or Frost filter should be applied to remove speckle. The third class is areas of high signal reflectivity which may represent areas of isolated point targets, and in this case the original observed values should be preserved; such areas should not be filtered when $CV_w \geq \sqrt{1 + \frac{2}{N}}$. [41]. Similarly Shi *et. al.* [31] modified the Kuan filter using the same concept, modifying the original algorithm based on assuming the scene reflectivity to be gamma distributed rather than Gaussian distributed as was suggested by Kuan [38].

4.6 Results and comparison of speckle filters

As a result of the importance of speckle removal issue in this thesis, where the data will be prepared for data fusion at a later stage, after processing for textural enhancement in the next chapter. All the speckle filters just described were carefully tested, and one has been selected based on maximum reduction of speckle together with minimum loss of textural information. Another consideration taken into account for selecting the speckle

filter is that the filtered image should have large variance (better grey level distribution), since the image variance is usually an indicator of information content.

The modified versions of these filters suggested by Lopes *et. al.* [39] and Shi *et. al.* [31] were also tested but excluded because extracting point targets in the SAR image is only important for calibration procedures. Furthermore, these point targets shown in the filtered image make photo-interpretation less effective because they appear as large as up to 7 by 7 pixels of white spots in the image.

The SAR input image has been initially contrast stretched using the Balance Contrast Enhancement Technique (BCET) [43] with controlled mean set to 127. This contrast stretching (see appendix A-2) improves the image appearance and makes it occupy the whole range of grey levels. Contrast stretching using the BCET method gave better results in the speckle filtering. Throughout using each speckle filter algorithm, two images were produced, one being the filtered image and the second the speckle itself. The speckle image is used as an indicator of textural information loss and can be visually evaluated. Any patterns or shapes which are present in the speckle image output indicates a loss of textural information. This method of evaluation has been found effective and is proposed for the first time in this thesis. The algorithm used to produce the speckle image is:

$$I_{speckle} = (I_{input} / I_{filtered}) \times S \quad (4.19)$$

where:

I_{input} = input SAR image before filtering.

$I_{filtered}$ = output SAR image after filtering using SAR speckle filter.

$I_{speckle}$ = output SAR speckle.

S = scaling factor

During evaluation of the Lee filter it was found that the processing time was rapid and speckle was suppressed, but at the expense of textural information loss, especially in large filter windows. The Kuan filter gave similar results to the Lee filter, but takes more time to process and shows darker background in the filtered image. The Frost filter gave the best results, with no textural loss especially when the filter is 3 by 3 in window size. When the filter window becomes bigger, little textural information is found in the speckle output image but with total removal of speckle. The output of the Frost filtered image shows larger variance compared with the Lee and Kuan filtered images. The processing time is the only drawback of this type of filter, but is not critical in this work. The original contrast stretched non filtered image is shown in figure 4.6. The Frost 3 by 3 filtered image is shown in figure 4.7. Figure 4.8 shows the 5 by 5 Frost filtered image; note that the speckle is washed out completely from the image. Finally the speckle image produced by the 3 by 3 Frost filter is shown in figure 4.9. Note that there are no recognised textural or shape patterns in this image.

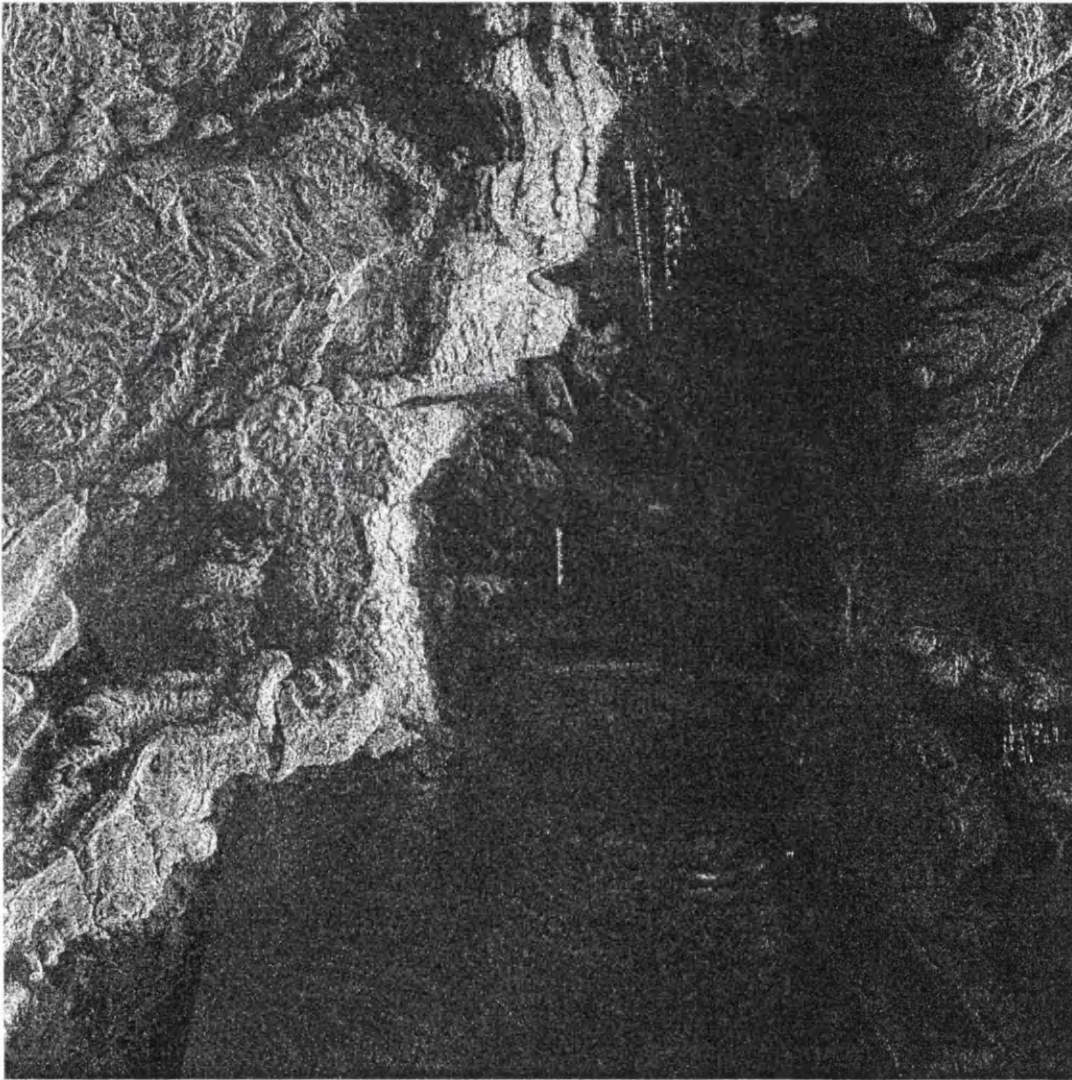


Figure 4.6 Original JERS-1 SAR 3-look image after applying BCET stretching. "MITI/NASDA retain ownership of the data"

Scale 1:204084

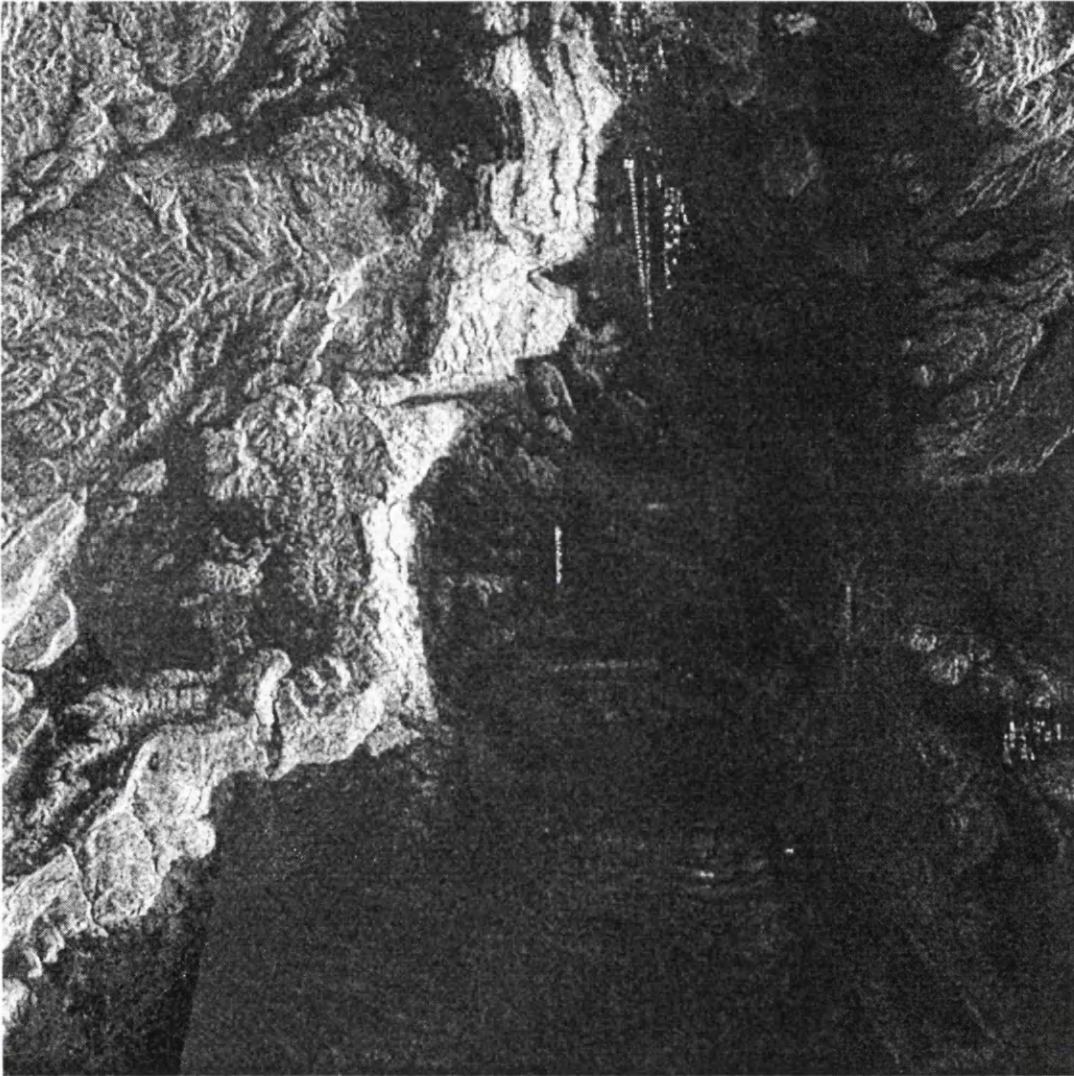


Figure 4.7 Frost 3 by 3 filtered image, note how speckle is removed. “ MITI/NASDA retain ownership of the data”.

Scale 1:204084



Figure 4.8 Frost 5 by 5 filtered image, speckle is removed completely with very little textural information loss. "MITI/NASDA retain ownership of the data".

Scale 1:204084

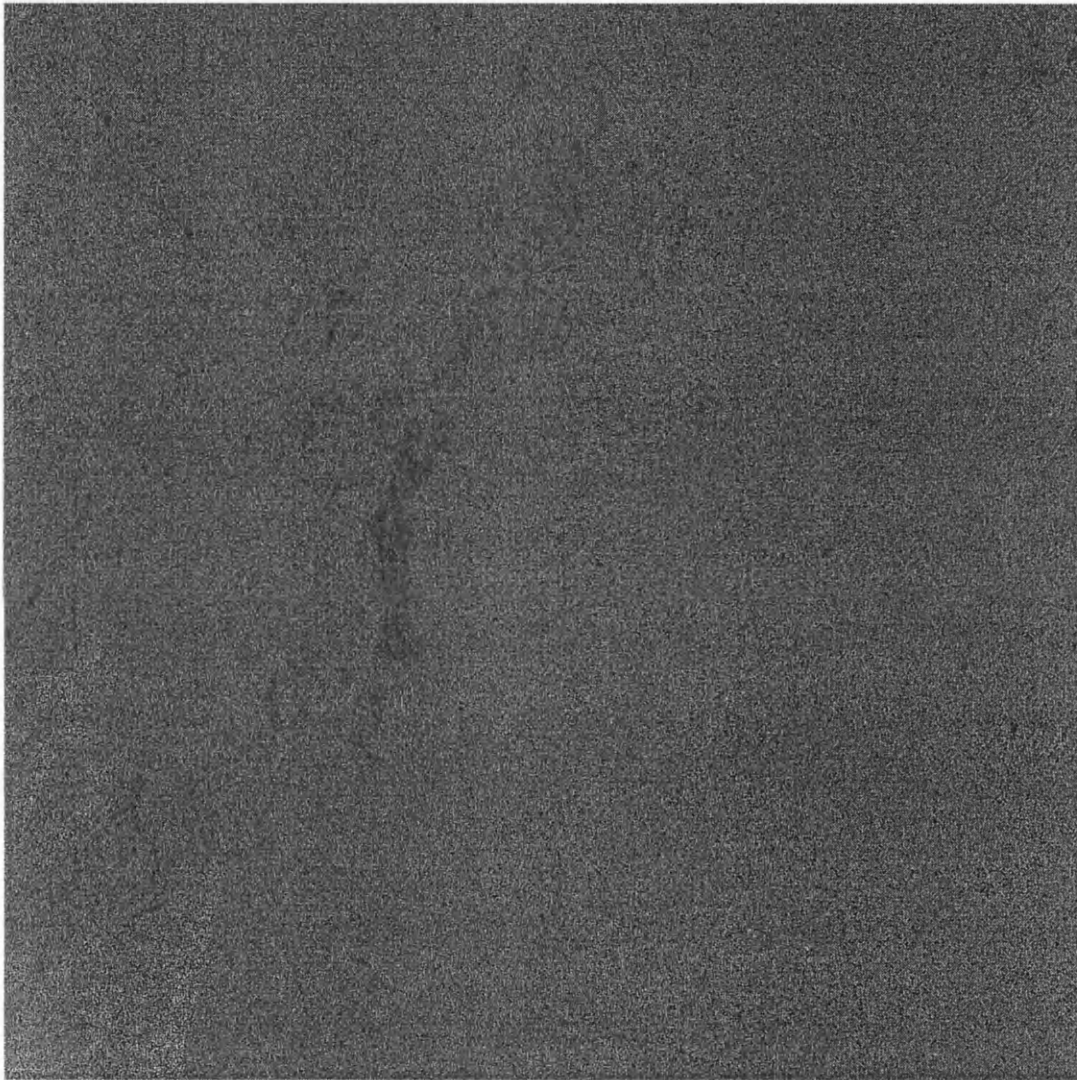


Figure 4.9 The speckle image extracted through the Frost 3 by 3 filtering process, note that there are no recognisable textural or shape patterns indicating no textural information loss.

Scale 1:204084

4.7 Conclusions and remarks

The most important step in preparing image data for fusion from different imaging sources is the image to image registration. It is simple to register two images having similar geometry and source, or two different radar images from different sources with similar imaging geometry. The problem arises when registering optical TM or MSS images with SAR images. The difficulty is for two reasons: one is that the geometrical aspects in acquiring the data from the sensors are different, in that the SAR is side-looking whereas the TM is nadir-looking. The second is that the SAR image pixel brightness depends on the surface roughness and the dielectric constant of the target, whereas the optical TM image pixel brightness depends on the reflectance of the target. For these reasons the data is not correlated, and accurate subpixel registration is difficult to achieve. The only way to produce accurate registration is by using a DEM illuminated by the same sun angle as the Landsat TM image, then the Landsat TM image is cross-correlated with the illuminated DEM to derive the residual translational misregistration [7]. If this process is used, the SAR and TM images can be precisely registered. For data with relatively flat terrains or oceans, or those for which no precision DEM is available, the normal warping transformation equations can be used and precise registration can be achieved.

Speckle in SAR images should be treated carefully because speckle reduces the image interpretability either for manual photo-interpretation or for direct automated mapping (classification). For that reason, speckle image production and visual evaluation is produced in this thesis as a new idea for speckle filter efficiency. It is a simple method and believed to be an important step of evaluation.

Atmospheric correction using the modified Chavez method of dark-object subtraction technique is simple and easy to implement. It is reasonable approach for haze removal because of the selection of appropriate atmospheric model. Other methods mentioned earlier in this chapter either difficult to implement or inaccurate (i.e. histogram shift

method). Reason of using such an adequate method of atmospheric correction will be shown clearly in chapter 6.

As depicted in the JERS-1 SAR images shown previously in figures 4.6-4.8, vertical white lines can be found in the upper part and in the centre of the SAR scene. This type of error is a system error, probably caused by the Antenna Gain Control (AGC). This type of error could not be corrected because it is irregular in shape and not exactly vertical (not in the same column line) and hence could not be modelled to be removed.

5.0 JERS-1 SAR spatial information extraction

The first step of data fusion after the data has been pre-processed is enhancing and extracting the spatial information component. In a further stage, the extracted spatial component is fused with the enhanced and extracted spectral information component for lithological mapping of the test site of the area of study. The spatial information enhancement can be accomplished by the use of a texture analysis technique.

Texture analysis is a rather recent but rapidly growing field in digital image processing, because of its importance in simulating the strong visual perception of human vision for both organised and unorganised patterns. From a geological point of view, the most important information which can be extracted from digital image data are the spectral and textural information, and both are employed for identifying rock types. Spectral information describes the average band-to-band tonal variations in a multiband image set, whereas textural information describes the spatial distribution of tonal values within a single band, and reveals the topographic and lithologic differences in the imaged terrain [44].

An accepted definition of texture is that given by Haralick [45]. He defined texture as two decomposable basic dimensions. The first dimension describes the local properties of pixels, and is termed the tonal primitive. The second dimension is related to the spatial organisation of the tonal primitive. The tonal primitives refer to a maximum connected set of pixels (i.e. regions) having a specific tonal properties such as the average tone, maximum and minimum tone. The tonal region can be evaluated in terms of area and shape. The spatial organisation refers to the layout of the tonal primitives and can be described as random, or with dependence upon one or n neighbouring primitives. Qualitatively, image texture can be evaluated visually as having one or more of the properties of fitness, coarseness, smoothness, granulation, randomness, lineation, or being mottled, irregular, or hummocky. Each of these textural shapes is translated into some property of the tonal primitives and the spatial interaction between these primitives [45].

The linear features which are classified as textural features are all features perceived by the human eye as straight lines or curved lines in the image, when their length is at least twice their width. Generally, and from a geological point of view, linear features can be classified as: relief features or relief change features; tonal features or tonal boundaries such as lithological boundaries; texture features such as texture lines or boundaries; and finally pattern features such as pattern boundaries or pattern displacement features [46].

Geologic interpretation of lines and lineation in remote sensing is always controversial, and there is no consensus interpretation as to whether the line feature could be geomorphologic or geologic (i.e. structural), and it is up to the user to determine the origin of such surface undulations in the image. Short [47] addressed this problem and studied the reliability of geologic lineation extraction from satellite images. Recent trends in extraction of structural geologic lineation utilise other complementary data, such as geophysical data (i.e. aeromagnetic and gravity data) and extensive field visits to ensure that the extracted lines are purely geologic. For this reason, lineation extraction and mapping has been excluded in this work. For visual interpretation purposes, it is useful to know that lineation lies in three distinct classes: the first class is fractures such as joints and faults, and mainly exist in textural and relief change features. The second class is lithological contacts and can be identified as textural or tonal boundaries. The third class is folds and can be distinguished in images as sinuous lines, and may occur in tonal, textural, or pattern boundaries. In geomorphologic image photointerpretation, low hills usually have little dissection and are generally smooth with convex surfaces, while high hills are highly dissected and have permanent ridge crests [46]. Mountain texture is distinguishable from hill texture by the extent of radar shadowing. Mountains are characterised by large shadows which may cover more than half of the mountain area, whilst hills cover less than half of the area. Fine grained sedimentary rocks such as claystone and shale show fine texture, while coarser grained sedimentary rocks show coarser texture. A massive texture with rugged and peak divides is a clear indicator of igneous rocks [48]. Parameters such as spatial resolution, radar wavelength, incident angle, and environment govern the above rules for texture and texture analysis.

5.1 Parameters controlling SAR for texture and lineation detection

Recognition and mapping of geological features in radar imagery is dependent upon many parameters such as wavelength, polarisation, spatial resolution, angle of illumination and look direction [49], slope changes, surface roughness and microrelief, environment, rock types, dielectric properties [50], speckle noise, and the textural and lineation enhancement technique used.

Wavelength is an important parameter in textural analysis because texture is highly dependent on the SAR wavelength used. An example is that if a shorter wavelength is used, the imaged surfaces will be dominated by diffuse scattering and will be shown as a rough surface. If the surface is imaged by longer wavelength the surface will be depicted as smooth surface and hence its texture will be shown as dark and smooth. Polarisation also influences texture, for example like polarised waves are most sensitive to the spatial frequency corresponding to the Bragg resonant condition, and for rough surfaces the returned SAR signal is a result of a mixture of surface and subsurface contribution [51]. Jaskolla *et. al.* [3] claimed that the usefulness of L-band is restricted for lithologic discrimination as a result of the roughness criterion, and is not sensitive to the textural construction of natural rock surfaces.

Spatial resolution of the image used for textural analysis is rather vital. If the textural feature of the ground is less than the pixel size, the textural feature will not be depicted by the imaging system. Moreover, because textural analysis studies show how the pixel is interrelated to its neighbouring group of pixels, the imaging system aimed at textural analysis must have a ground resolution pixel size much smaller than the textural feature. Effective spatial resolution, image scale, and look direction have been studied by Yamagushi [52] for lineation detection in SAR images. He concluded that the optimum detectability is a function of spatial resolution of the imaging system R_s , image scale S_l , and the human visual system which cannot physically differentiate more than a few lines within 0.1mm width. Thus he formed his rule of optimum detectability of lineation which must satisfy the criterion $R_s \times S_l = 0.1 \text{ mm}$. From this, the scale of image product

aimed for photointerpretation, for example, must be 1:100,000 for 10 metre SAR resolution, which means a scale not smaller than 0.35×10^{-5} (i.e. 1:350,000) of this thesis work because the JERS-1 SAR image used is co-registered with the TM Landsat data which is of spatial resolution 28.5 metres.

For the illumination and look direction angles, previous studies have pointed out that low illumination angle is needed for lineation detectability, because the enhancement becomes maximum for topographic features due to the topographic exaggeration effect. For illumination direction on the other hand, it will optimally be enhanced if the feature trends are at the right or close to a right angle (perpendicular/orthogonal) to the direction of illumination. Trends of lineation which are parallel to the direction of illumination may not be seen. Yamagushi [52] proposed a new model, modified from previous work carried out by Wise in 1969, regarding the effective illumination direction. He suggested the enhancement of lineation becomes maximum if the lineation is in the range of 20-30 degrees from the illumination look direction. Figure 5.1 shows a lineation feature of length x_l illuminated by SAR of altitude h , as proposed by Yamagushi.

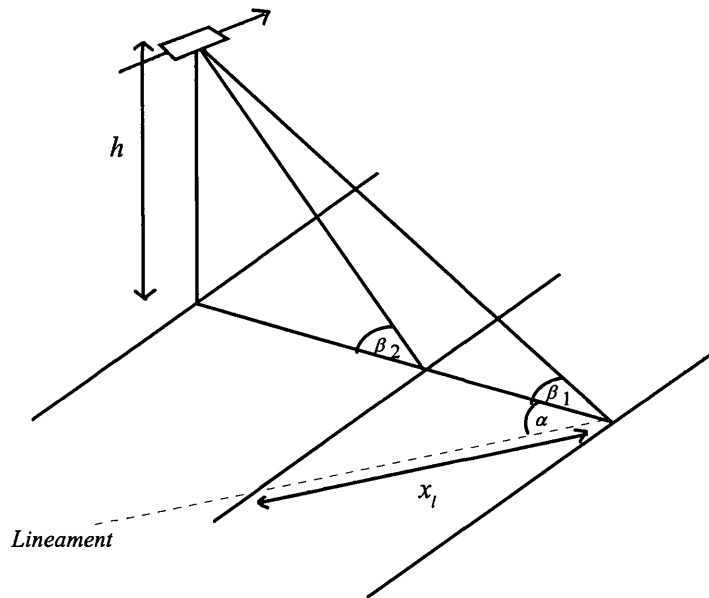


Figure 5.1 SAR illumination angle and lineation orientation relationships. (source: [52]).

From figure 5.1, the lineation length-imaging system height ratio x_l / h as proposed by Yamagushi [52] is :

$$x_l / h = (\cot \beta_1 - \cot \beta_2) / \cos \alpha \quad (5.1)$$

The x_l / h becomes maximum when α lies in the range of 20 to 30 degrees.

The surface roughness parameter can be estimated easily using the Rayleigh criterion which separates Rayleigh scattering from diffuse scattering of the ground surfaces. The criterion of Rayleigh scattering [53] is:

$$h_r < \frac{\lambda}{8 \cos \theta} \quad (5.2)$$

where:

h_r = height of terrain irregularities

θ = incidence angle

In the case of the JERS-1 SAR, $h_r = 3.58\text{cm}$, which means that rock sizes or topographic features with less than 3.58cm height will show Rayleigh scattering (smooth surface) and features with height of more than 3.58cm will show diffuse scattering (rough surface). If the ground surface is covered by dry sand or aeolian deposits that usually occur in the hyper arid areas, scattering may occur from the subsurface bedrock and may be calculated from equation 5.2, substituting $\theta = \sin^{-1} \frac{\theta}{\sqrt{\varepsilon}}$ and $\lambda = \frac{\lambda}{\sqrt{\varepsilon}}$ where ε is the dielectric constant of the penetrated sediments [53]. In the test site, field work investigation showed the study area is arid (but not hyper arid) as a result of its closed location to the sea as shown previously in figure 1.1. Furthermore, visual investigation to SAR data of the test site did not shows any subsurface penetration.

Rough surfaces give strong backscattering, as a result of the increased number of scatterers and corner reflectors. Such surfaces also cause a geometric distortion as a result of foreshortening, layover and shadowing. The resultant SAR image usually shows very bright V shaped features with many dark areas appearing in the image. Such surfaces may not reflect a proper texture when analysed for rock identification. To overcome this problem, a proper SAR image geometric correction using DEM and calibrated backscattered SAR signals must be made [33].

Environment influences the texture appearance of the imaged surfaces. An example is that if the area of study is humid, the SAR backscatter will be weak as a result of strong absorption of the SAR signal due to the presence of water in the ground sediments. Also in a humid environment, soil and vegetation will cover the rock units and hence the geologic features will be obscured. In arid land, rock texture analysis using SAR is ideal because no soil or vegetation covers the rock units, and the backscatter will be much stronger as a result of the absence of water in the sediments. Furthermore, and because weathering is not linearly constant, which affects physically more of areas of higher altitude and chemically more of low lands, and hence different texture of the same rock unit may show some differences as a result of topographic attitude.

Texture analysis for geological mapping is not very successful compared with other image texture applications such as urban mapping or forest inventory. The problem arises because geologists mainly classify rock types based on parameters such as mineralogical contents of the rock type, palaeontological content, age, and geographic location, which may not always coincide with the texture appearance of the rock type.

5.2 Previous studies in texture, and texture analysis in geology

Multispectral imaging systems and SAR have over the past two decades led to the phasing out of black and white aerial photography. Surprisingly, texture analysis is still of paramount importance when used for geological photointerpretation, with computer classification as a parallel effort using spectral information. This is because texture gives

valuable spatial information and the same image processing techniques used for black and white photographs can be used for multispectral optical and SAR image data.

Most image processing techniques used for texture analysis can be classified as follows [54]: The Fourier power spectrum, the co-occurrence grey level matrix second order statistics, or what is called the Haralick Grey Level Co-occurrence Matrix (GLCM), the grey level difference statistics and finally, the grey level run length statistics. Other techniques which use different kernel size and weight (i.e. filtering), such as that shown by Moore [55] or Laws microstructure filters [56], are also available, but have not been tested or used in this work.

The Fourier power spectrum texture enhancement technique has been previously used when texture is a function of wavelength and direction [57]. High spatial frequencies in an image represent rigid terrain or coarse texture, and low frequencies represent flat terrain or smooth texture. The technique relies on transforming the image into the spectral domain using a two dimensional *FFT*, and convolving the resultant spectrum image with a 2 dimensional filter, and finally reconstructing the convolved image by the use of the inverse *FFT*. It has been found that the *FFT* power spectrum method is powerful for enhancing periodic textural features such as sand dunes or any repetitive structures. High relief (rigid) and low relief terrains can also be enhanced using this method, as can lineation enhancement. Weszka *et. al.* [54] at that time introduced different kind of filters implemented on the *FFT* transformed images because the previously known filters used in the Fourier power spectrum are known to be only sensitive to the size (spatial frequency of the image) or to the orientation of the spatial information, but not to both together in the same time. These filters designed by Weszka are the intersections of the combination of rings and wedges at different angles and lengths. The traditional *FFT* filters and the filters of ring and wedge intersections are shown in figure 5.2.

The other textural analysis techniques mentioned earlier are implemented in the spatial domain using neighbourhood pixel statistical measures (i.e. local property values). The

simplest and oldest digital filters specifically designed for texture enhancement, many still available in commercial digital image processing softwares, are basically designed from the work carried out by Hsu [58]. He designed 3 by 3 and 5 by 5 window size convolving filters to measure 23 statistical variables in the digital image scenes. The reason for using filters of small window size was because the task was mapping detailed terrain types based on classification of individual pixels, rather than a group of pixels or scenes, using these statistical measures of texture. He used eight digitised aerial photographic scenes of the State of New York for land use mapping by the use of linear discriminant functions based on the Mahalanobis statistics for classification. He also used these textural algorithms to map geologic features such as granites in the Duffer Peak Quadrangle in Nevada [59]. Supervised and unsupervised classification was also carried out on the enhanced textural images of the MSS data used in the study. He concluded that granitic features can easily delineated in arid areas such as Nevada with some degree of confidence using these textural enhancement algorithms.

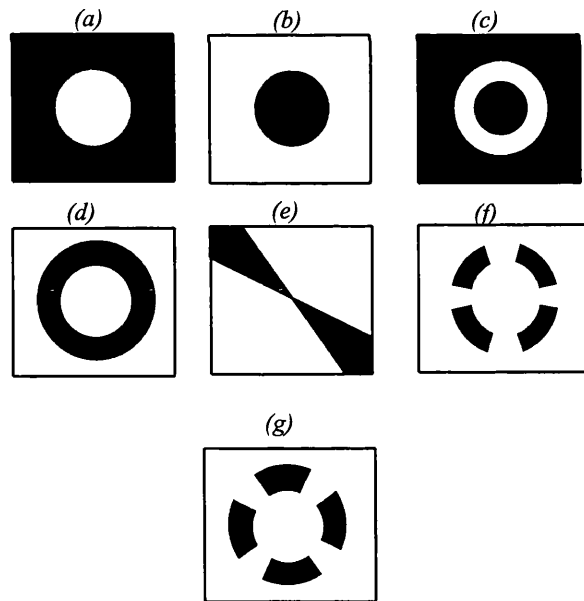


Figure 5.2 Binary filters implemented on the FFT transformed images, the size of the filter has to be equal to the size of the image. Black = zero, white = 1. (a) lowpass-filter, (b) highpass-filter, (c) bandpass-filter, (d) cut pass filter, (e) directional filter eliminates all 45 degree lineation features, and (f and g) are wedge-ring intersection filters of different angles. (Source a-c [60], d [56], e [61]).

The Grey Level Co-occurrence Matrix (GLCM) second order statistics and the grey level run length statistics methods are shown to have comparable performance in texture analysis techniques [54]. They were also shown to be better at extracting the textural features from natural image scenes.

In this work, the *FFT* method, the first order statistics, the second order GLCM, and the texture unit/texture spectrum method discussed by He *et. al.* [62], and Wang *et. al.* [63] are considered. These were tested on the JERS-1 SAR 3 by 3 Frost filtered image shown previously in figure 4.7. A final decision was taken to use the Haralick GLCM method because it shows much better class separability using the Transformed Divergence classes separability test.

Recent work in texture techniques and analysis with conclusions is discussed in the following review articles.

Gong *et. al.* [64] compared and used three types of textural approaches for classifying northeastern Metropolitan rural-urban areas in Toronto. They compared and used the Hsu textural measure, the Grey Level Co-occurrence Matrix (GLCM) texture measure described by Haralick *et. al.* [65], and the texture unit-spectrum approach used by He and Wang [62], Wang and He [63]. They produced and combined 30 texture images with the original SPOT HRV data for classification using the Maximum Likelihood decision rule.

Franklin and Peddle [66], Peddle and Franklin [67] used the GLCM texture measures and combined the textural information image results with DEM and the spectral information from MSS, TM, and airborne C-SAR to classify the Gros Morne National Park in eastern Canada. They achieved 86.7% mapping accuracy by the combination of the spectral and spatial information.

In 1990, He and Wang [62], Wang and He [63] developed a new approach for texture analysis, namely the texture-spectrum measure. The advantage of this measure is in its simplicity, using only a 3 by 3 window measurement which is not affected by direction of orientation measurement. Texture units are produced and the texture spectrum is extracted to be used as an input in classification procedure. This method showed a 97.5% overall accuracy of classifying natural textural scenes in the Brodatz album.

Digital processing of orbital SAR images to enhance geologic structure of the Mazinaw Lake area in the Canadian Shield has been evaluated by Masuoka *et. al.* [68] using SIR-B and Seasat SAR data. Many pre-processing procedures were used prior to image enhancement techniques, including speckle reduction using k-nearest neighbour filter and illumination azimuth biasing reduction using 3 different look direction images co-registered together, to enhance all possible directions of lineation. A variety of edge enhancement operators were tested in their work, including Laplacian, Moore-Waltz, Compass (Prewitt edge mask), Roberts, and Sobel edge enhancement filters. They found that a modified version of a Moore-Waltz filter is the appropriate filter for edge enhancement. Colour composites were also produced using the statistical Principal Component Transform (PCT) of the three different look images and were utilised for manual photointerpretation.

Haralick *et. al.* [65] addressed a new method for texture feature extraction using the Grey Level Co-occurrence Matrix (GLCM). This method uses a matrix called the co-occurrence matrix derived from statistics based on the neighbouring pixels. These statistics summarise the relative frequency distribution of how often one grey level will appear in a specified spatial relationship to another grey level on the image under investigation. In their study, they showed the power of GLCM to categorise many features based on their texture in many kinds of data, including micrographs, panchromatic aerial photographs, and multispectral satellite images. Haralick [45] also surveyed and evaluated most of the textural enhancement approaches, including the GLCM technique.

Using the Fourier Transform technique for texture analysis, Excell *et. al.* [69] showed that the Fourier textural technique only gives good performance with textural features of a strongly periodic nature. In their work, they extracted and separated the dust clouds from the agricultural fields using a specifically designed filter implemented on a Fourier transformed image of Landsat TM band 4 in the south-east of Iraq.

As a result of the increased popularity of the GLCM method, recent studies in texture analysis discuss mostly the usefulness of this method and its application in many disciplines, including geologic mapping. Marceau *et. al.* [70] raised the issue of GLCM decision requirements concerning the number of variables which should be taken into account when GLCM is used. These variables include the spatial resolution, the spectral band used, the quantization level, the size of the moving window, the interpixel distance (d) and angle direction (α) during the co-occurrence computation, and finally the GLCM statistical measures used. In their study, they measured the influence of such variables on the improvement of classification accuracy to map Bonaventure in the Baie des Chaleurs in Canada using SPOT XS data. The results of their work show that large (enough) window sizes are most effective because they capture the textural patterns of classes. Care in selecting the window size is vital, because if a window of small size is chosen the textural patterns may not be captured. If a large window size is selected, pixels from other classes may be misclassified. A similar investigation has been carried out by Baraldiet *et. al.* [71], testing the most relevant statistical measures of the GLCM. They showed that among the 14 statistical measures originally proposed by Haralick, the most effective GLCM statistical measures are energy, contrast, variance, correlation, entropy, and inverse difference moment.

Shanmugan *et. al.* [44] were one of the early users of the GLCM texture enhancement method on SAR data, to classify large scale geological formations over Tennessee, USA, using Seasat SAR data. They successfully classified many sedimentary rock types including shale, sandstone, and siltstone through combining and averaging the 0, 45, 90, and 135 degree orientations of the GLCM calculation. Scatterograms of their GLCM

statistical measures show very good separability of the classes, which demonstrates the usefulness of this method.

5.3 Strategy used in this study for texture enhancement

In the data fusion process which will be discussed in the following chapters, two main image outputs will be prepared from the fused data. The first output is analogous i.e. texturally and spectrally fused colour images specifically adapted for photointerpretation. The second image set output is a fused image data set prepared for automated mapping using multivariate analysis (i.e. computer classified image where all rock type classes of the study area are delineated automatically).

In the first analogous output, the textural image component is the original registered and despeckled (5 by 5 Frost filtered) SAR image. This image was shown in figure 4.8. The decision has been taken to use this image simply because the textural information in the SAR image is naturally exaggerated for visual depiction, and only one textural image has to be used in the image processing fuser tools (i.e. colour and principal component transforms) which separate the spatial from the spectral information and combine them back after proper processing. The second fused outputs used for automated mapping are: a data set of both enhanced spectral and textural information; a data set of textural information component which is extracted using the GLCM method; a spectral information data set which is enhanced using BCET, these are shown in chapter 7.

Based on the two dimensional co-occurrence matrix such as that shown in figure 5.3, Haralick [45,48,65] used this matrix for a fixed distance (d) and angular spatial relationship (θ) between the image pixels, and produced what is called the Grey Level Co-occurrence Matrix GLCM. From the GLCM, many second-order statistical measures can be calculated and a new images can be constructed from these measures which reflects the neighbouring pixel relationships (and so reveals image texture). The derivation of the GLCM texture analysis is simplified in the following section:

Let:

$f(x,y)$ = image I of length x and width y . $x \in [0, x_n]$, $y \in [0, y_n]$; $x, y \in I$

g_n = the number of grey levels in f .

\overline{CM} = the grey level co-occurrence matrix, which is a square matrix of dimension g_n as shown in figure 5.3.

$\overline{CM}_{i,j}$ = the (i,j) th entry in the matrix.

$\overline{CM}_{i,j}$ represents the counts of how many times two neighbouring pixels are separated by a fixed distance (d) at angle (θ), one with grey level i and the other with grey level j . These entries represent the GLCM.

		g			
		0	1	2	3
g	0	#(0,0)	#(0,1)	#(0,2)	#(0,3)
	1	#(1,0)	#(1,1)	#(1,2)	#(1,3)
	2	#(2,0)	#(2,1)	#(2,2)	#(2,3)
	3	#(3,0)	#(3,1)	#(3,2)	#(3,3)

Figure 5.3 GLCM of an image of grey level g_n ranges from 0-3. If the image is 8bit, the GLCM will be 256 by 256 in dimension. The $\#(i,j)$ entry refers to the number of times grey level in the image of intensity i and j in the GLCM separated by a distance d and angle θ have been neighbours. Note that the GLCM is symmetrical along its diagonal (i.e. $\#(i,j) = \#(j,i)$).

Using the Haralick normalised and symmetric GLCM, seven statistical textural image features derived from the \overline{CM} have been produced in this thesis work, where six of these measures were recommended by Baraldi *et. al.* [71] and five of these features were recommended by Shanmugan *et. al.* [44] for geological mapping. Many window sizes and distances (d) have been tested to produce the GLCM texture measures. Finally, it has been found that a window of size 5 by 5 and of $d = 1$ performs better when a transformed

divergence separability test is used on the training areas of the test site. Angles θ of 0, 45, 90, and 135 degrees are combined and averaged. The seven GLCM statistical measures used are as follows:-

$$1- \text{The Inverse Difference Moment} = \sum_{i=0}^{g_n-1} \sum_{j=0}^{g_m-1} \frac{\overline{CM}(i, j)}{[1 + (i - j)^2]} \quad (5.3)$$

The Inverse Difference Moment (IDM) texture parameter measures the image homogeneity, for example it gives large values for areas with small grey level differences, and it is inversely correlated with the textural measures of contrast and energy shown in equations (5.4) and (5.8). Figure 5.4 shows the output image of IDM texture measure. The bright patches along mountain ranges in the figure represent high homogeneity as a result of specular reflection of the SAR signals.

$$2- \text{The contrast} = \sum_{i=0}^{g_n-1} \sum_{j=0}^{g_m-1} \overline{CM}(i, j) \times (i - j)^2 \quad (5.4)$$

The contrast texture parameter measures the differences between the highest and lowest spatial frequency values in a contiguous set of pixels (i.e. window). Figure 5.5 shows the output image of this measure.

$$3- \text{Dissimilarity} = \sum_{i=0}^{g_n-1} \sum_{j=0}^{g_m-1} \overline{CM}(i, j) \times |i - j| \quad (5.5)$$

Figure 5.6 shows the output image of the texture measure of dissimilarity.

$$4- \text{Mean} = \sum_{i=0}^{g_n-1} \sum_{j=0}^{g_m-1} \overline{CM}(i, j) \times (i) \quad (5.6)$$

Figure 5.7 shows the output image of the mean texture measure.

$$5- \text{Entropy} = - \sum_{i=0}^{g_n-1} \sum_{j=0}^{g_m-1} \overline{CM}(i, j) \times \log(\overline{CM}(i, j)) \quad (5.7)$$

The entropy parameter measures the disorder of the image or the image randomness [67]. For example, when the image is not texturally uniform, the entropy is very high because the entries of the GLCM have small values. The angular second moment and

entropy measures are inversely correlated. Figure 5.8 shows the output image of the entropy texture measure.

$$6- \text{ Angular second moment} = \sum_{i=0}^{g_n-1} \sum_{j=0}^{g_m-1} \overline{CM(i,j)}^2 \quad (5.8)$$

The angular second moment is sometimes called the texture energy [41], and measures the texture uniformity. For example, high ASM or energy values occur when the grey level distribution over a window is constant or repetitive (i.e. periodic). Figure 5.9 shows the output image of ASM texture measure.

$$7- \text{ Correlation} = \sum_{i=0}^{g_n-1} \sum_{j=0}^{g_m-1} \frac{\overline{CM(i,j)} \times (i - \mu) \times (j - \mu)}{\sigma^2} \quad (5.9)$$

The correlation texture parameter is a measure of the grey tone linear dependencies in the image. High correlation values mean that there is a linear relationship between the grey levels of pixel pairs in the window. Figure 5.10 shows the output image of the texture measure of correlation.



Figure 5.4 GLCM texture measure of Inverse Difference Moment, "MITI/NASDA retain ownership of the data".

Scale 1:204084

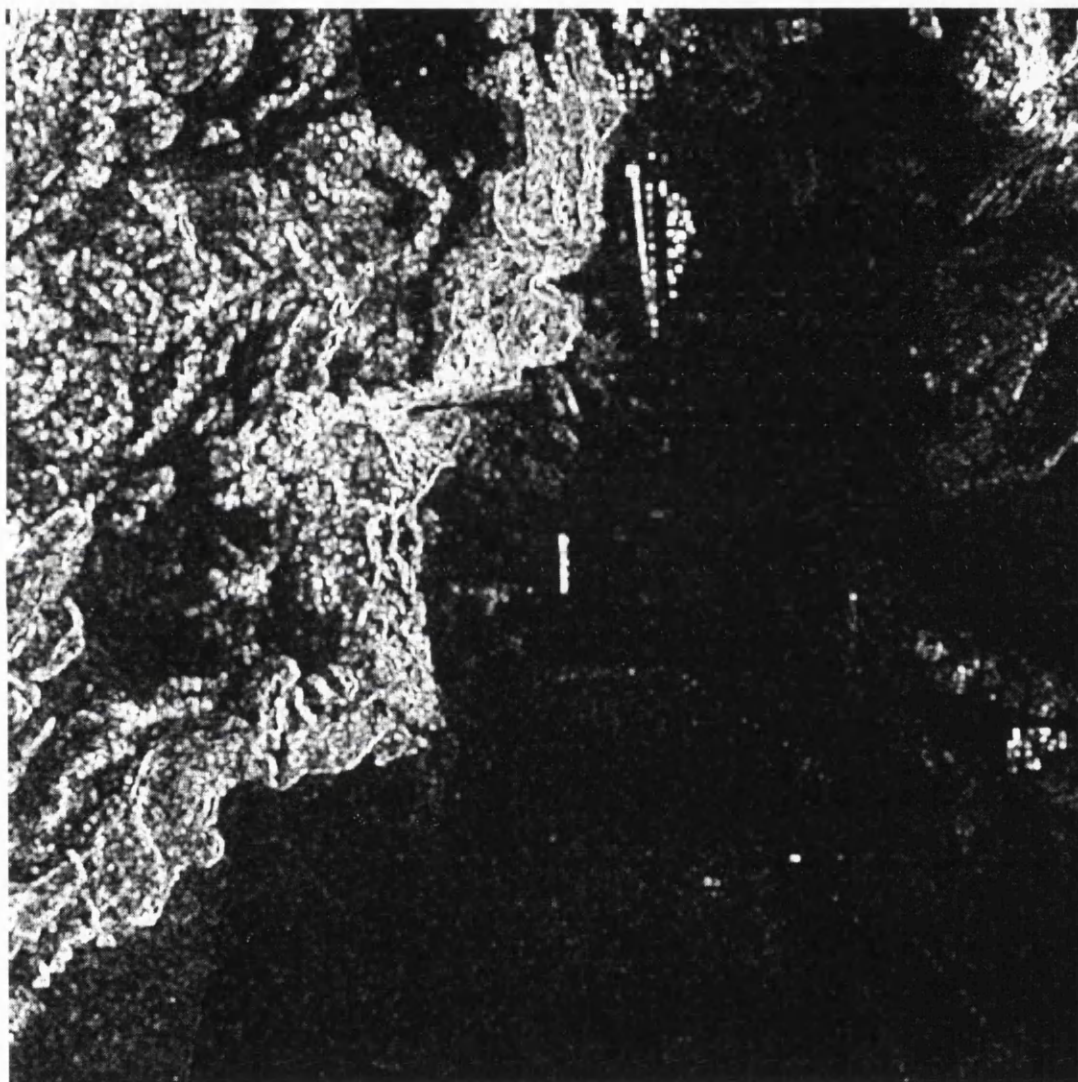


Figure 5.5 GLCM texture measure of contrast, "MITI/NASDA retain ownership of the data".

Scale 1:204084

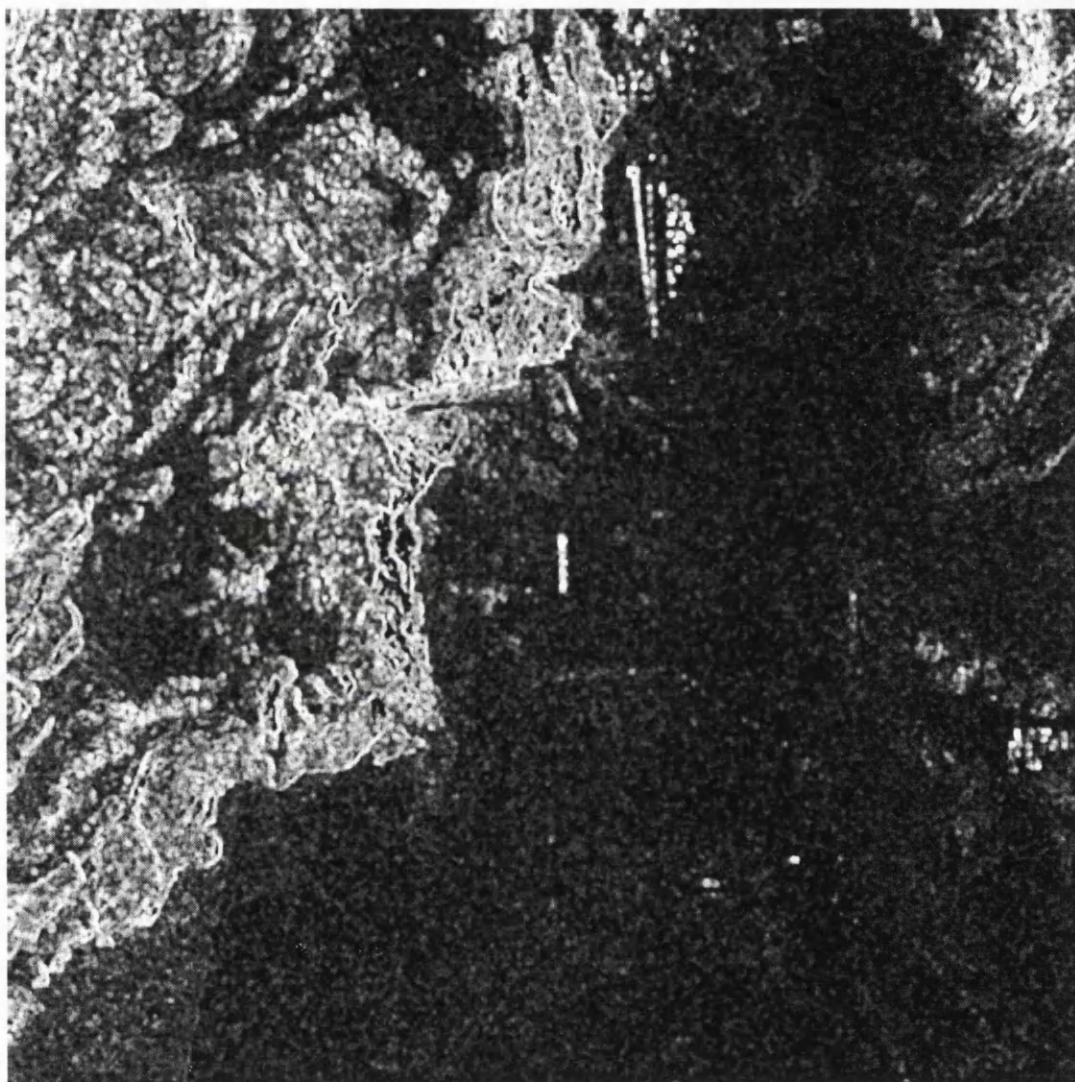


Figure 5.6 GLCM texture measure of dissimilarity, "MITI/NASDA retain ownership of the data".

Scale 1:204084

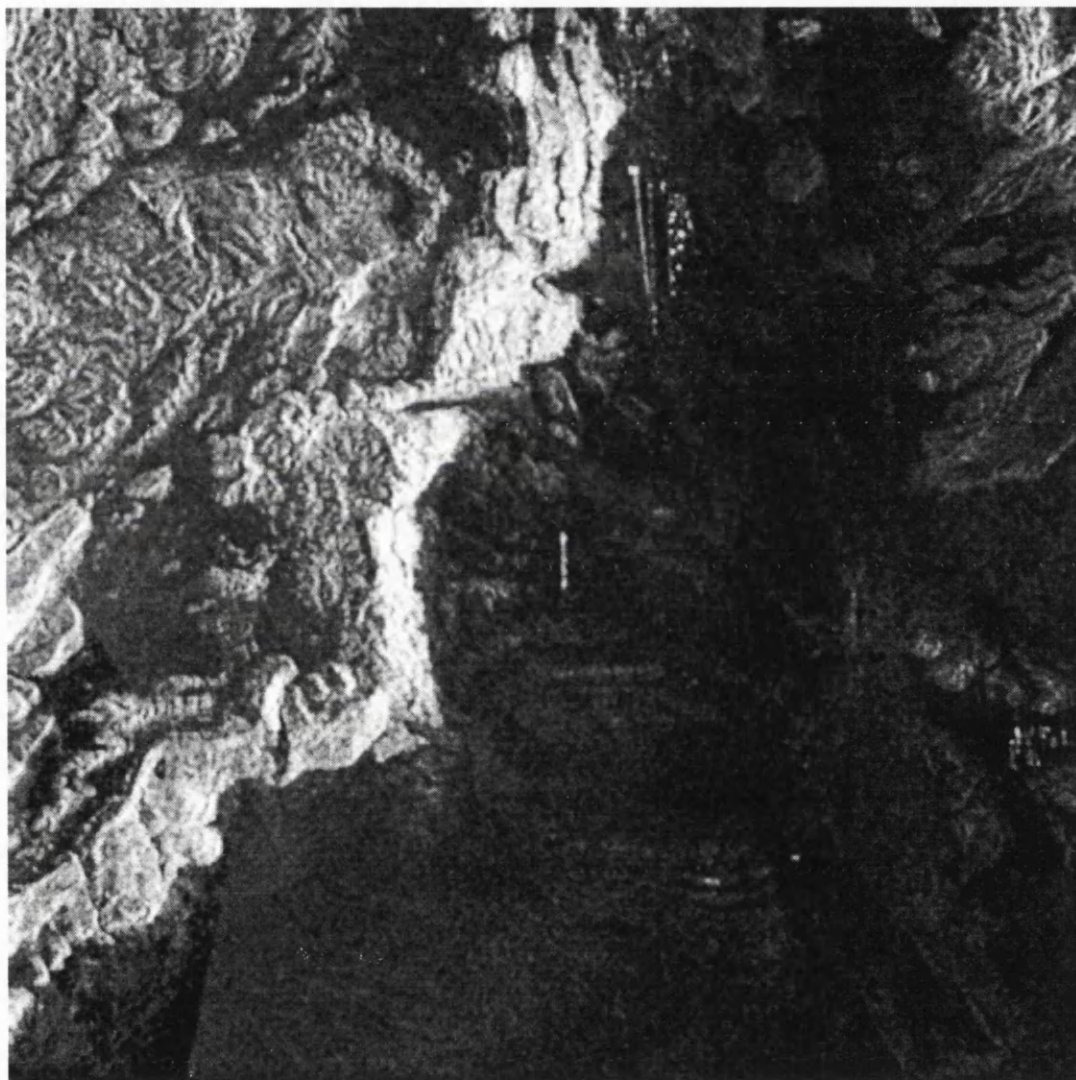


Figure 5.7 GLCM texture measure of mean, "MITI/NASDA retain ownership of the data".

Scale 1:204084

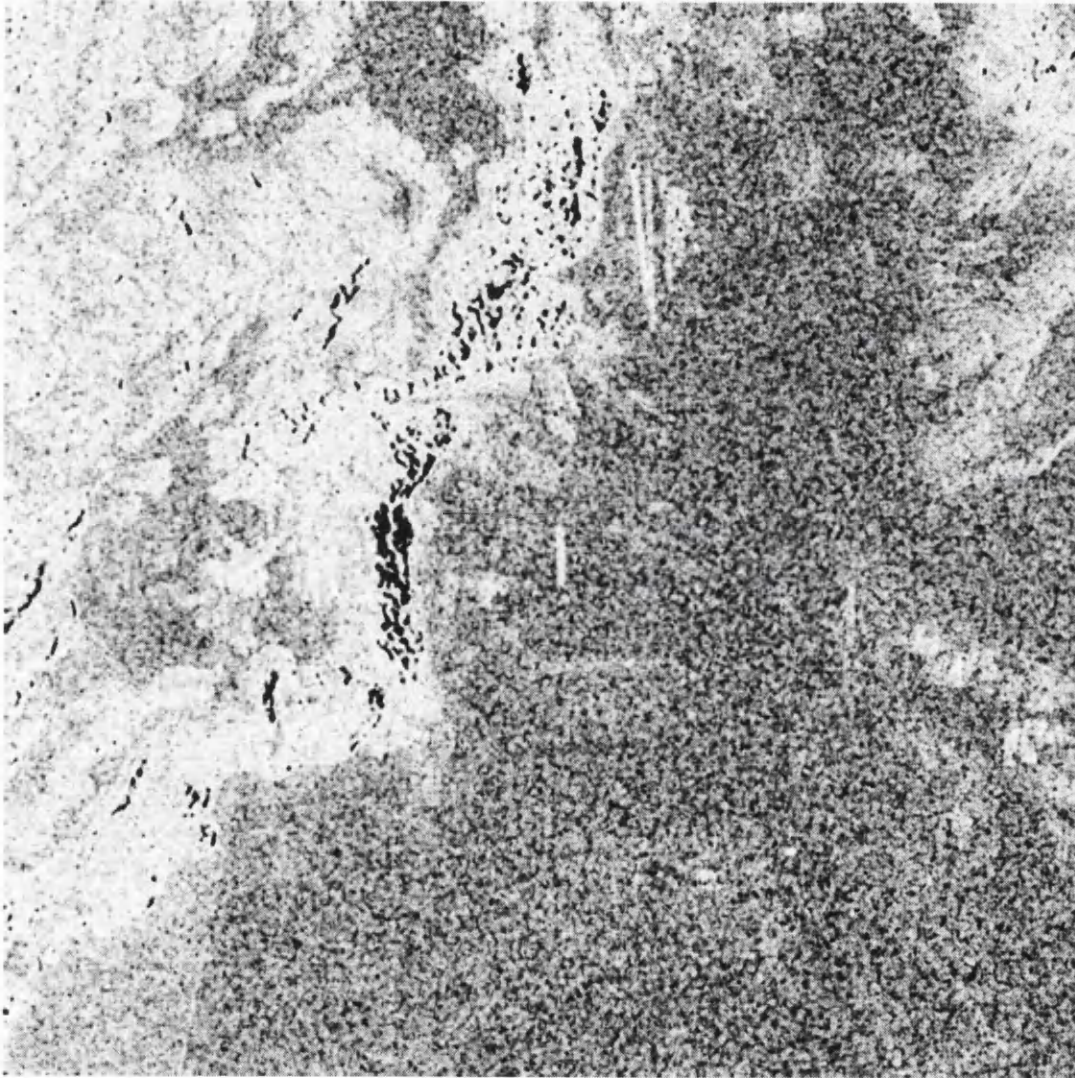


Figure 5.8 GLCM texture measure of Entropy, "MITI/NASDA retain ownership of the data".

Scale 1:204084

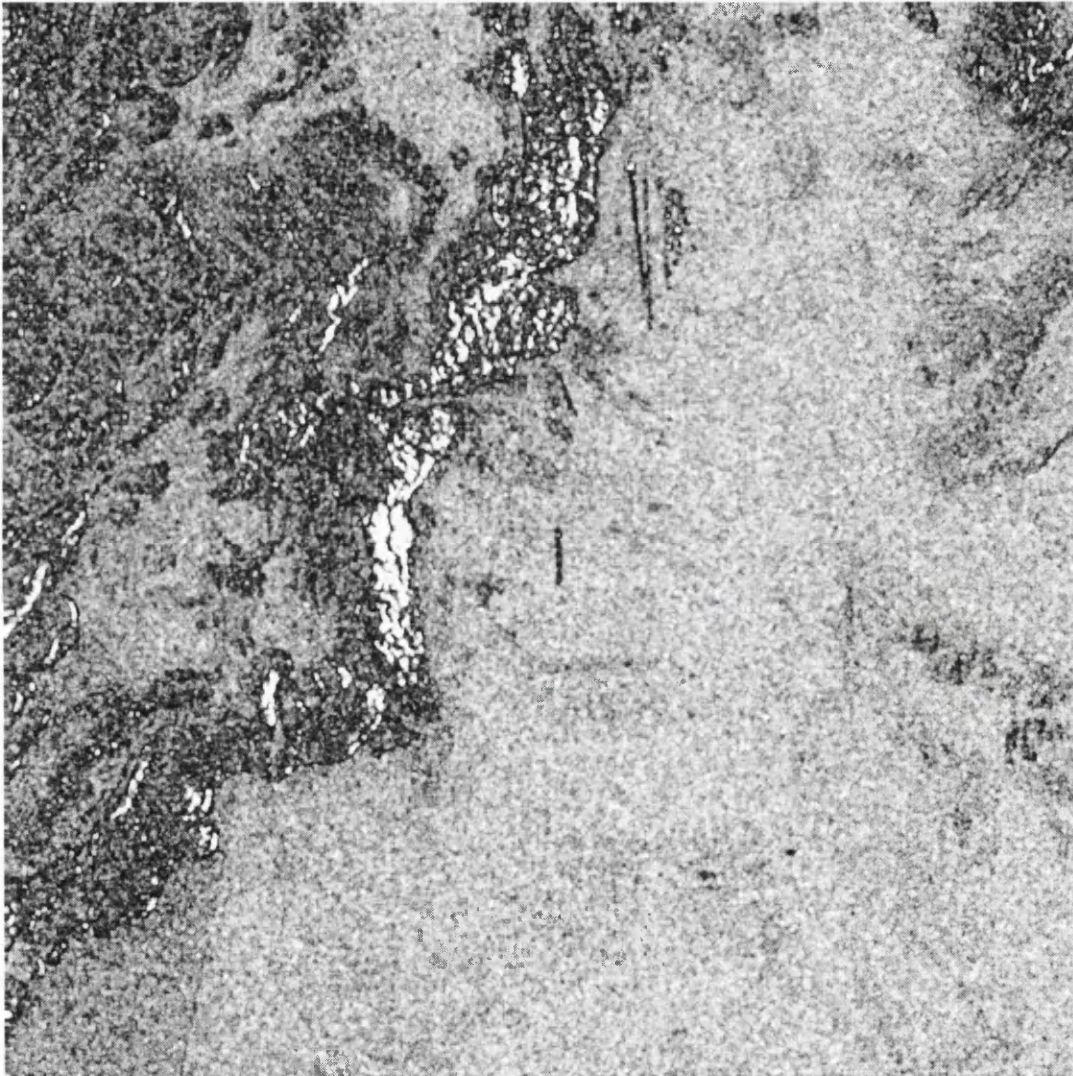


Figure 5.9 GLCM texture measure of angular second moment ASM, "MITI/NASDA retain ownership of the data".

Scale 1:204084



Figure 5.10 GLCM texture measure of correlation, "MITI/NASDA retain ownership of the data".

Scale 1:204084

For photointerpretation purposes in this work, firstly it is important to keep in mind that the shown textural enhanced images in the previous figures are of scale 1:204084, which is reasonably adequate and satisfies the Yamagushi detectability criterion. Referring back to the figures 5.4 - 5.10, some of the textural enhanced images show exaggerated rock textures of the mountainous areas in the left half of the images (the Magnah Massif). These include the measures of contrast, dissimilarity, mean, and correlation. Other enhanced textural images show clear and distinct textures of the low relief area in the right half of the images (the Afal Plain). These include the IDM, entropy, and the ASM textural measures. The Bad' formation shows up clearly in the original SAR despeckled filtered image, and some of the texture images, such as the GLCM texture measure of mean output image.

Using the images of seven textural measures together, a textural signature can be produced for all rock type classes selected from the training areas of the test site. It is important to note that these classes textural signatures derived originally from a single source of the JERS-1 SAR image where seven textural images have been produced. By implementing the transformed divergence separability test on these classes as shown in table 5.1, we can roughly estimate how accurate our results will be when we use class clustering or similar classification techniques.

From table 5.1 the sum of class separability is 84.85. If all of these classes are perfectly separable (i.e. 2×55), we can directly estimate that 77.13%¹ of the rock unit pairs can be lithologically differentiated. Such results are quite promising, because we can differentiate more than three quarters of the area rock types with the use of texture enhanced images derived from a single SAR image without using any other information.

¹ Percentage of separability = [sum of classes separability / (2 * Number of classes)] * 100.

Class	Jurfayn	Atiyah	Musayr	Nutaysh	Bad'	Lisan	Conglo.+ Gravel	Gravel Sheets	Sabkhah	Alluvium
Atiyah	0.68457									
Musayr	1.17114	0.28480								
Nutaysh	0.82148	0.28347	0.50204							
Bad'	1.91680	1.63035	1.85004	1.75678						
Lisan	2.00000	2.00000	2.00000	2.00000	2.00000					
Conglo.+ Gravel	2.00000	2.00000	2.00000	2.00000	2.00000	1.09797				
Gravel Sheets	2.00000	2.00000	2.00000	2.00000	2.00000	1.69625	1.03382			
Sabkhah	2.00000	2.00000	2.00000	2.00000	2.00000	0.16707	1.24607	1.79624		
Alluvium	2.00000	2.00000	2.00000	2.00000	2.00000	0.12357	1.42437	1.90420	0.19978	
Aeolian silt+ sand	2.00000	2.00000	2.00000	2.00000	2.00000	0.07102	1.32050	1.84500	0.19390	0.03717

Table 5.1 Textural signature separability table of the test site training classes after using The seven GLCM texture measure of the SAR image data. The Transformed Divergence separability test algorithm is used to calculate training classes separability.

5.4 Conclusions and remarks

The GLCM showed better results when tested for texture enhancement, but in the same time it has a major drawback which cannot be solved. This limitation is resulted from the window size selection. For example, if the classes of smooth textures such as Aeolian silt and sand, Alluvium, Sabkhah, and Lisan which need small window size to extract their texture properly. In the same time, other classes which have rough textures, such as Jurfayn and Atiyah, may require a bigger window size. In other words, every texture class may need its own GLCM window size. If many GLCM window sizes are implemented and finally averaged, the results show not much improvement because averaging GLCM texture from different window sizes suppress the extracted texture itself.

Another limitation is SAR geometric distortions such as layover, foreshortening, and shadows. No good results can be gained on such areas using GLCM or any other textural enhancement techniques.

6.0 Image data fusion - optimisation for visual analysis

This chapter describes in detail the use of data fusion as an optimisation tool for visual analysis. The definition of image data fusion, the reasons for data fusion, and the data fusion models are firstly given.

6.1 Introduction

Data fusion generally refers to a scientific set of procedures which process, manipulate, and identify objects and locate their position using data from a number of sources. It has been developed in the fields of both imaging and non imaging remote sensing, and aims to solve diverse sets of problems having common characteristics. In non-imaging systems, data fusion employs mathematical and statistical algorithms upon the input from multiple readings of the sensor(s) from an object, to determine its identity and position. These mathematical and statistical approaches include clustering and classification algorithms [72]. In imaging remote sensing systems, additional procedures are used to manipulate and optimise data for visual and automated analysis.

Possibly the best example of data fusion system is the human brain, which combines all the collected information from the sensing organs, then analyses this in conjunction with a constantly corrected and updated database amassed from experience. The fused data is then used to identify and/or locate the object being sensed [72]. In imaging remote sensing, and in particular data fusion, refers to the technique of integrating different image data sets with the use of image processing techniques such as: preparing and optimising the data for integration (i.e. geometric correction, atmospheric and radiometric correction between the different data sets); visual analysis between the data sets such as colour composition; colour and statistical transforms such as red-green-blue intensity-hue-saturation ($RGB \Leftrightarrow IHS$) transform; Brovey transform; principal component transform and reverse principal component transform ($PCT \Leftrightarrow PCT^{-1}$) and finally; the use of classification techniques between the different image data sets. In the literature, data fusion can be found under many terms, such as distributed sensing, data integration, data

synergism, data merging etc. Nowadays, data fusion techniques span many industrial, medical, military, and civilian applications in modern human life.

In the science of remote sensing, for both types of active and passive imaging systems, the remote sensing instrument measures the intensity of the reflected, scattered, or emitted (i.e. thermal sensing) radiation from an object. This is directly related to the physical and chemical properties of the object being imaged as a result of scattering and absorption of the radiation field. From this phenomenon, and ignoring atmospheric influences and systems instability, the measured quantity (i.e. radiance, intensity, power, amplitude, etc.) can be expressed by the following relationship [73]:

$$E = R(\lambda, X, Y, Z, \theta, \phi, T, P) \quad (6.1)$$

where:

E = measured energy from the imaged object as a function of the parameters $(\lambda, X, Y, Z, \theta, \phi, T, P)$.

R = reflection, emission, or scattering radiation of the object.

λ = wavelength used for imaging the object.

X, Y, Z = spatial co-ordinates of the object being imaged.

θ, ϕ = view direction of the sensor with respect to the object (i.e. elevation angle and azimuth viewing angle).

T = imaging acquisition time.

P = polarisation of the sensor (only if an active imaging system is used).

From the above relation, it is obvious that the maximum possible information from the imaged object can be evaluated in only five terms. These terms are known as the object signature. The object signature can be defined (if a two dimensional form is used for simplicity) as the behaviour of the object being imaged, determined by one constant parameter and changing one of the other parameters. The five signatures that define the object, as proposed by Gerstl [73], are shown in figure 6.1 and are discussed in more detail in the following section.

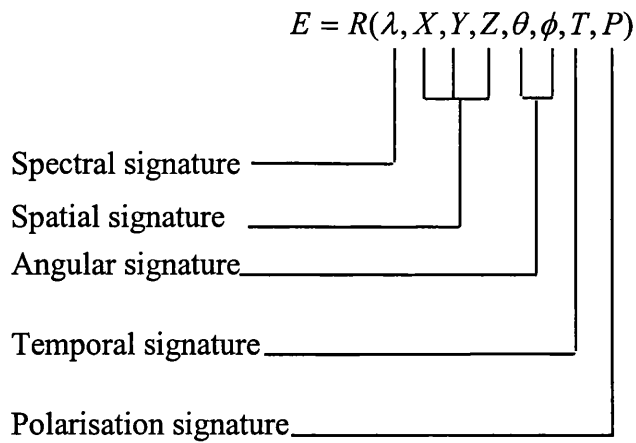


Figure 6.1. All possible information which can be collected by remote sensing platforms (Modified from: [73]).

The spectral signature refers to the reflectance/emittance of an object as a function of the wavelength λ . Such a signature could be gathered by a satellite sensor capable of sensing an object in many different wavelengths (e.g. Landsat TM sensor, SIR-C, Radarsat etc.) or from different satellites having different wavelengths, extracting what is known as extended spectral signature. Such information is valuable for geologic remote sensing for mapping varieties of rock units. The spatial signature is defined as the reflectance or emittance contrast between different neighbouring pixels that allow an object pattern to be recognised (e.g. synoptic view of rock types boundaries, textures, and geomorphology). Angular signature refers to how the object behaves when viewed from many different angles. Unfortunately, with the exception of SPOT satellites, most optical remote sensing sensors are nadir viewing and do not have the ability to extract such valuable information. SAR imaging systems have this capability to illuminate objects from many angles to extract the object's angular signatures. The temporal signature is another important piece of information that can be collected by remote sensing satellites, and refers to reflectance/emittance or scattering behaviour of an object over time (e.g. when imaged many times over certain period). This signature give information about the temporal changes that may happen to the object. Examples of temporal changes in geological applications include tectonically active areas such as earthquakes and volcanic activity detection and mapping, environmental changes and natural hazards. The last

piece of information that can be collected by remote sensing satellites is the polarisation signature. This information can be achieved only through the use of active remote sensing imaging systems such as imaging radar. The optical remote sensing platforms cannot be used for such a purpose because they use sunlight as the main source for sensing, which is unpolarised [73].

Using of the signature information that can be collected by remote sensing, the goals of the data fusion techniques are:

- 1- Maximising the ability to visualise and simply interpret such information in the image data set.
- 2- Using only the valuable information which leads to identifying the object being imaged and extracting its identity and position.
- 3- Removing the data redundancy by utilising the data fusion techniques as a method of optimisation either for visualisation or classification techniques (i.e. minimising data volume while maximising information content) .
- 4- Employing all possible information available to deduce new information about the object being imaged.

6.2 Models of data fusion

Data fusion can be of many models based on the data derivation, including platform sensors and wavelengths configuration. As shown previously in chapter 4, registration between these data is vital, and constitutes a very important part of the fusion preparation. The registration can be of two types, either registration between bands onboard the platform, or registration on the ground using ground truth information such as maps or previously geocoded images with the aid of digital elevation models. In the case of onboard registration between bands, it can be achieved only between different bands using the same sensor and platform and the same viewing geometry. An example of such registration is the Landsat data, SPOT data, and multifrequency/polarisation airborne and spaceborne SAR data. Such registration is highly accurate because the

viewing geometry between bands in the sensor is the same. Registration on the ground between bands with different sensors and platforms is more complicated, and usually less accurate if compared with onboard registration. Examples of the latter type of registration include registration between optical and SAR data, and registration between bands from the same sensor from different times for temporal studies.

The data fusion models are:-

- 1- The multispectral model
- 2- The multispectral/multisensor model
- 3- The multitemporal model
- 4- Model of fusion with ancillary data (i.e. ground truth, GIS etc.)

The multispectral fusion model refers to that of the same sensor which collects data in different wavelengths at the same acquisition time. In this model, registration between these data is achieved aboard the platform. Spectral signatures of targets can be achieved based on the response of each band to the target. The number of bands used are important in this model to achieve better spectral signature representation. Polarisation signature can also be included if an active imaging system is used. Examples of such a model include all type of sensors that collect data in many wavebands simultaneously, such as Landsat series, SPOT series, SIR-C, Radarsat, etc.. Figure 6.2 (a) shows this configuration.

The multispectral/multisensor model refers to the combination of many imaging sensor data where some or all of these sensors are multispectral. Valuable information about the imaged features (signatures) can be gained in this configuration, but the information could be redundant (i.e. correlated) and hence data should be carefully manipulated. High capacity storage is also needed because of the huge amount of such data. The registration is vital in this model and can only be achieved on the ground using ground truth data such as control points or maps. In this thesis, data is collected using this model. Another version of this fusion model is the multisensor model which can be represented by having

many data sets of the same features or area using many different platforms, either using the same wavelength or in different wavebands. Different viewing angles can also be used but practically not desirable because of the registration difficulty. Spectral and angular signatures can be collected through this configuration. The polarisation signature can also be acquired if the sensors are active and able to transmit and receive polarised signals. Figure 6.2 (b) shows this configuration. The multitemporal model refers to any of the previously mentioned models but gathering information at different times or periods to monitor and/or achieve temporal variation of a target(s).

Models of fusion with ancillary data may include any configuration with the above models with additional information such as ground based information incorporated. Such ground based data may includes ground surveying, GIS data, geophysical imaging or non-imaging data, and geochemical data. Experimental results using this fusion model are shown by Carrete [61], Karpuz *et. al.* [74], and Hutchinson [75].

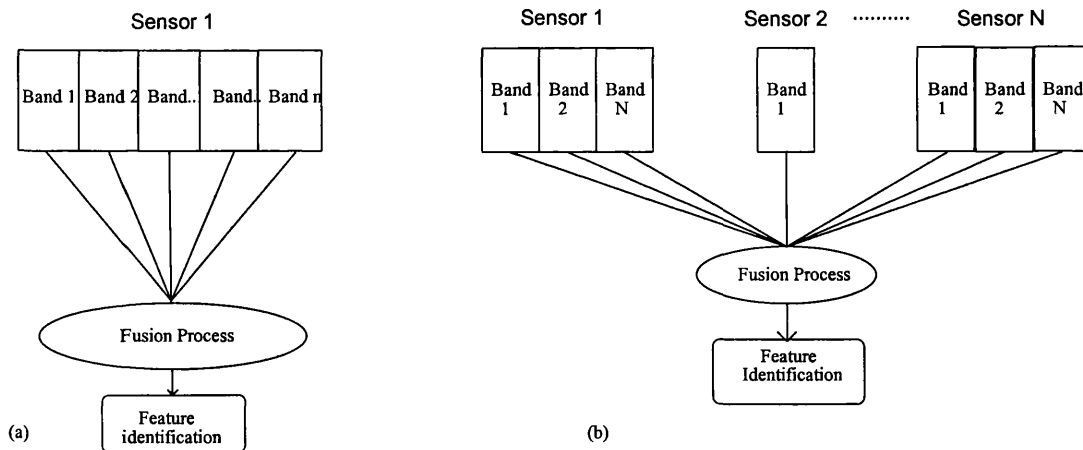


Figure 6.2. Configuration of fusion models (a) the multispectral model, (b) the multispectral / multisensor fusion model.

6.3 Background and previous work in image data fusion

A review of image data fusion literature has led to the conclusion that there are three trends in this field. The first trend involves the enhancement of patterns and objects (neglecting the patterns or objects background) either using single or colour composite image by the use of hierarchical techniques or what are called multiresolution pyramidal methods [76-80]. The second trend involves the visual enhancement of multisensor and multispectral image data sets, and finally the third trend involves classification schemes of multisensor and multispectral image data.

The aim of this work involves both of the second and third trends in image data fusion, where the two image data sets are used (Landsat-5 TM and JERS-1 SAR). These are fused for both visual interpretation and classification schemes for lithological mapping. The spatial information has been extracted previously from the SAR data and has been presented in chapter 5.

In this chapter, basic data fusion techniques previously used for visual enhancement will be discussed. A new simple technique is developed which solves the band selection/reduction problem, this technique has been modified and integrated based on the work carried out by He and Wang [62] and Wang and He [63] for textural analysis. Output results of this method are supported by qualitative and quantitative analysis. Chapter 7 will discuss the issue of data fusion through the use of image processing classification techniques.

Data fusion tools used for visual enhancement schemes have been grouped in this thesis into the following methods: data fusion by image processing colour composition, data fusion by image processing arithmetic combination, data fusion by image processing colour transforms, and data fusion using the multivariate principal component transform (PCT).

The earliest and simplest form of data fusion tool was through the production of colour composites. The colour composite is a fusion process because we combine three different image layers, either from the same sensor or from different sensors, and assign them to the primary colours of red, green, and blue. Arithmetic image combination data fusion refers to the technique of image addition, subtraction, multiplication and division between different image bands, and to combining the outputs to produce colour composites. One of the well known data fusion tools of this kind is the Brovey transform. The colour transform tool is another effective method for data fusion, because it gives flexibility to the user to take a full control over the spectral and spatial components of the fused images. Finally, the PCT data fusion tool is the most effective method [81] used for visual enhancement. The following is a literature review of data fusion methods used for visual optimisation.

Daily *et. al.* [82] were some of the pioneers who used image data fusion techniques studying surficial geologic units in Death Valley in California, using dual polarised L band airborne SAR and Landsat-2 MSS images. Firstly they co-registered the data set using tie points, and then linearly combined all Landsat MSS bands to produce one band component called the total intensity Landsat MSS image. The SAR bands of co-polarised VV and cross polarised VH were used with the total intensity image to produce a colour composite image for the final visual interpretation. They claimed that MSS and SAR data are complementary, and that MSS data cannot be used alone for rock spectral signatures because rocks are usually coated by desert varnish (staining). At that time, reasonable results were achieved in their work.

Pohle, and van Genderen [83-84] discussed the benefits and types of image fusion techniques. They investigated the appropriate fusion techniques for mapping the northern Netherlands as a calibration site, then applied the technique to map Bengkulu, Sumatra in Indonesia. They used Landsat TM, SPOT, and ERS-1 SAR data. The six bands of TM (excluding the thermal band) were transformed using the standardised principal component transform. The second and third principal components were used, and the first principal component was replaced by SPOT panchromatic 10 metre resolution band data

to enhance the spatial resolution and to preserve the spectral information of the TM data. At the same time, the ERS-1 SAR band is also used as a band replacement for the first PCT to provide the textural information of the SAR and the spectral information of the TM data. A reverse PCT procedure is then used and the output images are displayed as a fused colour composite for visual analysis. They also contributed to work carried out by Van Zuidam [85] using data fusion techniques for coastal environmental studies of the Wadden Sea in Netherlands. High resolution aerial black and white photographs, SPOT, ERS-1 SAR, and Landsat TM data were used in this study. Colour transformation from RGB to IHS was used. Image replacement was used in the intensity component (I) by another appropriate image, such as SAR and a high spatial resolution image. The output is then retransformed back to the RGB colour space and displayed as a colour composite.

Lichtenegger [86] studied the northern part of the Isle of Anglesey in the Irish Sea using the colour combination fusion technique with Seasat SAR and Landsat TM data. He linearly combined the TM visible bands and assigned their output to the green gun of the computer monitor. The Seasat SAR image was assigned to red, and the band 5 of TM was assigned to blue, producing a colour composite. He claimed that he achieved good results with his fusion technique, but with some registration mismatches between the two data sources of TM and Seasat SAR data especially in the high elevation areas due to the foreshortening effects of the SAR. He also, with other contributors [87] demonstrated the importance of data fusion technique in land use mapping in Tunisia. They used Landsat TM, MSS, SPOT HRV and Seasat SAR data, after data registration and Frost filtering of the SAR image were applied. They assigned the TM band 4 to the red gun as a vegetation information of the area of study. A linear combination of TM bands 2 and 3/2 used as optical brightness were assigned to the green gun. The Seasat SAR used for surface roughness and dielectric properties were assigned to the blue monitor gun. A colour composite was produced for visual interpretation.

Nezry *et. al.* [88] studied the tropical vegetation biomass of the Sumatra island of Indonesia, using combined remote sensing data of SIR-B L-band SAR and SPOT multispectral data. After the image to image registration process, SAR filtering was

applied using a window of 11 by 11 pixels to reduce speckle effects. The final stage of the processing was using a pattern recognition technique by combining the SAR and the optical data to classify the surface units of the study area.

Yesou *et. al.* [81] showed similar investigation work to that carried out by Pohle and van Genderen mentioned earlier; they used Seasat SAR and SPOT data to produce a geological map of Armorican massif in west France. After registration of the two image sets using around 32 tie points (GCPs), polynomial warping and Lee filtering for SAR despeckling, many fusion techniques were assessed, including PCT, fusion using linear combination, and fusion by colour IHS transform. They claimed that the linear transform fusion gives poor results, but the PCT on the 4 bands (SPOT and SAR) show good performance for visual analysis.

A traditional method of manual and visual analysis using multi-scale and multi-source of data was carried out by Raymond *et. al.* [89] by using SPOT and airborne L band 1.5 metre resolution SAR data and aerial photographs. They studied the geologic structure for oil exploration in Herault, south of France. An intensive field investigation and manual interpretation of the data using drainage pattern analysis and multi-scale imagery was performed. Their method of study led to a discovery of hidden faults in the study area.

Rothery *et. al.* [90] and Rothery [91] studied the geology of the Socompa volcano in north Chile. They used Landsat TM, and the MOMS-1 20 metre resolution optical instrument flown on STS 11 mission of the Space Shuttle in 1983. The optical MOMS-1 data acquired at low solar elevation angle shows enhanced textural information as a result of shadow effects. The TM data was used for good rock discrimination. Utilising information from both sensors, they co-registered the data set for fusion techniques after sampling the MOMS-1 data to 30 metre resolution and using 20 tie points for a first order polynomial transform. Three methods of data fusion for visual enhancement were tested in their work. The first method was performing PCT on the TM bands 4, 5, and 7 and the first PC image was set to a uniform value (i.e. 90), then a reverse PCT was used. The new

output images were then multiplied by the MOMS band and colour composite has been produced. The second and third method are fusion using the colour transform of the colour models RGB-IHS, and RGB-YIQ respectively. The I and Y images were set to uniform values then a reverse procedure has been performed to achieve RGB images without spatial information. The spatial information was then added to the RGB images by multiplying them with the MOMS-1 image. The results of the three methods show very good enhancement for visual analysis. A detailed study of MOMS-1 and comparison of this instrument with TM and SPOT has been shown by Henkel *et. al.* [92].

Franklen *et. al.* [93] fused image data from the same sensor of SPOT HRV (multispectral 3 bands 20 metre resolution and single band panchromatic 10 metre) to achieve higher spatial resolution of the multispectral data. A 9% improvement on the classification accuracy of vegetation communities in Southwest Yukon in Canada has been achieved by the use of PCT, colour transform, and regression between the panchromatic and the multispectral data. In their study, they show that only 56% classification accuracy was achieved with colour composition. A 54% classification accuracy was achieved by using regression between the panchromatic band and the 3 multispectral bands. Fusing using the PCT achieved 59%, and finally 65% accuracy if the colour transform RGB-IHS algorithm is used.

Geological mapping of the northwest of Aswan in Egypt was shown by Rast [94] using data fusion of SIR-A SAR and Landsat MSS after co-registration between the two image data sets. Previous geological maps were also used as ground truth data. Two fusion techniques are used through colour transform and linear combination between the MSS bands. In his first approach he combined the information of ratioing the MSS bands of 4/5 as a hue component, 6/7 as a saturation component and the SIR-A SAR as the intensity component and then displayed them as colour composites. The second approach involved is using the hue and saturation component of the transformed MSS colour composite. The intensity component is the SAR image. In his work he showed an improved application of radar and optical data for geoscientific mapping.

Paris and Kwong [95] studied the effectiveness of combining Landsat TM and SIR-B L-band SAR data to study the vegetation biomass of Fresno County in California. The data was co-registered using normal tie points. A linear progressive transformation was applied on the data to quantitatively extract percent ground cover of green vegetation of their study area.

Forest type discrimination has also been studied by Leckie [96] using data fusion techniques of a test site near Chalk river, Ontario, Canada. The data used are 8 dual bands of airborne X and C- SAR bands. The visible and near-infrared data were also acquired for the study area using an airborne 9 band Daedalus scanner. Median filtering was applied on SAR data to reduce speckle. The SAR and optical data were then co-registered using third order polynomial transform with a 33 tie points. Spectral signatures of vegetation classes have been achieved because of the amount of data used (8 SAR bands and 9 optical bands). Fusion has been achieved using Maximum likelihood classification of the data sets with accuracy of 74 percent.

As the fusion technique can improve the spatial resolution integrity, Cliché *et. al.* [97] used a linear combination fusion algorithm between SPOT HRV panchromatic and multispectral modes. The results of their processing were similar to those of high resolution colour infra-red airphotos. Chavez [98] used a similar fusion technique and applied it between 4 metre spatial resolution panchromatic digitised aerial photographs and Landsat TM satellite images. The technique is to firstly geometrically duplicate TM pixels 7 times (expand every TM pixel 7 times in the x and y directions) and then the expanded image is smoothed to remove the blocky pattern. The second step is image co-registration between both data sets. The fusion is then accomplished by using linear combination between the digitised aerial photograph and every single band of TM. Images are then displayed as colour composites. Welch *et. al.* [99] also showed similar results in their fusion technique between SPOT multispectral data and Landsat TM data. City of Atlanta TM and SPOT images were chosen for the demonstration. After co-registration between the data set, a linear combination between bands was used for

fusion. They claimed that if both spatial and spectral information is needed, a better fusion approach is to use the RGB-IHS colour transform fusion algorithm.

Chavez [100] compared and presented the results of the three methods of image data fusion using TM and SPOT panchromatic data using south of Phoenix, Arizona as a test site. The aim of the fusion was to gain higher spatial resolution of the TM data from the SPOT PAN image while preserving the spectral information of the TM data. Firstly the TM data has been enlarged 3 times to geometrically match the SPOT PAN data and low pass filtered to eliminate the blockiness introduced by the enlargement process. Registration between the two data sets was then performed using the PAN as a reference image. The three fusion methods used for comparisons were the PCT, the colour transform of RGB-IHS, and the arithmetic combination method (the PAN data is high pass filtered then added pixel by pixel to the TM bands). The comparison results show that the arithmetic method is much better because it does not distort the original spectral information of the TM data.

Evans *et. al.* [51] evaluated the polarimetric L-band airborne SAR imagery for geologic and vegetation mapping in many areas including Death Valley in California, the Wind River Basin in central Wyoming, and the coastal plain in western South Carolina. Colour composites were used for visual analysis. They showed that the like-polarised H-H returns are most sensitive to the rough surfaces resulted from the spatial frequency corresponding to the Bragg resonant. The cross-polarised H-V or V-H returns mostly resulted from surface multiple scatterers and subsurface volume scatterers. They superimposed the SAR bands (HH, VV, HV) and produced colour composites ready for visual interpretation in mapping applications. Evans [101] also used many colour composites of imagery data of TM, TIRS data (6 thermal imaging channels), and L-band polarimetric airborne SAR studying sedimentary rocks of Deadman Butte in Wyoming, USA. The parallelepiped classifier algorithm was also used for the mapping.

The parallelepiped classifier algorithm was also implemented by Haack *et. al.* [102] on the Landsat TM and SIR-B SAR data to locate villages along the Blue Nile in Sudan. The

SAR data was found to be very powerful for locating villages because of the high dielectric properties and the geometrical shapes of man made features. 94.1 % accuracy has been achieved in the mapping.

A fusion technique between SIR-B SAR and Landsat-5 TM data was also used by Welch *et. al.* [103] for cartographic feature extraction of the coastal plain of Georgia. Both of their image data sets are registered to topographic maps. The SAR data is then co-registered to the TM data using polynomials of 1-3 orders. In their fusion approach, they tested all known fusion procedures and found the best results were achieved by using colour transform (IHS-RGB). SAR data was modulated as saturation, TM band-3 for hue, and TM band-4 modulated as intensity. They selected TM band 3 and 4 because of their high signal to noise ratio. Transformation of the IHS to RGB of the data showed that the micro-relief had been enhanced. Several non-linear spatial operators (filters) were also applied on the SIR-B SAR data to extract lines and edges in this work.

Munehika *et. al.* [104] have revised the technique of data fusion. A good historical review of data fusion techniques was also provided in their work. They categorised the aims of merging (fusion) as for display, manipulation of spatial information and to maintain radiometric integrity. The merging technique they used is particularly similar to that used by Chavez [98]. They used high spatial resolution panchromatic SPOT data and fused it with TM data to increase the spatial resolution of the TM. They claimed that the technique they used increased the TM interpretability and the classification accuracy.

Toll [105] studied the possibility of using Seasat SAR and Landsat MSS data for regional land-use and land-cover mapping of the eastern fringe area of Denver, Colorado. After co-registration using 50 ground control points and cubic resampling for the warping, the spectral signature of different classes has been evaluated in the study and a linear discriminant classification technique is used.

Carper *et. al.* [106] studied data fusion technique using the colour transform technique. In their study they used SPOT panchromatic and multispectral data as input aimed to

increase the spatial resolution of the multispectral data from 20 to 10 metres and preserve the original colour appearance. They showed that the replacement image (the panchromatic) should be correlated to the intensity component of the multispectral data otherwise subtle intensity differences may be obscured.

Grasso [107] showed the significance of fusion technique for thematic mapping and geologic mapping in particular. He demonstrated the impact of digital image processing upon remote sensing geologists and compared the recent developments with the traditional methods of using aerial photographs for geological mapping. In his work, he claimed that the aerial photographs still play an important role in the field of geology because of their high spatial resolution which is not revealed by satellites such as Landsat TM data. From this point of view, data fusion is the best method for extracting both spatial and spectral information between aerial photographs and Landsat TM images. The colour transform fusion method is shown to be the best method for geologic application purposes. Registration accuracy between the two data sets is very important and any error in the co-registration will lead to mismatch between the spectral and spatial information during the IHS transformation.

The IHS method of merging has been studied extensively as a merging method for imagery data from different sources. Daily [108], for example, implemented this method for a single Seasat SAR image using filtering and colour transform to produce colour composite image. Harries [109] used this method as a good integration method of SAR data with other data including geophysical, thematic, and other radar data. Also the IHS method has been used as a good fusion method with colour shaded or colour thematic maps with imagery data [110].

Vrabel [111] used many known methods of data fusion including two new approaches to increase the spatial image resolution using optical airborne data. In the study, the new algorithms which include the colour normalisation (CN) technique (i.e. similar to the

Brovey transform fusion method) and Sparkle method¹ were used and compared. Results show both of which performed significantly better than IHS or arithmetic transforms.

6.4 The colour composite band selection/reduction problem - A new solution

From the literature review given in the previous section, it is now clear that maximum visual enhancement is achieved by the use of colour composite. Three bands are firstly selected and then transformed using the image data fusion tools (i.e. image processing techniques) with either the colour transform, PCT, or arithmetic procedure then an other image component (SAR, SPOT PAN, or digitised airphoto.) is introduced during the transformation process. The procedure relies on the manipulation of the spectral information gained by the original three bands selected from the original image set. The induced fourth band represents the spatial and textural information where each is brought together after the transformation procedure and displayed for visual interpretation.

The above procedure will not make any confusion about the selection if the spectral data set consists only of three image bands such the case of SPOT multispectral data because the whole image data set will be used. If the case is more than three spectral bands, a problem will arise on the band selection and the user will argue for which bands should be used as the basic spectral information.

The colour composite band selection issue has been mentioned in the introduction of chapter one as a description of the problems in attaining the goal of this thesis. In this section, this problem will be discussed in detail and a new solution is introduced in the next section (section 6.5).

Suppose theoretically we have an image set that consists of four spectral bands, where every band consists of a pronounced spectral feature (i.e. class) as shown in figure 6.3. To select a colour composite from these four bands for visual assessment there are two

¹ The Sparkle algorithm is a proprietary algorithm developed by the Environmental Research Institute of Michigan (ERIM). There is no detailed explanation about it in Verbel's work.

problems. The first is that there are four groups of band combinations (Appendix A-1) for producing the colour composite. Secondly, a serious problem is that any band combination method will cause one of the spectral features (class) to be missing when the colour composite is displayed. Practically, such theoretical assumption of the images set shown in figure 6.3 may not occur in real life remote sensing images, but definitely occurs as a less recognition (visually and/or automated) of some of the classes during the colour composite band combination selection scheme.

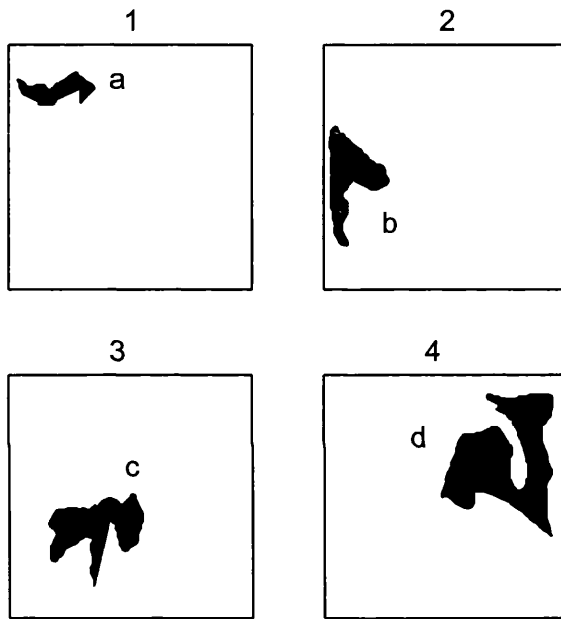


Figure 6.3 A theoretical image set consists of four bands, band-1 shows clear feature (class-a), band-2 shows feature b, band-3 shows feature c, and band-4 shows feature d.

The problem of band selection for colour composite production has been raised previously by Chavez *et. al.* [112], Sheffield *et. al.* [113] and Liu *et. al.* [114] and can be solved statistically by the correlation between the image bands (Appendix A-3). Another method is the use of the transformed divergence separability test, which is believed to give reasonable results for both visual and automated assessments [115], but its drawback is it works only with pair of classes and hence every class pair may have different band combination. This is shown in the separability test tables throughout this thesis and in section 6.6 in particular.

Referring back to the assumed theoretical image set in figure 6.3, any suggested method using the works of [112-115] will not give useful results because one spectral information of a feature or class will not be present in the selected colour composite, whatever the selection is. If the statistical method of selection is used in such theoretical example, the optimum selection will be bands 2, 3, and 4 because the correlation between these bands is the lowest. Band 1 will be the lowest rank for combination selection because the spectral feature in band 1 is spatially smaller compared with other features in band 2, 3, and 4. This is because the correlation is taken between bands as whole (the whole image pixels are used), and hence such methods are image dependent which is another drawback.

Solutions such as arithmetic image combination, PCT between bands, or even colour transform are available to the user for displaying such data sets and producing a colour composite. If such an approaches are used, the following have to be taken in account:-

- 1- The band arithmetic may produce a new data set in addition to the original data. Furthermore, the spectral information of the new data set, may be altered, modified, or changed from the original.
- 2- The PCT procedure will not give good results if the original data are not highly correlated¹ [116], because some spectral information will be found in the lower spectral component images. Also if the original data are highly correlated, difficulty in visual analysis results from colour saturation and distortion of the output data.
- 3- A colour transform cannot be implemented if more than 3 bands are used, unless the procedure is done repeatedly, good results may not be guaranteed.

If the image data set consists of more than 4 spectral bands, such as the case of this thesis work, the situation becomes difficult and solution of this problem is important. The spectral information of every feature must be extracted within every image to produce only three new images that can be displayed and assessed. These new images can be used

¹ If data is not correlated, PCT should not be used because PCT is a decorrelation procedure and PCT in this case has no meaning.

as a basis for fusion such as introducing spatial or textural information. The new suggested method of solving this problem is shown in the next section.

6.5 Using the spectral unit as a method of TM spectral coding

It has been mentioned in chapter 5 (p.124) that He and Wang [62] and Wang and He [63] developed a method of textural measure, which is based on a simple algorithm named the “texture unit” to extract the texture spectra. An approach has been developed for the first time in this thesis adopting the same logic of He and Wang’s work with some modification to extract the TM spectral units as a coding method of the six TM bands. The algorithm is shown as follows:

Let the spectral unit number of every pixel vector in n bands be limited by the three values 0.0, 0.5, or 1.0 based on the test of this pixel vector value with its vector mean such as:

$$UP_{x,y,i} = \begin{cases} 0.0 & \text{if } x_{x,y,i} < \mu_{x,y,i} \\ 0.5 & \text{if } x_{x,y,i} = \mu_{x,y,i} \\ 1.0 & \text{if } x_{x,y,i} > \mu_{x,y,i} \end{cases} \quad (6.2)$$

where:

$UP_{x,y,i}$ = the spectral unit number of pixel at location x and y , in the band number i where $i=1,2,\dots,N$.

$\mu_{x,y,i}$ = the mean vector reflectance of the same pixel location. It is equal to

$$\frac{1}{N} \sum_{i=1}^N BV_i, \text{ and } BV_i \text{ is the brightness value of the pixel at band } i.$$

Because $UP_{x,y,i}$ has three possible unit values (i.e. 0.0, 0.5, or 1.0), the number of possible codes in total are 3^N (i.e. 729 code for TM data). To code this pixel vector (its spectral code) the following equation is used:

$$Spectral \ code = \frac{1}{S} \sum_{i=1}^N UP_{x,y,i} \times 3^{i-1} \quad (6.3)$$

where:

S is a scaling factor

In this work, the scaling factor is used to ensure the output TM spectral coded image does not exceed 8-bits. But at this step, it is recommended not to use the scaling factor and left to equal unity (i.e. $S=1$). Scaling can be used after creating the spectral coded image using equations 6.2 and 6.3, and the output spectral coded is stored in 32 bit image file.

To simplify the process, table 6.1 shows a numerical example of the method of coding applied on 10 pixel vectors of TM bands 1-5, and 7 noting that the mean of every pixel vector has been set to an integer value.

Pixel No.	B1	B2	B3	B4	B5	B7	μ_i	UP_1	UP_2	UP_3	UP_4	UP_5	UP_6	Scode
1	99	112	115	121	137	109	115	0	0	0.5	1	1	0	112.5
2	55	39	61	66	87	92	67	0	0	0	0	1	1	324
3	30	157	79	104	121	144	106	0	1	0	0	1	1	327
4	0	0	0	0	0	0	0	0.5	0.5	0.5	0.5	0.5	0.5	182
5	181	181	181	181	181	181	181	0.5	0.5	0.5	0.5	0.5	0.5	182
6	0	42	84	126	168	210	105	0	0	0	1	1	1	351
7	210	186	126	84	42	0	105	1	1	1	0	0	0	13
8	255	0	0	0	0	0	255	0.5	0	0	0	0	0	0.5
9	0	130	135	140	145	150	91	0	1	1	1	1	1	363
10	0	100	135	225	170	170	138	0	0	0	1	1	1	351

Table 6.1. A numerical example of applying the spectral coding method.

6.5.1 Properties of the spectral coding algorithm

- 1- Referring back to the numerical example shown in table 6.1, it has been pointed out (in theory) the maximum number of codes is 729 numerical values. Practically, such

number of combinations cannot be achieved because the minimum code value is 0.5 and the maximum value is 363 (i.e. pixel number 8 and 9 respectively). This results in 727 combinations (i.e. $(364 \times 2) - 1$).

- 2- Another important property in the spectral coding method is that similar spectral shapes have similar spectral code values; this is shown in pixels number 4 and 5 in the numerical example in table 6.1, where pixels with different topographic-albedo information have the same code number.
- 3- A proper atmospheric correction method should be used to ensure all shadow pixels have the code number 182 (i.e. pixel number 4). If a loose method of atmospheric correction is used or the data is over corrected, shadow pixels may bias from the code number 182 and hence show different spectral class code. For that reason the dark-pixel subtraction method is used in this work (shown in 4.3) to ensure the data is atmospheric corrected properly.
- 4- Pixels of albedo-topographic information and shadow pixels have similar spectral code number, and hence the output spectral coded image has no topographic information, this is because $\mu_{x,y,i}$ is used in equation 6.2.
- 5- The spectral coding method adopted here is sensitive to any biased pixels (i.e. noise). Such spectral code may coincide with other spectral code; this is shown in pixel vector 6 and 10 where pixel vector number 10 has noise in band 1 (zero) and band 4 (255).
- 6- There is no hardware that can display more than 8-bit image in one graphic plane card. Hence, if the data is not scaled (which is desired) but viewed in the computer screen, it will automatically be scaled to 8-bit resulting of the mixing of some spectral coded pixels which visually results in the loss of some spectral information.
- 7- To find the S value for scaling to 8-bit image (equation 6.3), one method is setting $S = 1.42$ (i.e. $363/255$) but this method may result in the loss of coding. With minimum

loss of information, one method can be proceeded by producing the spectral code image and storing it in 32 bit image file, then subtracting the spectral coded image from its minimum code value (i.e. shifting the spectral coded image histogram to zero value), then calculating the maximum code value and dividing it by 255 and finally, rounding off the output and saving it in 8 bit image.

- 8- The more bands used, the wider range of coding, reflecting reasonable results. This is based on the rule 3^N where N is the number of bands. For example coding the 6 TM bands is more appropriate than coding SPOT multispectral 3 bands.

6.5.2 Procedure of producing the spectral coded image

The following is the procedure of producing the spectral coded TM image:-

- 1- stretch the optical TM images to occupy the intensity range value (0-255) using BCET. BCET is used to make sure the bands used are equally stretched in mean, minimum, and maximum.
- 2- calculate the mean image using the 6 TM bands. Real numbers should be rounded off to integer values. The mean image is named in this work the albedo-topographic information image.
- 3- create a six floating point numerical variable (i.e. $a_1, a_2, a_3, \dots, a_6$) to calculate and store the spectral unit numbers UP_1, UP_2, \dots, UP_6 using equation 6.2.
- 4- create the spectral coded image using equation 6.3 and assign the output to 32 bit output image.
- 5- convolve the spectral coded image by using the mode filter (either 3x3 or 5x5) to neglect biased coded pixels (spectrally contaminated pixels) which are geographically located within the same coded class or window.

6- scale (if desired) the image produced by step 4 to an 8-bit image.

6.5.3 Results of using the spectral coded image of TM data and creating colour composite

Figure 6.4 shows the TM spectral coded image after scaling. The image is displayed in grey scale. Spectral pseudo-colour coded image is also displayed and shown in figures 6.5. The spectrally TM pseudo-colour coded image can be evaluated visually after assigning every specific pixel's intensity values to a specific colour for an easy and quick visual assessment. The drawback may result from the high number of spectral coded classes. Figure 6.5 shows the spectral pseudo-colour coded image with 158 class. The number of classes have been calculated from the image histogram.

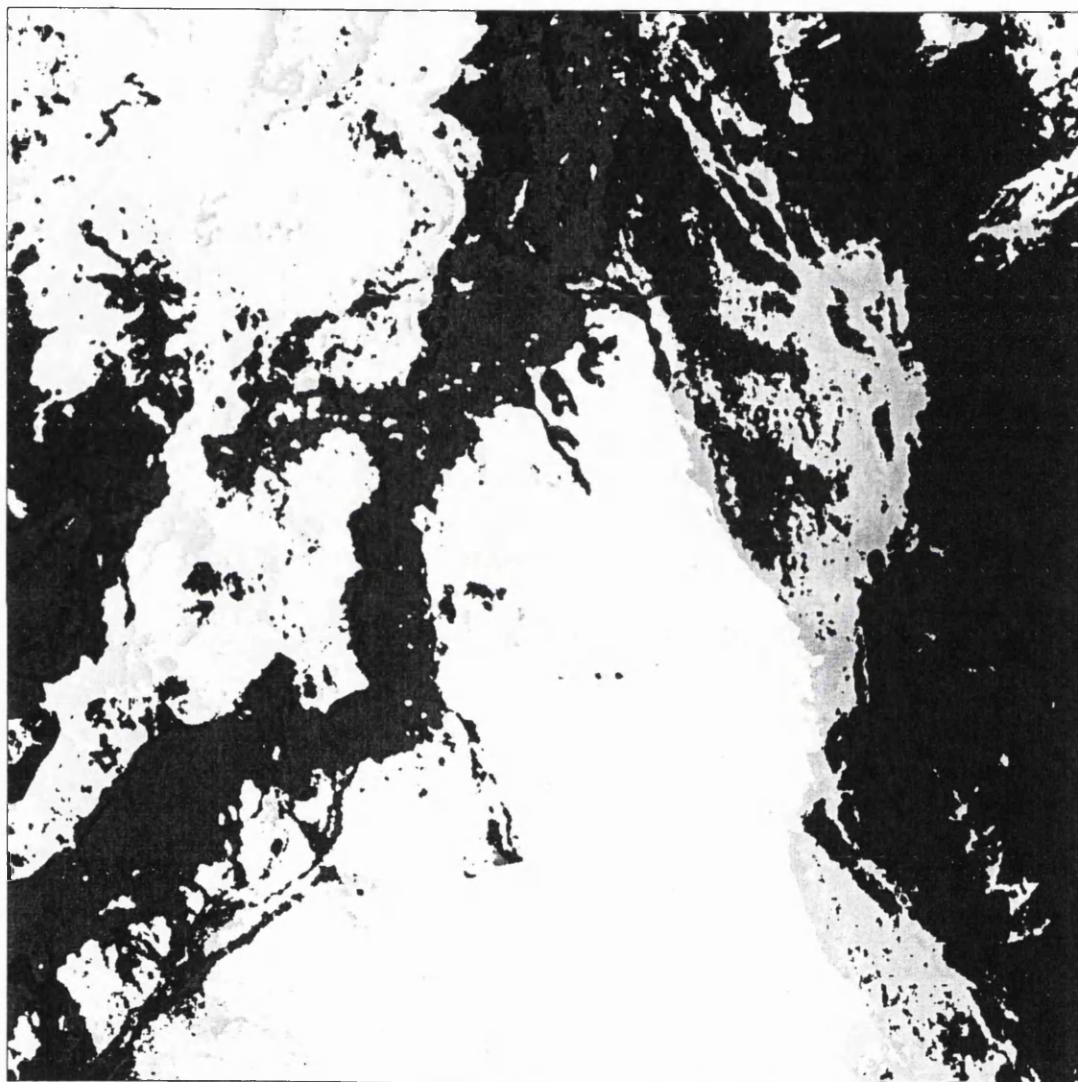


Figure 6.4 A grey scaled TM spectral coded image after applying 5x5mode filter and scaled to 8-bit.

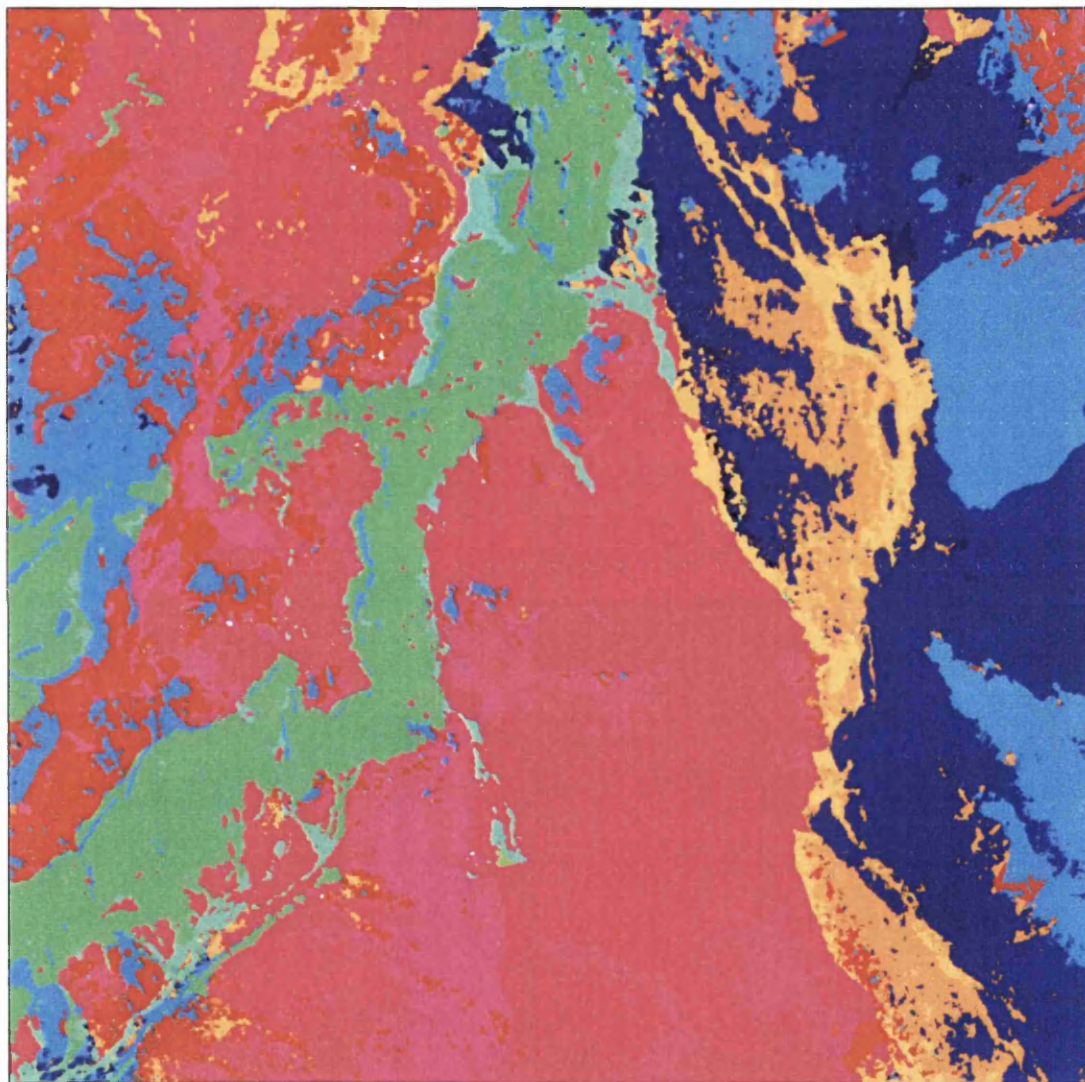


Figure 6.5. Pseudo-colour coded image of the spectral coding of the 6 TM image data.

The classes separability analysis (represented by class ellipsoids) using both of the spectral coded image and the albedo-topography information image shows a promising result, which is shown in figure 6.6, in which every class ellipsoid² shows good separability.

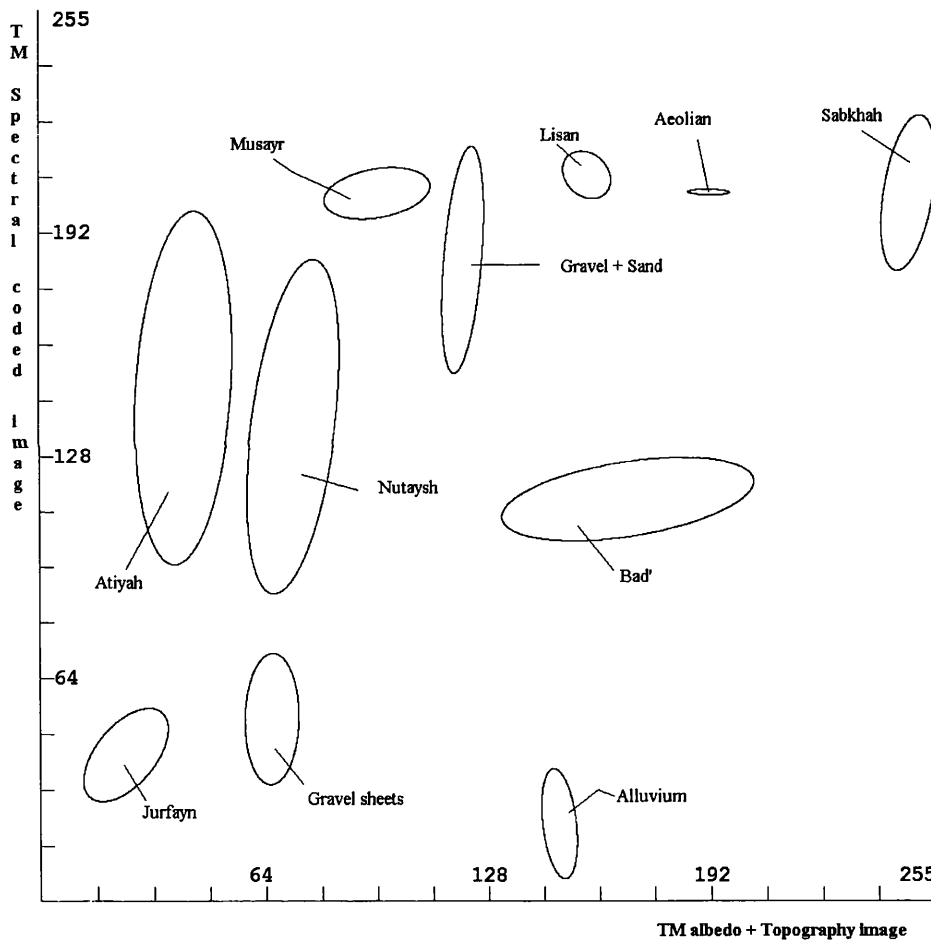


Figure 6.6 Class ellipsoids of the test site using the TM spectral coded image plotted on the abscissa and the TM albedo and topographic information image plotted in the ordinate.

² Class ellipsoids is a graphical representation of separability. They can be drawn using the covariance matrices and the eigenvectors of the classes. The eigenvectors and values of the inverse covariance matrix of classes define the direction and length of the major and minor ellipse axes.

To produce a colour composite image using the spectral coding technique, pixels in this case are represented by the three measures of: the spectral coded; the albedo-topographic image (which is an important property of photointerpretation and in the same time to compensate the loss of such property during the coding process); and finally, the maximum-minimum (range) of the pixel vector spectra. This is to ensure every pixel vector in a specific class is represented in a more accurate way and does not coincide with pixel from different class. Such representation is shown graphically in figure 6.7.

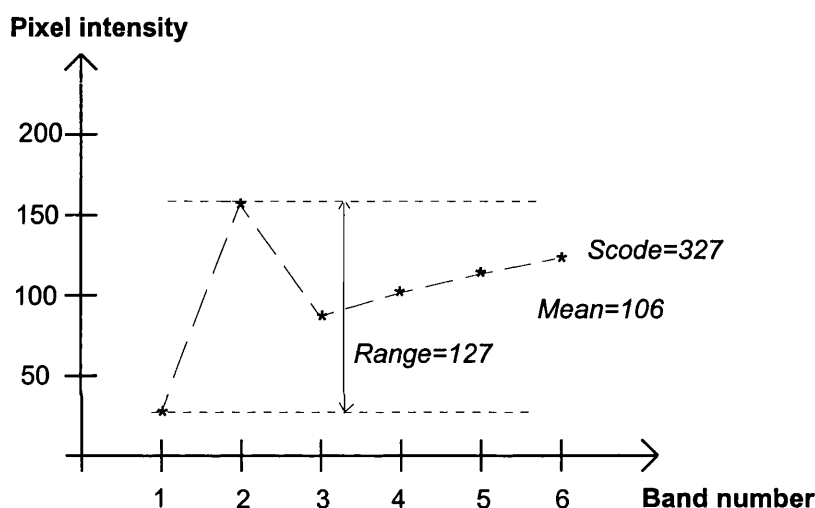


Figure 6.7 Representing a pixel vector of colour composite using the spectral code value, the albedo-topographic information, and the range value. Pixel number 3 in table 6.1 is taken for the representation.

Such representation of every pixel in the TM data is shown in the spectral coding colour composite of the test site in figure 6.8: where red is assigned to the spectral coded image; green assigned to albedo and topographic information image; and finally blue is assigned to the range image. Such method is adopted in this thesis for the first time to ensure a better presentation of every pixel vector (i.e. pixel is presented by its code, mean, and range). This is to compensate any uncertainty or data loss. The separability measure between the class pairs in the spectral coded colour composite shows an amassed results, this is shown in table 6.2, where all classes are perfectly separable (with the exception of

Atiyah-Nutaysh). Comparison of this technique shown in table 6.2 with the original 6 TM image data (after being BCET stretched) shown in table 6.3 is almost the same with minor variations. For example average separability using the new method is 1.99001, minimum is 1.46412. and maximum is 2.0, and conversely in the separability test using all the TM image data, the minimum is 1.69744 which is better but still these two classes are poorly or inseparable, the mean separability is 1.99294, and finally the maximum separability is 2.0.

Class	Jurfayn	Atiyah	Musayr	Nutaysh	Bad'	Lisan	Conglo.+ Gravel	Gravel Sheets	Sabkhah	Alluvium
Atiyah	200000	-	-	-	-	-	-	-	-	-
Musayr	200000	200000	-	-	-	-	-	-	-	-
Nutaysh	200000	1.46412	200000	-	-	-	-	-	-	-
Bad'	200000	200000	200000	200000	-	-	-	-	-	-
Lisan	200000	200000	1.99999	200000	200000	-	-	-	-	-
Conglo.+Gravel	200000	200000	200000	1.99891	200000	200000	-	-	-	-
Gravel Sheets	199087	200000	200000	200000	200000	200000	200000	-	-	-
Sabkhah	200000	200000	200000	200000	200000	200000	200000	200000	-	-
Alluvium	200000	200000	200000	200000	1.99676	200000	200000	200000	200000	-
Aeolian silt+sand	200000	200000	200000	200000	200000	200000	200000	200000	200000	200000

Table 6.2 The Transformed divergence separability test of class pairs of the training areas using the TM spectral coded colour composite image data (Albedo-topographic image and the range image are automatically stretched).

	Jurfayn	Atiyah	Musayr	Nutaysh	Bad'	Lisan	Conglo.+ Gravel	Gravel sheets	Sabkhah	Alluvium
Atiyah	1.97011	-	-	-	-	-	-	-	-	-
Musayr	200000	1.99994	-	-	-	-	-	-	-	-
Nutaysh	1.99997	1.69744	1.96753	-	-	-	-	-	-	-
Bad'	200000	200000	200000	200000	-	-	-	-	-	-
Lisan	200000	1.99998	1.99999	200000	200000	-	-	-	-	-
Conglo.+ Gravel	200000	200000	200000	1.99906	200000	1.99860	-	-	-	-
Gravel sheets	1.99874	1.99942	200000	1.98199	200000	200000	200000	-	-	-
Sabkhah	200000	200000	200000	200000	200000	200000	200000	200000	-	-
Alluvium	200000	200000	200000	200000	200000	200000	200000	200000	200000	-
Aeolian silt+sand	200000	200000	200000	200000	200000	1.99938	200000	200000	200000	200000

Table 6.3 Transformed divergence separability test using all TM bands (1-5,7) between the training areas of the test site. BCET is applied firstly on the image data

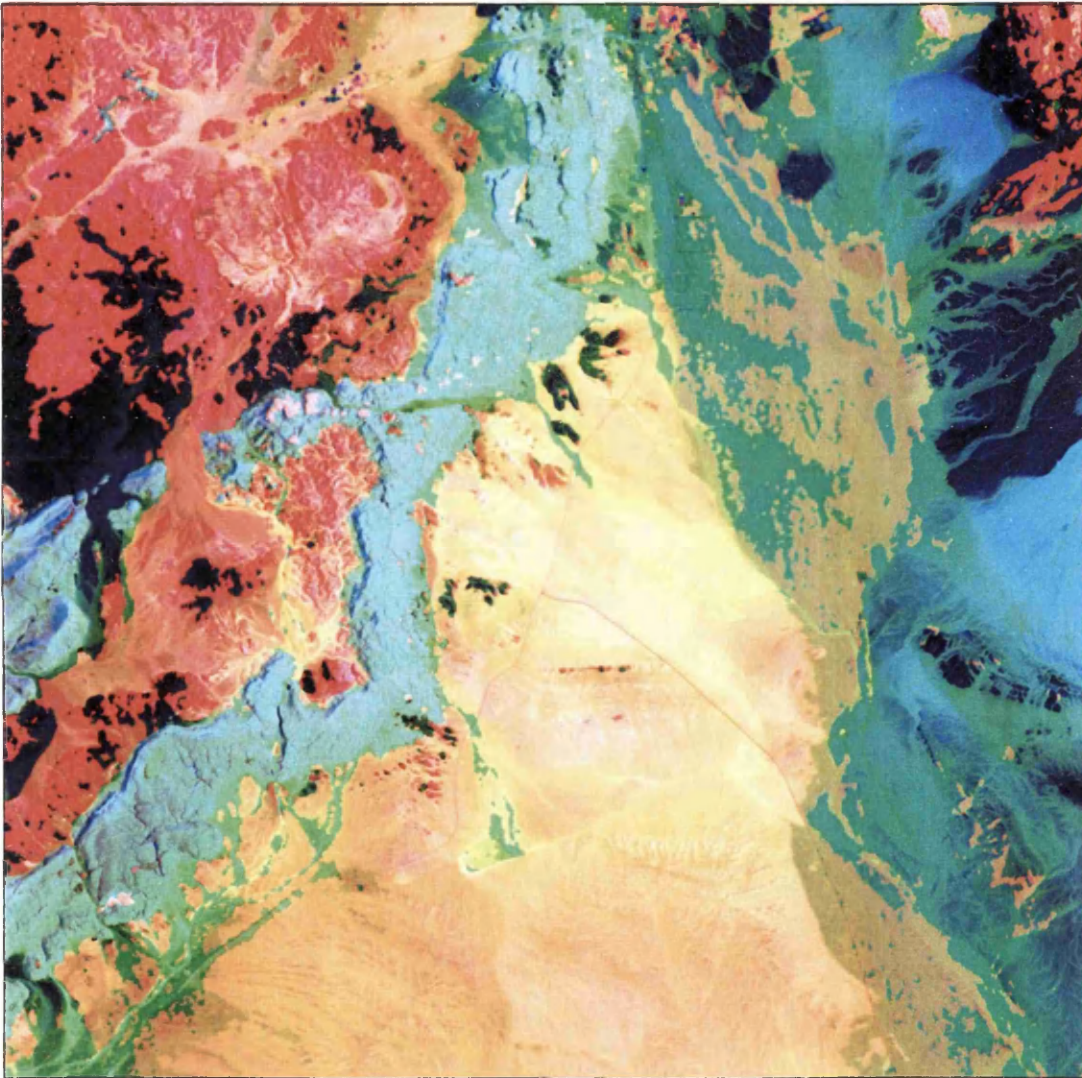


Figure 6.8 a colour composite using spectral code of the 6 TM bands, the albedo-topographic image, and the range image displayed in red, green, and blue respectively. Automatic stretching has been applied on the green and blue bands only.

6.6 Comparison between the spectral coded colour composite and the traditional methods of colour composite selection

In this section, a random set of colour composites of the test area are displayed, compared visually and quantitatively assessed, and in addition the best colour composite selection is examined using the methods discussed earlier using Chavez *et. al.* [112], Sheffield *et. al.* [113], and Liu *et. al.* [114] after being contrast enhanced using the BCET developed by Liu [43,114] to ensure no colour bias occur between the displayed bands. From the covariance matrix of the six TM bands used (shown in appendix B-1), the following in table 6.4 shows the first best two ranks of bands combination and the last (worst) bands combination for colour composites. The full ranking of the colour composite bands combination table is shown in appendix B-2.

Rank	Determinant	Band comb.	OIF	Bands comb.	IOBS	Band comb.
1	550945300	1,5,7	60.555	1,5,7	0.660283	1,5,7
2	517319600	2,5,7	54.450	2,5,7	0.696099	1,4,7
...
20	2039992	2,3,4	39.309	2,3,4	0.963189	2,3,4

Table 6.4 The first, second, and worst bands combination of the six TM bands after applying BCET.

In the case of colour composite of TM bands 3,2, and 1 displayed in red, green, and blue respectively (natural colour composite) shown in figure 6.9, some of the rock units are distinguishable. These rock classes are: Jurfayn (dark bluish-green); Atiyah (brown); and Bad' formation (creamy whitish in colour), and finally the Sabkhah (white). Separability measure using these three bands is shown in table 6.5 with minimum separability 0.68844, average separability 1.93057, and maximum separability is 2.0. Quantitatively, eight of the classes pairs using this colour composite combination are poorly to inseparable (i.e. pairs less than 1.9).

Class	Jurfayn	Atiyah	Musayr	Nutaysh	Bad'	Lisan	Conglo.+ Gravel	Gravel Sheets	Sabkhah	Alluvium
Atiyah	1.7081	-	-	-	-	-	-	-	-	-
Musayr	1.77180	1.92826	-	-	-	-	-	-	-	-
Nutaysh	1.71503	1.76086	0.68844	-	-	-	-	-	-	-
Bad'	1.99980	1.99991	1.98191	1.99584	-	-	-	-	-	-
Lisan	2.00000	2.00000	1.99999	2.00000	1.99878	-	-	-	-	-
Conglo. +Gravel	2.00000	2.00000	1.97632	1.99828	1.99997	1.91921	-	-	-	-
Gravel Sheets	1.81597	1.99296	1.23188	1.73032	1.99999	2.00000	1.99868	-	-	-
Sabkhah	2.00000	2.00000	2.00000	2.00000	1.99061	2.0000	2.00000	2.00000	-	-
Alluvium	2.00000	2.00000	2.00000	2.00000	1.99998	1.99412	2.00000	2.00000	2.00000	-
Aeolian silt+sand	2.00000	2.00000	2.00000	2.00000	1.98818	1.99856	2.00000	2.00000	2.00000	1.99716

Table 6.5 Separability measure of the lithologic classes using bands combination 3,2,1 of the TM image data. Data are BCET stretched.

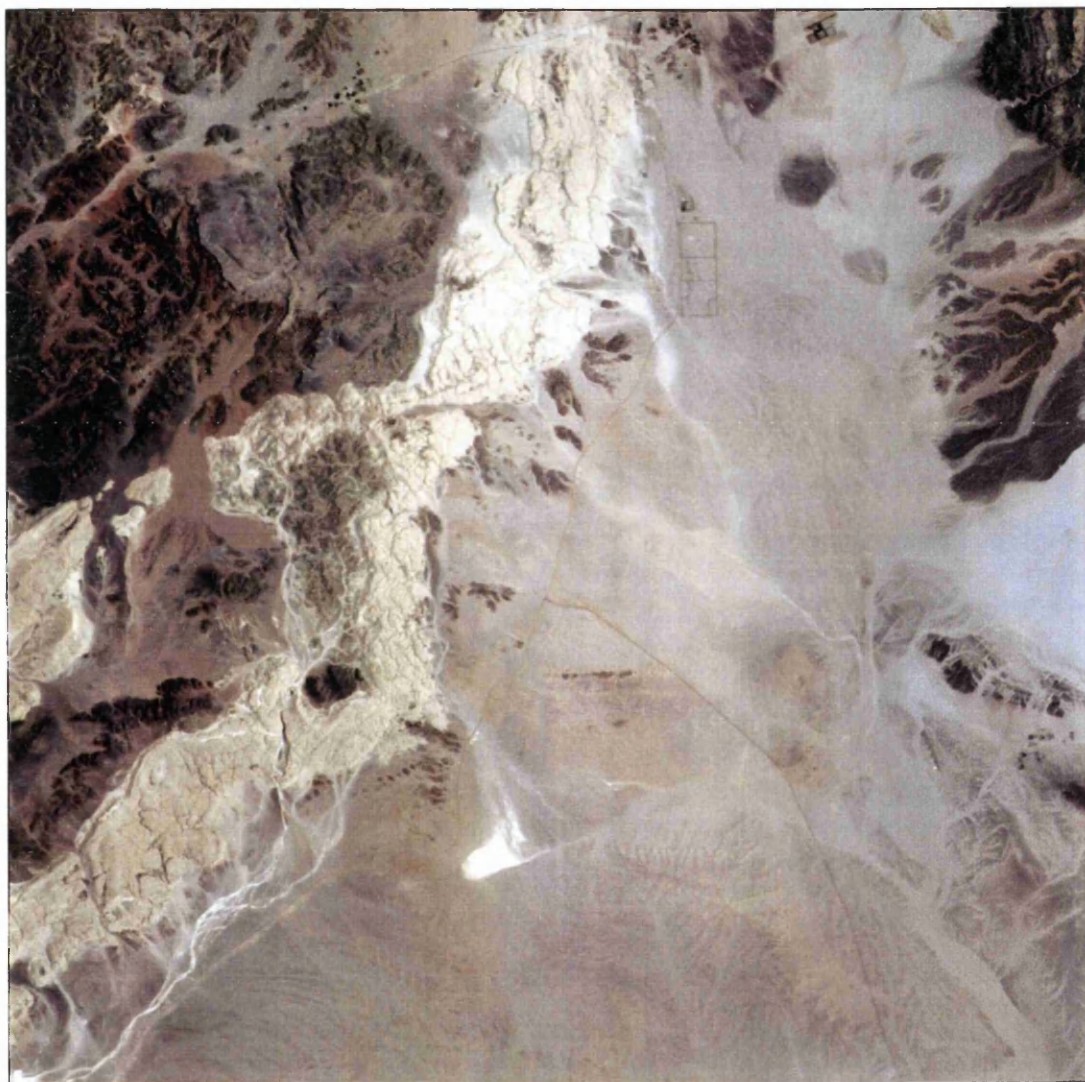


Figure 6.9. Colour composite of TM bands 3, 2, and 1 displayed in red, green, and blue respectively. Data is firstly BCET stretched.

Using a combination of TM bands 4,3, and 2 (as the lowest rank of bands combination) displayed in red, green, and blue respectively as shown in figure 6.10, do not visually show much differences from 3,2, and 1 bands combination for lithological point of view. It shows only clear vegetation farms (palm trees found during the field visit) in the upper part of the image. Quantitatively and by the use of the separability test of lithological classes pairs as shown in table 6.6, the minimum separability is 1.10912, the average separability is 1.94607, and the maximum separability is 2.0. Some improvement of separability has been achieved using this band combination compared with the natural colour band combination, but still there are seven pair of classes which are poorly separable.

Class	Jurfayn	Atiyah	Musayr	Nutaysh	Bad'	Lisan	Conglo.+ Gravel	Gravel Sheets	Sabkhah	Alluvium
Atiyah	1.83494	-	-	-	-	-	-	-	-	-
Musayr	1.96549	1.92757	-	-	-	-	-	-	-	-
Nutaysh	1.78885	1.79328	1.10912	-	-	-	-	-	-	-
Bad'	1.99999	1.99940	1.96141	1.99460	-	-	-	-	-	-
Lisan	2.00000	2.00000	1.99989	2.00000	1.99878	-	-	-	-	-
Conglo. +Gravel	2.00000	2.00000	1.96720	1.98927	1.99998	1.97466	-	-	-	-
Gravel Sheets	1.77548	1.98616	1.88288	1.13811	2.00000	2.00000	1.99973	-	-	-
Sabkhah	2.00000	2.00000	2.00000	2.00000	1.99361	2.00000	2.00000	2.00000	-	-
Alluvium	2.00000	2.00000	2.00000	2.00000	1.99999	1.99999	1.99997	2.00000	2.00000	-
Aeolian silt+sand	2.00000	2.00000	2.00000	2.00000	1.95579	1.99793	2.00000	2.00000	2.00000	1.99998

Table 6.6. Separability measures between class pairs of the test site using the bands combination 4,3, and 2 of TM data. BCET is firstly applied.



Figure 6.10 Colour composite using bands 4, 3, and 2 displayed in red, green, and blue respectively. Data are stretched using BCET.

In the colour composite 5,3,1 case displayed in red, green, and blue respectively shown in figure 6.11, much better visual and quantitative improvements have been achieved. Visually, Jurfayn (dark blue), Atiyah (greenish-blue) and Musayr (in brown hue) are distinguishable, also Bad' (in creamy yellowish-white) and most of the sedimentary rock classes are easily to delineate (i.e. Nutaysh in greenish-blue and Musayr in brown). Without careful visual assessment: Jurfayn, Atiyah, and Nutaysh can be delineated as one rock unit (the dark bluish-greenish in colour) and can not visually easily separated from each other. Quantitatively, the separability using TM bands 5, 3, and 1 after applying the BCET shows better results than the former combinations with only three pair of classes are poorly separable. The minimum separability is 1.35823, average separability is 1.98169 and, finally maximum separability is 2.00000; this is shown in table 6.7.

Class	Jurfayn	Atiyah	Musayr	Nutaysh	Bad'	Lisan	Conglo.+ Gravel	Gravel Sheets	Sabkhah	Alluvium
Atiyah	1.88655	-	-	-	-	-	-	-	-	-
Musayr	2.00000	1.99699	-	-	-	-	-	-	-	-
Nutaysh	1.99983	1.35823	1.89083	-	-	-	-	-	-	-
Bad'	2.00000	2.00000	1.99760	1.99396	-	-	-	-	-	-
Lisan	2.00000	2.00000	2.00000	2.00000	1.99873	-	-	-	-	-
Conglo. +Gravel	2.00000	2.00000	1.99998	1.99825	1.99998	1.97981	-	-	-	-
Gravel Sheets	1.98369	1.96909	2.00000	1.94671	2.00000	2.00000	2.00000	-	-	-
Sabkhah	2.00000	2.00000	2.00000	2.00000	2.00000	2.00000	2.00000	2.00000	-	-
Alluvium	2.00000	2.00000	2.00000	2.00000	2.00000	1.99999	2.00000	2.00000	2.00000	-
Aeolian silt+sand	2.00000	2.00000	2.00000	2.00000	1.99575	1.99703	2.00000	2.00000	2.00000	2.00000

Table 6.7. Separability measures between class pairs of the test site using the bands combination 5,3, and 1 of TM data. BCET is firstly applied.

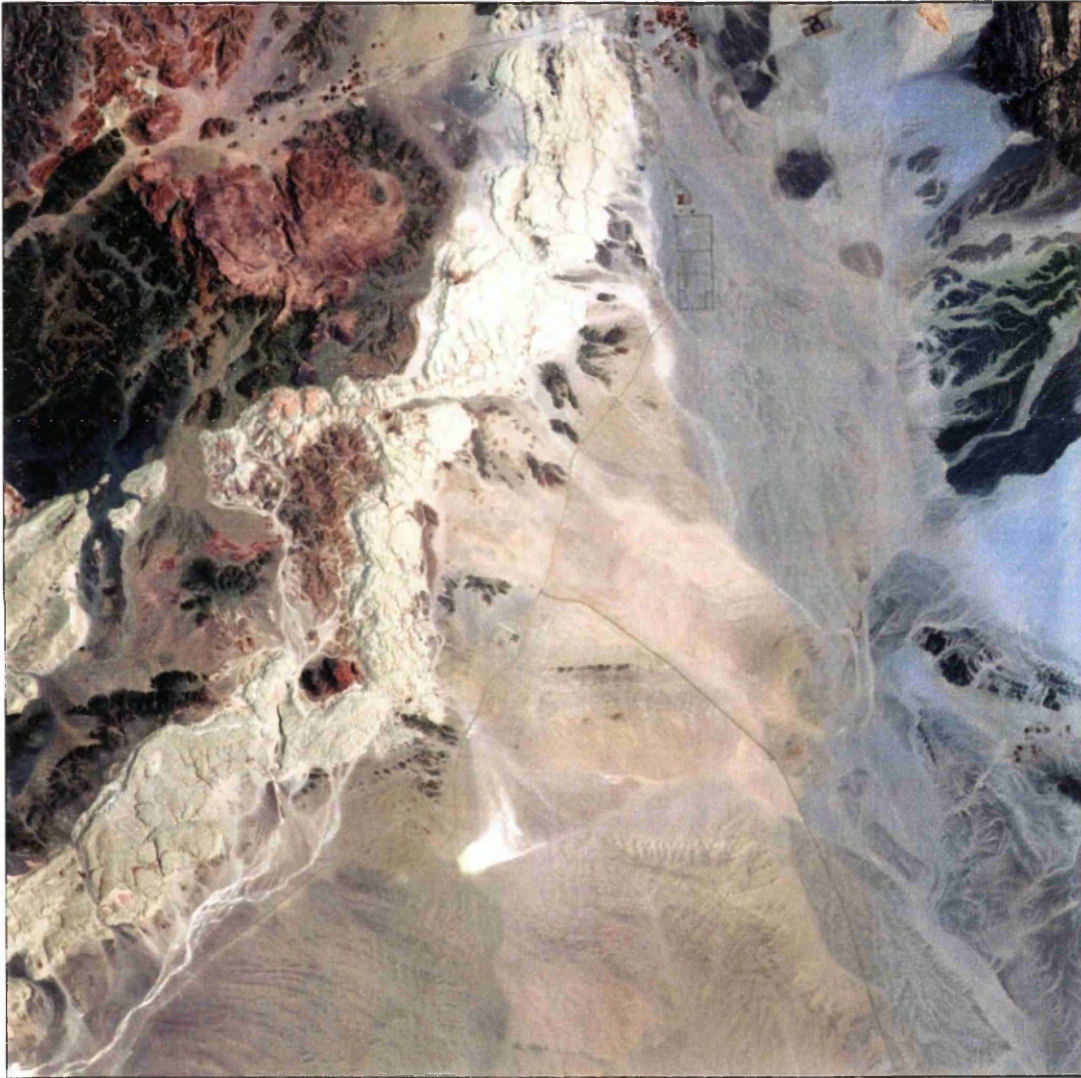


Figure 6.11 Colour composite using bands 5, 3, and 1 displayed in red, green, and blue respectively. Data are stretched using BCET.

Using bands combination 7, 4, and 1 displayed on red, green, and blue respectively, the colour composite visually shows similarity in distinguishing the rock unit classes with 5,3,1 bands combination. This is shown in figure 6.12. The only difference is the bad' formation is bluish-cyan in colour. Most rock unit classes are easily to delineate. Quantitatively, some improvements have been achieved (comparing with 5,3,1 bands combination), examples includes: Jurfayn-Atiyah and Nutaysh-Atiyah, conversely, Musayr-Nutaysh pair is separability reduced and Nutaysh-Gravel sheets pair of classes became inseparable. At the same time, still there are three class pairs which are inseparable, this is shown in table 6.8. From the table, the average separability is 1.98114, the minimum separability is 1.39836 and finally, the maximum separability is 2.0.

Class	Jurfayn	Atiyah	Musayr	Nutaysh	Bad'	Lisan	Conglo.+ Gravel	Gravel Sheets	Sabkhah	Alluvium
Atiyah	191866	-	-	-	-	-	-	-	-	-
Musayr	200000	199312	-	-	-	-	-	-	-	-
Nutaysh	199876	139836	180893	-	-	-	-	-	-	-
Bad'	200000	199995	200000	199997	-	-	-	-	-	-
Lisan	200000	200000	199999	200000	200000	-	-	-	-	-
Conglo.+Gravel	200000	200000	199977	199818	200000	199550	-	-	-	-
Gravel Sheets	199692	199092	199971	186936	200000	200000	199995	-	-	-
Sabkhah	200000	200000	200000	200000	200000	200000	200000	200000	-	-
Alluvium	200000	200000	200000	200000	200000	199985	200000	200000	200000	-
Aeolian silt+sand	200000	200000	200000	200000	200000	199477	200000	200000	200000	199999

Table 6.8. Separability measures between class pairs of the test site using the bands combination 7, 4, and 1 of TM data. BCET is firstly applied.

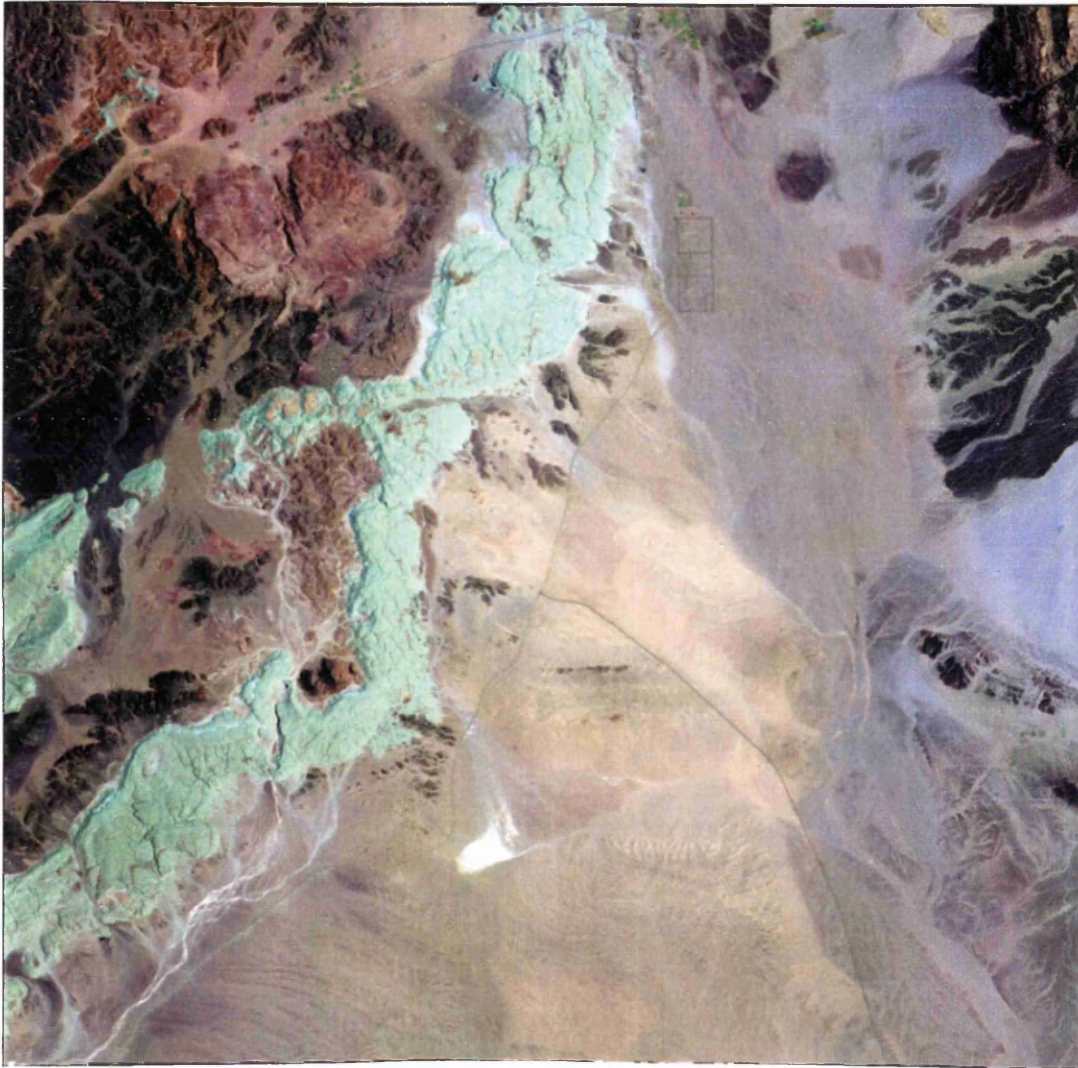


Figure 6.12 Colour composite using bands 7, 4, and 1 displayed in red, green, and blue respectively. Data are stretched using BCET.

As recommended by best bands combination shown in table 6.4, bands 7, 5, and 1 have been displayed in red, green, and blue respectively and are shown in figure 6.13. Visually, this band combination is almost similar to the 7, 4, and 1 bands combination but with some hue differences between the rock classes in the two colour composite. Strictly, the 7, 4, and 1 colour composite may show some visual improvements over 7, 5, and 1 combination in distinguishing some of the classes (i.e. distinct Musayr class) but quantitatively, the 7, 5, and 1 combination is the best among all displayed colour composites since only two pair of classes are inseparable. This is shown in table 6.9 with a minimum separability of 1.29978, the average separability is 1.97748 (which is less than 5,3,1 and 7,4,1 combination but only with two inseparable classes which is the most important), and finally the maximum separability is 2.0.

Class	Jurfayn	Atiyah	Musayr	Nutaysh	Bad'	Lisan	Conglo.+ Gravel	Gravel Sheets	Sabkhah	Alluvium
Atiyah	1.92436	-	-	-	-	-	-	-	-	-
Musayr	2.00000	1.98039	-	-	-	-	-	-	-	-
Nutaysh	1.99958	1.29978	1.67898	-	-	-	-	-	-	-
Bad'	2.00000	2.00000	1.99987	2.00000	-	-	-	-	-	-
Lisan	2.00000	2.00000	1.99940	2.00000	2.00000	-	-	-	-	-
Conglo. +Gravel	2.00000	2.00000	1.99549	1.99729	2.00000	1.99557	-	-	-	-
Gravel Sheets	1.97847	1.95917	2.00000	1.95998	2.00000	2.00000	2.00000	-	-	-
Sabkhah	2.00000	2.00000	2.00000	2.00000	2.00000	2.00000	2.00000	2.00000	-	-
Alluvium	2.00000	2.00000	2.00000	2.00000	2.00000	1.99962	2.00000	2.00000	2.00000	-
Aeolian silt+sand	2.00000	2.00000	2.00000	2.00000	2.00000	1.99360	2.00000	2.00000	2.00000	2.00000

Table 6.9. Separability measures between class pairs of the test site using the bands combination 7, 5, and 1 of TM data. BCET is firstly applied.

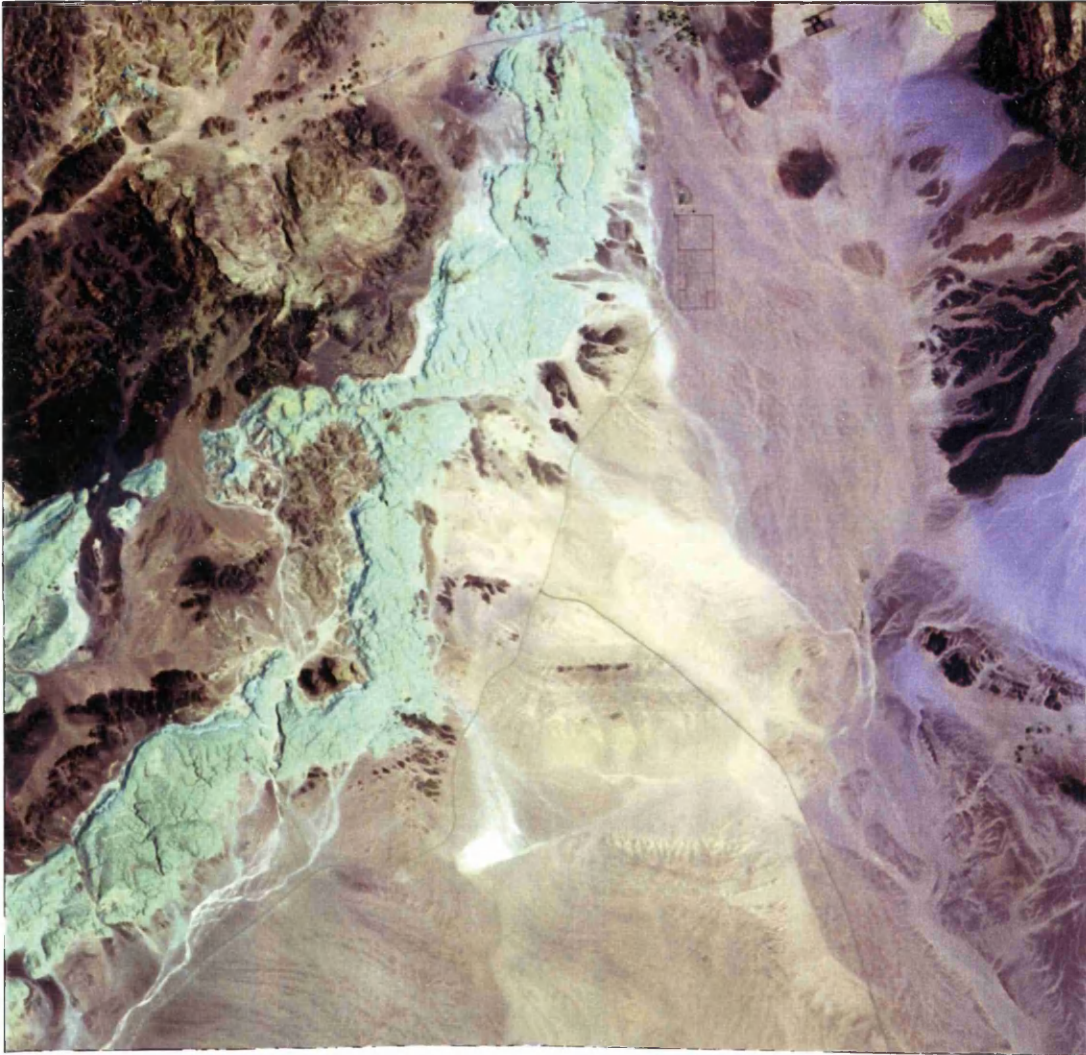


Figure 6.13 Colour composite using bands 7, 5, and 1 displayed in red, green, and blue respectively. Data are stretched using BCET.

6.7 Image fusion using colour transform

Colour is known to be a powerful descriptor that simplifies object identification and extraction from a scene. In visual image analysis performed by humans, the motivation for colour is that the human eye can discriminate thousands of colour shades, but only around twenty shades of grey level [60].

Image processing of colours can be divided into two major areas, full colour and pseudo-colour processing. In the first instance, the three image layers are assigned to the three primary colours or the three monitor guns and superimposed on the image layers to produce a coloured image (i.e. fig. 6.9-6.13). The pseudo-colour processing can be achieved by assigning a shade of colour or colours to a particular monochromatic intensity or range of intensities of a single layer of image (i.e. fig. 6.5).

Colours that human beings perceive from an object are determined by the nature of light reflected from the object. A body that reflects light which is relatively balanced in all visible wavelengths appears white to the observer, whereas objects that absorb all visible wavelengths appear black. Objects that reflect part of the visible wavelength appear as the colour associated with that wavelength in the visible electromagnetic spectrum.

Characterisation of light is an important subject in the colour science. If the light is achromatic (void of colours), its attribute is only its intensity and can be expressed by a scalar measure of grey level ranging from black, to greys, and finally white. Chromatic light spans the electromagnetic energy spectrum from approximately 400 to 700 nm. [60].

Three basic quantities are used to describe the quality of chromatic light source: radiance, luminance, and brightness. Radiance is the total amount of energy that flows from the light source, and is usually measured in Watts. Luminance, which is measured in lumens (lm), is the amount of energy that the observer can perceive from the light source, (e.g. the observer is unable to perceive energy in the infrared or microwave, in

this case the luminance would be zero, but they have their significant energy of radiance). Brightness is a subjective descriptor that is particularly difficult to measure, it embodies the achromatic notation of intensity and is one of the key factors in describing colour sensation [60].

All colours can be simplified as combinations of what are called the primary colours, red = 700nm, green = 546nm, and blue = 435.8nm in wavelengths. These colours can be added in equal amounts to produce the secondary or complementary colours of light which are: magenta = red and blue, cyan = green and blue, and yellow = red and green. If the three primary colours are added equally, this will give the additive component of colours which is white. If the three secondary colours are added equally, this will give the subtractive component of colours which is black.

The characteristics which are used to distinguish one colour from the other are brightness, hue, and saturation. As already indicated, brightness embodies the achromatic notion of intensity. Hue is an attribute associated with the dominant wavelength in the mixture of light, thus hue represents dominant colours as perceived by an observer. Saturation refers to the relative purity or the amount of white light mixed with the hue. An example is that pure spectrum colours are fully saturated, whereas pink colours (red + white) or lavender (violet + white) are less saturated, with the degree of saturation being inversely proportional to the amount of white light added.

If hue and saturation are taken together they are called the colour chromaticity, and therefore a colour may be characterised by its brightness and chromaticity. The amount of red, green, and blue needed to form any particular colour are called the tristimulus values and are denoted as X , Y , and Z respectively. A colour can then be specified by its trichromatic coefficients x , y , and z . These coefficients are:-

$$x = \frac{X}{X + Y + Z} \quad (6.4)$$

$$y = \frac{Y}{X + Y + Z} \quad (6.5)$$

$$z = \frac{Z}{X + Y + Z} \quad (6.6)$$

where x , y , and z are red, green, and blue trichromatic coefficients respectively, and the sum of these coefficients is equal to 1 as shown from the above equations.

Colours can be represented by many proposed models. These models are oriented either toward the hardware (such as for colour monitors and printers) or toward applications where colour manipulation is the goal. The hardware oriented models most commonly used in practice are the RGB (red, green, blue) model for colour monitors and for most colour video cameras. Another hardware oriented model is the CMY (cyan, magenta, yellow) model which is basically used for colour printers, and finally the YIQ model, which is the standard model used for colour TV broadcast (Y corresponds to luminance, I and Q are two chromatic components called in-phase and quadrature respectively) [60].

A model used for colour image manipulations is the IHS (intensity, hue, saturation) model. The advantage of this model is its ability to separate the spatial component (I) from the spectrum component (H and S) of the manipulated colour.

The colour models most often used in image processing are the RGB and the IHS models. The YIQ model is less important in image processing, where the CMY is used basically in hardcopy image production. A transform between the RGB model and the IHS model is mostly used for multispectral and multisensor image fusion purposes. The RGB and IHS models will be discussed in the following paragraphs to simplify the understanding of fusion using colour transform techniques.

The RGB model is simply based on a three dimensional Cartesian coordinate system as shown in figure 6.14. Each colour appears in its primary spectral components of red

(1,0,0), green (0,1,0), and blue (0,0,1) in the three corners of the colour cube. The secondary colours of cyan (0,1,1), magenta (1,0,1), and yellow (1,1,0) are at the other three corners. Black is at the origin (0,0,0), and white (1,1,1) is at the corner farthest from the origin.

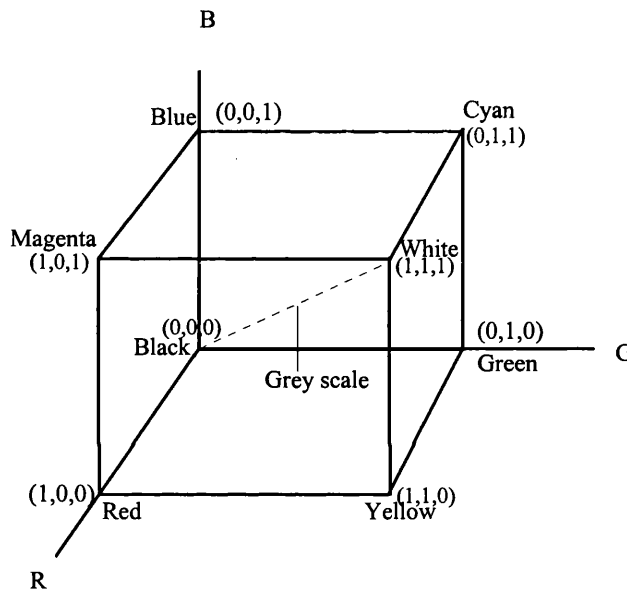


Figure 6.14. The RGB colour model (modified from [60]).

The grey scale extends from black to white along the line joining these two points. The colours are points on the corners of the cube, and are defined by vectors extending from the origin. For simplification, all colour values have been normalised from zero to one and all values are assumed to be in the range of 0 and 1.

Images in the RGB colour model consist of three independent image layers, one for each primary colour. When fed into an RGB monitor, these three images combine in the phosphor screen to produce a colour composite image. Thus the use of the RGB model for image processing makes sense when the images are expressed in terms of three colour layers [60].

As mentioned earlier, the IHS colour model owes its usefulness in image processing to two aspects, one is the intensity component (I) which is decoupled from the colour information in the image and represents the spatial aspect, and the second is that the hue and saturation (H, S) components are intimately related to the way in which human beings perceive colours. These features make the IHS model a valuable tool for developing a fusion technique in image processing based on the colour sensing properties of the human visual system [60]. Figure 6.15 shows the IHS colour model.

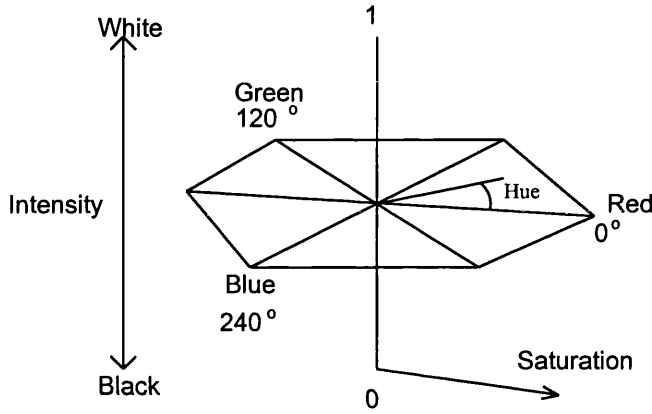


Figure 6.15. The IHS model (modified from [118]).

The conversion formulas between the colour models of RGB to IHS and back to RGB ($\text{RGB} \Leftrightarrow \text{IHS}$) are straightforward. Gonzalez *et. al.* [60] state them as follows:

$$I = \frac{1}{3}(R + G + B) \quad (6.7)$$

$$S = 1 - \frac{3}{(R + G + B)}[\min(R, G, B)] \quad (6.8)$$

$$H = \cos^{-1} \left\{ \frac{\frac{1}{2}[(R - G) + (R - B)]}{\sqrt{[(R - G)^2 + (R - B)(G - B)]}} \right\} \quad (6.9)$$

The conversion back to red, green, and blue is dependent on the angle of the hue as shown in figure 6.15 and can be transferred to the pixel brightness value interval. The conversion formulas are as follows [60]:

1- When $0^\circ < H \leq 120^\circ$

(H ranges from 0 to 85 in brightness values of 8 bit images).

$$b = \frac{1}{3}(1 - S) \quad (6.10)$$

$$r = \frac{1}{3} \left[1 + \frac{S \cos H}{\cos(60^\circ - H)} \right] \quad (6.11)$$

$$g = 1 - (r + b) \quad (6.12)$$

2- When $120^\circ < H \leq 240^\circ$

(H ranges from 85 to 170 in brightness values of 8 bit images)

$$H = H - 120^\circ \quad (6.13)$$

$$r = \frac{1}{3}(1 - S) \quad (6.14)$$

$$g = \frac{1}{3} \left[1 + \frac{S \cos H}{\cos(60^\circ - H)} \right] \quad (6.15)$$

$$b = 1 - (r + g) \quad (6.16)$$

3- When $240^\circ < H \leq 360^\circ$

(H ranges from 170 to 255 in brightness values of 8 bit images)

$$H = H - 240^\circ \quad (6.17)$$

$$b = \frac{1}{3} \left[1 + \frac{S \cos H}{\cos(60^\circ - H)} \right] \quad (6.18)$$

$$g = \frac{1}{3}(1 - S) \quad (6.19)$$

$$r = 1 - (g + b) \quad (6.20)$$

Based on the trichromatic coefficients shown previously in equations 6.4-6.6, another important spatial-spectral fusion technique has been derived [4] called the Brovey transform [119]. It uses the selected three bands for colour display as RGB and uses the fourth image which is SAR or Panchromatic aerial photograph. The following transformation equations are used for the fusion process:

$$R = \left(\frac{R}{R + G + B} \right) \times I \quad (6.21)$$

$$G = \left(\frac{G}{R + G + B} \right) \times I \quad (6.22)$$

$$B = \left(\frac{B}{R + G + B} \right) \times I \quad (6.23)$$

where:

R , G , and B = red, green, and blue layers.

I = the image intended to be included with the spectral data, such as the SAR image or aerial photograph.

One important characteristic of both $RGB \Leftrightarrow IHS$ is that it is scene independent (every pixel is manipulated independently from the other scene pixels. The Brovey transform also has this characteristic because both are pixel basis (not scene basis).

6.8 TM and SAR colour transform fusion

The objective of image data fusion for geologic remote sensing is to combine both of the spatial and spectral information. By the use of the TM spectral colour coded composite, the whole spectral information available in the six TM image data set has been preserved in such three image layers (the TM spectral coded colour composite), this is shown for comparison in tables 6.2 and 6.3. As mentioned in section 6.7, one

important characteristic of the IHS model is the separation of the spatial component (I) from its spectral components (H and S). This spatial component or image can be replaced by the JERS-1 SAR spatial information image, which contains the textural information. Another fusion tool that separates the image spectral and spatial components from each other using the colour transform is the colour chromaticity method which is represented by the Brovey transform. Such methods have been discussed theoretically and then will be practically implemented on the TM spectral colour coded composite and SAR images. A visual and quantitative analysis will then be given on the output results using both techniques, and in the same time, the colour composite of bands 7, 5, and 1 is also colour fused with the SAR data and compared visually and quantitatively with the new output results.

Referring back to the TM spectral coded colour composite image (figure 6.8) in section 6.5.3, strictly, it might be possible to restore this image to simulate normal colour composites, this is because most remote sensing geologists are well familiar with colour composites photo-interpretation. Furthermore, the spatial information in figure 6.8 is less pronounced if compared with normal colour composites. To restore such an image, by assigning the spectral coded image to the hue component (H) after applying histogram equalisation on this image, the topographic-albedo information image to the intensity component (I), and the range image to the saturation component (S) after being automatically stretched, then reversing these components to RGB ($IHS \Rightarrow RGB$), a new image can be produced with better (to some extent) spatial information representation, and at the same time preserving the spectral information which is represented by the spectral coded image. Such an image is shown in figure 6.16. From the image and from the photo-interpretation point of view, rock units are shown as follows: In the upper left corner of the image, Jurfayn is shown up as dark green; Atiyah is saturated dark brown; Musayr is violet-pinkish; and Nutaysh is brown. Bad' (extending from the upper, middle, to lower left corner) is light greenish-yellowish in colour. Quaternary and surficial deposits are also shown clearly in the image. For example: Lisan formation (in the lower centre of the image) is pinkish with nearly flat topographic relief with horizontal lineation; Alluvium deposits (in the lower left corner) is shown as light brownish; gravel

sheets deposits are blue (and orange as an interclass variation); conglomerate and gravel lithologic unit (in the left and upper left of the image) is light green; Sabkhah (in the lower middle) is light creamy yellowish to orange in colour; and finally the aeolian silt and sand unit (in the centre of the image) is in saturated pink-magenta with smooth surface. Comparatively, quantitative analysis of this image (figure 6.16) represented by table 6.10 with the original spectral coded colour composite (figure 6.8) represented by table 6.2 shows some improved separability between the classes pair Gravel sheets-Jurfayn from 1.99087 to 1.99933 but some of the classes separability is slightly reduced. The maximum reduction is Atiyah-Nutaysh from 1.46412 to 1.14619, the slight reduction still made the classes well separable. From the separability table 6.10, the minimum separability is 1.14619, the average separability is 1.98278, and the maximum separability is 2.0. One class pair (Atiyah-Nutaysh is still inseparable).

Class	Jurfayn	Atiyah	Musayr	Nutaysh	Bad'	Lisan	Conglo.+ Gravel	Gravel Sheets	Sabkhah	Alluvium
Atiyah	200000	-	-	-	-	-	-	-	-	-
Musayr	200000	200000	-	-	-	-	-	-	-	-
Nutaysh	200000	1.14619	200000	-	-	-	-	-	-	-
Bad'	200000	200000	200000	200000	-	-	-	-	-	-
Lisan	200000	200000	200000	200000	200000	-	-	-	-	-
Conglo.+ Gravel	200000	200000	200000	1.99939	200000	1.99842	-	-	-	-
Gravel Sheets	1.99933	1.95452	200000	1.95531	200000	200000	200000	-	-	-
Sabkhah	200000	200000	200000	200000	200000	200000	200000	200000	-	-
Alluvium	200000	200000	200000	200000	1.99999	200000	200000	200000	200000	-
Aeolian silt+ sand	200000	200000	200000	200000	200000	200000	200000	200000	200000	200000

Table 6.10 Transformed divergence separability test of the lithologic training areas of the test site using $IHS \Rightarrow RGB$ where I = the 6 TM spectral coded image after being histogram equalised, I = albedo-topographic information image, and finally S = the range image. Data are automatic stretched after restoring to RGB model.

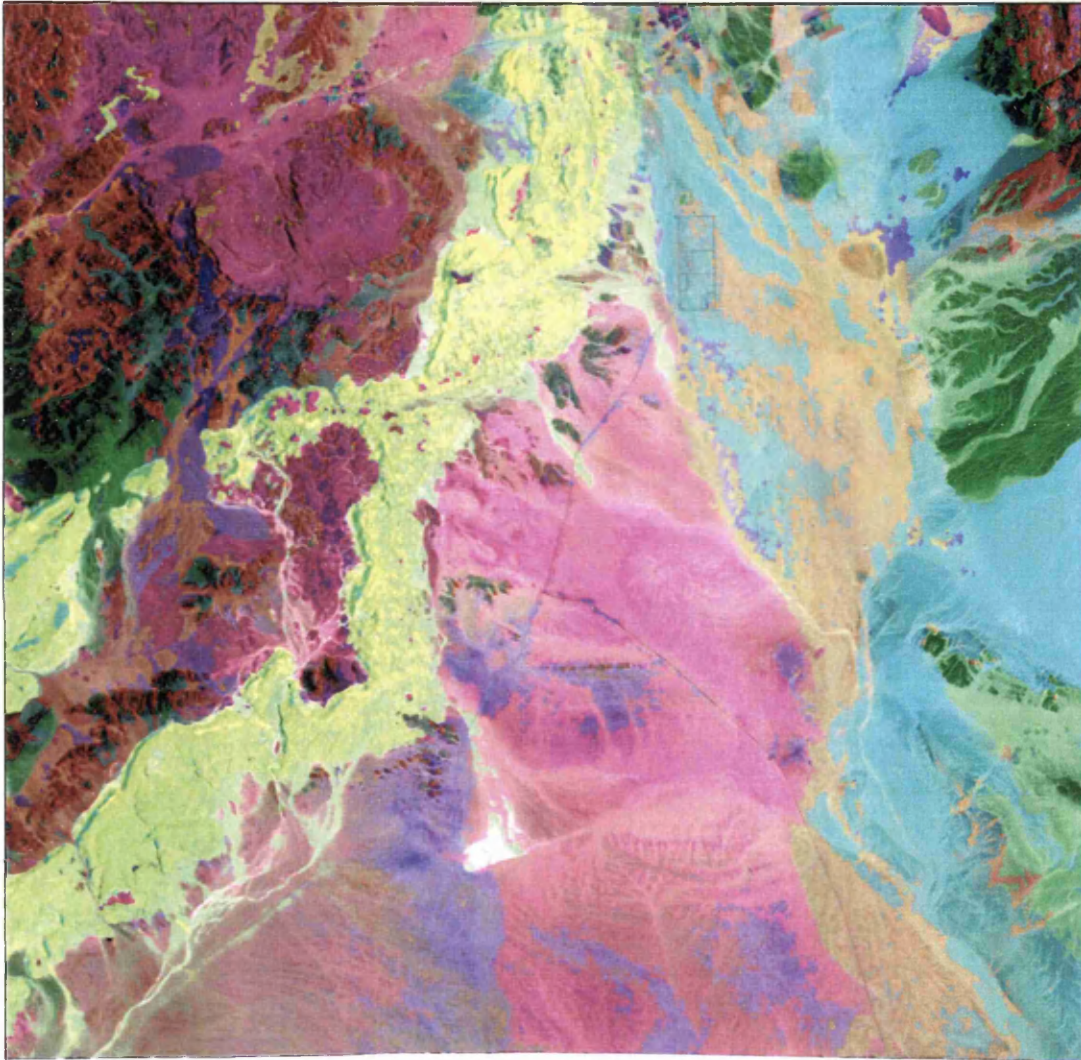


Figure 6.16 IHS \Rightarrow RGB TM spectral coded colour composite transformed image. The image created using the intensity component (I) as the albedo-topographic information image, the hue component (H) as the spectral coded image after being histogram equalised, and finally the saturation component (S) as the range image.

JERS-1 SAR image data can be introduced (fused) with the TM spectral image data for visual assessment (in particular) creating a colour composite in many ways. In this thesis, one method is introducing it directly by replacing the albedo-topographic information image when the TM spectral coded colour composite is used, in this case, the method of fusion is by the use of colour composite (data from both sensors displayed in RGB) without using colour transform; or by the use of colour transform either by introducing the SAR data as an intensity component (I) and reversing the IHS to RGB (equations 6.10 - 6.20); or by the use of Brovey transform (equations 6.21 - 6.23) which can also be used using both SAR and the TM spectral colour coded composite.

In the first method, the spectral coded image is assigned to red, the JERS-1 SAR image assigned to green after implementing 5 by 5 Frost filter and stretching, and finally the range image is stretched and assigned to blue. This image is shown in figure 6.17 and the separability test measure between the lithologic classes is shown in table 6.11. Visually, most of the rock units are pronounced either spectrally or texturally or both. Examples include: Jurfayn (in green colour), Bad' (in cyan-light blue), Conglomerate and gravel (right side of the image) is in cyan-greenish colour, Gravel sheets in violet to dark blue in colour, Alluvium in the lower left side of the image is in red, Lisan is in dark pinkish-red. Some of the rock unit classes are difficult to delineate and/or mixed (in colour) to other classes, these include Atiyah, Musayr, Nutaysh, and Sabkhah.

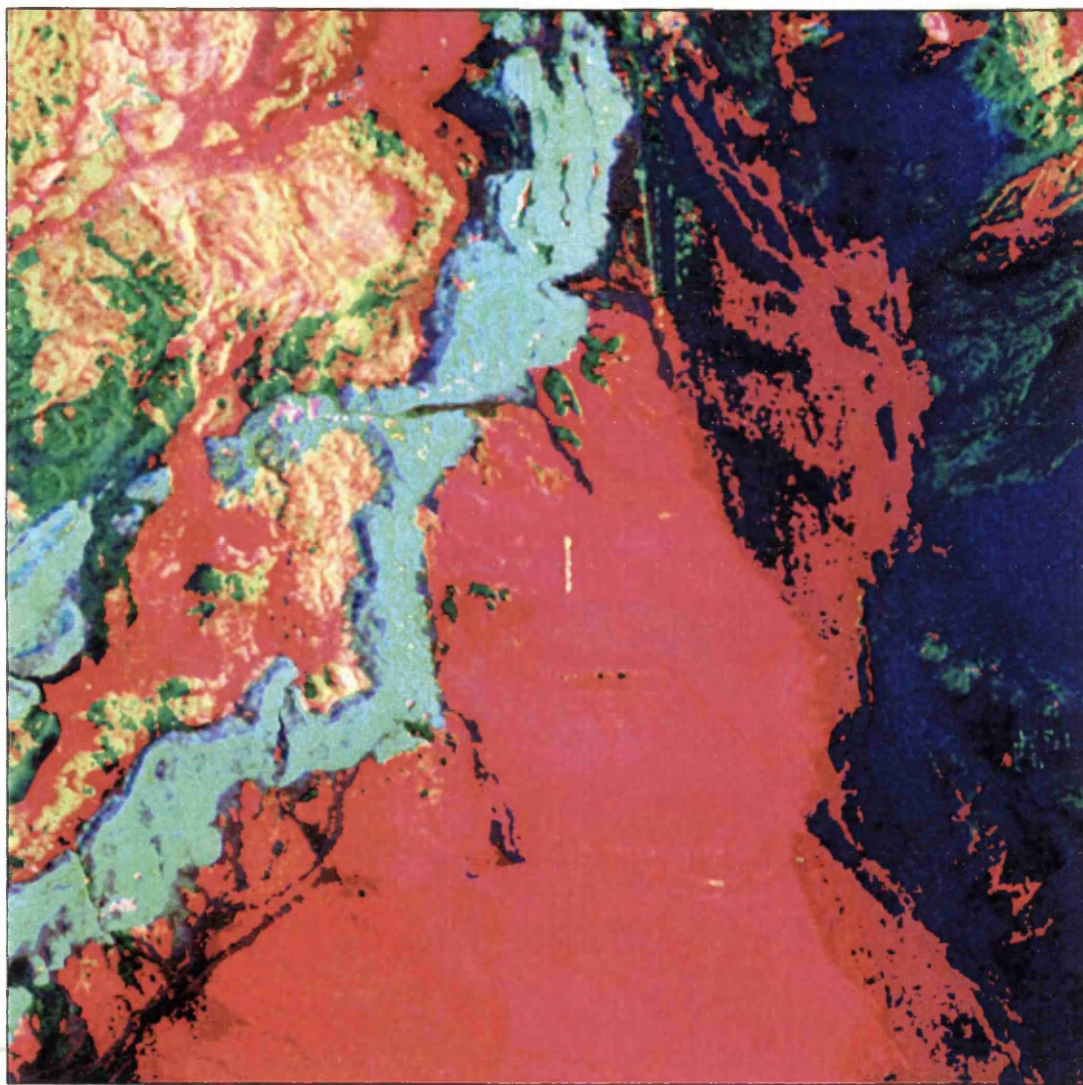


Figure 6.17. Fused colour composite of the test site. The spectral coded image assigned to red, 5 by 5 Frost filtered and stretched SAR assigned to green, and range image assigned to blue.

Quantitatively, separability between classes is reduced and four pairs of lithologic units became inseparable. This is due the albedo-topographic image (which is not used) and spectral coded image represent good separability. From table 6.11, the average separability is calculated as 1.93089, the minimum separability is 0.13416, and the maximum separability is 2.0

Class	Jurfayn	Atiyah	Musayr	Nutaysh	Bad'	Lisan	Conglo.+ Gravel	Gravel Sheets	Sabkhah	Alluvium
Atiyah	200000	-	-	-	-	-	-	-	-	-
Musayr	200000	200000	-	-	-	-	-	-	-	-
Nutaysh	200000	0.13416	200000	-	-	-	-	-	-	-
Bad'	199109	199964	200000	199995	-	-	-	-	-	-
Lisan	200000	200000	199883	200000	200000	-	-	-	-	-
Conglo.+ Gravel	200000	193494	200000	195365	200000	199999	-	-	-	-
Gravel Sheets	134100	200000	200000	200000	200000	200000	200000	-	-	-
Sabkhah	200000	199987	199999	199999	200000	1.85167	0.99511	200000	-	-
Alluvium	200000	200000	200000	200000	200000	200000	200000	199912	199999	-
Aeolian silt+sand	200000	200000	200000	200000	200000	200000	200000	200000	200000	200000

Table 6.11. Transformed divergence separability test of the training lithologic classes in the fused colour composite shown in figure 6.17.

In a similar manner to the technique applied to produce the image shown in figure 6.16 transforming the colour model IHS to RGB model ($IHS \Rightarrow RGB$), the 5 by 5 Frost filtered and stretched SAR is used as the intensity component, spectral coded image is used as the hue component, and finally the range image is used as the saturation component to produce the RGB fused colour composite. This is shown in figure 6.18. As expected, this fused colour composite did not show the same image quality as the image shown in figure 6.16 even though both of them were produced using the same colour transform technique. This is due to the fact that the albedo-topography image coupled with the spectral coded TM image shows high separability (refer to figure 6.6) whereas the separability test of SAR coupled with the spectral coded image shows low separability³. Visual analysis of figure 6.18 (strictly), still shows that some of the lithologic classes are

³ Separability of the lithologic training classes (represented by the class ellipsoids) using both images has been tested. Figure is not included because of its less importance.

well pronounced (spectrally and texturally) while others may be depicted either texturally or spectrally, but not both. The classes that can be differentiated spectrally and texturally are: Jurfayn; Bad'; Musayr; and Lisan. Classes that can be differentiated spectrally only are: the Gravel sheets; Lisan; and Alluvium (the brown colour in the lower left part in the image). Classes have similar spectral properties but can be differentiated texturally only are: Jurfayn with conglomerate and gravel; and to some extent Nutaysh with Atiyah. Quantitatively, the transformed divergence separability test applied on the lithologic classes using this fused colour composite image is shown in table 6.12. Separability values are reduced intensively making six pairs of classes inseparable. From the table, the average separability is 1.92137, the minimum separability is 0.07992, and the maximum separability is 2.0

Class	Jurfayn	Atiyah	Musayr	Nutaysh	Bad'	Lisan	Conglo.+ Gravel	Gravel Sheets	Sabkhah	Alluvium
Atiyah	1.82197	-	-	-	-	-	-	-	-	-
Musayr	2.00000	1.99864	-	-	-	-	-	-	-	-
Nutaysh	1.69222	0.07992	1.99732	-	-	-	-	-	-	-
Bad'	2.00000	2.00000	2.00000	2.00000	-	-	-	-	-	-
Lisan	2.00000	1.99999	1.99908	2.00000	2.00000	-	-	-	-	-
Conglo. +Gravel	1.96736	1.96643	1.99995	1.96483	2.00000	1.99869	-	-	-	-
Gravel Sheets	1.29685	1.98652	2.00000	1.98431	2.00000	1.99999	1.99176	-	-	-
Sabkhah	2.00000	2.00000	1.99997	2.00000	2.00000	1.67661	1.29133	2.00000	-	-
Alluvium	2.00000	2.00000	2.00000	2.00000	2.00000	2.00000	2.00000	2.00000	2.00000	-
Aeolian silt+sand	2.00000	2.00000	1.99997	2.00000	2.00000	2.00000	2.00000	2.00000	1.96158	2.00000

Table 6.12 Transformed divergence separability test results applied on the fused IHS \Rightarrow RGB colour composite image using the TM spectral coded image as hue, the SAR image as intensity, and the range image as saturation components.

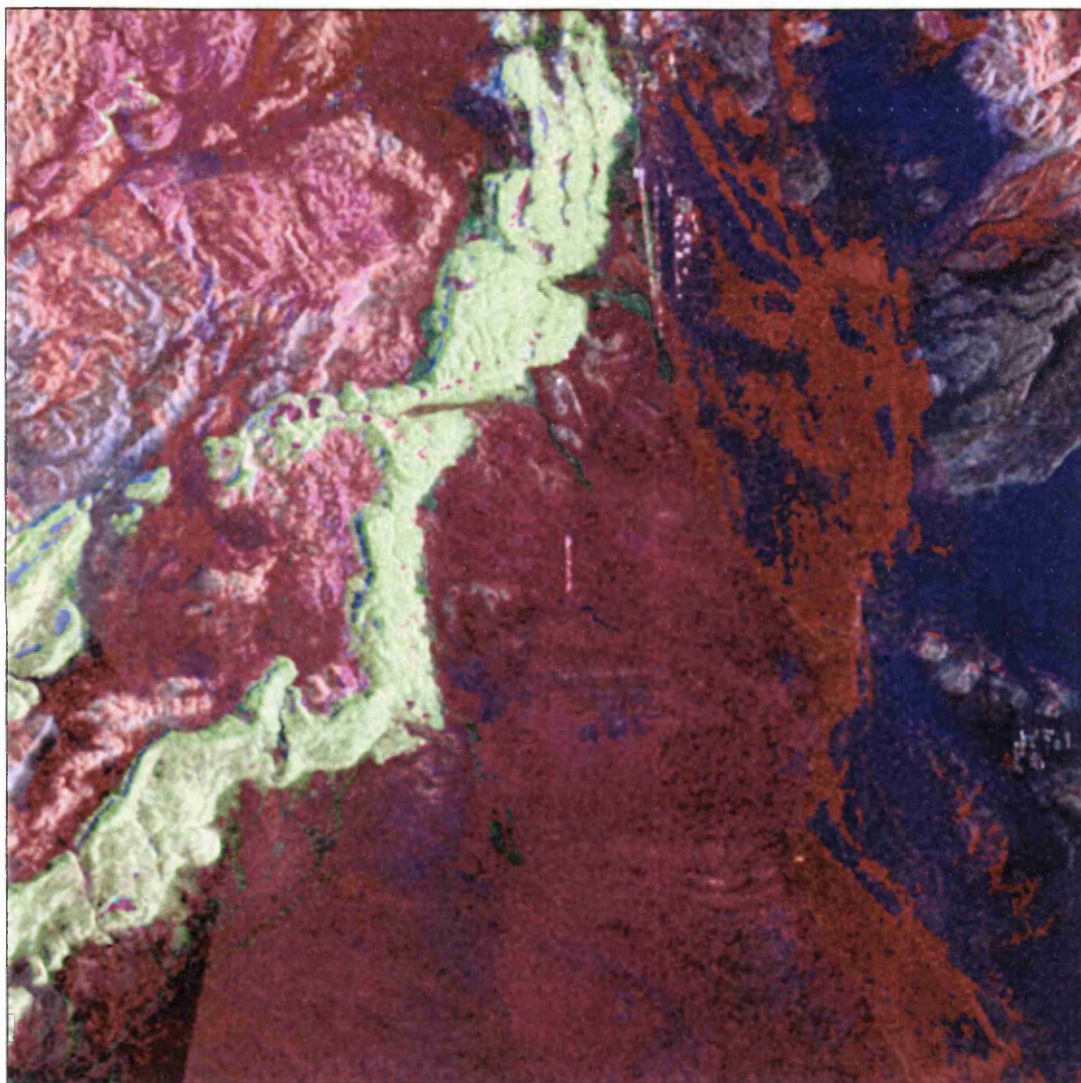


Figure 6.18 Reverse $IHS \Rightarrow RGB$ fused colour composite image using the TM spectral coded image as hue, the SAR image as intensity, and the range image as saturation components.

A complete procedure of colour transform from RGB model to IHS mode and then reversing back to the RGB model is demonstrated in figure 6.19 using the 6 TM spectral coded image assigned to red, topographic and albedo image assigned as green, and range image assigned as blue (green and blue images were previously automatic stretched). The intensity component of the IHS model has been replaced by an automatic stretched and 5 by 5 Frost filtered JERS-1 SAR. A reverse process has been implemented to the IHS model to bring the data back to its RGB original model. The photo-interpretation of the output image shown in figure 6.19 is as follows: In the upper left side of the image, Jurfayn is in greyish-light blue with rough texture; Atiyah is in rough texture with light orange hue, Musayr is in pinkish colour with rough to moderate texture, Nutaysh is hardly separable from Atiyah because both are similar in colour and texture; Bad' is in light green colour with blocky texture; Conglomerate and gravel class has similar colour of Jurfayn but with smooth to lineated (in some areas) texture; Gravel sheets class has a violet colour with smooth texture; Lisan Formation rock class has a smooth texture and in dark pinkish-reddish colour; Alluvium class is shown in brown colour and smooth in texture; Sabkhah (in the lower middle of the image) is in dark green; and finally, Aeolian silt and sand class is indistinguishable. Quantitatively and using the transformed divergence separability test between these classes using this fused image as shown in table 6.13, it can be noticed the separability is also reduced and seven pairs of classes became inseparable. From table 6.13, the minimum separability is 0.10506, maximum separability is 2.0, and the average separability is 1.92980.

Class	Jurfayn	Atiyah	Musayr	Nutaysh	Bad'	Lisan	Conglo.+ Gravel	Gravel Sheets	Sabkhah	Alluvium
Atiyah	1.87517	-	-	-	-	-	-	-	-	-
Musayr	2.00000	1.99705	-	-	-	-	-	-	-	-
Nutaysh	1.88311	0.10506	1.99178	-	-	-	-	-	-	-
Bad'	1.99999	1.99804	1.99978	1.99838	-	-	-	-	-	-
Lisan	2.00000	2.00000	1.99978	2.00000	2.00000	-	-	-	-	-
Conglo.+Gravel	1.99962	1.93091	1.99957	1.94542	2.00000	1.99945	-	-	-	-
Gravel Sheets	1.34489	1.98411	2.00000	1.98684	2.00000	2.00000	1.99973	-	-	-
Sabkhah	2.00000	2.00000	1.99999	2.00000	2.00000	1.76711	1.84868	2.00000	-	-
Alluvium	2.00000	2.00000	2.00000	2.00000	2.00000	1.99998	2.00000	2.00000	2.00000	-
Aeolian silt+sand	2.00000	2.00000	2.00000	2.00000	2.00000	1.57194	2.00000	2.00000	1.91236	2.00000

Table 6.13 Transformed divergence separability test of the lithologic classes using the image constructed in figure 6.19.

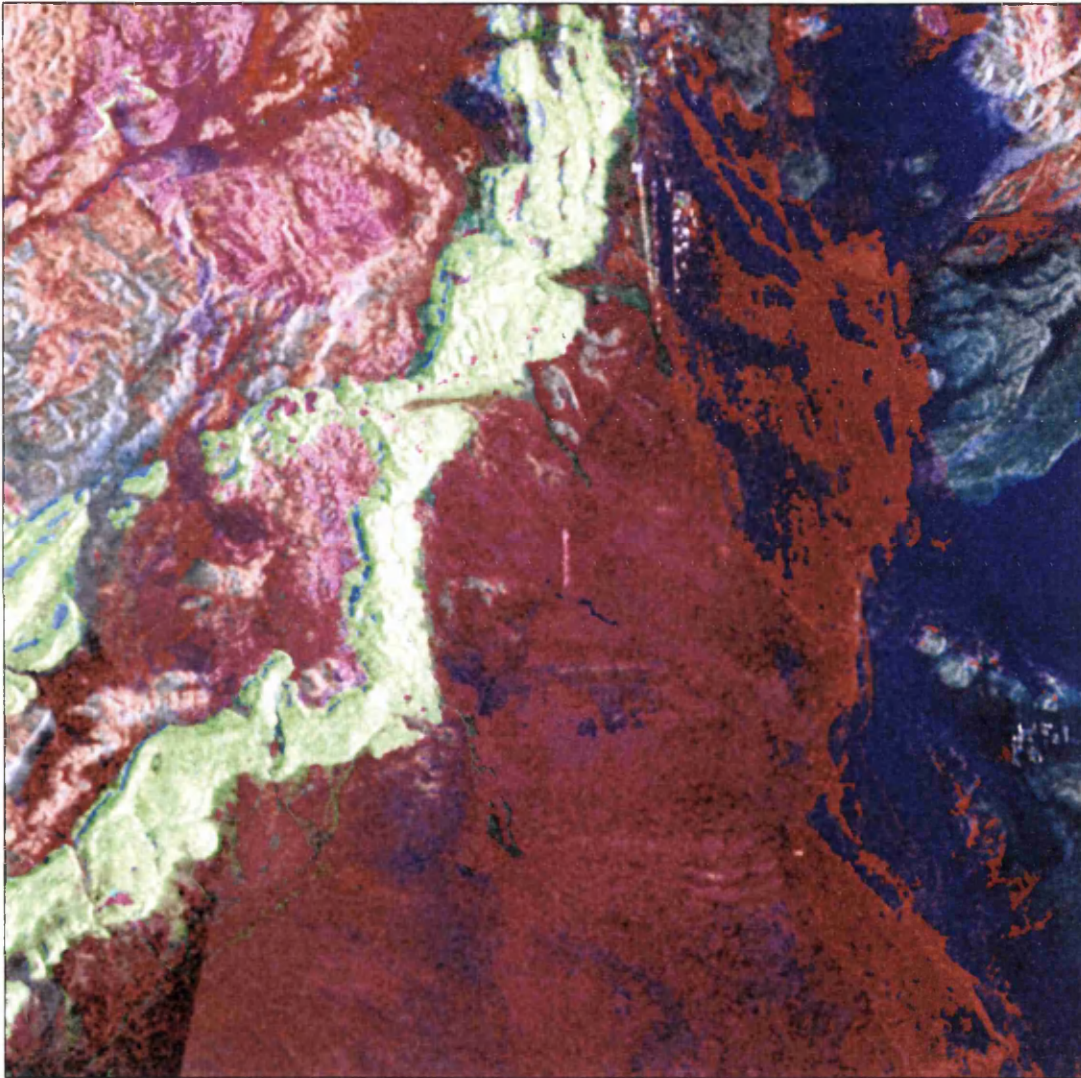


Figure 6.19 RGB \Rightarrow IHS \Rightarrow RGB fused colour composite image using the 6 TM spectral coded image as red, albedo-topographic information image as green, and range image as blue. The intensity output image result is replaced by SAR image, and a reverse procedure is applied to reconstruct a RGB model. The replaced SAR is 5 by 5 Frost filter and automatic stretched.

For comparison purposes, a similar technique of $RGB \Rightarrow IHS \Rightarrow RGB$ image fusion has been implemented on the original TM bands 7, 5, and 1 after being BCET stretched, where the intensity component is replaced by JERS-1 SAR after implementing 5 by 5 Frost filter and automatically stretched. This is shown in figure 6.20. In the visual analysis of this image, Jurfayn rock class is shown in the left edge of the image as bluish violet with rough texture, Atiyah and Nutaysh classes have the same colour (light pinkish-to light brown, Bad' is easily to delineate and has a cyan colour with blocky texture, other quaternary and surficial rock classes are distinguishable except the Aeolian silt and sand in the middle of the image which is not detectable. Quantitatively, and from table 6.14 where the transformed divergence separability test is applied on these classes using this colour image, situation became difficult where twelve class pairs are inseparable. From the table, the minimum separability is 0.15240, the average separability is 1.87967, and the maximum separability is 2.0.

Class	Jurfayn	Atiyah	Musayr	Nutaysh	Bad'	Lisan	Conglo.+ Gravel	Gravel Sheets	Sabkhhah	Alluvium
Atiyah	1.63713	-	-	-	-	-	-	-	-	-
Musayr	1.99719	1.75632	-	-	-	-	-	-	-	-
Nutaysh	1.64932	0.15240	1.63683	-	-	-	-	-	-	-
Bad'	2.00000	2.00000	1.99884	1.99995	-	-	-	-	-	-
Lisan	1.99993	1.99986	1.99934	1.99997	2.00000	-	-	-	-	-
Conglo.+ Gravel	1.81907	1.81727	1.99539	1.84401	2.00000	1.94660	-	-	-	-
Gravel Sheets	1.73165	1.96819	1.99999	1.98648	2.00000	1.99996	1.98151	-	-	-
Sabkhhah	1.99724	1.99990	2.00000	1.99998	2.00000	1.99177	1.20182	1.99882	-	-
Alluvium	1.99999	2.00000	2.00000	2.00000	2.00000	1.99963	2.00000	1.99631	1.99999	-
Aeolian silt+sand	1.99970	1.99986	1.99969	1.99995	2.00000	0.50307	1.86020	1.99999	1.91687	1.99999

Table 6.14 Transformed divergence separability test of the lithologic classes using the image constructed in figure 6.20.

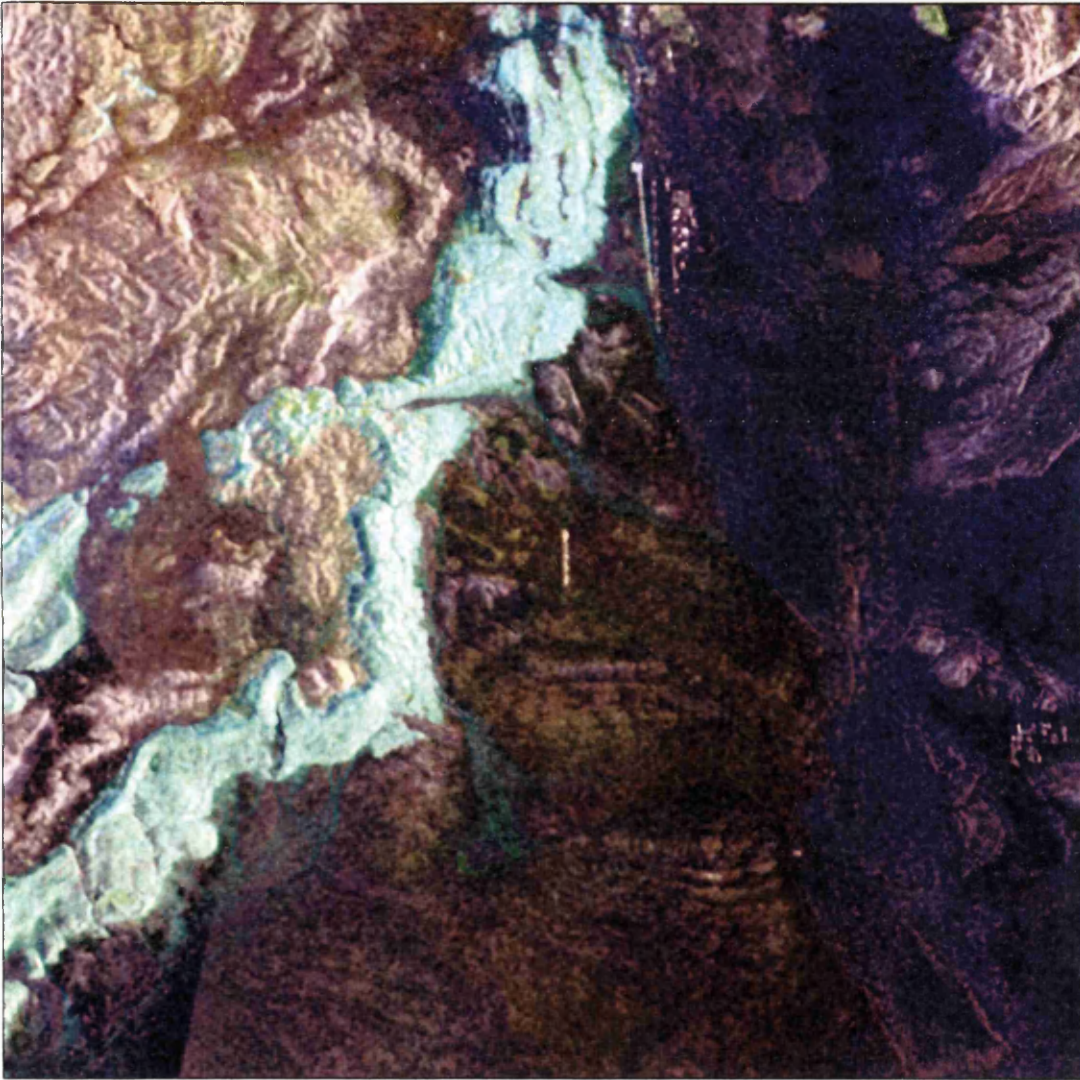


Figure 6.20 $RGB \Rightarrow IHS \Rightarrow RGB$ fused colour composite image using TM bands 7, 5, and 1 as red, green, and blue respectively. The intensity output image result is replaced by SAR image, and a reverse procedure is applied to reconstruct a RGB model. The replaced SAR is 5 by 5 Frost filter and automatic stretched.

In the case of using Brovey transform as a data fusion tool, whereas the six TM spectral coded image, the albedo and topographic information image, and the range image are used to produce the trichromatic coefficients then multiplied by the 5 by 5 Frost filtered and automatic stretched SAR. Figure 6.21 shows the output image using this kind of transform. Visually, rock textures are less pronounced but spectrally most of the rock classes are showing up and easily to map, for example: Jurfayn (in the left side of the image, and in the upper right corner) is in violet colour; Atiyah is in red and the rock boundaries between the two classes (Jurfayn and Atiyah) is easily to delineate; Musayr is in reddish-pink; Nutaysh is in orange; Bad' is in cyan. Quaternary deposits can also be delineated (but with less degree of accuracy in some cases), examples are: Lisan is in dark brown; Alluvium is in brown; Gravel sheets class is in dark cyan to bluish-green in colour; conglomerate and gravel is in violet (can be mapped as Jurfayn because both of which have the same hue); Sabkhah class (in the lower middle) is in dark yellowish colour; and finally Aeolian silt and sand class obscured and difficult to map. In quantitative point of view as shown in table 6.15, six pairs of classes are inseparable, the minimum separability is 1.36682, the maximum separability is 2.0, and finally the average separability is 1.96243.

Class	Jurfayn	Atiyah	Musayr	Nutaysh	Bad'	Lisan	Conglo.+ Gravel	Gravel Sheets	Sabkhah	Alluvium
Atiyah	1.79060	-	-	-	-	-	-	-	-	-
Musayr	1.99947	1.69834	-	-	-	-	-	-	-	-
Nutaysh	1.99871	1.36682	1.43472	-	-	-	-	-	-	-
Bad'	2.00000	1.99999	1.99989	1.99349	-	-	-	-	-	-
Lisan	2.00000	2.00000	2.00000	2.00000	2.00000	-	-	-	-	-
Conglo.+ Gravel	2.00000	2.00000	2.00000	2.00000	2.00000	1.99921	-	-	-	-
Gravel Sheets	1.99322	2.00000	1.99999	2.00000	1.99946	1.99977	2.00000	-	-	-
Sabkhah	2.00000	2.00000	2.00000	2.00000	2.00000	1.99994	1.76919	1.99999	-	-
Alluvium	2.00000	2.00000	2.00000	2.00000	2.00000	2.00000	2.00000	1.89956	1.99998	-
Aeolian silt+sand	2.00000	2.00000	2.00000	2.00000	2.00000	1.99284	2.00000	2.00000	1.99820	2.00000

Table 6.15 Transformed divergence separability test of Brovey transformed fused images of the six TM spectrally coded image, the albedo-topographic information image, the range image, and the JERS-1 SAR image after Frost filtered. All images were automatically stretched except the spectral coded image.



Figure 6.21 Brovey transformed colour composite image using the six TM spectral coded image, albedo and topographic information image, the range image, and finally the JERS-1 SAR after being 5 by 5 Frost filtered. All images are automatically stretched (except the spectral coded image).

In comparison, the Brovey transform image fusion technique has been applied on the original TM images of bands 7, 5, and 1 after being BCET stretched. The 5 by 5 Frost filtered and automatically stretched SAR is used as the intensity component image. The output results are shown in figure 6.22. Texturally, this image shows slightly better results than figure 6.21. Conversely, and from the spectral point of view, figure 6.21 shows up better visual results especially when it comes to delineate the Quaternary deposits. Quantitatively, as shown in table 6.16, seven class pairs are inseparable, the minimum separability is 0.86249, average separability is 1.89369, and maximum separability is 2.0

Class	Jurfayn	Atiyah	Musayr	Nutaysh	Bad'	Lisan	Conglo.+ Gravel	Gravel Sheets	Sabkhah	Alluvium
Atiyah	1.62175	-	-	-	-	-	-	-	-	-
Musayr	1.99901	1.19963	-	-	-	-	-	-	-	-
Nutaysh	1.98054	0.86249	1.14596	-	-	-	-	-	-	-
Bad'	1.99994	1.94933	1.99141	1.93461	-	-	-	-	-	-
Lisan	2.00000	2.00000	1.99974	2.00000	2.00000	-	-	-	-	-
Conglo. +Gravel	2.00000	2.00000	2.00000	1.99857	2.00000	1.73908	-	-	-	-
Gravel Sheets	1.95960	1.99809	2.00000	1.99942	2.00000	2.00000	1.99996	-	-	-
Sabkhah	2.00000	2.00000	2.00000	2.00000	2.00000	1.99981	1.43981	2.00000	-	-
Alluvium	2.00000	2.00000	2.00000	2.00000	2.00000	1.99992	1.99978	1.97543	2.00000	-
Aeolian silt+sand	2.00000	2.00000	2.00000	2.00000	2.00000	0.88820	1.52351	2.00000	1.94737	2.00000

Table 6.16 Transformed divergence separability test of Brovey transformed images using bands 7, 5, 1, and JERS-1 SAR.



Figure 6.22 Brovey transformed colour composite image using the TM spectral bands 7, 5, 1, and the JERS-1 SAR after being 5 by 5 Frost filtered and automatically stretched. The TM bands are BCET stretched.

6.9 Data fusion using the principal component transform

The principal component transform (PCT) is a well known technique used in statistics as a multivariate analysis method used for highly correlated data [116]. The technique uses the eigenvectors of the covariance matrix (or the correlation matrix if the PCT is standardised to reduce the lower PCs noise) as multiplication factors to produce a new uncorrelated data set. The mathematical derivation of the PCT is shown in appendix A-5.

The principal component transform in multispectral/multisensor image data fusion relies on the dominant information in whole spectral bands (i.e. topographic and spatial information) being gathered in the first principal component transformed image. This characteristic means that the PCT is a valuable technique for separation of the spatial from the spectral information. Its drawback is that it is scene dependent as a result of using the covariance or correlation matrix, and hence two adjacent PC transformed scenes cannot be mosaicked because these scenes will not be matched because of their colour differences.

There are two ways to use the PCT technique to display the fused image data as a colour composite image. One is neglecting the first principal component and using only the second and the third principal components, replacing the first principal component by the SAR image. The second is performing the PCT on the selected colour composite and replacing the first PC with the SAR image and then reversing the SAR, the second and the third PCs by the use of the transpose matrix of the eigenvectors of the original input bands to achieve (to some extent) the original colour composite but with the insertion of the SAR image.

The second method used for the PCT fusion has been used on the spectral coded colour composite image with the insertion of the 5 by 5 Frost filtered SAR image. Figure 6.23 shows the reversed PCT of the spectral coded colour composite data set after replacing the first principal component by the 5 by 5 Frost filtered SAR image. From figure 6.23,

to some extent, the texture of the rock classes is well presented as well as the spectral information of many rock units. Conversely, some of the rock classes may be difficult to differentiate, these include: Jurfayn; Atiyah; and Nutaysh. Other rock units are clearly demonstrated, these include: Musayr (in magenta to light blue); Bad'; and the Quaternary deposits which can be differentiated texturally rather than spectrally. Quantitatively, separability test of this method of fusion is shown in table 6.17. From the table, seven class pairs are inseparable, the average separability is 1.92666, the minimum separability is 0.76478, and finally the maximum separability is 2.0.

Class	Jurfayn	Atiyah	Musayr	Nutaysh	Bad'	Lisan	Conglo.+ Gravel	Gravel Sheets	Sabkhah	Alluvium
Atiyah	0.76478	-	-	-	-	-	-	-	-	-
Musayr	2.00000	1.85017	-	-	-	-	-	-	-	-
Nutaysh	1.99534	1.29954	1.58817	-	-	-	-	-	-	-
Bad'	2.00000	1.99999	1.93321	1.99137	-	-	-	-	-	-
Lisan	2.00000	2.00000	2.00000	2.00000	2.00000	-	-	-	-	-
Conglo. +Gravel	2.00000	2.00000	1.99992	1.99985	1.99999	1.99688	-	-	-	-
Gravel Sheets	1.99490	1.89767	1.99622	1.88799	2.00000	2.00000	1.99974	-	-	-
Sabkhah	2.00000	2.00000	2.00000	2.00000	2.00000	2.00000	2.00000	2.00000	-	-
Alluvium	2.00000	2.00000	2.00000	2.00000	2.00000	0.77459	1.99991	2.00000	2.00000	-
Aeolian silt+sand	2.00000	2.00000	2.00000	2.00000	2.00000	1.99704	2.00000	2.00000	2.00000	1.99926

Table 6.17 Transformed divergence separability test of the reversed principal component transform using the input image data: the six TM spectral coded image; the albedo and topographic information image; and the range image. The first principal component output is replace by 5 by 5 Frost and automatic stretched image.

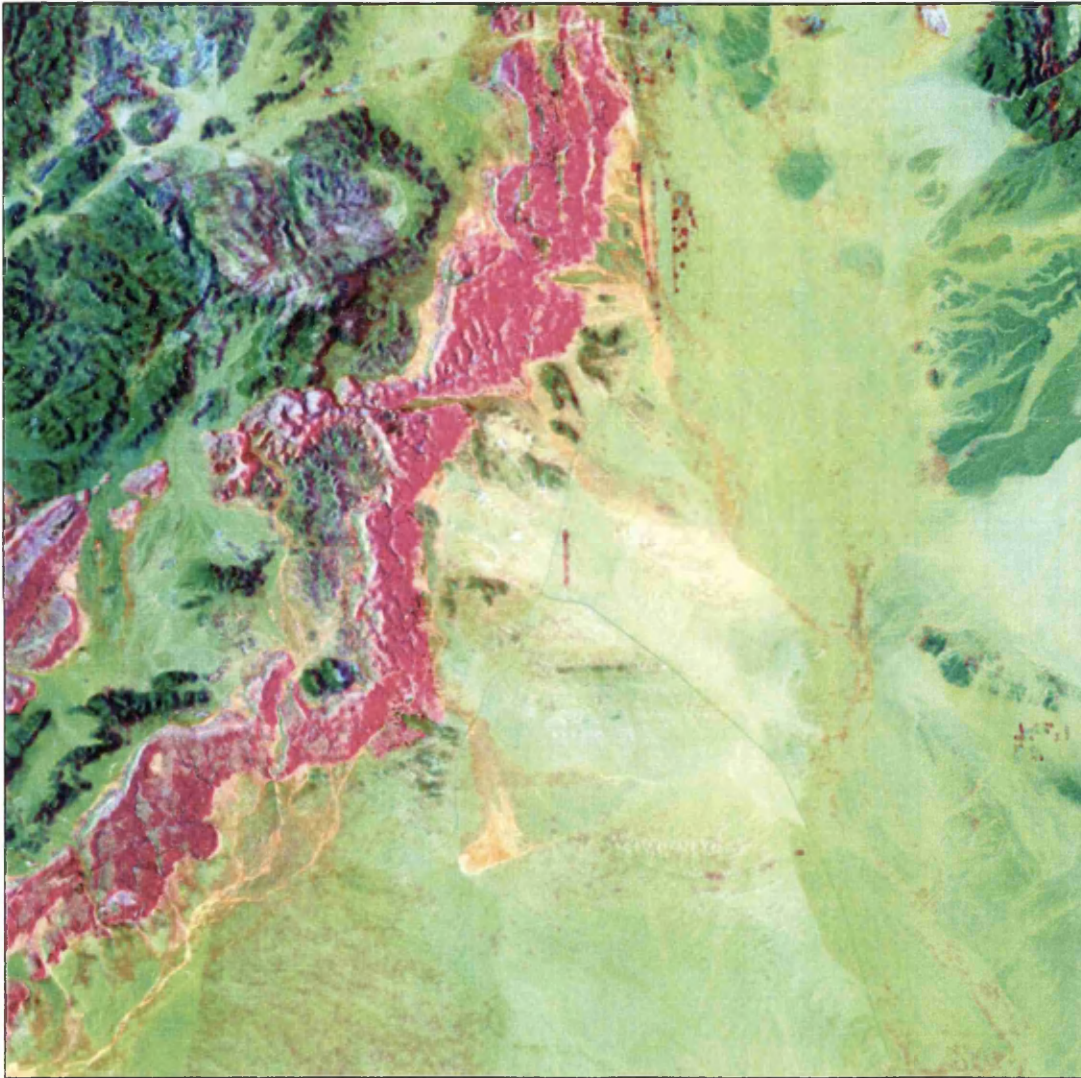


Figure 6.23 Reversed principal components transformed applied on the six TM spectral coded colour composite image after replacing the first principal component by the JERS-1 SAR after being 5 by 5 Frost filtered and automatically stretched.

In figure 6.24 for comparison purposes, and using the same technique but using the original TM bands 7, 5, and 1 after being BCET stretched. The output image may shows better representation of the rock classes (spectrally and texturally), an example is the Jurfayn rock unit which became more distinguishable comparing with figure 6.23, other rock classes also clear and easily to map as well as in figure 6.23. Quantitatively and from table 6.18, there are eight pairs of classes still inseparable (comparing with seven pairs in table 6.17), the minimum separability is 0.50371, the average separability is 1.89907, and the maximum separability is 2.0.

Class	Jurfayn	Atiyah	Musayr	Nutaysh	Bad'	Lisan	Conglo.+ Gravel	Gravel Sheets	Sabkhah	Alluvium
Atiyah	1.76207	-	-	-	-	-	-	-	-	-
Musayr	1.99882	1.20285	-	-	-	-	-	-	-	-
Nutaysh	1.81987	0.50371	1.53904	-	-	-	-	-	-	-
Bad'	1.99890	1.95643	1.99609	1.99163	-	-	-	-	-	-
Lisan	2.00000	1.99984	1.99940	1.99996	2.00000	-	-	-	-	-
Conglo.+ Gravel	1.99726	1.98081	1.99831	1.95805	2.00000	1.95095	-	-	-	-
Gravel Sheets	1.96181	1.98617	1.99908	1.97773	2.00000	1.99813	1.54308	-	-	-
Sabkhah	2.00000	2.00000	2.00000	2.00000	2.00000	1.99166	1.97666	1.99663	-	-
Alluvium	2.00000	2.00000	2.00000	2.00000	2.00000	1.99971	2.00000	2.00000	1.99990	-
Aeolian silt+sand	2.00000	1.99974	1.99979	1.99987	2.00000	0.56898	1.84031	1.98850	1.96700	1.99992

Table 6.18 Transformed divergence separability test of the reversed principal component transform using the input image data of TM bands 7, 5, and 1. The first principal component output is replace by 5 by 5 Frost filtered and automatic stretched image.

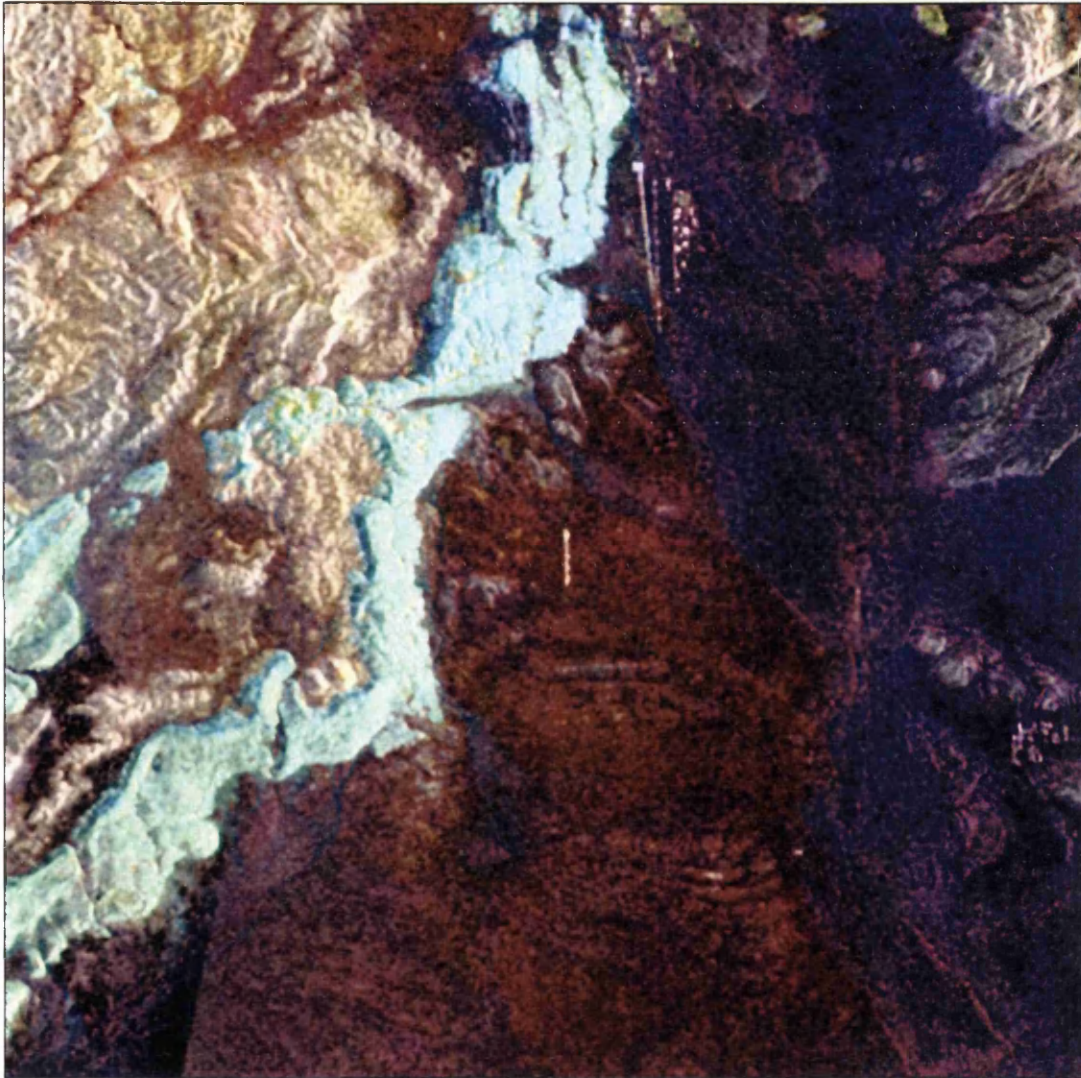


Figure 6.24 Reversed principal components transformed colour composite image using the TM spectral bands 7, 5, 1, and replacing the first principal component by the JERS-1 SAR after being 5 by 5 Frost filtered and automatically stretched.

As a result of producing the colour composites, the spectral coded colour composite, the fused colour composites, a visual analysis of these images supported by previous field visit, a new proposed lithologic map of the test site is given in figure 6.25 noting that most of the rock units are delineated using the six TM spectral coded colour composite, the reversed IHS \Rightarrow RGB TM spectral coded colour composite, and the fused image data with SAR. The displayed colour composites were also taken into account during the construction of the lithologic map.

6.10 Conclusions and remarks

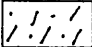



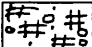
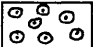
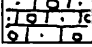
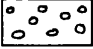
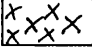

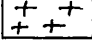
From the images and the separability test tables shown throughout this chapter, it is possible to come up with the following conclusions and hints:-

- 1- Visual recognition of classes and separabilities between pair of classes vary from one colour composite combination to another, but some classes become well separable (visually and quantitatively) with low colour combination ranks using the statistical methods of colour composite selection. The best example is the colour combination of TM bands 4, 3, and 2 (the lowest ranking) gives very good results visually and quantitatively in separation between the class pair Atiyah-Nutaysh with separability of 1.79328 (table 6.6). This number could not be gained even using all TM data when tested for separability.
- 2- The best colour composite band combination shown was the TM bands 7, 5, and 1. In this combination there are two pairs of classes are inseparable. This leads to the idea of not using colour composites for automated mapping (classification), unless all pairs of classes are perfectly separable.
- 3- The use of all the spectral image data (all 6 TM bands) does not necessary increase classes separability. An example is band combination 4, 3, and 2 for class pair Atiyah-Nutaysh and the same class pair using all TM data (table 6.3).
- 4- The new method of the six TM spectral colour coding technique shows a good way of producing colour composites. No colour composite bands combination can show good

separability as the new method of producing spectral colour coded composite. For comparison, the colour composite of combination 4, 3, and 2 shows seven pair of classes are inseparable, the colour composite 5, 3, and 1 shows three pair of classes inseparable, even the best colour composite combination using bands 7, 5, and 1 gives two pair of classes inseparable. In the case of the new method of spectral colour coded composite, it shows only one pair of classes is inseparable but this is due to the nature of this pair of classes (inseparable using all bands or using any combination, but may vary from combination to combination).

- 5- Colour transform, and PCT technique for data fusion reduce (quantitatively) the separability between classes, this is due to increasing the class dispersion (standard deviation) during the transformation process.
- 6- Quantitatively, the fused spectral coded colour composite with SAR image data shows better separabilities (less inseparable class pairs) compared with the fused colour composite of bands 7, 5, and 1 when fused with SAR.
- 7- All fused colour composite should not be used as input for automated mapping (classification).
- 8- The spectral coding method for producing colour composite is new and sound approach for colour composite production. It is a simple and fast procedure, but its limitation is of very little loss of class pairs separability which means it is not an error free method.

Legend

6		Lisan	11		Aeolian silt and sand
5		Bad'	10		Sabkhal
4		Nutaysh	9		Conglomerate and gravel
3		Musayr	8		Gravel sheets
2		Atiyah	7		Alluvium
1		Jurfayn			

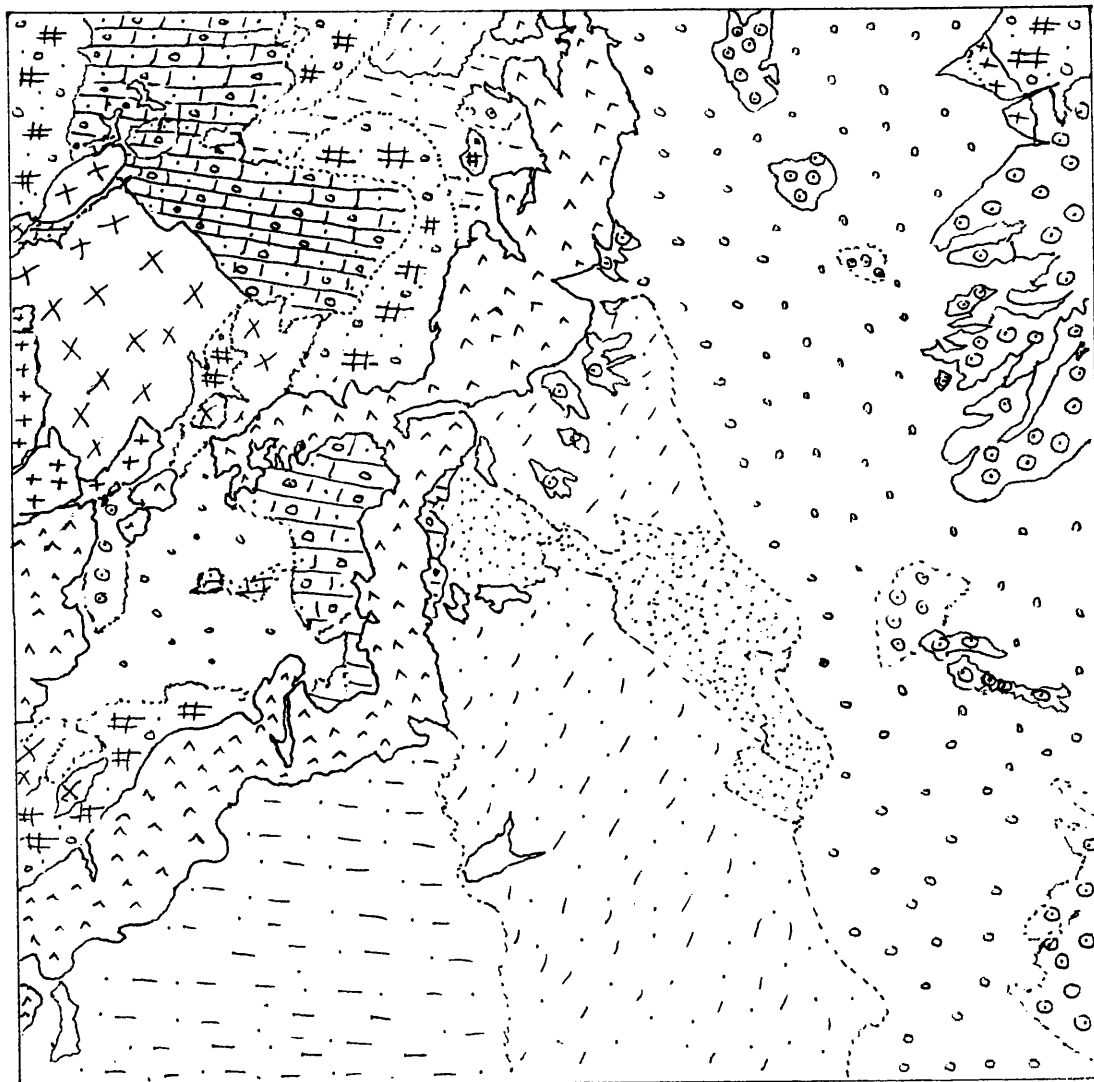


Figure 6.25 An interpretation lithologic map of the test site.

Scale 1:204084

7.0 Image data fusion for automated mapping

The motivation of image data fusion for multisensor imaging systems is for visual optimisation and automated mapping with accurate classification. For visual optimisation, the goal is to generate an interpretation of the scene not obtainable with data from a single imaging sensor, investigated in chapter 6. For automated mapping (classification), the goal is to reduce uncertainty associated with the data from individual sensors, and hence reduce the classification error rate.

The scheme of image data fusion as an aid to accurate classification in this thesis involves many steps. Firstly and by the use of all image data from both sensors (6 TM image bands and 7 GLCM texture measures, the 6 TM spectral bands, and the 7 GLCM texture measures), the transformed divergence separability test results were assessed to obtain general idea of the accuracy of the results. The second step is the use of the classifier with the use of new approach of selecting the classified pixels based on the sequential maximum likelihood classification. Traditional post-classification smoothing procedures for the classified pixels during classification were also used. All of these steps will be discussed in the appropriate sections and the previous work in image data fusion for classification is also given in this chapter.

7.1 The maximum likelihood classifier

Image classification refers to the automatic labelling of every image pixel to a specific thematic group, based on the comparison of the pixel signature to specific statistical characteristics (classes). The result is a thematic map showing all types and geographic location and distribution of these classes. Important steps have to be carefully followed in the remote sensing image classification procedures, including the appropriate classification scheme or level of details, the selection of training areas and their sizes, the proper manipulation for the input spectral and spatial input images and test of classes separability, the selection of the classification algorithm and the post classification filtering and finally the classification accuracy assessment [18].

The labelling process in image classification can be achieved using two methods, one where the information classes are selected by the user and their statistics are determined, called supervised classification. The second method is that the computer itself determines clusters or groups of pixels having distinguishable and common statistical characteristics, and this method is called unsupervised classification. Unsupervised classification is usually used when there is no information about the classes in the studied images and it is usually not preferable because the classes created are thematically unknown and variable. Many clustering algorithms are used in unsupervised classification, including the ISODATA algorithm which is based on the split and merge in the iteration procedures. Other algorithms include the clusters means such the k-means clustering algorithm, and finally an algorithm called the Narendra-Goldberg clustering algorithm which uses the peaks and valleys of the multidimensional histogram created from the n -bands used [142].

Within supervised classifiers, three types are well known. These are the minimum distance to the mean, the parallelepiped classifier and the maximum likelihood classifier. The minimum distance to mean classifier (sometimes termed the centroid classifier) assigns each pixel to the closest class mean. Its drawback is that it does not take into account the classes variability, which causes a dispersion in the class cluster. The second (parallelepiped) classifier uses the class dispersion (the standard deviation) and the mean of the class cluster. It gives better results than the minimum-distance-to-mean but its problem comes when the dispersion of the classes clusters are overlapped and in this case the labelled pixels which exist in these overlapped areas will be uncertainly classified. The third classifier is the maximum likelihood decision rule classifier which uses the mean, the dispersion and the correlation between classes clusters. The maximum likelihood classifier (MLC) is the most appropriate and accurate labelling algorithm used in image classification [18,41,142].

The maximum likelihood classification may use a discriminant function rule such as the Mahalanobis distance, as shown in equation (7.9), which is applied in this thesis. The process of the MLC is classifying the entry pixel vector X to the class C if and only if:-

$P_c \geq P_i$ where $i = 1, 2, 3, 4, \dots, C$ possible classes.

$$P_c = -0.5[X - \mu_i]^T [Cov_i]^{-1} [X - \mu_i] - \left\{ \frac{n}{2} \log 2\pi \right\} - (0.5 \log |D_i|) \quad (7.9)$$

where:

μ_i = vector mean of the class i .

Cov_i = covariance matrix of the class i .

n = number of image channels used.

D_i = determinant of the covariance Cov_i .

For example, to classify the unknown pixel vector X into a class, the MLC decision rule computes the values P_c for each class previously defined, and then assigns the pixel vector X to the class that has largest value to that class.

The *a priori* information (i.e. a weighting represents the probability associated with each class) can be included in the MLC discriminant function by the user for each class to bias some classes over the others. It can be included in the equation (7.9) as $+\log(\text{Pr}_i)$ where:-

$$\text{Pr}_i = \frac{W_i}{\sum_{i=1}^c W_i}, \quad W \text{ is a weighting number introduced for every class } i.$$

7.2 The post classification filtering

The classified image is usually contaminated by single pixels or very small groups of pixels that are classified to a class that is surrounded by a larger class. These pixels are called island themes [41] and are usually a classification error which may result from contaminated spectral signatures, imaging system errors, shadowing, or the misregistration between the bands used. Many techniques can be used to filter these

errors out. The well known filters used are the mode filter and the sieve filter. The mode filter replaces the pixel's brightness value by its most frequent occurring value (i.e. its surrounding) within a specified window. The sieve filter is more sophisticated for removing the island themes, by merging the small group of pixels by their largest ones and preserve edges in the same time. Both these filters have been tested, and it was found that the sieve filter is most adequate because it preserves the linear or the small elongated theme classes.

7.3 Previous work in classification

Several methods have been used in the past to classify multisource data. The following shows some of this work.

Kaufman and Pfeiffer [120] compared image optimisation versus classification procedures using two different test sites. One is the south of Saudi Arabia, and the second is the Rhine-Graben area in Germany. They found that for applications where structural information is the goal (i.e. geology), the optimised image products are preferred because relief information is preserved. Classification is superior if the goal is identifying surface signatures over wide areas.

Metternicht [121] discussed the problem of how to deal with insufficient discrimination among classes using fused SPOT XS and ERS-1 SAR image data in the Flevoland area of the Netherlands. A combination of supervised and unsupervised (clustering) is used for training area selection to form a hybrid strategy for maximum likelihood classification. He claimed that the training areas selection is a very important part in classification and any inadequate method used in training class selection could lead to an erroneous class determination.

A new statistical classification approach based on the Bayesian method of multi-source image data fusion, taking into account the temporal changes during the image acquisition has been proposed by Solberg *et. al.* [122]. The performance of this approach showed

significant improvements in the error rate by testing it using Landsat TM and ERS-1 SAR for land-use classification over an area of Kjeller, Norway.

Munehika *et. al.* [104] used a simple mathematical combination method (termed the ratio method) between Landsat TM and SPOT XS and Panchromatic image data. This method was used to improve the radiometric image integrity. Results show visually improved images and improvement in classification accuracy of 6% using a maximum likelihood classifier. Images from Rochester, New York were used in the study.

Revision of combination techniques of satellite images and ancillary data to improve classification has been illustrated by Hutchinson [75]. These techniques include: preclassification scene stratification, classification modification (i.e. modifying prior probabilities) and postclassification class sorting. He found that the stratification method is deterministic and cannot accommodate gradations between strata (areas), and because this method of combination is performed before classification, incorrect classification can invalidate the entire classification. The modified priors combination used during the classification needs intensive sampling, which is somewhat beyond that which is conducted in normal spectral classification. The postclassification sorting is a new technique and is used in geographic information systems. As suggested, it is conceptually simple and easily implemented but it is also deterministic. However, it offers some advantages in that it only deals with only problem classes, and errors resulting from the sorting role can be corrected easily.

Lozano-Garcia *et. al.* [123] studied the effects of combining SAR with optical data, investigating if there are any improvements in the classification results using combined SIR-B SAR with different viewing angles, and Landsat TM data mapping the forest cover east of the Lake City, Florida. Firstly, they found in the preliminary results that the performance of per-pixel classifier algorithms will not be satisfactory if speckle is not removed from the SAR data, hence a median filter with two iterations was applied to the SAR data. In the training process, two methods were used for TM, and combined TM and SAR. For the TM data alone, clustering was used to develop training statistics. In the

study, two classification methods were also used. One is by the use of the Maximum Likelihood Classifier (MLC), the other algorithm is a contextual classifier called ECHO (Extraction and Classification of Homogenous Objects). ECHO uses an algorithm that merges adjacent pixels that are found to be similar according to certain statistical criteria. Separability between classes was intensively tested for band combinations during the classification evaluations, and it was found that increasing the number of bands does not necessarily improve classification accuracy. Some improvements have been achieved using the ECHO classifier in the appearance of the resulted classified images. The ECHO classifier has been illustrated and fully described by Landgrebe [124].

Nezry *et. al.* [88] combined SIR-B and optical SPOT-1 XS data for classifying vegetation of central Sumatra, Indonesia. Speckle reduction was performed first on a SAR image, then the maximum likelihood classifier was used on the combined data classifying the tropical vegetation of the study area.

Ari [125] suggested a new approach classifying spectral/spatial data with high class variability by the use of statistics of a small spatial window in the image, which can be used in a unified way with the Gaussian statistics of the spectral data. TM data has been used in the study and 7% increased accuracy has been achieved using the MLC technique.

Dobson *et. al.* [126] combined ERS-1 and JERS-1 SAR data for a knowledge based classification method of mapping the vegetation cover of an area adjacent to Lake Superior, Michigan. Results were then compared with AVHRR NDVI (Advanced Very High Resolution Radiometer Normalised Deference Vegetation Indices) based classification combined with ancillary data. Comparison results shows that the combined SAR data are superior to AVHRR where 94% accuracy has been achieved.

Lobo *et. al.* [127] combined ERS-1 SAR and Landsat TM image data to classify agricultural and land use regions in the Ebro valley, north east of Spain. A combination of image segmentation, linear canonical discriminant analysis and tasselled cap

transforms were used on the imagery data with the combination of a MLC techniques to segment, and classify the data.

Gong *et. al.* [128] developed a new contextual classification procedure for land-use mapping. Their method involves many steps including: frequency table generation, the reduction of the n-bands multispectral data to a limited grey level single band image through the use of a modified algorithm of PCT (named eigen-based level vector reduction), training area selection and finally the minimum-distance classifier using city-block metric. SPOT XS was used to implement this technique to map the town of Markham, northeastern rural-urban fringe of Metropolitan, Toronto. A previous study has also been carried out by the same authors [129] of using the spatial information to improve the classification using the same satellite data over the same area of study. In this technique, they applied Laplacian high pass filtering and thresholding the band 1 to extract the structural information. Together with the first and second PCT images, the three bands were then classified using the minimum distance to mean classifier after selecting the appropriate land-cover classes. They showed that their overall classification accuracy has increased from 76.6% to 86.1% by the use of structural enhanced band used as spatial input in the classification.

Fung *et. al.* [130] illustrated that the spatial classes of land-cover and land-use consist of many spectral classes. These classes can be extracted by implementing a spatial filter on the derived spectral classes image. A per-pixel conventional method of classification is firstly used to derive the spectral classes. They implement this technique using a small image acquired by SPOT XS over Hong Kong.

Pultz *et. al.* [131] used SAR image texture measures of the GLCM to classify an agricultural area of Melfort, Canada. Two different SAR images (with different wavelength, polarisation, and incident angle) were used in their study after implementing smoothing filtering to reduce speckle. Raw, filtered, and texture images were all used for MLC to produce the classified image.

Benediktsson *et. al.* [132] added one step ahead in multisource classification by comparing statistical classification methods with neural network methods. They modified the statistical Bayesian classification algorithm by adding the concept of reliability weightings based on the separability of the features. They finally compared the statistical measures including the minimum-distance to mean, MLC and the modified Bayesian classifier with the neural network classifier using the delta rule and generalised delta rule algorithms. Comparisons have been made on MSS image data, elevation data, and slope and aspect data over a mountainous small area in Colorado. The results of their work showed that neural network method employing the generalised delta rule has a great potential as a pattern recognition method for multisource remote sensing data, but its drawback is complexity in computation and its learning time which can be long if a large amount of data is used. The modified Bayesian statistical method works well for combining multisource data and gave significant improvement in the overall classification accuracy.

A complex mountainous environment classification has been undertaken using three stages of operation as proposed by Franklin *et. al.* [133-134]. These stages include quadtree segmentation where the image is subdivided into four equal quads successively, then each quad is tested for homogeneity after the successive partitioning. If the quad passes the test, the entire quad is then classified. If the quad fails, further partitioning is made, and so on until the one pixel level is reached. The homogeneity test uses the coefficient of variation and range statistics. The second stage of classification is the minimum-distance-to-mean classifier. In this stage, pixels that have not been segmented in the first stage may be handled by the second step using the per-pixel classifier. In stage three of the classification process, where some pixels may not be correctly identified in prior stages, a new test including ancillary information or by examining their spectral curves or classify them as borders if they exist between two classes. They tested their approach using a mountainous area south of Yukon, Canada, using SPOT XS and DEM data.

The knowledge based expert system is currently one of the new trends for image classification using combined spectral and spatial information. Johnsson [135] showed a good example of such a technique using SPOT image data for land-use classification. The steps within such a technique are rather long, involving spectral classification, determination of size and neighbour relations for the segments in the spectrally classified image, and rule-based classification of the image segments into land-use categories. In the rule-based classification phase, the image segments are treated as objects with a set of properties. Such a technique involves a conversion from a raster format to a list of objects and vice versa.

Usually, non-classified pixels which show salt and pepper appearance of the classified images are removed using modal spatial filtering technique. Wang *et. al.* [136] used a new filtering technique as post processing on the classified image to remove such unclassified pixels and small polygons, and at the same time preserving class edges, corners, and small linear classes. They used a convolution filter of size one pixel inside a larger window frame (i.e. 3 by 3, 4 by 4, etc.) which process unclassified pixels based on their surrounding classes. Many iterations can be implemented on the classified scene. They demonstrated their technique using airborne C-band multipolarisation data acquired over agricultural area south of Ontario, Canada. Classification has been carried out using the MLC algorithm.

Wang *et. al.* [137] proposed a new error assessment methodology in classification accuracy which resulted from the uncertainties in training areas by the use of many training trails and calculating the RMSE (Root Mean Square Error) pixels. Accuracy is then converted to percentage by dividing the RMSE pixels by the entire image pixels.

Image classification accuracy assessment and factors controlling the accuracy has been reviewed in detail by Congalton [138]. He reported that as recently as the early 1980s many classification studies only report a single number to express the accuracy of classification as an overall accuracy. Such a number is misleading because it does not show accuracy within every class or category. He recommends the use of the error matrix

(also called confusion matrix) after using an appropriate fitting procedure or normalisation of the matrix to eliminate the differences in the sample sizes when the matrix is being created. Other considerations that may affect the classification accuracy assessment and should be taken into account are: ground data collection method, classification scheme or what is called level of detail, spatial autocorrelation, sample size and sampling scheme. Further to this work, Fitzgerald *et. al.* [139] introduced the idea of using the agreement level criteria using the Kappa statistic on the error matrix suggested by Congalton. Another method of displaying the classification accuracy (i.e. overall, user and producer) on the computer screen has been suggested by Fisher [140] instead of tabulating the error matrix.

7.4 The sequential approach of classification used for both the spectral and textural input data.

In this work, three data sets have been produced and used as an input for the classifier. These are: the spectral information data set (the 6 TM bands); the textural data set (the 7 textural measures of GLCM derived from JERS-1 SAR); and finally the textural-spectral data set (6 TM bands and 7 textural GLCM measures). The transformed divergence separability tests were firstly investigated prior implementing the MLC. This is for two reasons: one is to know how the SAR textural data contributes separability in the spectral data and secondly; the contribution of separability is used as a judgement of detecting the pixels of uncertainty (on other word the performance of the sequential classification). The transformed divergence separability test using all of TM and seven textural measures of GLCM is shown in table 7.1. Note how separability between classes pairs increased giving the means of using textural information with spectral information. From the table, the average separability is 1.99797, the minimum separability is 1.92295, and the maximum separability is 2.0. Furthermore, note how the classes pair Atiyah-Nutaysh became separable using textural information. If the TM spectral information used alone, this classes pair will never be separable and accurately classified (refer to table 6.3 in page 141 for comparison).

Class	Jurfayn	Atiyah	Musayr	Nutaysh	Bad'	Lisan	Conglo.+ Gravel	Gravel Sheets	Sabkhhah	Alluvium
Atiyah	198775	-	-	-	-	-	-	-	-	-
Musayr	200000	199997	-	-	-	-	-	-	-	-
Nutaysh	199999	192295	197836	-	-	-	-	-	-	-
Bad'	200000	200000	200000	200000	-	-	-	-	-	-
Lisan	200000	200000	200000	200000	200000	-	-	-	-	-
Conglo.+ Gravel	200000	200000	200000	200000	200000	199958	-	-	-	-
Gravel Sheets	200000	200000	200000	200000	200000	200000	200000	-	-	-
Sabkhhah	200000	200000	200000	200000	200000	200000	200000	200000	-	-
Alluvium	200000	200000	200000	200000	200000	200000	200000	200000	200000	-
Aeolian silt+sand	200000	200000	200000	200000	200000	199954	200000	200000	200000	200000

Table 7.1 Transformed divergence separability test using both of all TM bands (1-5,7) and the seven GLCM textural measures between the training areas of the test site. The TM data is BCET stretched and the GLCM measures are automatically stretched.

The sequential (staged) classification approach adopted in this thesis for the first time is used to take into account the following issues: accuracy problem; geometric and systematic distortions; and finally the lithologic mapping geologic point of view. Accuracy assessment problem for example in classification is debatable, and can be evaluated in many ways, discussed in details by Congalton [138]. By the use of sequential classification, decision to classify a pixel is based on assessing the pixel if classified coincidentally using: texturally; spectrally; and texturally-spectrally taking into account the separability between classes, this kind of classification performance is used here for the first time. Geometric and systematic distortions play a major factor in textural information in particular, for example pixels which represent layover, shadows, foreshortening, or system errors cannot be classified texturally (from SAR) but can be assessed spectrally (from TM), such pixels may represent the source of errors (uncertainty) especially if their spectral separability is low (less than 1.9).

In geologic point of view, pixels cannot be classified based on their spectral information and neglecting their textural information, for example deposits such as Alluvial fans filling valleys or Wadis can be classified based on their source rock and hence become part of this rock class because they have the same spectral information as the source rock

class. By the use of the sequential classification, such pixels should be assessed spectrally (alone) and texturally (alone) and if they are classified to a particular class in both assessments, then it is believed that these pixels belong to this particular class, if not, other assessment is carried out using textural-spectral information against spectral information. If the assessment does not coincide, these pixels are either preferred to left unclassified (zero filled) or filled by the textural-spectral classified image with high degree of certainty (based on table 7.1) but not sure to be classified correctly.

The sequential classification approach used in this thesis is a logical decision making using the MLC. It works as follows: In stage zero, classify the image based on its spectral information (layer-1); classify the image based on its textural information (layer-2) and finally; classify the image based on its spectral-textural combined information (layer-3). If the pixel for example is classified texturally-spectrally (layer-3) which has high separability as shown in table 7.1 to a specific class and found spectrally (alone) still to belong to the same class (less separability as shown in table 6.3) then, this pixel is believed to belong to this particular class and should be classified to this class (coincidence of texture-spectral combined information with spectral information alone). All pixels in the image will first pass this test and the classified pixels will be stored (layer-4). In the second stage or sequence, only pixels which did not meet this criteria will go to the second test or stage which is if these pixels are classified texturally alone (low in separability as shown in table 5.1) but coincide with spectral classification (layer-1) which gives high separability, then these pixels will be classified to their particular classes. Pixels which do not coincide to this criteria will be left to zero-fill. In the third stage of test, pixels which are not classified in the earlier stages will be left unclassified (because not relying on textural information alone (low separability), spectral information alone (higher separability but not taking into account the geological point of view). The only choice will be classified based on the textural-spectral information (very good separability which came originally from the spectral information). Such pixels may be taken as “not sure but may be truly classified” and can be used (strictly) as the source of errors and statically calculated for data fusion classification performance. A schematic diagram of this sequential classification is shown in figure 7.1.

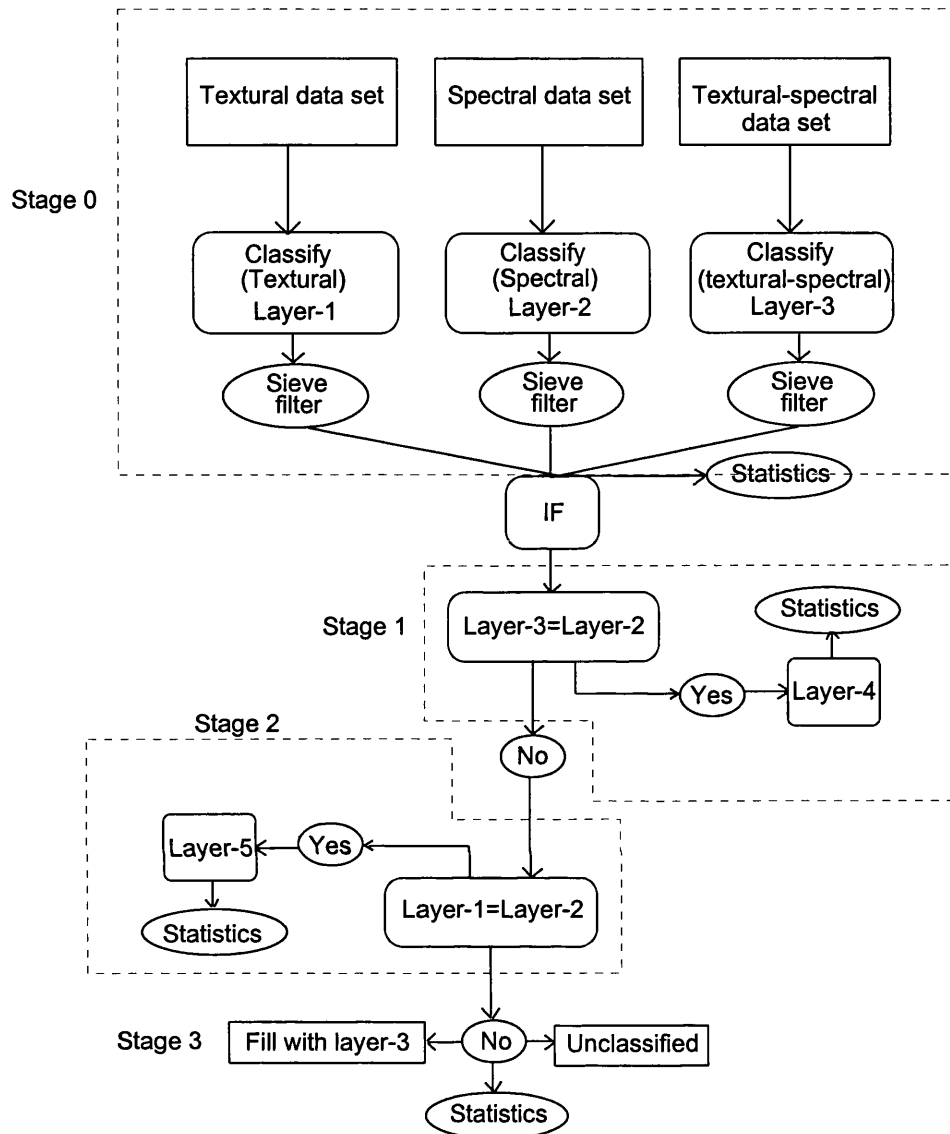


Figure 7.1 Flow diagram shows the MLC sequential classification scheme used to lithologically classify the test site.

It is important to note that the use of sequential classification is an attempt to benefit from the correctly classified pixels from textural-spectral data set which could be biased texturally either negatively or positively and make this bias only positively through the information of the spectral data set. If the pixels are found to be biased negatively, other information is used for compensation, this information is the coincidence of texture

information with spectral information data sets and replace these negatively biased pixels. If these pixels are still biased, there is no more information about them and either left unclassified or replaced by their original source. This method is not attempt of preference texture over spectral information or even textural-spectral information, it is only how to benefit from the two sensors represented by the three data sets in a constructive way.

7.5 Classification results

Running the sequential classification using MLC produces three types of data; the primary classified images (stage zero), the classified pixels of stage one and two represented by partially classified image; and the statistical calculations for each stage which include the number of classified pixels for each class, and the number of pixels not classified (i.e. no. of biased pixels). After stage 2 and in the final stage, two classified images are produced, one is the classified image produced in stage two combined with stage 1 but filling the unclassified pixels in this stage by the classified pixels produced in stage zero from the textural-spectral data set. The second classified image in this stage is the combined classified images in stage 1 and stage 2 with zero-fills of the negatively biased pixels

From stage zero, figure 7.2 represents the classified image based on the seven GCLM textural measures produced previously in chapter 5. As a result of low separability between many classes pairs, the classified image is poor but it is believed that there are many pixels are classified correctly. This is shown in figure 7.7 when the texturally classified pixels coincide with the spectrally classified pixels. Figure 7.3 shows the classified image using six TM optical spectral data only, and figure 7.4 shows the classified image using the combined information of spectral and textural data (7 GLCM textural measures and 6 TM spectral). Statistics of each classification are collected, combined and given in table 7.2.

Lithologic class name	Number of Pixels (Textural C.)	Number of Pixels (Spectral C.)	Number of Pixels (Textural-spectral C)
Jurfayn	80482	27906	21425
Atiyah	38835	63414	70690
Musayr	114545	78207	71226
Nutaysh	67475	83461	71336
Bad'	54465	183077	175582
Lisan	72780	170073	172830
Cong.+Gravel	109490	117810	132058
Gravel sheets	121634	53450	58560
Sabkhah	101359	1594	1477
Alluvium	204985	215658	213126
Aeolian silt+sand	82526	53926	60266
Σ	1048576	1048576	1048576

Table 7.2 Statistics of stage zero classification results using the seven GLCM textural measures alone, the six TM optical data alone, and the combined textural-spectral data.

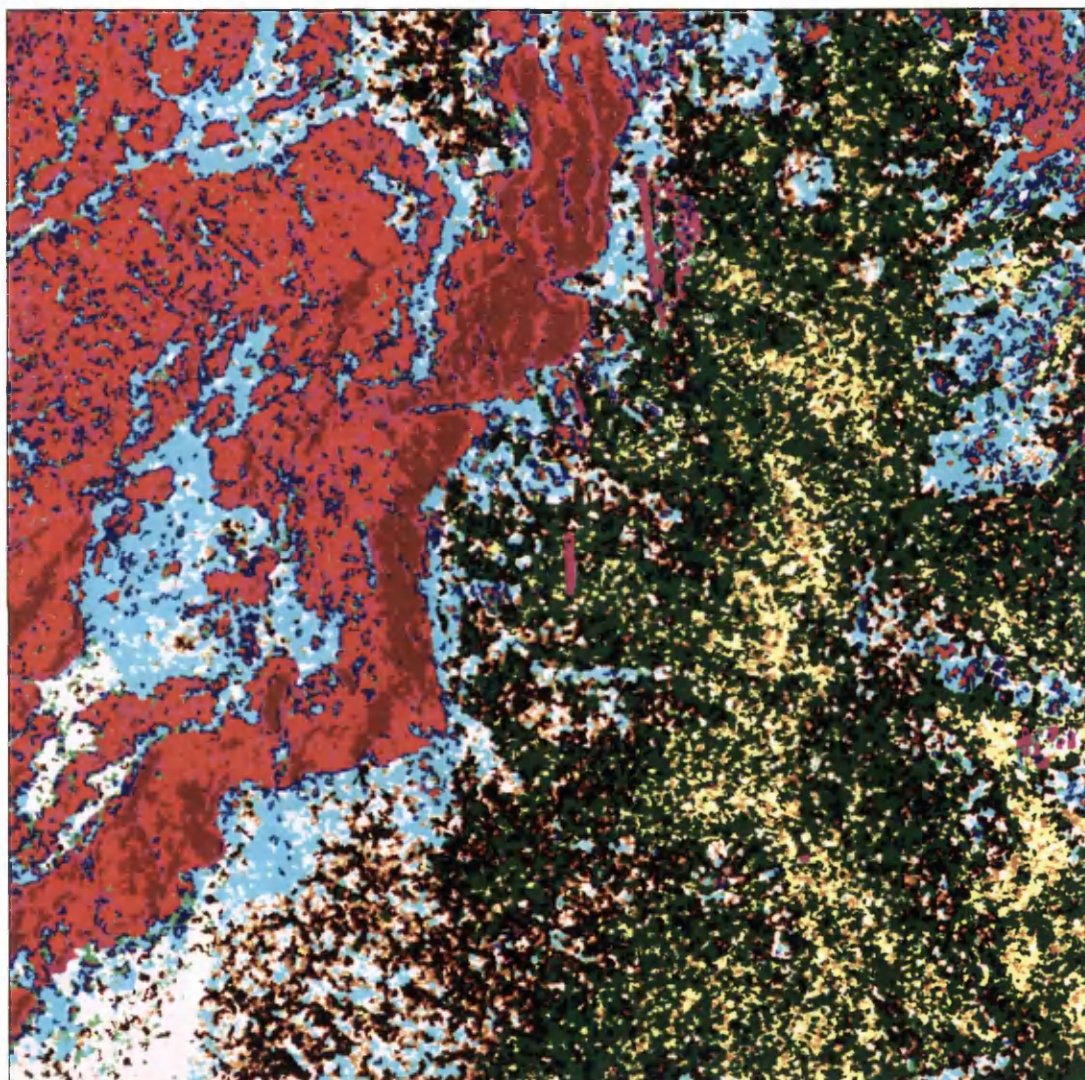
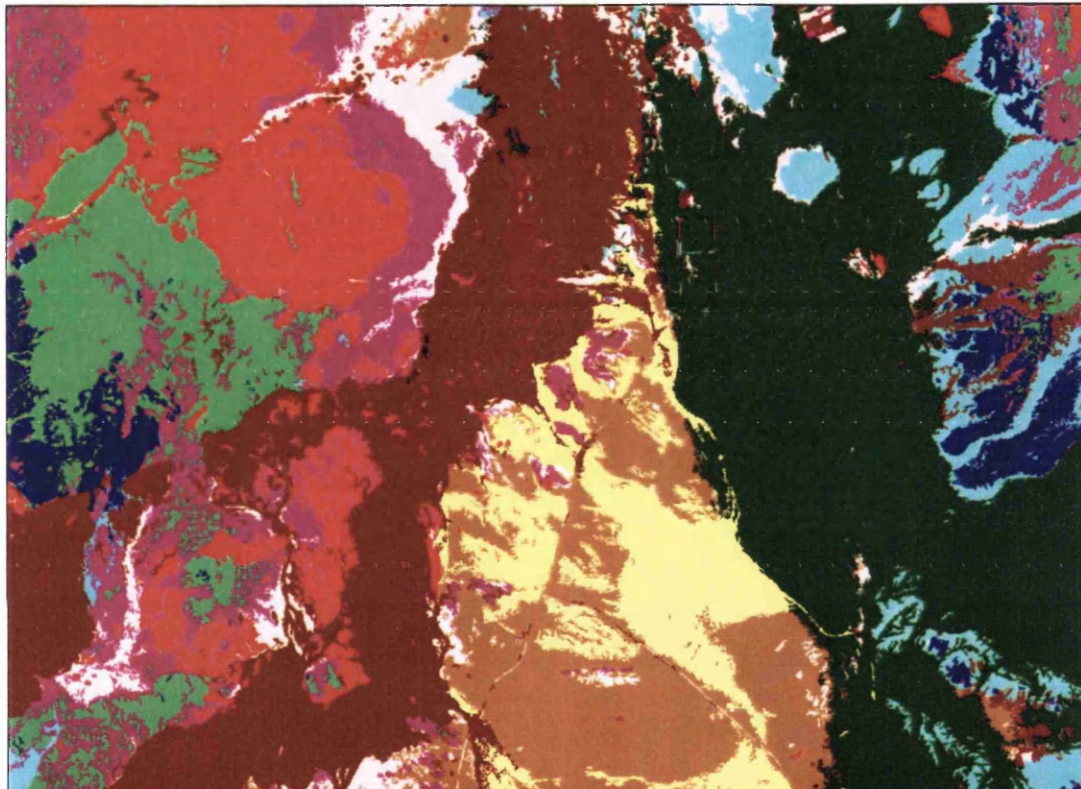


Figure 7.2 The classified image pixels of stage zero sequential classification using textural information only. Classification is poor but many pixels are classified correctly.






Scale 1:204084

Legend

	Nutaysh		Conglomerate and gravel		
	Musayr		Alluvium		Aeolian silt & sand
	Atiyah		Lisan		Gravel sheets
	Jurfayn		Bad'		Sabkhah



Legend

	Nutaysh		Conglomerate and gravel		
	Musayr		Alluvium		Aeolian silt & sand
	Atiyah		Lisan		Gravel sheets
	Jurfayn		Bad'		Sabkhah

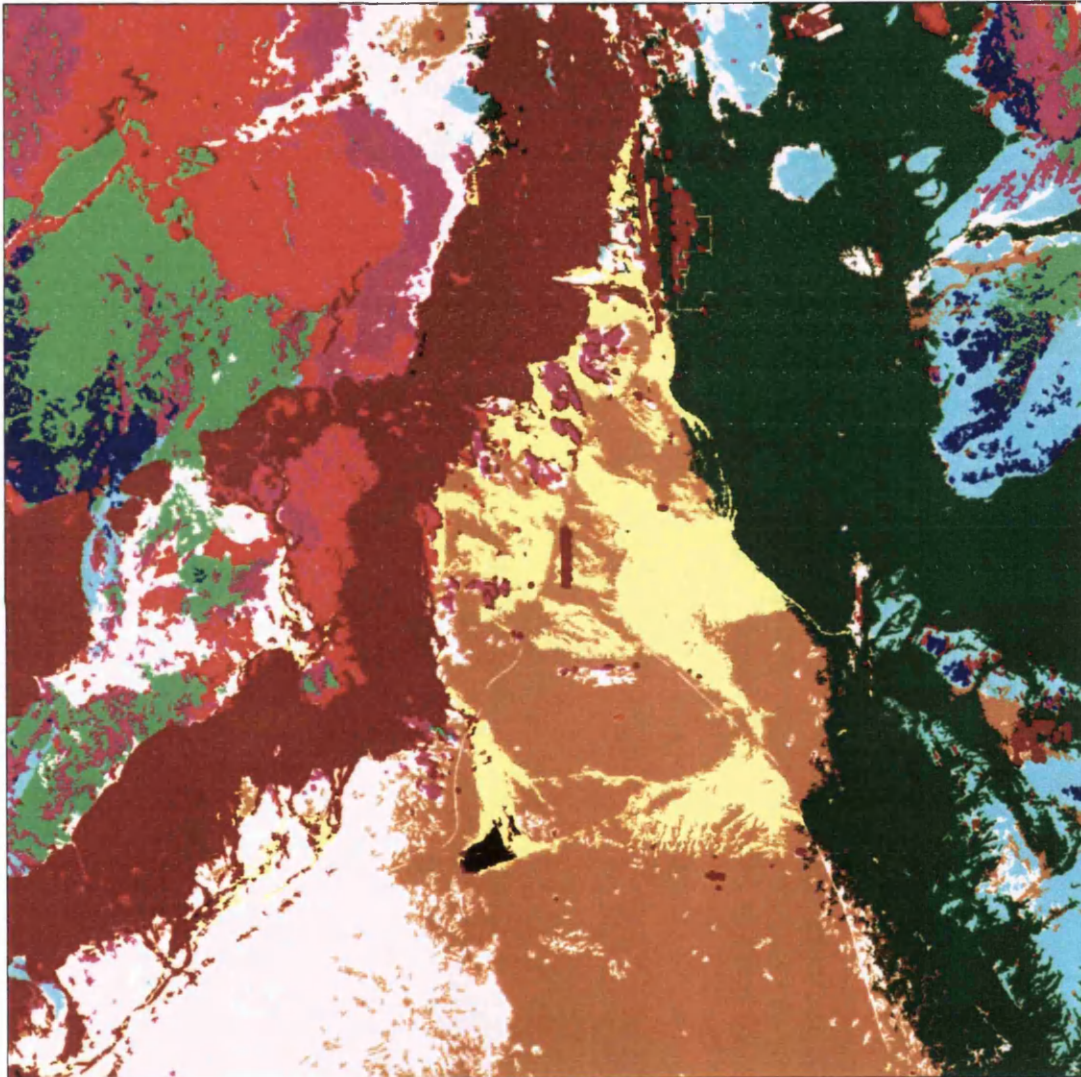


Figure 7.4 The classified image pixels of stage zero sequential classification using the textural-spectral information. Classification is good but many pixels are biased and may be classified incorrectly. This classified image is the basic image for sequential classification tests.

Scale 1:204084

In stage one sequential classification, the textural-spectral classified image (figure 7.4) will pass through the test of comparison with the spectrally classified image (figure 7.3) to detect the biased pixels and separate them for test from the classified image. Pixels which pass the test represent the spectral information alone will be preserved, pixels fails in this test are the biased pixels. This is shown in figures 7.5 and 7.6. Figure 7.5 shows the pixels passed the test and assigned to their particular classes. Figure 7.6 shows the biased pixels, the image is displayed in its binary form (black and white, black=fail, white=pass) for better visualisation. Note that these failed pixels are concentrated in the rock boundaries, valleys deposits, geometric co-registration shifts, system errors (i.e. AGC resulted from SAR system), or non lithologic materials which not included or represented by their training areas such as small farms, roads etc..

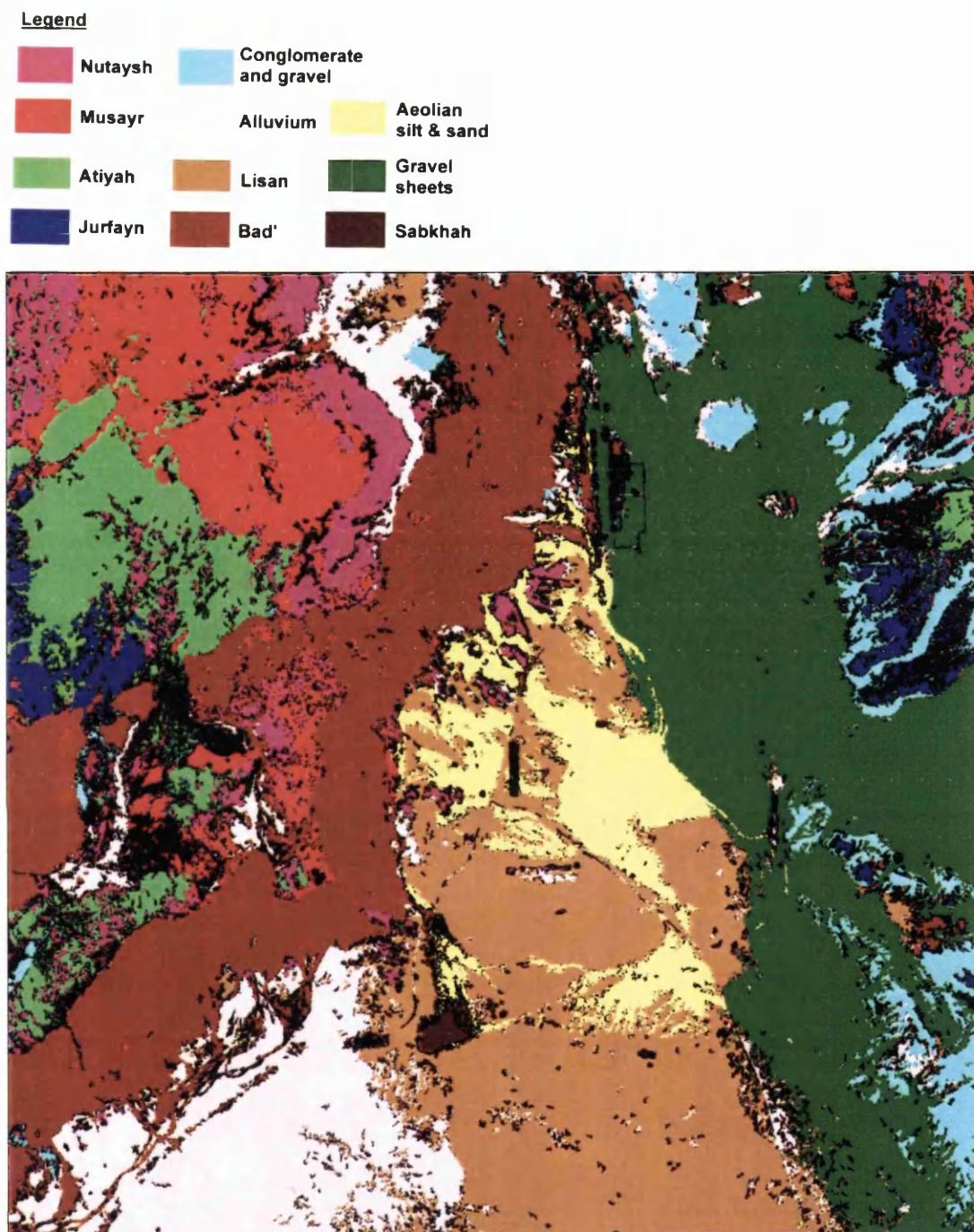


Figure 7.5 The classified image pixels of stage one sequential classification. Biased pixels are detected and set to black, non biased pixels set to their appropriate classes and no further test will be carried out on these pixels .

Scale 1:204084

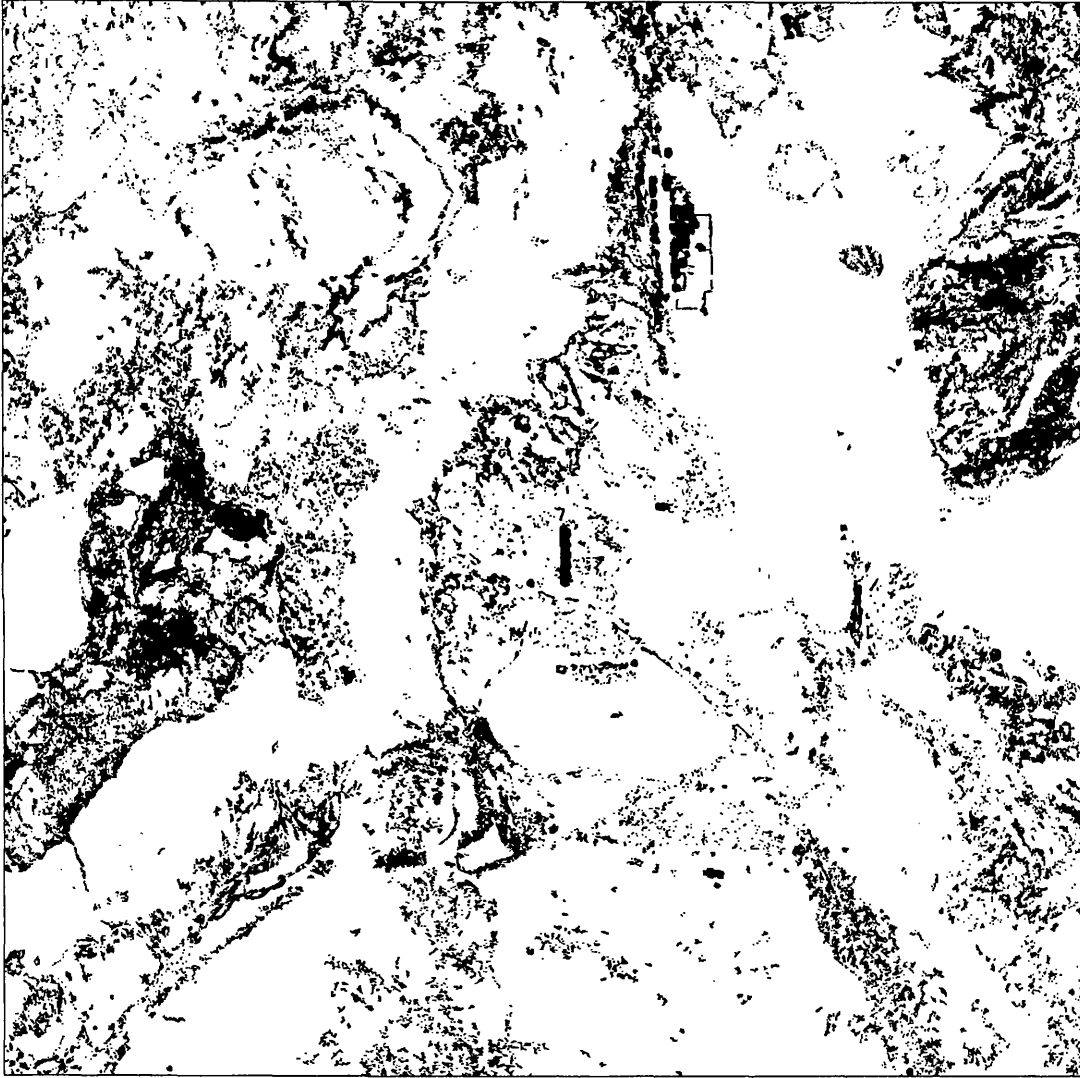


Figure 7.6 The detected biased pixels of stage one sequential classification. Biased pixels are detected and set to black, non biased pixels set to white, note that the black pixels represent patterns such as rock boundaries (spectrally contaminated classes), valley deposits, and geometric and systematic errors, etc. .

Scale 1:204084

After detecting and separating these biased pixels in the first stage, the correct texturally classified pixels have been detected in stage two from the texture classified image by using a similar test between the texturally classified image (figure 7.2) against the spectrally classified image (figure 7.3) and pixels which agree to have the same class are separated and assigned to their appropriate classes, pixels fail to agree in the test are set to black, this is shown in figure 7.7. After producing this image, and in stage three, the biased pixels of figure 7.6 will be replaced by pixels of figure 7.7. If the replaced pixels are still black (unclassified), two choices are available, either set them as negatively biased (unclassified or black) as shown in figure 7.8, or replace them by their original classes values in the textural-spectral classified image (figure 7.9).

The collected statistics during stages one, two, and three are shown in table 7.3. By simple calculation using stage 1, 2, and the final image produced in the final stage as shown in figure 7.9, every class performance is calculated after detecting the negatively biased pixels. The overall performance of this kind of classification is also given by dividing the summation of all classified pixels in stages 1 and 2 by the whole number of pixels giving a figure of 88.9% performance.

Lithologic classes	Stage 1	Stage 2	$\sum Stages$	Biased (negative)	Final	% Performance
Jurfayn	19500	563	20063	1634	21697	92.4
Atiyah	59066	83	59149	13123	72272	81.8
Musayr	66510	361	66871	4172	71043	94.1
Nutaysh	54167	272	54439	12557	66996	81.2
Bad'	159499	48	159547	15797	175344	91.0
Lisan	158478	253	158731	11572	170303	93.2
Cong.+Grvl	101241	373	101614	29130	130744	77.7
Grvl sheets	45225	289	45514	13778	59292	76.7
Sabkhah	1280	1	1281	56	1337	95.8
Alluvium	213442	979	214421	5040	219461	97.7
Aeolian silt + sand	50818	71	50889	9198	60087	84.7
Not yet classified	119350	116057	116057	116057	0	Overall = 88.9

Table 7.3 Statistics of each stage during the sequential classification of lithologic units of the test site.

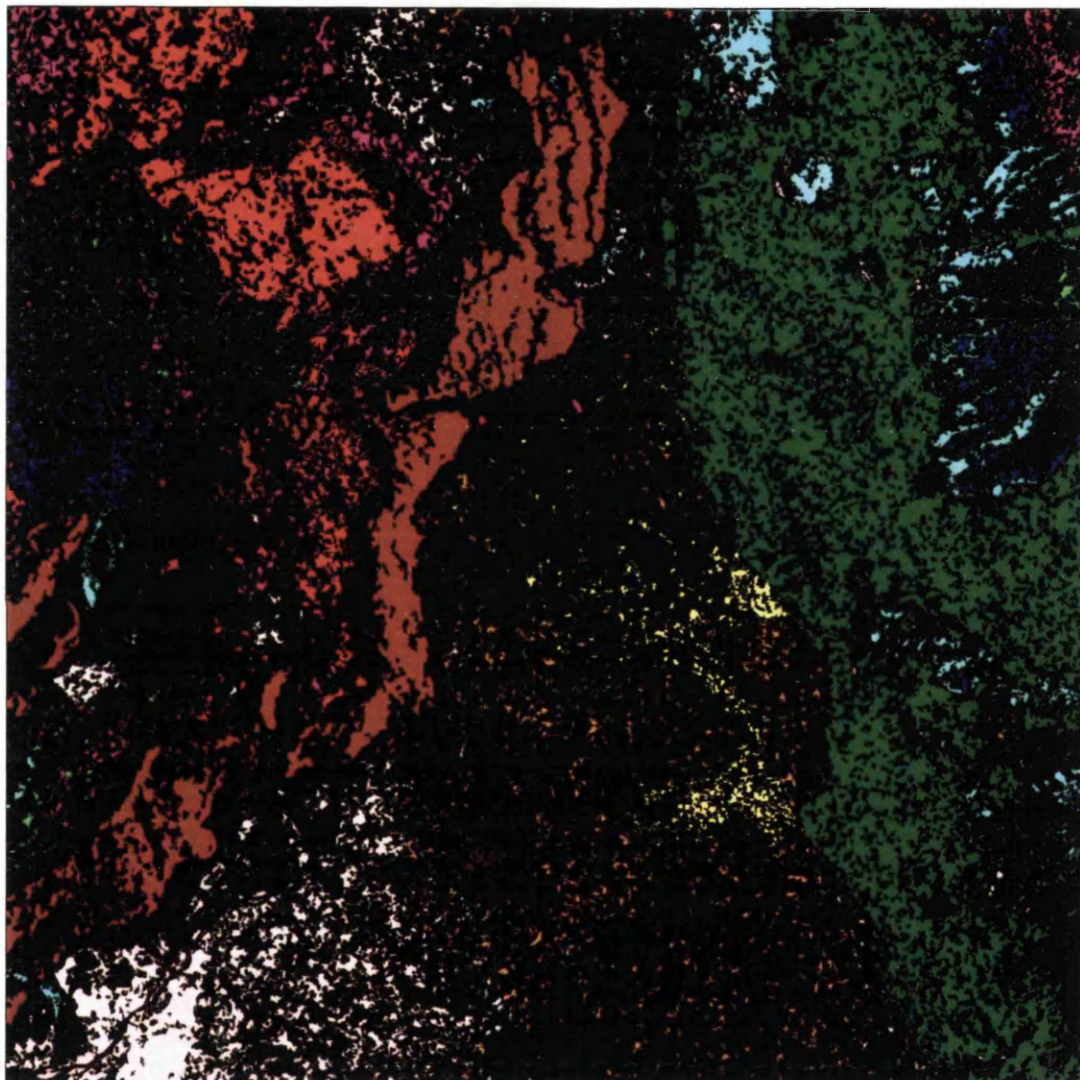


Figure 7.7 Sequential classified pixels of stage 2 showing the texturally classified pixels which agree to have the same class of the spectrally classified pixels. This image also show the correctly classified pixels texturally.

Scale 1:204084

Legend

Nutaysh	Conglomerate and gravel	
Musayr	Alluvium	Aeolian silt & sand
Atiyah	Lisan	Gravel sheets
Jurfayn	Bad'	Sabkhah

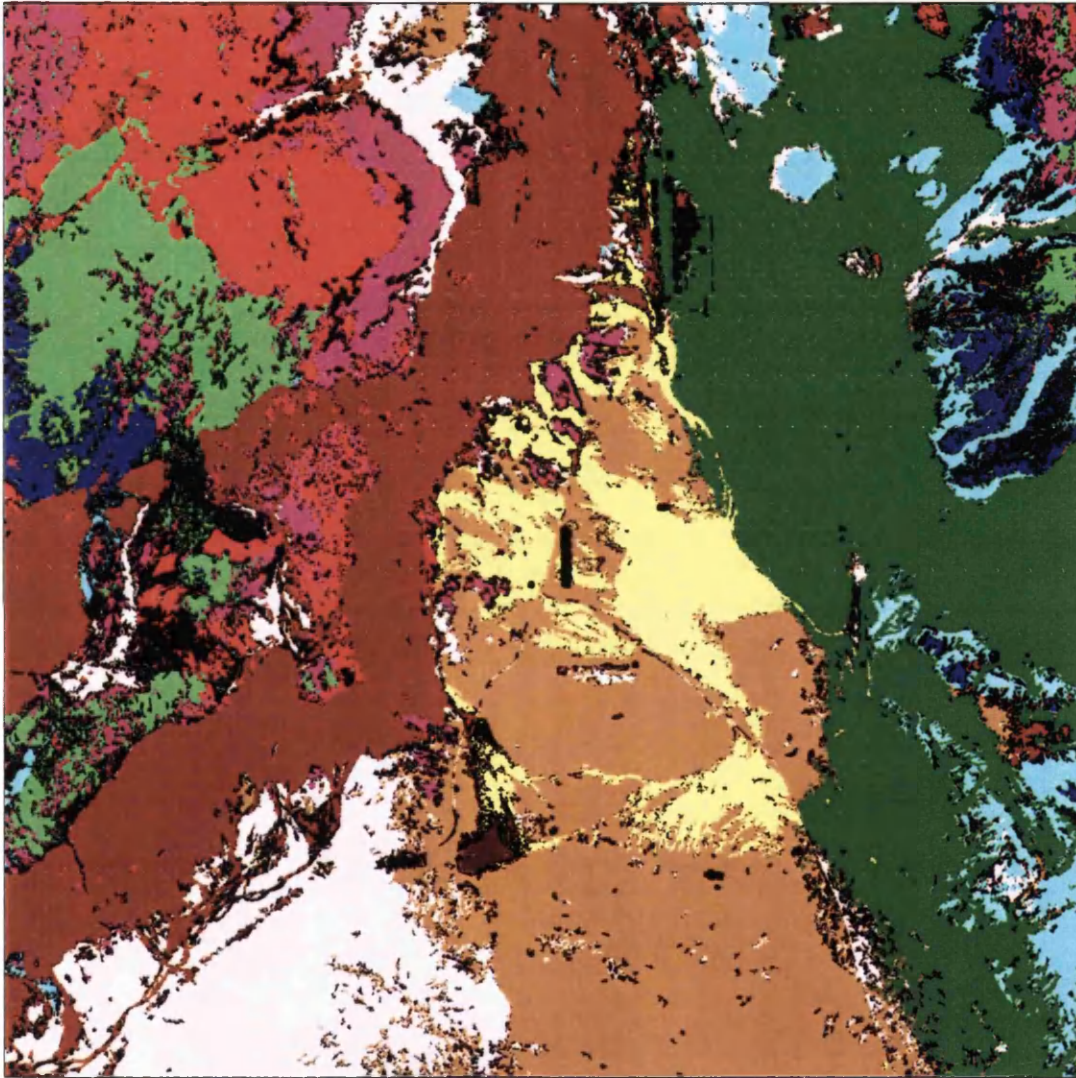


Figure 7.8 Final classified pixels of stage 3 sequential classification. Pixels which are negatively biased are set to black (unclassified).

Scale 1:204084

Legend

Nutaysh	Conglomerate and gravel	
Musayr	Alluvium	Aeolian silt & sand
Atiyah	Lisan	Gravel sheets
Jurfayn	Bad'	Sabkhah

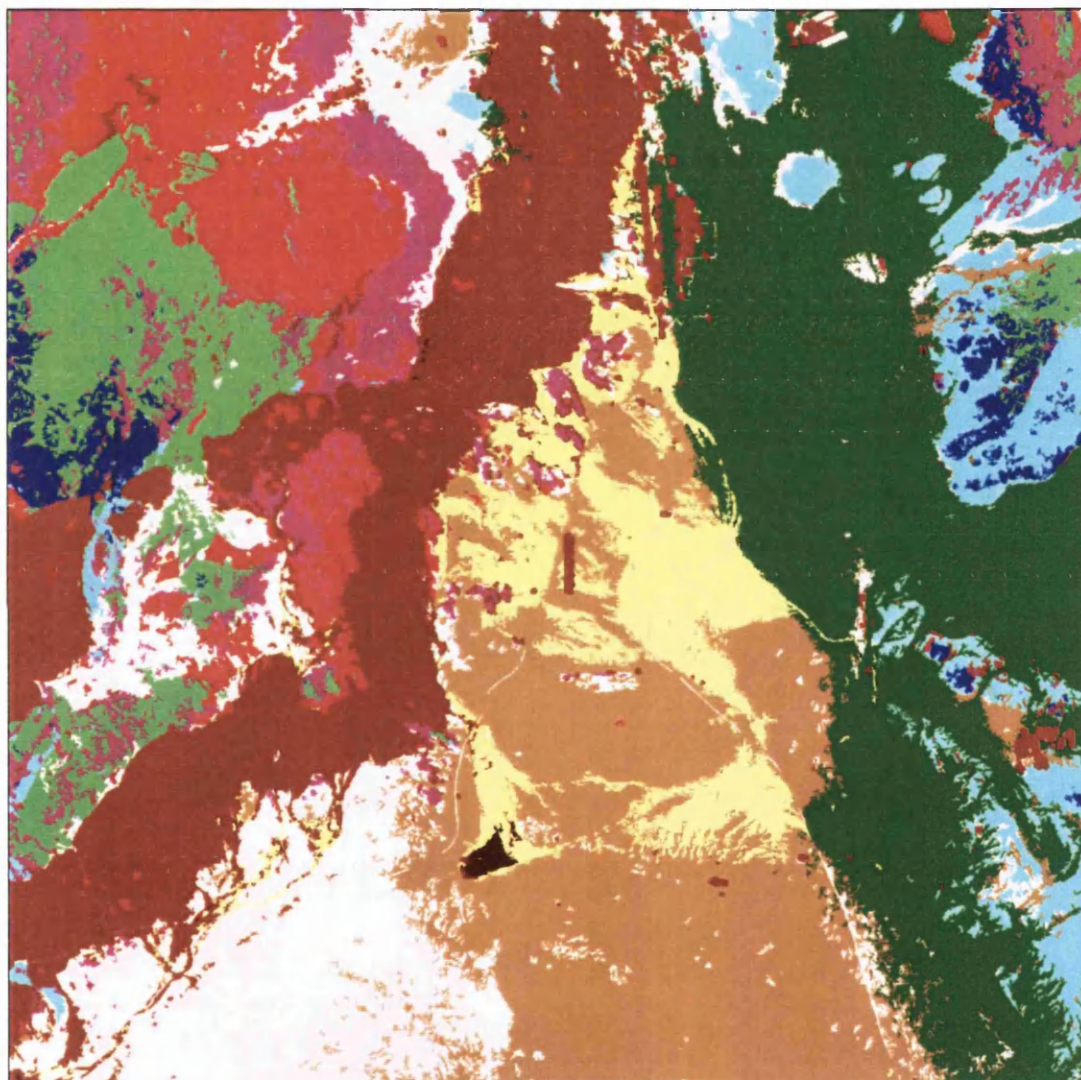


Figure 7.9 Final classified pixels of stage 3 sequential classification. Pixels which are negatively biased are set to their source of texturally-spectrally classified image.

Scale 1:204084

7.6 Accuracy estimation

Estimation of accuracy is an important final stage of every project and reveals the improvements and merits of the techniques used. In particular, the classification accuracy in remote sensing is vital and is the actual judgement of the success of the work. At the same time it is problematic especially in this work as a results of the following: The map produced by Clark [2] is not accurate when investigated during the field work; some of the lithologic classes of the test site have been renamed and/or reclassified (i.e. the Quaternary deposits) and finally; some of the lithologic boundaries are either not recognised in Clark's map, incorrectly mapped, or could not be detected during the photo-interpretation procedure when fused images are produced in chapter 6. As a result of that, a new map has been produced as an integrated lithologic map combining the map produced by Clark [2] and the map produced in chapter 6 as an interpretation of the images produced (i.e. figure 6.25). This integrated map has been digitally scanned, formatted to exactly match the classified images, and every lithologic class has been assigned to a specific colour exactly the same as the classified images. This integrated lithologic map is shown in figure 7.10.

It is important to notice the following issues related to the integrated map used as a ground truth data:

- 1- The integrated lithologic map is used as a ground truth verification to estimate the classification accuracy. At the same time it is believed that this map is far from the 100% accuracy figure. 100% accurate ground truth data is rarely valid in remote sensing [138].
- 2- The classification accuracy results used in this work are estimated as a bottom line (i.e. worst conditions) and it is believed that the results are much better than the accuracy figure given for each class or the overall accuracy.
- 3- All image pixels are used for the classification accuracy estimation. Training areas used for classification are also included, this gives the accuracy estimation is full and inclusive accuracy estimation.

Legend

Nutaysh	Conglomerate and gravel	
Musayr	Alluvium	Aeolian silt & sand
Atiyah	Lisan	Gravel sheets
Jurfayn	Bad'	Sabkhah

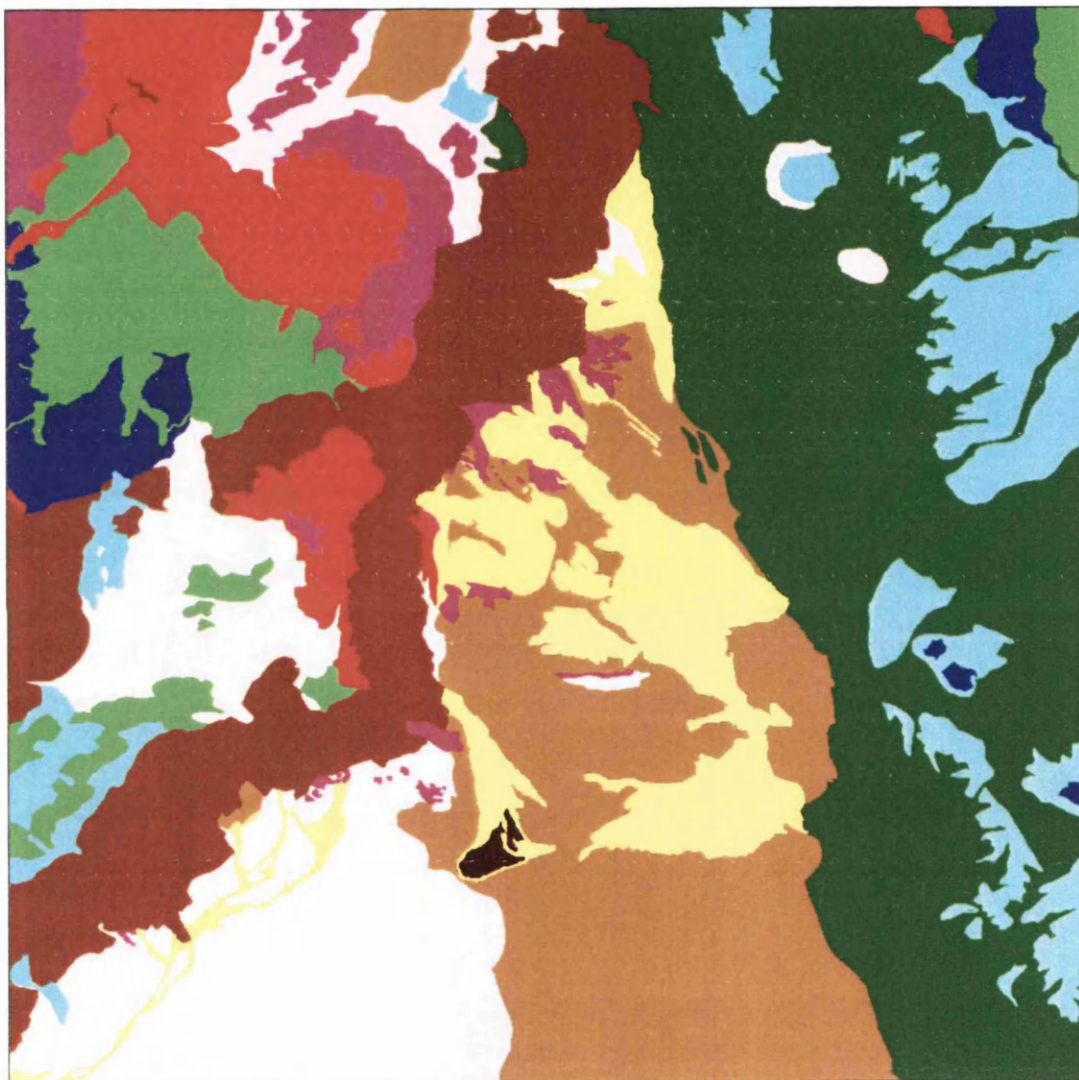


Figure 7.10 An integrated lithologic map of the test site used as a reference data (ground truth) for accuracy estimation of the classified images previously produced in section 7.5.

Scale 1:204084

Accuracy assessment scheme in this work has been applied to investigate the performances of the followings: the texturally classified image (shown in figure 7.2); the spectrally classified image (shown in figure 7.3); the textural-spectral classified image (shown in figure 7.4) and finally; the sequentially classified image where negatively biased pixels are set to the textural-spectral classified image (this is shown in figure 7.9). The other important reason for such investigation is to compare accuracies between the four classified images.

Accuracy of the textural classified image as expected, is low which only reveal less than 30 percent overall accurately classified pixels (around 304087 pixels). This is because the textural separability between the lithologic classes is low and the reference data (the integrated map) is not very accurate. The error accuracy matrix calculated for the textural image is shown in table 7.4 (including the omission or producer's accuracy and the commission or user's accuracy of each class). The method of producing the error matrix is simple and straightforward, it is described in detail by Congalton [138].

The accuracy of classification of the spectral data is shown in table 7.5. As shown in figure 7.3, lithologic classes patterns are shown clearly, which simply reflects the advantage of the spectral data used in this work. The overall accuracy is estimated of a figure of 75.3% (789577 pixels of the imaged test site). This figure of overall accuracy is not believed to be low because the original reference data (the integrated digitised map) is not accurate.

In the case of the textural-spectral classified image (figure 7.4) and its high separability property between its classes. The estimated overall accuracy of this classified image is 76.921% meaning around 806575 pixels of the whole image pixels are correctly classified. The error accuracy matrix of the texturally-spectrally classified image is shown in table 7.6.

Finally and in table 7.7, and using the sequentially classified image shown previously in figure 7.9. The overall accuracy is improved (but not in a recognised figure) showing

overall accuracy of 76.994% accurate (around 807340 pixels of the test site). This small accuracy improvement (+ 0.073% or + 765 pixels) is believed to be an important indicator of the use of the sequential classification method used in this thesis because of two reasons: firstly it proves the logic of using the sequential classification is correct and beneficial for lithologic mapping; secondly is that the sequential classification is a good method of confirming if the classified pixels (in stage zero) are correctly classified or not, and only the correctly classified pixels (i.e. 807340 pixels) are selected in the final stage of the sequence.

Integrated Map	Classified image data											Σ Row	Commission %
	Jurfayn	Atiyah	Musayr	Nutaysh	Bad'	Lisan	Cong+Gvl	Gravel s.	Sabkhah	Alluvium	Aeolian		
-----												----	----
Jurfayn	5307	11774	9956	8213	12011	991	7133	9407	6	3996	1543	70337	7.5%
Atiyah	1114	2403	2086	2177	3273	566	3798	3972	0	2026	938	22353	10.7%
Musayr	9193	26243	31583	14744	41432	97	2545	2816	0	901	109	129663	24.3%
Nutaysh	5526	13088	10486	7119	24467	450	912	1356	0	2962	1577	67943	10.4%
Bad'	504	2675	2424	1165	47434	0	26	166	0	25	32	54451	87.1%
Lisan	33	53	95	266	221	11641	13761	4270	93	13904	4987	49324	23.6%
Cong+Gvl	140	374	624	681	1386	13903	37973	13102	42	19690	10347	98262	38.6%
Gravel s.	3143	8068	8701	8160	7347	8548	49806	24788	0	10392	9796	138749	17.8%
Sabkhah	146	52	80	436	322	26836	22330	8144	541	30013	10602	99502	0.5%
Alluvium	256	12	120	101	69	74527	7644	13803	1030	128014	30681	256257	50%
Aeolian	22	0	19	21	0	16353	856	3635	32	33320	7477	61735	12%
Σ Column	25384	64742	66174	43083	137962	153912	146784	85459	1744	245243	78089	Σ Rows or ΣColumns 1048576	
Omission %	21%	3.7%	44.7%	16.5%	34.4%	7.5%	25.8%	29%	31%	52.2%	9.6%	Overall accuracy 29%	

Table 7.4 Classification accuracy confusion matrix of every lithologic unit of the test site using textural classification.

Integrated Map	Classified image data											Σ Row	Commission %
-----	Jurfayn	Atiyah	Musayr	Nutaysh	Bad'	Lisan	Cong+Gvl	Gravel s.	Sabkhah	Alluvium	Aeolian	----	----
Jurfayn	14920	562	6	0	63	0	0	13172	0	131	0	28854	51.7%
Atiyah	4773	46543	2516	1278	81	0	2632	5593	0	136	0	63552	73.2%
Musayr	34	2530	52117	4434	1775	780	14132	428	0	323	167	76720	68%
Nutaysh	2976	13414	7054	30462	1026	214	15897	9668	0	378	103	81192	37.5%
Bad'	66	929	3879	1424	132638	1617	16460	5064	523	8127	12787	183514	72.2%
Lisan	0	0	73	1081	100	135138	10367	110	5	5785	15714	168373	80.2%
Cong+Gvl	2	53	382	4057	1188	8042	84874	1944	0	11618	1556	113716	74.6%
Gravel s.	2181	711	25	98	345	0	480	38379	0	11655	9	53883	71.2%
Sabkhah	0	0	0	0	115	0	0	0	1178	0	123	1416	83.2%
Alluvium	432	0	119	0	183	2305	1887	11101	0	206638	1052	223717	92.3%
Aeolian	0	0	3	249	448	5816	55	0	38	452	46578	53639	86.8%
Σ Column	25384	64742	66174	43083	137962	153912	146784	85459	1744	245243	78089	Σ Rows or ΣColumns 1048576	
Omission %	58.7%	71.9%	78.7%	70.7%	96.1%	87.8%	57.8%	45%	67.5%	84.2%	59.6%	Overall accuracy 75.3%	

Table 7.5 Classification accuracy confusion matrix of every lithologic unit of the test site using the spectral classification.

Integrated Map	Classified image data												Σ Row	Commission %
-----	Jurfayn	Atiyah	Musayr	Nutaysh	Bad'	Lisan	Cong+Gvl	Gravel s.	Sabkhah	Alluvium	Aeolian	----		
Jurfayn	13252	493	4	0	53	0	0	7286	0	109	0	21197		62.5%
Atiyah	6290	47374	2617	1224	132	0	5166	9510	0	283	0	72596		65.2%
Musayr	49	2208	50650	4135	1752	254	10768	497	0	226	218	70757		71.6%
Nutaysh	4087	12993	7775	29875	1433	176	5267	4762	0	652	149	67169		44.5%
Bad'	94	1130	4186	2192	132089	2252	11715	2783	152	9447	9547	175587		75.2%
Lisan	0	0	102	565	41	133963	10845	906	6	9885	14497	170810		78.4%
Cong+Gvl	7	252	677	4670	1343	8381	99382	3393	1	10291	2520	130917		76%
Gravel s.	1174	292	64	261	205	0	774	45619	0	11113	3	59505		76.7%
Sabkhah	0	0	0	0	66	0	0	0	1192	0	78	1336		89.2%
Alluvium	431	0	81	1	133	2357	1830	10703	0	202574	464	218574		92.6%
Aeolian	0	0	18	160	715	6529	1037	0	393	663	50613	60128		84.1%
Σ Column	25384	64742	66174	43083	137962	153912	146784	85459	1744	245243	78089	Σ Rows or ΣColumns 1048576		
Omission %	52.2%	73.1%	76.5%	69.3%	95.7%	87%	67.7%	53.4%	68.3%	82.6%	64.8%	Overall accuracy 76.921%		

Table 7.6 Classification accuracy matrix of every lithologic unit of the test site using textural-spectral classification.

Integrated Map	Classified image data													Σ Rows	Commission %
-----	Jurfayn	Atiyah	Musayr	Nutaysh	Bad'	Lisan	Cong+Gvl	Gravel s.	Sabkhah	Alluvium	Aeolian	----			----
Jurfayn	13360	508	4	0	54	0	0	7644	0	127	0	21697	21697	21697	61.6%
Atiyah	6239	47268	2578	1224	131	0	5167	9389	0	276	0	72272	72272	72272	65.4%
Musayr	50	2234	50877	4172	1759	254	10765	493	0	221	218	71043	71043	71043	71.6%
Nutaysh	4074	13062	7606	29842	1416	176	5268	4761	0	642	149	66996	66996	66996	44.5%
Bad'	94	1131	4169	2186	132086	2247	11657	2725	152	9364	9533	175344	175344	175344	75.3%
Lisan	0	0	98	567	42	133955	10816	869	6	9493	14457	170303	170303	170303	78.6%
Cong+Gvl	7	248	665	4673	1342	8381	99454	3330	1	10115	2528	130744	130744	130744	76%
Gravel s.	1129	291	65	259	219	0	771	45427	0	11128	3	59292	59292	59292	76.6%
Sabkhah	0	0	0	0	66	0	0	0	1193	0	78	1337	1337	1337	89.2%
Alluvium	431	0	97	1	133	2421	1849	10821	0	203235	473	219461	219461	219461	92.6%
Aeolian	0	0	15	159	714	6478	1037	0	392	642	50650	60087	60087	60087	84.3%
Σ Column	25384	64742	66174	43083	137962	153912	146784	85459	1744	245243	78089	Σ Rows or ΣColumns 1048576	1048576	1048576	
Omission %	52.6%	73%	76.9%	69.3%	95.7%	87%	67.8%	53.2%	68.4%	82.9%	64.9	Overall accuracy 76.994%			

Table 7.7 Classification accuracy confusion matrix of every lithologic unit of the test site using the sequential classified image where biased pixels are filled by the textural-spectral classified image.

7.7 Conclusions and remarks

The sequence or staged classification works in a method of comparison between the texturally-spectrally classified pixels with spectrally classified pixels to detect the biased (positively or negatively) pixels and perform a small test to find out if the biased pixels are positive or negative (stage one). If positive, then they are saved, if the bias is negative, other pixels derived from a logically constructive comparison (texture against spectral) are replaced. If the comparison of texture against spectral fails, either the original classified pixels derived back, or lifted unclassified. It works as priorities, the more class pixels classified in the earlier stage, the better performance can be gained in this particular class. Conversely, the less pixels classified in this stage for a particular class, the less performance can be achieved. Table 7.3 shows this characteristic. This is a general rule in classes performance, but the classes pixels left unclassified after the third stage is the key of the classes performance.

Pixels left unclassified may be classified based on their textural-spectral information which is still high in separability (table 6.1). Such pixels are believed to be source of errors resulting on relying on their biased spectral information rather than textural information. This is shown in figure 7.6 where pixels of system errors, Valley deposits, and classes boundaries show clearly in this figure. This give rise to an easy way of calculating the performance of both of each class and overall performance of the whole image.

Care in selecting the test site training areas and their sizes is an important key factor in classification. To select a training area, comparison between the measured spectral data collected from the rock samples with the TM data is important. This is to insure both of data has similar shapes. If bias occur, the selected training area may contain contaminated pixels which gives a wider spread in the class standard deviation resulting in reduction of transformed divergence separability test figure. The size of the training area representing each class should meet the criteria $Z > 5(n^2 + n)$ where Z is the number of pixels of each

class and n is the number of image bands used [41]. This is for a better representation of class statistics used in MLC.

Because texture with spectral information are used in the sequential classification, and it is believed that the spectral information derived from TM sensor is reliable. The textural information should be presented in a better way, this include geometric correction, speckle reduction, and the algorithm used to enhance texture. If such factors achieved, performance of the sequential classification will increase.

Sequence or staged classification works only with two or more than two types of information (signatures) collected from the same sensor or different sensors. Because it is based on comparison between pixels information, accurate registration between these pixels (if two or more sensors used) is an important part of data preparation for fusion. Thus, misregistration may increase dramatically the error rate during classification.

The sequential classification can work in a different way of steps, for example it can work as the spectral versus textural first, then textural-spectral versus spectral second, and fill biased pixels in the first step by pixels of the second step. If there are still biased pixels, fill these zero pixels by the textural-spectral classified original source. Such method has been tested in this work and showed nearly identical results (visually and statistically) to the method used here.

Finally, the sequential classification is simple and easy method. It is proved in this thesis that it is a good way to benefit from two imaging sensors information.

8.0 Conclusions

The main objective of this thesis has been to show the usefulness of satellite image data fusion using the JERS-1 SAR textural information and the Landsat-5 optical spectral information, and employing both for lithological mapping using a selected test site located in the north west of Saudi Arabia. This site was composed of varieties of igneous, sedimentary, and surficial lithological units of age range from Proterozoic to recent Cenozoic eras. A reasonable geologic knowledge of this site has been built based on a field visit, spectral analysis of the collected rock samples, a previously compiled geological map, and many processed colour composites and fused colour composites used for visual interpretation.

In order to utilise the two data sets from the optical TM and the SAR image data, many aspects have been demonstrated to carry out the data fusion and create a constructive feedback for both utilising and interpreting the fused image data. These aspects include: reviewing the theoretical background of the nature of the two imaging systems and their benefits for geologic mapping, preparing the two image data sets and making them suitable for fusing, and finally extracting the valuable spatial and spectral information for the fusing techniques.

The aspects mentioned above can be termed the information feedback and pre-processing for image data fusion. The pre-processing includes the atmospheric correction of the optical data, the geometric co-registration of the SAR image data to the optical TM data and finally the speckle removal of the SAR image data.

An intermediate step between the pre-processing and image data fusion is the extraction of the textural information from the SAR image data, since the SAR is inherently sensitive to the shapes and structures of lithologic features surfaces. The Grey Level Co-occurrence Matrix (GLCM) works better than other spatial enhancement techniques. This judgement is based on the statistical Transformed Divergence separability tests upon the predefined lithologic features selected during the field work in the test site.

Image data fusion is broadly divided into two parts based on its benefit: one is data fusion aimed at maximising the visual interpretability of the image data. From a geological point of view this can be achieved if both the spectral and textural information of the geologic units in the image data are enhanced and displayed. The second part is maximising the lithological units separabilities using both spectral and textural information to be automatically recognised. This is through the use of a discriminant function, and makes the computer directly decide to spatially label every pixel to its relevant rock unit class based on a learning procedure. The learning procedure is feeding the computer with the rock unit's multivariate statistics. This method is the classification process by the use of supervised maximum likelihood decision rule and the resultant is a thematic map delineating all rock type classes.

An effort has been made in this thesis to develop a new method to solve the problem of selecting which spectral bands are used to represent the spectral information component in the colour composite displayed images where there are twenty possible combination of the optical TM data and all of these combinations can be used for visual interpretation. The newly developed method is named the spectral coding method,

Because spectral information is represented by colours in the colour composite, and these colours only show up if the spectral information used in the primary colours of red, green, and blue. The spectral TM coded image, the albedo-topographic image (the mean reflectance of the six TM data) image, and the range image (maximum-minimum pixel vector value) are used as a TM spectral colour coded composite technique which shows up a colourful image and at the same time preserve the maximum separability between classes if the whole TM six bands are used together.

A set of fuser tools have been applied on the spectral colour coded composite image, where these tools work as a splitting mechanism mediator to split the spectral information from its spatial information and then induce the inherently maximised spatial information available in the SAR image. These tools include the *RGB-HSI-RGB*, the

PCT, and the chromaticity Brovey transform techniques. The spectral colour coded composite image and the fuser tools are a group of procedures dedicated for image data fusion aimed at visual interpretation. These procedures are tested on the selected test site and results show that the visual interpretability makes recognition of the rock classes easy.

In the second part of image data fusion aimed at classification, the two image data set (the 6 optical TM bands and the 7 textural measures produced by the GLCM) are treated separately, and in combination intending to benefit from both data sources for better (confirmed) classification results. A new method of classification is used and named the sequential classification. The sequential classification is a method of implementing the classifier (i.e. MLC) on the spectral image data derived from the TM data, the seven textural GLCM measure data derived from JERS-1, the textural-spectral combined image set of enhanced spatial and spectral information using the Mahalanobis distance, and a final thematic maps are automatically produced using these three data sets. The accuracy assessments of the produced thematic maps proved that the textural data set is incomparable with the spectral data accuracy assessment. The spectral data derived from TM is much better, but the textural data set is useful for the sequential classification.

8.1 Ideas for further work

The TM spectral colour coding technique is a new method to build spectrally coded colour composite production where the image dimensionality is reduced, and at the same time the feature's spectral separability is preserved. The method works very well in the case of TM data because there are only six optical spectral image bands. It works for any kind of application because the key factor of spectral information for visual interpretation is preserved. Problems may arise if spectral coding is implemented on hyperspectral image data because the code number will exponentially increase leading to new issues such as storage and scaling. In such case, the spectral coding algorithm should be modified to suite such kind of data.

For geological mapping where lithological and structural mapping are combined together, it is believed that the DEM's are important information which should be included. Such data can be utilised to extract the terrain attitudes and aspects (i.e. slope, watershed, drainage patterns, etc.) which may help with the combination of the lithologic maps to delineate automatically the structural features. Reliable rules are critically needed to establish such an idea for automated geological mapping and may be through the use of advanced sequential classification (i.e. hierarchical).

Appendix (A)

A-1 Band combination:

Combinations are a special case of permutations, where a combination neglects the order of permutation arrangement [117]. Suppose we have n bands combined in r number (i.e. r items together).

The number of possible combination is nC_r .

$${}^nC_r = \frac{n!}{r!(n-r)!} \quad (A.1)$$

where:

$n!$ = factorial of n .

$r!$ = factorial of r .

$(n-r)!$ = factorial of $(n-r)$.

We can code the combination table in C programming easily as follows:

a) If three pixel triplet is needed to create colour composite (3D-DCVR):-

```
/* Let n = number of bands used = 6, r = 3 (i.e colour composite of pixels of band Q, R,  
and S */
```

```
int n=6;
```

```
int Q, R, S;
```

```

for (Q=1; Q<n-1; Q++){
    for (R=Q+1; R<n; R++){
        for (S=R+1; S<n+1; S++){

printf("\n%d\t%d\t%d",Q,R,S);  /* print the combination table */

        }}}

```

A-2 Balance Contrast Enhancement Technique (BCET)

The BCET technique was proposed by Liu [43], Liu and Moore [114] to avoid colour bias when a colour composite is displayed. The method is simply refer to a special contrast stretching of the image while at the same time allowing the output image minimum, maximum and mean to be user specific. Two methods can be used, one is using a segment of parabola curve derived from the input image, the other method is similar to that of the first but using a segment of cubic curve. In this work, data is stretched by the use of a parabolic curve. The mathematical derivation is as follows [43]:-

The parabolic equation is:

$$Y = A(X - B)^2 + C \quad (\text{A.2})$$

where:

Y = output image pixel.

X = input image pixel.

A , B , and C are coefficients.

To derive A , B , and C coefficients, we have to calculate the following from the input image pixels x_i . Let:

h = maximum pixel value of input image = $\text{Max}(x_i)$

l = minimum pixel value of input image = $\text{Min}(x_i)$

e = mean value of input image pixels = $\frac{1}{N} \sum_{i=1}^N x_i$

If the user works with 8 bit images, the maximum H and minimum L will be set to 255 and zero respectively. The output image mean E will be set by the user selected value.

$$R = \frac{1}{N} \sum_{i=1}^N x_i^2 \quad (\text{A.3})$$

$$T = (h^2 \times E) - 255R + 255l^2 \quad (\text{A.4})$$

$$K = 2[(h \times E) - (255e) + (255l)] \quad (\text{A.5})$$

The coefficients can be calculated as:

$$A = \frac{255}{(h-l)(h+l-2B)} \quad (\text{A.6})$$

$$B = \frac{T}{K} \quad (\text{A.7})$$

$$C = -A(l-B)^2 \quad (\text{A.8})$$

Note that most of the time the above method of stretching works well but under some circumstances it may not give the desired mean as a result of the nature of the input image. Such a situation can be resolved if clipping factors are taken from the input image histogram tails. More information about this problem is discussed in Liu's work detailed in the references [43,114].

A-3 Band selection

Band selection for colour composite production can be problematic as a result of which combination scheme is desired. Users may prefer testing image combination visually or implementing some statistical calculations, these statistical approaches are:-

a) OIF band selection method

Chavez *et. al.* [112] were the first people to address the colour composite band selection problem and its solution statistically. She used the equation below for best colour composite bands. The method is named the optimum index factor (OIF). The maximum OIF between any three bands from the combination table is referred to be the best combination:

$$OIF = \frac{\sum_{i=1}^3 \sigma_i}{\sum_{i=1}^3 |C_{i,j}|} \quad (A.9)$$

where:

σ_i = standard deviation of band i .

$C_{i,j}$ = correlation coefficient between bands i and j .

b) Sheffield and Chase method.

Sheffield and Chase [113] developed another method of best bands selection for colour composite. It performs better than the Chavez method. The method can be simplified as follows:-

Step1- Produce the main variance - covariance matrix of all bands used.

Step2- From the main variance - covariance matrix, produce all the 3 by 3 covariance matrix which represents all possible combinations of bands. Note that the matrices are symmetrical along their diagonals.

Step3- Evaluate the third order determinant for every matrix and use bands of the maximum determinant matrix as the best bands for colour composite combination.

c) Index of optimal band selection (IOBS) method

This method was developed by Liu and Moore [114] for best band triplet selection. It shows better performance than the Sheffield and Chase determinant method and the OIF method of Chavez, because results from both methods are affected by the contrast stretching of the bands used. The IOBS for best colour composite is the minimum value produced by the equation below from the combination table.

$$IOBS = \text{Max}(C_{i,j}, C_{i,k}, C_{j,k}) \sqrt{C_{i,j}^2 + C_{i,k}^2 + C_{j,k}^2} \quad (\text{A.10})$$

where:

$C_{i,j}, C_{i,k}, C_{j,k}$ = correlation coefficients of the three bands i, j , and k .

A-4 Separability measure between classes

Separability or discrimination measure between classes refers to how the class pairs in the data set are not similar or coincide (degree of overlap). This can be calculated from the class statistics by many methods with a high degree of accuracy. The class refers to the intensity of pixels value of a specific geographic homogenous area selected by the user in the image set.

In the one channel case, separability between pair of classes can be measured based simply on their means and standard deviations. Separability (S) between class i and class j is then [32]:

$$S = \frac{|u_i - u_j|}{\sigma_i + \sigma_j} \quad (\text{A.11})$$

where:

u_i, u_j = means of classes i and j .

σ_i, σ_j = standard deviation of classes i and j .

Such a separability measure of a single band can also be evaluated visually by plotting the class means on the abscissa and the class standard deviations on the ordinate. It is important that classes are assumed to be Gaussian distributed and values of S from the above equation give 90% correct separation (correct classification) if S exceeds 1.5 [143]

When many bands are used, the separability measure becomes more computationally intensive, especially when we have n bands, m classes, r combinations and bearing in mind that the evaluation is pairwise. In this case the number of evaluations becomes ${}^nC_r \times {}^mC_2$ [24] and it becomes impossible to evaluate the separability measure manually.

There are three measures of separability between pairs of classes, these include: the divergence measure, the Jeffries-Matusita (JM) distance measure (also called the Bhattacharyya distance) and finally the Transformed Divergence measure. The Divergence measure is sometime quite misleading as the result of the divergence increases quadratically with separation between classes [24].

The most popular method of separability measure is the Transformed Divergence (TD) measure, it is more computationally economical and performs as effectively as the JM method.

The TD measure of pair of classes i and j on n bands is [41]:

$$TD_{i,j} = 2 \times (1 - e^{-D_{i,j}/8}) \quad (\text{A.12})$$

where :

$$D_{i,j} = 0.5 \times [u_i - u_j]^T \times [Cov_i + Cov_j]^{-1} \times [u_i - u_j] \\ + 0.5 \times \text{Trace}[[Cov_i \times Cov_j]^{-1} + [Cov_j \times Cov_i]^{-1} - 2 \times I]$$

$[u_i - u_j]^T$ = transpose matrix of mean vectors of classes i and j where every class consists of n channels.

$[Cov_i, Cov_j]^{-1}$ = Inverse matrix of covariances of classes i and j .

$Trace[...]$ = Trace of the matrix [...], it is equal to the sum of the diagonal elements of the matrix [...].

I = The identity matrix.

The TD separability measure between pair of classes can ranges from 1.000 to 2.000 in its magnitude, such ranges are classified as:-

$0.000 < TD < 1.000$ = Very poor separability.

$1.000 < TD < 1.900$ = Poor separability.

$1.900 < TD \leq 2.000$ = Good separability.

A-5 The principal component transform

Since the multispectral and multisensor data are multidimensional, they can be constructed in a vector space with as many axes as there are spectral components or sensor components [24]. These components, or vectors, are equal to the number of sensors or spectral bands associated with each pixel. A particular pixel in an image can be plotted as a point in such space with co-ordinates that correspond to the appropriate spectral component (e.g. scatterogram). Figure A.1 shows a plot of three layers of image means.

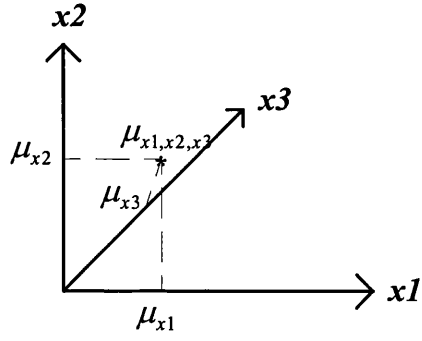


Figure A.1 Three dimensional presentation of mean vector consists of three components or layers.

The mean value of such a vector in one layer or spectral band $x1$ is:

$$\mu_{x1} = \frac{1}{k} \sum_{i=1}^k x1_i \quad (\text{A.13})$$

where:

k = number of individual pixels.

$x1$ = pixel brightness value in band 1.

i = pixel number

The mean between three vectors $x1, x2$ and $x3$ is:

$$\mu_{x1, x2, x3} = \begin{bmatrix} \mu_{x1} \\ \mu_{x2} \\ \mu_{x3} \end{bmatrix} \quad (\text{A.14})$$

The variance σ_{x1}^2 of the vector $x1$ is:

$$\sigma_{x1}^2 = \frac{1}{k} \sum_{i=1}^k (x1_i - \mu_{x1})^2 \quad (\text{A.15})$$

The corrected sum of product $SP_{x1,x2}$ between pair of vectors such as $x1$ and $x2$ is:

$$SP_{x1,x2} = \sum_{i=1}^k (x1_i - \mu_{x1})(x2_i - \mu_{x2}) \quad (A.16)$$

The Covariance $Cov_{x1,x2}$ between a pair of vectors such as $x1$ and $x2$ is:

$$Cov_{x1,x2} = \frac{SP_{x1,x2}}{k-1} \quad (A.17)$$

The correlation $C_{x1,x2}$ between the two vectors $x1$ and $x2$ is:

$$C_{x1,x2} = \frac{Cov_{x1,x2}}{\sqrt{\sigma_{x1}^2 \sigma_{x2}^2}} \quad (A.18)$$

From the covariance and correlation between every pair of vectors (spectral or sensor bands), we can create covariance and correlation matrices, their order being equal to the number of vectors or bands. These matrices are symmetric (e.g. equal to their transpose).

The covariance matrix of n vectors is:

$$Cov_{x1,x2,x3,\dots,xn} = \begin{bmatrix} Cov_{x1,x1} & Cov_{x1,x2} & Cov_{x1,x3} & \dots & Cov_{x1,xn} \\ Cov_{x2,x1} & Cov_{x2,x2} & Cov_{x2,x3} & \dots & Cov_{x2,xn} \\ Cov_{x3,x1} & Cov_{x3,x2} & Cov_{x3,x3} & \dots & Cov_{x3,xn} \\ \dots & \dots & \dots & \dots & \dots \\ Cov_{xn,x1} & Cov_{xn,x2} & Cov_{xn,x3} & \dots & Cov_{xn,xn} \end{bmatrix} \quad (A.19)$$

Note that the covariances between the same vectors are equal to their variances. For example the covariance of vector $x1$ and vector $x1$ is the variance of the vector $x1$:

$$Cov_{x1,x1} = \sigma_{x1}^2 \quad (A.20)$$

and also:

$$Cov_{x1,x2} = Cov_{x2,x1} \quad (A.21)$$

The correlation matrix between n vectors is:

$$C_{x1,x2,x3,\dots,xn} = \begin{bmatrix} C_{x1,x1} & C_{x1,x2} & C_{x1,x3} & \dots & C_{x1,xn} \\ C_{x2,x1} & C_{x2,x2} & C_{x2,x3} & \dots & C_{x2,xn} \\ C_{x3,x1} & C_{x3,x2} & C_{x3,x3} & \dots & C_{x3,xn} \\ \dots & \dots & \dots & \dots & \dots \\ C_{xn,x1} & C_{xn,x2} & C_{xn,x3} & \dots & C_{xn,xn} \end{bmatrix} \quad (A.22)$$

The correlation between the same vectors $C_{x1,x1} = C_{x2,x2} = \dots = C_{xn,xn} = 1$. The value of the correlation matrix elements range from -1 to 1. If the correlation between a pair of vectors (e.g. bands) is close to -1, this means the data is highly inversely correlated (one is increasing and the other is decreasing or vice versa). If the value is zero, this means no correlation at all exists between the vector pairs. If the value is 1 or close to it, the vector pairs or band pairs are highly correlated.

Naturally, remote sensing multispectral and multisensor imaging data are highly correlated because of the identity (spectral response) of the same ground targets are closely similar in many cases and the topographic relief (scene albedo) gives the same spectral response for whatever band used. This means there is a redundancy in the data. To overcome this, data sets or vectors can be translated through their mean vectors to

produce new sets of bands which are uncorrelated, and more than 90% of the data set variances will be moved to the first few new translated vectors. This leads to compressing the information (e.g. variances) and remove the redundancy and the rest of the translated components that are low in information and mainly consist of noise. This method of translation is called the Karhunen-Loeve or Principal Component Transform [18,24,60]. The PCT is widely used as a multispectral/multisensor data fusion technique and as a method of image data compression, decorrelation. Recently it has been applied as a good fuser technique because the common information in the data set such as image albedo will go to the first PCT component and this component can be replaced by another image.

The PCT of the data is based on translating the data sets through their eigenvectors of the covariance matrix. This can be shown in the following:

Let $A = \text{the covariance matrix} = \text{Cov}_{x_1, x_2, x_3, \dots, x_n}$

$x \neq 0$

$\lambda = \text{eigenvalues or the latent roots of the matrix } A.$

$$A \times x = \lambda x \quad (\text{A.23})$$

The corresponding solution of the equation A.23 is called the eigenvectors of A .

Expressing this in the covariance matrix to get the eigenvalues and eigenvectors:

$$\begin{bmatrix} Cov_{x1,x1} & Cov_{x1,x2} & Cov_{x1,x3} & \dots & Cov_{x1,xn} \\ Cov_{x2,x1} & Cov_{x2,x2} & Cov_{x2,x3} & \dots & Cov_{x2,xn} \\ Cov_{x3,x1} & Cov_{x3,x2} & Cov_{x3,x3} & \dots & Cov_{x3,xn} \\ \dots & \dots & \dots & \dots & \dots \\ Cov_{xn,x1} & Cov_{xn,x2} & Cov_{xn,x3} & \dots & Cov_{xn,xn} \end{bmatrix} \times \begin{bmatrix} x1 \\ x2 \\ x3 \\ \dots \\ xn \end{bmatrix} = \lambda \begin{bmatrix} x1 \\ x2 \\ x3 \\ \dots \\ xn \end{bmatrix} \quad (A.24)$$

$$= Cov_{x1,x1}x1 + Cov_{x1,x2}x2 + Cov_{x1,x3}x3 + \dots + Cov_{x1,xn}xn = \lambda x1$$

$$Cov_{x2,x1}x1 + Cov_{x2,x2}x2 + Cov_{x2,x3}x3 + \dots + Cov_{x2,xn}xn = \lambda x2$$

$$Cov_{x3,x1}x1 + Cov_{x3,x2}x2 + Cov_{x3,x3}x3 + \dots + Cov_{x3,xn}xn = \lambda x3$$

$$\dots$$

$$Cov_{xn,x1}x1 + Cov_{xn,x2}x2 + Cov_{xn,x3}x3 + \dots + Cov_{xn,xn}xn = \lambda xn$$

This simplifies to:

$$(Cov_{x1,x1} - \lambda)x1 + Cov_{x1,x2}x2 + Cov_{x1,x3}x3 + \dots + Cov_{x1,xn}xn = 0$$

$$Cov_{x2,x1}x1 + (Cov_{x2,x2} - \lambda)x2 + Cov_{x2,x3}x3 + \dots + Cov_{x2,xn}xn = 0$$

$$Cov_{x3,x1}x1 + Cov_{x3,x2}x2 + (Cov_{x3,x3} - \lambda)x3 + \dots + Cov_{x3,xn}xn = 0$$

$$\dots$$

$$Cov_{xn,x1}x1 + Cov_{xn,x2}x2 + Cov_{xn,x3}x3 + \dots + (Cov_{xn,xn} - \lambda)xn = 0$$

$$= \begin{bmatrix} (Cov_{x1,x1} - \lambda) & Cov_{x1,x2} & Cov_{x1,x3} & \dots & Cov_{x1,xn} \\ Cov_{x2,x1} & (Cov_{x2,x2} - \lambda) & Cov_{x2,x3} & \dots & Cov_{x2,xn} \\ Cov_{x3,x1} & Cov_{x3,x2} & (Cov_{x3,x3} - \lambda) & \dots & Cov_{x3,xn} \\ \dots & \dots & \dots & \dots & \dots \\ Cov_{xn,x1} & Cov_{xn,x2} & Cov_{xn,x3} & \dots & (Cov_{xn,xn} - \lambda) \end{bmatrix} \times \begin{bmatrix} x1 \\ x2 \\ x3 \\ \dots \\ xn \end{bmatrix} = \begin{bmatrix} 0 \\ 0 \\ 0 \\ \dots \\ 0 \end{bmatrix} \quad (A.25)$$

$$\lambda = \lambda_1, \lambda_2, \lambda_3, \dots, \lambda_n$$

From (A.23)

$$A \times x - \lambda x = 0 \quad (\text{A.26})$$

Because we cannot subtract matrices from scalar numbers such as λ , we introduce the unit matrix I [117]:

$$(A - \lambda I)x = 0 \quad (\text{A.27})$$

where I = unit matrix which is $I = A \times A^{-1}$

For this set of homogeneous linear equations (the right hand constants are all zeros), and to have a non-trivial solution, $|A - \lambda I|$ must be zero.

$$|A - \lambda I| = \begin{vmatrix} (Cov_{x1,x1} - \lambda) & Cov_{x1,x2} & Cov_{x1,x3} & \dots & Cov_{x1,xn} \\ Cov_{x2,x1} & (Cov_{x2,x2} - \lambda) & Cov_{x2,x3} & \dots & Cov_{x2,xn} \\ Cov_{x3,x1} & Cov_{x3,x2} & (Cov_{x3,x3} - \lambda) & \dots & Cov_{x3,xn} \\ \dots & \dots & \dots & \dots & \dots \\ Cov_{xn,x1} & Cov_{xn,x2} & Cov_{xn,x3} & \dots & (Cov_{xn,xn} - \lambda) \end{vmatrix} = 0 \quad (\text{A.28})$$

$|A - \lambda I|$ is called the characteristic determinant of A and $|A - \lambda I| = 0$ is the characteristic equation. On expanding the determinant, this gives a polynomial of degree n which is the number of spectral bands. The solution of the characteristic equation gives the values of λ which are the eigenvalues or the new image variances of the transformed data set.

The eigenvalues obtained from the characterised determinant of the covariance matrix A have corresponding solutions of x called the eigenvectors (equation no. A.23). These eigenvectors are column matrices. The corresponding solution for the highest value of λ is the first eigenvectors column and so on for the rest of λ s and their corresponding eigenvector solutions. The eigenvectors can be aligned in columns corresponding to their values of λ s in descending order as shown below:

$$\begin{matrix} \lambda_1 & \lambda_2 & \lambda_3 & \dots & \lambda_n \end{matrix}$$

$$\begin{bmatrix} E_{1,1} \\ E_{2,1} \\ E_{3,1} \\ \dots \\ E_{n,1} \end{bmatrix}, \begin{bmatrix} E_{1,2} \\ E_{2,2} \\ E_{3,2} \\ \dots \\ E_{n,2} \end{bmatrix}, \begin{bmatrix} E_{1,3} \\ E_{2,3} \\ E_{3,3} \\ \dots \\ E_{n,3} \end{bmatrix}, \begin{bmatrix} \dots \\ \dots \\ \dots \\ \dots \\ \dots \end{bmatrix}, \begin{bmatrix} E_{1,n} \\ E_{2,n} \\ E_{3,n} \\ \dots \\ E_{n,n} \end{bmatrix} \quad (A.29)$$

where: $\lambda_1 > \lambda_2 > \lambda_3 > \dots > \lambda_n$.

The values inside the columns of equation A.29 can be presented together in a matrix called the modal matrix.

The translation of the data sets is then performed from the values of equation A.29 and by implementing the equation below (A.30) where results are stored in a new image set.

$$NP_{i,j,\lambda_n} = \sum_{k=1}^n E_{i,j,\lambda_k} BV_{i,j,k} \quad (A.30)$$

where:

NP_{i,j,λ_k} = output pixel value in the position of i,j of the component k ,

E_{i,j,λ_k} = eigenvector values of component k ,

$BV_{i,j,k}$ = input pixel value in the position i,j in all spectral bands k .

If equation A.30 is applied to the transpose of eigenvectors of λ s, the resultant imagery components will be uncorrelated and are equal in their variances. This is called the decorrelation stretching technique [90]. It is frequently used by many remote sensing geologists to achieve colourful images as spectral enhancement technique. One of the methods used in PCT data fusion is replacing the first principal component by the SAR

image data then reversing the PC transformation after transposing the eigenvector matrix using equation A.30 to produce an equal number of images fused with the SAR data.

A-6. The variance-covariance matrix of the test site is shown in table A-6.

--	Band 1	Band 2	Band 3	Band 4	Band 5	Band7
Band 1	1890.06	-	-	-	-	-
Band 2	1532.91	1348.08	-	-	-	-
Band 3	1571.31	1411.28	1526.17	-	-	-
Band 4	1499.33	1381.30	1515.43	1545.16	-	-
Band 5	1758.41	1689.67	1883.97	1972.30	2849.40	-
Band 7	1350.98	1191.71	1310.19	1343.17	1984.11	1906.79

Table A-6 TM data set variance-covariance matrix. BCET applied prior calculation.

The following show the output results of best bands combination of the test site using the statistical methods explained previously in A-3.

RANK	DETERMINANT	BANDS	OIF	BANDS	IOBS	BANDS
1	550945300	01 05 06	60.555	01 05 06	0.660283	01 05 06
2	517319600	02 05 06	54.450	02 05 06	0.696099	01 04 06
3	493574000	01 04 06	53.956	03 05 06	0.707481	02 05 06
4	419800900	03 05 06	53.321	01 04 06	0.746328	01 03 06
5	324950400	01 03 06	52.980	04 05 06	0.761359	03 05 06
6	266732800	04 05 06	52.878	01 04 05	0.780404	01 02 06
7	185866000	01 04 05	52.554	01 03 05	0.797073	02 04 06
8	169051400	01 02 06	52.481	01 03 06	0.800558	01 03 05
9	167481200	01 03 05	51.768	01 02 05	0.808660	04 05 06
10	129242200	02 04 06	51.281	01 02 06	0.809931	01 04 05
11	109171600	01 02 05	48.207	02 04 06	0.825239	02 03 06
12	50767690	02 03 06	48.097	03 04 06	0.829750	01 02 05
13	49741310	02 04 05	47.871	02 03 06	0.840472	03 04 06
14	45492350	03 04 06	46.977	02 03 05	0.881120	02 04 05
15	30201340	02 03 05	46.900	02 04 05	0.895387	01 02 04
16	18858880	01 02 04	46.553	03 04 05	0.903108	02 03 05
17	16538050	03 04 05	43.684	01 03 04	0.918619	01 03 04
18	11120940	01 03 04	42.759	01 02 04	0.931608	03 04 05
19	8144984	01 02 03	41.562	01 02 03	0.941377	01 02 03
20	2039992	02 03 04	39.309	02 03 04	0.963189	02 03 04

References

- [1] Berger, Z., 1994, *Satellite Hydrocarbon Exploration: Interpretation and Integration Techniques*, Springer-Verlag Publishing Company.
- [2] Clark, M. D., 1987, *Geological map of the Al Bad' quadrangle (with report), sheet GM-81 C*, Kingdom of Saudi Arabia, Ministry of Petroleum and Mineral Resources, Directorate General of Mineral Resources.
- [3] Jaskolla, F., and Rast, M., 1988, Comparative geological evaluation of different remote sensing data of the Huggar Mountains (Algeria), In: *Proc. 4th International Colloquium on Spectral Signatures of Objects in Remote Sensing*, Aussois, France, 18-22 January 1988 (ESA SP-287).
- [4] Lillesand, T. M., and Kiefer, R. W., 1994, *Remote Sensing and Image Interpretation* (third edition), John Wiley & Sons.
- [5] *JERS-1 Data Users Handbook*, 1994, NASDA.
- [6] Elachi, R., 1987, *Introduction to the Physics and Techniques of Remote Sensing*, John Wiley & Sons.
- [7] Curlander, J. C., and McDonough, N. C., 1991, *Synthetic Aperture Radar, Systems & Signal Processing*, John Wiley & Sons, Inc.
- [8] Kahle, A. B., 1986, Measuring spectra in arid lands; In: *Desert and Arid Lands*, Ed. by El-Baz, F., 1986, Martinus Nijhoff Publishers.
- [9] Drury, S. A., 1987, *Image Interpretation in Geology*, Allen & Unwin Press.
- [10] Leberl, F. W., 1990, *Radargrammetric Image Processing*, Artech House Inc.
- [11] Elachi, R., 1988, *Spaceborne Radar Remote Sensing: Applications and Techniques*, IEEE Press.
- [12] Skolnik, M. I. (Editor), 1970, *Radar Handbook*, McGraw-Hill.
- [13] Levanon, N., 1988, *Radar Principles*, John Wiley & Sons.
- [14] Griffiths, H., 1998, Synthetic Aperture Radar: Tutorial, *IEEE Radar Conference, Dallas, Texas, May 14, 1998*.
- [15] Barber, B. C., 1985, Theory of digital imaging from orbital synthetic-aperture radar, *Int. J. Remote Sensing*, V.6, N. 7, 1009-1057.

- [16] Sieber, A. J., 1985, Statistical analysis of SAR Images, *Int. J. Remote Sensing*, V.6, N.9.
- [17] Lee, J. S., 1986, Speckle suppression and analysis for synthetic aperture radar images, *Optical Engineering*, V. 25, N. 5, 636-643.
- [18] Jensen, J. R., 1986, *Introductory Digital Image Processing: a Remote Sensing Perspective*, Prentice-Hall.
- [19] Haralick, R. M., 1973, Glossary and index to remotely sensed image pattern recognition concepts, *Pattern Recognition*, V.5, 391-403.
- [20] Billingsley, F. C., Data processing and reprocessing, Chapter 17 in the *Manual of Remote Sensing*, R. N. Colwell (Editor), Fall Church.
- [21] Cheng, P., Toutin, T., and Pohl, C., 1995, A comparison of geometric models for multisource data fusion, In: *Proc. GeoInformatics'95, Hong Kong*, V.1.,11-17.
- [22] Leila, M. G., and Manjunath, B. S., 1996, Registration techniques for multisensor remotely sensed imagery, *Photogrammetric Engineering and Remote Sensing*, V.62, N. 9, 1049-1056.
- [23] Stanton, S. Y., and Gilbert, J. R., 1984, Registration of a synthetic aperture radar image to thematic mapper imagery for remote sensing applications, *IEEE Transactions on Geoscience and Remote Sensing*, V. GE 22, N. 6, 557-563.
- [24] Richards, J. A., 1986, *Remote Sensing Digital Image Analysis: An Introduction*, Springer-Verlag, Berlin.
- [25] Crippen, R. E., 1987, The regression intersection method of adjusting image data for band ratioing, *Int. J. Remote Sensing*, V.8, N.2, 137-155.
- [26] Chavez, P. S., 1988, An improved dark-object subtraction technique for atmospheric scattering correction of multispectral data, *Remote Sensing of Environment* V.24, 459-479.
- [27] Markham, B. L., and Barker, J. L., 1985, Spectral characterization of Landsat thematic mapper sensors, *Int. J. Remote Sensing*, V.6, N.5, 697-716.
- [28] Vincent, R. K., 1973, Spectral ratio imaging methods for geological remote sensing from aircraft and satellites, In: *Proc. American Society of Photogrammetry, Management and Utilization of Remote Sensing Data Conference*, Sioux Falls, SD, 377-397.

- [29] Ford, J. P., 1982, Resolution versus speckle relative to geologic interpretability of spaceborne radar images: a survey of user preference, *IEEE Transactions on Geoscience and Remote Sensing*, V.GE-20, N.4, 434-444.
- [30] Ulaby, F. T., Moore, R. K., and Fung, A. K., 1982, *Microwave Remote Sensing Active and Passive, Volume II: Radar Remote Sensing and Surface Scattering and Emission Theory*, Artech House Publishing Company.
- [31] Shi, Z, and Fung, K. B., 1994, A comparison of digital speckle filters, *IGARSS*, V. 1-4, CH.734, 2129-2133.).
- [32] Dipack, R. P., and Aschbacher, J., 1993, Evaluation and performance tests of selected SAR speckle filters, In: *Proc. International Symposium "Operationalisation of Remote Sensing"*, 19-23ed April 1993, ITC, Enschede, The Netherlands.
- [33] Blom, R. G., and Daily, M., 1982. Radar image processing for rock-type discrimination. *IEEE Transactions on Geosciences and Remote Sensing*. GE-20, N.3, 343-351.
- [34] Mueller, P. W., and Hoffer, R. N., 1989, Low-pass spatial filtering of satellite radar data, *Photogrammetric Engineering and Remote Sensing*, V.55 N.6, 887-895.
- [35] Lee, J. S., 1980, Digital enhancement and noise filtering by use of local statistics, *IEEE Transactions on Pattern Analysis and Machine Intelligence*, V.PAMI-2, N. 2, 165-168.
- [36] Lee, J. S., 1983, A simple speckle smoothing algorithm for synthetic aperture radar images, *IEEE Transactions on Systems, Man, and Cybernetics*, V. SMC-13, N. 1, 85-89.
- [37] Frost, V., Stiles, J. A., Shanmugan, K. S., and Holtzman, J. C., 1982, A model for radar images and its application to adaptive digital filtering of multiplicative noise, *IEEE Transactions on Pattern Analysis and Machine Intelligence*, V.PAMI-4, N. 2, 157-165.
- [38] Kuan, D. T., Sawchuk, A. A., Strand, T. C., and Chavel, P., 1987, Adaptive restoration of images with speckle, *IEEE Transactions on Acoustics, Speech, and Signal Processing*, V. ASSP-35, N. 3, 373-382.
- [39] Lopes, A., Touzi, R., and Nezry, E., 1990, Adaptive speckle filters and scene heterogeneity, *IEEE Transactions on Geoscience and Remote Sensing*, V. 28, N. 6, 992-1000.
- [40] Tur, M., Chin, C., and Goodman, J. W., 1982, 'When is speckle noise multiplicative?.', *Applied Optics*, V. 21, N. 7, 1157-1159.

- [41] PCI, Inc., 1995, *EASI/PACE User Manuals*, version 6.0: PCI Incorporated, Toronto, Ontario, Canada, variously paged.
- [42] Lee, J. S., 1981, Refined filtering of image noise using local statistics, *Computer Graphics, and Image Processing*, V.15, 380-389.
- [43] Liu, G., J., 1991, Balance contrast enhancement technique and its application in image colour composition, *Int. J. Remote Sensing*, V. 12, N. 10, 2133-2151.
- [44] Shanmugan, K. S., Narayanan, V., Frost, V., Stiles, J., and Holtzman, J. C., 1981, Textural features for radar image analysis, *IEEE Transactions on Geoscience and Remote Sensing*, V. 19, N.3, 153-156.
- [45] Haralick, R. M., 1979, Statistical and structural approaches to texture, In: *Proc. IEEE*, V.67, N.5, 786-804.
- [46] Stefouli, M., and Osmaston, H. A., 1984, The remote sensing of geological linear features using Landsat: matching analytical approaches to practical applications, In: *Proc. Remote Sensing Society Annual Conference, Satellite Remote Sensing Review*, Reading, 1984, 227-236.
- [47] Short, N. M., 1987, Accuracy of lineaments mapping from space, *Internal Publication, NASA Goddard Flight Centre*.
- [48] Haralick, R. H., 1986, Statistical image texture analysis, Chapter 11 in *Handbook of Pattern Recognition and Image Processing*, Edited by Young, T. Y., and Fu King-Sun, Academic Press.
- [49] Rudant, J. P., Deroin, J. P., and Polidori, 1994, Multi-resolution analysis of radar images and its application to lithological and structural mapping; Larzac (South France) test site, *Int. J. Remote Sensing*, V.15, N.12, 2451-2468.
- [50] Elachi, C., 1980, Spaceborne imaging radar: geologic and oceanographic applications, *Science*, V.209, N.4461.
- [51] Evans, D. L., Farr, T. G., Ford, J. P., Thompson, T. W., and Werner, C. L., 1986, Multipolarization radar images for geologic mapping and vegetation discrimination, *IEEE Transactions on Geoscience and Remote Sensing*, V. GE 24, N.2, 246-257.
- [52] Yamaguchi, Y., 1985, Image-scale and look-direction effects on the detectability of lineaments in radar images, *Remote Sensing of Environment*, V.17, 117-127.
- [53] McCauley, J. F., Schaber, G. G., et al, 1982, Subsurface valleys and geoarchaeology of the eastern Sahara revealed by shuttle radar, *Science*, V.218, 1004-1020.

- [54] Weszka, J. S., Dyer, C. R., and Rosenfeld, A., 1976, A comparative study of texture measures for terrain classification, *IEEE Transactions on Systems, Man, and Cybernetics*, V.SMC-6, N. 4, 269-285.
- [55] Moore, G. K., 1983, Objective procedures for lineament enhancement and extraction, *Photogrammetric Engineering and Remote Sensing*, V. 49, N. 5, 641-647.
- [56] Pratt, W. K., 1991, *Digital Image Processing*, John Wiley & Sons Publishing Company.
- [57] Low, A., 1991, *Introductory Computer Vision and Image Processing*, McGraw-Hill Publishing Company.
- [58] Hsu, Shin-y., 1978, Texture tone analysis for automated land-use mapping, *Photogrammetric Engineering and Remote Sensing*, V. 44, N. 11, 1393-1404.
- [59] Hsu, Shin-y, 1986, Rock Type Discrimination with AI-Based texture analysis algorithms, In: *Proc. of Annual Meeting of ASPRS/AGSM*, (Washington, 1986), 169-178.
- [60] Gonzalez, R. G., and Woods, R. E., 1992, *Digital Image Processing*, Addison-Wesley Publishing Company.
- [61] Carrere,V.,1990, Development of multiple source data processing for structural analysis at regional scale, *Photogrammetric Engineering and Remote Sensing*, V.56, N.5, 587-595.
- [62] He, D. C., and Wang, L., 1990, Texture unit, texture spectrum, and textural analysis, *IEEE Transactions on Geoscience and Remote Sensing*, V.28, N.4, 509-512.
- [63] Wang, L., and He, D. C., 1990, A new statistical approach for texture analysis, *Photogrammetric Engineering and Remote Sensing*, V. 56, N. 1, 61-66.
- [64] Gong, P., Marceau, D. J., and Howarth, P. J., 1992, A comparison of spatial feature extraction algorithms for land-use classification with SPOT HRV data, *Remote Sensing of Environment*, V. 40, 137-151.
- [65] Haralick, R., Shanmugam, K., and Dinstein, I., 1973, Textural features for image classification, *IEEE Transactions on Systems, Man, and Cybernetics*, V.3, N.6, 611-621.
- [66] Franklin, S., and Peddle, D., 1990, Classification of SPOT HRV imagery and texture features, *Int. J. Remote Sensing*, V.11, N.3, 551-556.

- [67] Peddle, D., and Franklin, S. E., 1991, Image texture processing and data integration for surface pattern discrimination, *Photogrammetric Engineering and Remote Sensing*, V. 57, N. 4, 413-420.
- [68] Masuoka, P., Harris, J., and Lowman, P., 1988, Digital Processing of orbital radar data to enhance geologic structure: examples from the Canadian Shield, *Photogrammetric Engineering and Remote Sensing*, V.54, N.5, 621-632.
- [69] Excell, P. S., Campbell, D., Dodd, A., Newby, S., and Stevens, R., 1989, Classification of quasi-periodic textures in thematic mapper scenes using Fourier transforms, In: *Proc. of the 15th Annual Conference of the Remote Sensing Society*, 123-128.
- [70] Marceau, D., Howarth, P., Dubois, J., and Gratton, D., 1990, Evaluation of the gray-level co-occurrence matrix method for land-cover classification using SOPT imagery, *IEEE Transactions on Geoscience and Remote Sensing*, V.28, N.4, 513-519.
- [71] Baraldi, A., and Parmiggiani, F., 1995, An investigation of the textural characteristics associated with gray level co-occurrence matrix statistical parameters, *IEEE Transactions on Geoscience and Remote Sensing*, V.33, N.2, 293-304.
- [72] Hall, D. L., 1992, *Mathematical Techniques in Multisensor Data Fusion*, Artech House.
- [73] Gerstl, S. A., 1990, Physics concepts of optical and radar reflectance signatures, A summary review, *Int. J. Remote Sensing*, V.11, N.7, 1109-1117.
- [74] Karbuz, M. R., Olesen, D.R.O., Gabrielsen, R.H., and Herrevold, T., 1993, Application of multiple data sets to structural studies on Varagner Peninsula, Northern Norway, *Int. J. Remote Sensing*, V.14,N.5, 979-1003.
- [75] Hutchinson, C. F., 1982, Techniques for combining Landsat and ancillary data for digital classification improvement, *Photogrammetric Engineering and Remote Sensing*, V.48, N.1, 123-130.
- [76] Toet, A., van Ruyven, L. J., and Valenton, J. M., 1989, Merging thermal and visual images by a contrast pyramid, *Optical Engineering*, V. 28, N. 7, 789-792.
- [77] Toet, A., 1992, Multi-scale contrast enhancement with application with image fusion, *Optical Engineering*, V. 31, 1026-1031.
- [78] Burt, P. J., 1985, Merging images through pattern decomposition, *SPIE Applied Digital Image Processing*, V. 575, N. 3, 173-181.

- [79] Burt, P. J., and Kolczynski, R. J., 1993, Enhanced image capture through fusion, In: *IEEE 4th Int. Conference in Computer Vision*, V. 4, 173-182.
- [80] Wilson, T. A., Rogers, S. K., and Kabrisky, M., 1997, Perceptual-based image fusion for hyperspectral data, *IEEE Transactions on Geoscience and Remote Sensing*, V. 35, N. 4, 1007-1017.
- [81] Yesou, H., Besnus, Y., Rolet, J., Pion, J. C., and Aing, A., 1993, Merging Seasat and SPOT imagery for the study of geological structures in a temperate agricultural region, *Remote Sensing of Environment*, V.43, 265-279.
- [82] Daily, M. I., Farr, T., and Elachi, C., Schaber, G., 1979, Geologic interpretation from composited radar and Landsat imagery, *Photogrammetric Engineering and Remote Sensing*, V.45, N.8, 1110-1116.
- [83] Pohl, C., and van Gendren, J.L., 1993, Geometric integration of multi-image information, In: *Proc. Second ERS-1 Symposium-Space at the Service of our Environment*, Hamburg, Germany, ESA SP-361.
- [84] Pohl, C., and van Genderen, J. L., 1994, Multisensor fusion: optimization and operationalisation for mapping applications. *SPIE Proceedings, Conference on Signal Processing, Sensor Fusion & Target Recognition III*, Orlando, Florida, USA, 4-6 April 1994, P.17-25.
- [85] Van Zuidam, R. A., Pohl, C., and van Genderen, 1994, Synergy of remotely sensed data for coastal environmental studies: The Ameland-Waddensea example, Northern Netherlands, *Second Thematic Conference on Remote Sensing for Marine and Coastal Environments*, New Orleans, Louisiana, 323-334.
- [86] Lichtenegger, J., 1991, Combining optical/Infrared and SAR images for improved remote-sensing interpretation, *ESA Bulletin*, N.66, 119-121.
- [87] Lichtenegger, J., Dallemand, J. F., Reichert, P., and Rebillard, P., 1991, Multi-sensor analysis for land use mapping in Tunisia, *Earth Observation Quarterly* B. N.33, 1-6.
- [88] Nezry, E., Mougin, E., Lopes, A., and Gastellu-Etchegorry, 1993, Tropical vegetation mapping with combined visible and SAR spaceborne data, *Int. J. Remote Sensing*, V.14, N.11, 2165-2184.
- [89] Raymond, D., Deffontaines, B., and Rudant, J. P., 1994, Morphostructural analysis, radar and SPOT image interpretation as tools for petroleum exploration: an example from the Gabian-Pezenas area (Herault, Southern France), *Int. J. Remote Sensing*, V.15, N.12, 2469-2479.

- [90] Rothery, D. A., and Francis, P. W., 1987, Synergistic use of MOMS-01 and Landsat TM data, *Int. J. Remote Sensing*, V.8, N.3, 501-508.
- [91] Rothery, D. A., 1988, MOMS-1 used synergistically with Landsat TM, In: *Proc. 4th International Colloquium on Spectral Signatures of Objects in Remote Sensing*, Aussois, France, 18-22 January 1988 (ESA SP-287, April 1988).
- [92] Henkel, J., Terhalle, U., and Zilger, J., 1988, Digital analysis of MOMS-1, Landsat-TM and SPOT data of the Nakuru area (Kenya), In: *Proc 4th International Colloquium on Spectral Signatures of Objects in Remote Sensing*, Aussois, France, 18-22 January 1988 (ESA SP-287, April 1988).
- [93] Franklin, S. E., and Blodgett, C. F., 1993, An example of satellite multisensor data fusion, *Computers & Geosciences*, V.19, N.4, 577-583.
- [94] Rast, M., 1985, Digital combination of SAR and MSS optical data for identification of spectral signatures, In: *Proc. 4th International Colloquium on Spectral Signatures of Objects in Remote Sensing*, Les Arcs, France, 16-20 Dec. 1985 (ESA SP-247).
- [95] Paris, J. F., and Kwong, H. H., 1988, Characterization of vegetation with combined thematic mapper (TM) and shuttle imaging radar (SIR-B) image data, *Photogrammetric Engineering and Remote Sensing*, V.54, N.8, 1187-1193.
- [96] Leckie, D. G., 1990, Synergism of synthetic aperture radar and visible/infrared data for forest type discrimination, *Photogrammetric Engineering and Remote Sensing*, V.56, N.9, 1237-1246.
- [97] Cliche, G., Bonn, F., and Teillet, P., 1985, Integration of the SPOT panchromatic channel into its multispectral mode for image sharpness enhancement, *Photogrammetric Engineering and Remote Sensing*, V.51, N.3, 311-316.
- [98] Chavez, P.S., 1986, Digital merging of Landsat TM and digitized NHAP data for 1:24,000 scale image mapping, *Photogrammetric Engineering and Remote Sensing*, V.52, N.10, 1637-1646.
- [99] Welch, R., and Ehlers, M., 1987, Merging multiresolution SPOT HRV and Landsat TM data, *Photogrammetric Engineering and Remote Sensing*, V.53, N.3, 301-303.
- [100] Chavez, P. S., Sides, S. C., and Anderson, J. A., 1991, Comparison of three different methods to merge multiresolution and multispectral data: Landsat TM and SPOT panchromatic, *Photogrammetric Engineering and Remote Sensing*, V.57, N.3, 295-303.
- [101] Evans, D., 1988, Multisensor classification of sedimentary rocks, *Remote Sensing of Environment*, V.25, 129-144.

- [102] Haak, B. N., and Slonecker, E. T., 1994, Merged spaceborne radar and thematic mapper digital data for locating villages in Sudan, *Photogrammetric Engineering and Remote Sensing*, V.60, N.10, 1253-1257.
- [103] Welch, R., and Ehlers, M., 1988, Cartographic feature extraction with integrated SIR-B and Landsat TM images, *Int. J. Remote Sensing*, V.9, N.5, 873-889.
- [104] Munechika, K. C., Warnick, J.S., Salvaggio, C., and Schott, J.R., 1993, Resolution enhancement of multispectral image data to improve classification accuracy, *Photogrammetric Engineering and Remote Sensing*, V.59, N.1, 67-72.
- [105] Toll, D., 1985, Analysis of digital LANDSAT MSS and SEASAT SAR data for use in discriminating land cover at the urban fringe of Denver, Colorado, *Int. J. Remote Sensing*, V.6, N.7, 1209-1229.
- [106] Carper, W. J., Lillesand, T. M., and Kiefer, R. W., 1990, The use of intensity-hue-saturation transformations for merging SPOT panchromatic and multispectral image data, *Photogrammetric Engineering and Remote Sensing*, V.56, N.4, 459-467.
- [107] Grasso, D. N., 1993, Applications of the IHS color transformation for 1:24,000 scale geologic mapping: a low cost SPOT alternative, *Photogrammetric Engineering and Remote Sensing*, V.59, N.1, 37-80.
- [108] Daily, M., 1983, Hue-saturation-intensity split-spectrum processing of Seasat radar imagery, *Photogrammetric Engineering and Remote Sensing*, V.49, N.3, 349-355.
- [109] Harris, J. R., and Murray, R., 1990, IHS transform for the integration of radar imagery with other remotely sensed data, *Photogrammetric Engineering and Remote Sensing*, V.56, N.12, 1631-1641.
- [110] Edwards, K., and Davis, P. A., 1994, The use of intensity-hue-saturation transformation for producing colour shaded relief images, *Photogrammetric Engineering and Remote Sensing*, V.60, N.11, 1369-1374.
- [111] Vrabel, J., 1996, Multispectral imagery band sharpening study, *Photogrammetric Engineering and Remote Sensing*, V.62, N.9, 1057-1083.
- [112] Chavez, P., Berlin, G. L., and Sowers, L. B., 1982, Statistical method for selecting Landsat MSS ratio, *Journal of Applied Photographic Engineering*, V.1, 23-30.
- [113] Sheffield, C., and Chase, C., 1985, Selecting band combination from multispectral data, *Photogrammetric Engineering and Remote Sensing*, V. 51, N.6, 681-687.

- [114] Liu, G., J., and Moore, J., 1989, Colour enhancement and shadow suppression techniques for TM images, In: *Proc. 7th thematic conference on remote sensing for exploration geology*, Calgary, Alberta, Canada, 901-915.
- [115] Haack, B., and Jampolar, S., 1995, Colour composite comparisons for agricultural assessments, *Int. J. Remote Sensing*, V. 16, N. 9, 1589-1598.
- [116] Sharma, S., 1996, *Applied Multivariate Techniques*, John Wiley & Sones, Inc.
- [117] Stroud, K. A., 1995, *Engineering Mathematics*, 5th edition, The Macmillan Press Ltd.
- [118] Foley, J. D., vanDam, A., Feiner, S. K., and Hughes, J. F., 1996, *Computer graphics: Principles and Practice* (second edition in C), Addison-Wesley Publishing Company.
- [119] PCI, Inc., 1995, EASI/PACE, (*Technical support personal communication*), Toronto, Ontario, Canada.
- [120] Kaufman, H., and Pfeiffer, B., 1988, Image optimization versus classification- an application oriented comparison of different methods by use of thematic mapper data, *Photogrammetria*, V.42, 311-324.
- [121] Metternicht, G., 1995, Dealing with insufficient discrimination among informational categories: SPOT XS and ERS-1 data fusion, In: *Proc. Annual Conference of Remote Sensing Society*, 11-14 Sept. 1995, Southampton. U.K. 1267-1273.
- [122] Solberg, A. H., Jain, A. K., and Taxt, T., 1994, Multisource classification of remote sensed data: fusion of Landsat TM and SAR images, *IEEE Transactions on Geoscience and Remote Sensing*, V. 32, N.4, 768-777.
- [123] Lozano-Garcia, D. F., and Hoffer, R. M., 1993, Synergistic effects of combined Landsat TM and SIR-B data for forest resources assessment, *In. J. Remote Sensing*, V. 14, N. 14, 2677-2694.
- [124] Landgrebe, D. A., 1980, The development of a spectral-spatial classifier for Earth observational data, *Pattern Recognition*, V. 12, 165-175.
- [125] Arai, K., 1993, A classification method with a spatial-spectral variability, *Int. J. Remote Sensing*, V. 14, N. 4, 699-709.
- [126] Dobson, M. G., Ulaby, F., and Pierce, L. E., 1995, Land-cover classification and estimation of terrain attributes using Synthetic Aperture Radar, *Remote Sensing of Environment*, V. 51, 199-214.

- [127] Lopo, A., Chic, O., and Casterad, A., 1996, Classification of Mediterranean crops with multisensor data: per-pixel *versus* per-object statistics and image segmentation, *Int. J. Remote Sensing*, V. 17, N. 12, 2385-2400.
- [128] Gong, P., and Howarth, P. J., 1992, Frequency-based contextual classification and gray-level vector reduction for land-use identification, *Photogrammetric Engineering and Remote Sensing*, V. 58, N. 4, 423-437.
- [129] Gong, P., and Howarth, P., 1990, The use of structural information for improving land-cover classification accuracies at the Rural-Urban fringe, *Photogrammetric Engineering and Remote Sensing*, V. 56, N. 1, 67-73.
- [130] Fung, T., and Chan, K., 1994, Spatial composition of spectral classes: A structural approach for image analysis of heterogeneous land-use and land-cover types, *Photogrammetric Engineering and Remote Sensing*, V. 60, N. 2, 173-180.
- [131] Pultz, T. J., and Brwon, R. J., 1987, SAR image classification of agricultural targets using first- and second- order statistics, *Canadian Journal of Remote Sensing*, V. 13, N. 2, 85-91.
- [132] Benediktsson, J., Swain, P., and Ersoy, O., 1990, Neural network approaches versus statistical methods in classification of multisource remote sensing data, *IEEE Transactions on Geoscience and Remote Sensing*, V. 28, N. 4, 540-551.
- [133] Franklin, S., E., and Wilson, B. A., 1991, Spatial and spectral classification of remote-sensing imagery, *Computer & Geosciences*, V. 17, N. 8, 1151-1172.
- [134] Franklin, S., E., and Wilson, B. A., 1992, A three-stage classifier for remote sensing of mountainous environments, *Photogrammetric Engineering and Remote Sensing* V. 58, N. 4, 449-454.
- [135] Johnsson, K., 1994, Segment-based land-use classification from SPOT Satellite data, *Photogrammetric Engineering and Remote Sensing*, V. 60, N. 1, 47-53.
- [136] Wang, D., He, D.-C, and Benie, B., 1995, A line-preserving post-processing technique for maximum likelihood classification of SAR images, *Int. J. Remote Sensing*, V. 16, N. 11, 2081-2087.
- [137] Wang, M., and Howarth, P., 1993, Modelling errors in remote sensing image classification, *Remote Sensing of Environment*, V. 45, 261-271.
- [138] Congalton, R. G., 1991, A review of assessing the accuracy of classification of remotely sensed data, *Remote Sensing of Environment*, V. 37, 35-46.
- [139] Fitzgerald, R. W., and Lees, B. G., 1994, Assessing the classification accuracy of multisource remote sensing data, *Remote Sensing of Environment*, V. 47, 362-368.

- [140] Fisher, P. F., 1994, Visualisation of the reliability in classified remotely sensed images, *Photogrammetric Engineering and Remote Sensing*, V. 60, N. 7, 905-910.
- [141] Press, W., Flannery, B., Teukolsky, S., and Vetterling, W., 1988, *Numerical Recipes in C*, Cambridge University Press.
- [142] Mather, P. M., 1989, *Computer Processing of Remotely Sensed Images, An Introduction*, John Wiley & Sons.
- [143] Dobson, M. C., Pierce, L., Sarabandi, K., Ulaby, F. T., and Sharik, T., 1992, Preliminary analysis of ERS-1 SAR for forest ecosystem studies, *IEEE Transactions on Geoscience and Remote Sensing*, V.30, N.2, 203-211.

Programming References

Including the references 57, 118, and 141, the references listed below have been used during the programming work of this thesis.

- Lindley, C. A., 1991, *Practical Image Processing in C*, John Wiley & Sons.
- Stroo, E., (editor), 1990, *The Waite Group's Microsoft Quick C Programming*, Microsoft Press.
- The Math Works Inc. 1992, "*MATLAB, high performance numeric computation and visualization software. Reference guide*".